ABSTRACT

Title of dissertation: PHASE TRANSITIONS IN ENGINEERED ULTRACOLD QUANTUM SYSTEMS

Ryan M. Price, Doctor of Philosophy, 2016

Dissertation directed by: Dr. Ian Spielman
Department of Physics

The study of quantum degenerate gases has many applications in topics such as condensed matter dynamics, precision measurements and quantum phase transitions. We built an apparatus to create 87Rb Bose-Einstein condensates (BECs) and generated, via optical and magnetic interactions, novel quantum systems in which we studied the contained phase transitions.

For our first experiment we quenched multi-spin component BECs from a miscible to dynamically unstable immiscible state. The transition rapidly drives any spin fluctuations with a coherent growth process driving the formation of numerous spin polarized domains. At much longer times these domains coarsen as the system approaches equilibrium.

For our second experiment we explored the magnetic phases present in a spin-1 spin-orbit coupled BEC and the contained quantum phase transitions. We observed ferromagnetic and unpolarized phases which are stabilized by the spin-orbit couplings explicit locking between spin and motion. These two phases are separated by a critical curve containing both first-order and second-order transitions joined at a critical point. The narrow first-order transition gives rise to long-lived metastable states.

For our third experiment we prepared independent BECs in a double-well potential, with an artificial magnetic field between the BECs. We transitioned to a single BEC by lowering the barrier while expanding the region of artificial field to cover the resulting single BEC. We compared the vortex distribution nucleated via conventional dynamics to those produced by our procedure, showing our dynamical process populates vortices much more rapidly and in larger number than conventional nucleation.

PHASE TRANSITIONS IN ENGINEERED ULTRACOLD QUANTUM SYSTEMS

by

Ryan M. Price

Dissertation submitted to the Faculty of the Graduate School of the
University of Maryland, College Park in partial fulfillment
of the requirements for the degree of
Doctor of Philosophy
2016

Advisory Committee:
Dr. Ian Spielman, Advisor
Professor Steven Rolston, Chair
Professor Victor Galitski
Dr. Alexey Gorshkov
Professor Chris Reynolds

Table of Contents

Chapter 1

Introduction

Bose-Einstein condensates (BECs), a quantum state of matter first predicted by Satyendra Nath Bose and Albert Einstein in 1924, describe a macroscopic occupation of bosonic particles into their ground state. With the advent of new laser cooling techniques in the 1980s and early 1990s [1–4], the first experimental generation of BEC was achieved in 1995 [5, 6], with Eric Cornell, Carl Wieman and Wolfgang Ketterle earning the Nobel prize in 2001 for their achievements in the field. Not long after, the field for studying ultracold degenerate gases exploded with research such as creating degenerate fermions [7], observations of superfluidity [8] and the realization of periodic lattice systems, such as the Bose-Hubbard model [9].

The experimental techniques of atomic physics together with ultracold degenerate gases lend themselves well to acting as quantum simulators. The experimental tools of atomic and optical physics has a great track record for yielding high precision measurements, including the creation of atomic clocks that keep time over the age of the universe [10], measure the electron dipole moment to 1 part in 10^{-29} [11], provide super sensitivity for searching for gravitational waves [12] or other scientific endeavors [13–15]. By using similar techniques, we can have high precision control of interactions and potentials that a trapped degenerate gas is subjected. By using optically or magnetically engineered interaction in degenerate gases, both naturally occurring systems and novel quantum systems can be engineered and studied. The thesis is focused on the use of ^{87}Rb BECs subjected to engineered potentials to study novel quantum systems.

1.1 Thesis Overview

Chapter 2 discusses a brief introduction to the physics of Bose-Einstein Condensates

Chapter 3 provides a overview of the methods of laser cooling and trapping used in the experiment to bring atomic gases to the degenerate regime

Chapter 4 provides an overview of the RbLi experimental apparatus. This includes the information about the vacuum system, various laser setups, computer data control and acquisition systems and electromagnetic coil design and control.

Chapter 5 discusses the dynamics of spin dependent interactions. Here we quench a two spin component condensate from a condition which is miscible to an immiscible state. The spin-dependent interactions drive the dynamics of spin domain formation and coarsening.

Chapter 6 explores the physics and implementation of Raman coupling in our experiment. Also discussed is the physics and and implementation of a spin 1 system in the $F = 1$ hyperfine ground state of ^{87}Rb.

Chapter 7 extends the physics of the spin-1 system to a system with magnetic ordering. Interestingly we find that a spin-1 SOC system contains phase transitions of first and second order.

Chapter 8 describes the novel nucleation method of vortices in a BEC subjected to synthetic magnetic fields. Common methods to generate high vortex number utilize rapid rotation that generates vortices on the edge of the system and slowly relax into the bulk of the condensate. By contrast, here I explored a system with engineered high magnitude, localized synthetic magnetic fields between two separated BECs. The low density and high magnetic field drives rapid generation, and high number, of vortices in the system.

Appendix A covers the theory of operation and implementation of the flux gate magnetic field stabilization system.

Appendix B discusses the FPGA instrumentation system that I had developed.

Chapter 2

An Overview of Bose-Einstein Condensation Theory

Bose-Einstein Condensation is the quantum phenomenon wherein an ensemble of bosons, particles with an integer unit of total angular momentum, will all occupy the ground state of the system, forming a quantum state of matter. This process occurs when a combination of high particle density and low temperatures crosses a critical value, formulated ahead in Section 2.1.2. Here I describe the basic mechanisms and relationships for the physics of Bose-Einstein condensates (BECs) mostly as a supplementary reference to the physics studied in our experiment (Chapters 5, 7, and 8). For readers interested in a much more comprehensive description of the physics involving Bose-Einstein condensation, I would refer them to the texts by Pethick and Smith [16] or by Pitaevskii and Stringari [17].

2.1 Origins of Bose-Einstein Condensation

All matter can be described in the context of matter-wave duality, wherein a particle has an associated matter wave length, given by the de Broglie wavelength $\lambda_{\mathrm{DB}} = h/p$ where h is Planck's constant and p is the momentum of the particle [18]. In most cases, the classical model of particles described by hard spheres or point particles is valid, for at high temperatures the atomic wavepacket is smaller than typical sizes of the atom. By

combining the formalism for the momentum $p = mv$, and the equipartition theorem for free particles[1] we can define the de Broglie wavelength:

$$\lambda_{\mathrm{DB}} = \frac{h}{\sqrt{3mk_{\mathrm{B}}T}} \tag{2.1}$$

With k_{B} being Boltzmann's constant. For a gas with N particles in a volume V, the equilibrium density will be $n = N/V$ particles per volume. For example's sake we say each particle occupies a uniform volume, we can approximate the average inter-atomic spacing as $d \sim n^{-1/3}$. We can calculate a critical temperature T_{C} when the de Broglie wavelength is on the order of the inter-particle spacing:

$$T_{\mathrm{C}} \sim \frac{h^2 n^{2/3}}{mk_{\mathrm{B}}} \tag{2.2}$$

From this simple argument for a uniform gas we can see the critical temperature in which condensation occurs depends primarily on the density of the particles. With an even more basic approach of simply arranging the relevant units of the system to form a temperature will yield the relationship in Equaiton 2.2 [16]. That said, the derivation of the critical temperature for condensation is derived in the following sections.

2.1.1 Bose-Einstein Statistics

In classical physics the statistical mechanics of a system of many particles, such as a gas, is characterized by the Maxwell-Boltzmann distribution, a probability density function that describes the probability of a particle possessing a given velocity. Maxwell-Boltzmann statistics for distinguishable particles can similarly model the probability of a particle possessing a given energy:

$$p(E) = e^{-(E-\mu)/(k_{\mathrm{B}}T)} \tag{2.3}$$

Where k_{B} is Boltzmann's constant, T is the temperature of the ensemble, and μ is the chemical potential. However, this distribution of energies applies to classical, distinguish-

[1] the equipartition theorem states that for a given temperature, the energy will be evenly distributed into all degrees of freedom. For a monoatomic gas, the three translation modes gives $\frac{1}{2}m\langle v\rangle^2 = \frac{3}{2}k_{\mathrm{B}}T$.

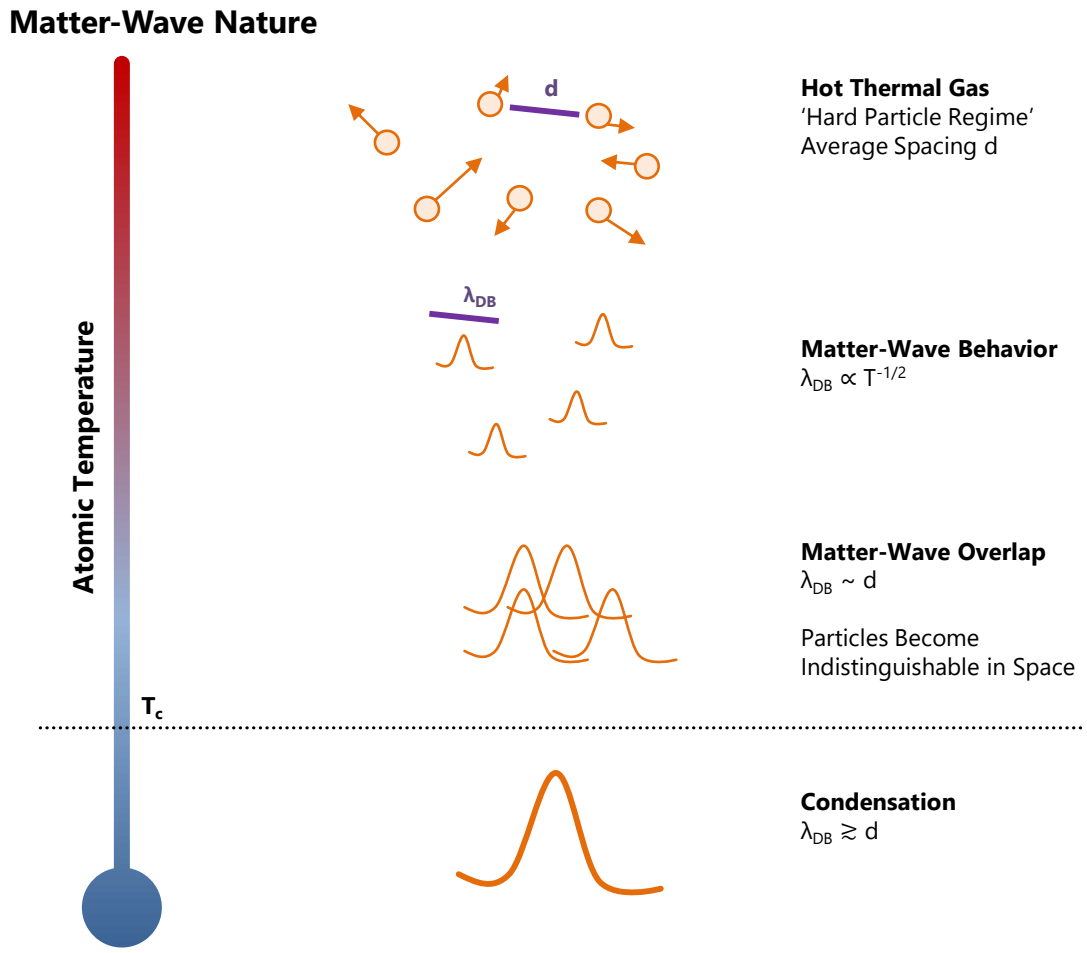

Figure 2.1: At high temperatures, using a 'billiard ball' model of atoms colliding is valid. As temperatures lower, the de Broglie wavelength becomes larger and the matter-wave nature becomes evident. Once the associated wavelength is large enough, the atoms become coherent, and in the case of bosons, condense. Wonderful figure adapted from the Ketterle MIT group website.

able particles. If we have an ensemble of identical bosons, particles with integer spin, we lose distinguishable nature, and the distribution is now described by the Bose-Einstein distribution:

$$p(E) = \frac{1}{e^{(E-\mu)/(k_{\mathrm{B}}T)} - 1} \tag{2.4}$$

Note that in the limit of high temperatures, the Bose-Einstein distribution becomes equivalent to the Maxwell-Boltzmann distribution. For the derivation of the statistics for both classical and indistinguishable particles from microcanonical or grand canonical approaches, I recommend reading the statistical mechanics book by Pathria [19].

2.1.2 Critical Temperature for Condensation

The interesting difference between the two probability distributions comes in at *low* temperatures. If we have N atoms in an atomic ensemble, we should be able to sum along the probability distribution in steps of energy along with the degeneracy in energies and get a result of N as well. This gives us an the relationship:

$$N = \int_0^\infty p(E)d(E)\,\mathrm{d}E \tag{2.5}$$

Where $p(E)$ is the probability of occupation at an energy E, and $d(E)$ is the density of states, a measure of the degeneracy of the states in the system. It is worth mentioning that the Bose-Einstein distribution requires that the chemical potential μ is always less than the lowest energy in the system, E_0. For an arbitrary density of states function, we require that the integrand is a positive value as the probability and the density of states are both positive semi-definite quantities[2]. Combining Equation 2.4 and Equation 2.5. In expanded form, we have:

$$N = \int_0^\infty \frac{d(E)}{e^{(E-\mu)/(k_\mathrm{B}T)} - 1}\,\mathrm{d}E \tag{2.6}$$

As stated, $d(E)$ must be positive as it is a function that counts the available energy levels nearby the energy E. For entire integrand to be positive, we require the exponent in the denominator to be greater than zero:

$$(E_i - \mu)/(k_\mathrm{B}T) \geq 0 \tag{2.7}$$

$$\therefore E_i \geq \mu \quad \forall\, E_i \tag{2.8}$$

Which implies that independent of the specifics of the energy levels and degeneracy of the system, the chemical potential must be lower than the ground state energy level.

If we consider the system in a box, specifically a three dimensional infinite square well potential, the allowed energies go as $E = \hbar^2 k^2/2m$, with the vector k having components

[2] I'm not one to define negative probability or a negative counting of energy levels

$k_i = \pi n_i / L_i$, where n_i is the energy level in the square potential in the $\hat{\mathbf{e}}_i$ direction, and L_i is the size of the box in the $\hat{\mathbf{e}}_i$ direction. This gives us a density of states [20]:

$$d(k) = \frac{Vk^2}{2\pi^2} dk \tag{2.9}$$

If we rewrite Equation 2.9 using the relationship $E = \hbar^2 k^2 / 2m$, and for simplicity use the standard thermodynamic definition $\beta = 1/k_{\mathrm{B}}T$, we can rewrite the particle number N more cleanly as:

$$N = \frac{Vm^{3/2}}{\sqrt{2}\pi^2\hbar^3} \int_0^\infty \frac{E^{1/2}}{e^{\beta(E-\mu)} - 1} \, \mathrm{d}E \tag{2.10}$$

This expression is analytically unsolvable. However, in the special case of $\mu = 0$, $T = T_c$, we can evaluate the integral, yielding the critical temperature for condensation. Using Equation 2.10 and noting that $N/V = n$, the density of the gas, and making the substitution $x = \beta E$:

$$N/V = n = \frac{m^{3/2}}{\sqrt{2}\pi^2\hbar^3\beta^{3/2}} \int_0^\infty \frac{x^{1/2}}{e^x - 1} \, \mathrm{d}x \tag{2.11}$$

The integral, in terms of x, can be evaluated by the identity:

$$\int_0^\infty \frac{x^{s-1}}{e^x - 1} \, \mathrm{d}x = \Gamma(s)\zeta(s) \tag{2.12}$$

Where Γ is the Gamma function, and ζ is the Riemann Zeta function. Using this identity in Equation 2.11 and solving for the temperature T, we get:

$$T_c = \frac{2\pi\hbar^2 n^{2/3}}{m k_{\mathrm{B}}} \zeta(3/2)^{-2/3} \tag{2.13}$$

Which has a similar functional form as the quick derivation in Equation 2.2, but with a well defined constant of proportionality. Furthermore, we can define a quantity called the phase space density ρ such that $\rho = n\lambda_{\mathrm{DB}}^3$ which describes the number of particles contained in a volume given by λ_{DB}^3. When $\rho \simeq 1$, the atomic wavefunctions begin to overlap at the beginning of condensation. To increase the phase space density in the

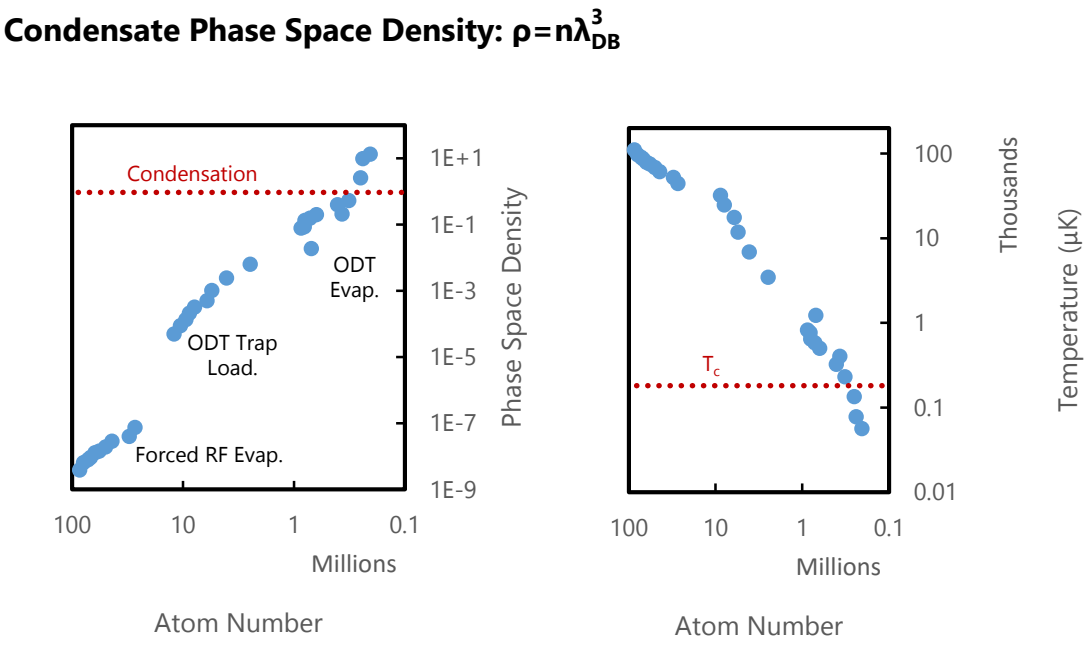

Figure 2.2: Calculations of the phase space density ρ during our evaporative cooling stages discussed in Chapter 3

experiment, we deploy laser cooling and evaporative cooling techniques (Chapter 3) to simultaneously increase the density and lower the temperature to approach $\rho \sim 1$ (Figure 2.2).

2.1.3 The Condensate Fraction

To determine the number of particles in the system that have condensed into the ground state, we can consider the particle number $N_{\mathrm{Tot}} = N_0 + N_{\mathrm{ex.}}$. We can quickly compute the number of particles in the ground state, N_0 using Equation 2.4. For systems with a large number of particles, we can make the approximation of $\mu = 0$ for the excited states as $E_1 - \mu \simeq E_1 - k_{\mathrm{B}}T/N_0 \simeq E_1$. Therefore, as in Equation 2.5, we can calculate the number of particles in the excited states:

$$N_{\mathrm{ex.}} = \int_0^{\infty} \frac{d(E)}{e^{\beta E} - 1}\, \mathrm{d}E \tag{2.14}$$

Where d(E) is the density of states for the given system. We are interested in the condensed fraction of atoms, that is:

$$\frac{N_0}{N_{\mathrm{Tot}}} = \frac{N_{\mathrm{Tot}} - N_{\mathrm{ex.}}}{N_{\mathrm{Tot}}} = 1 - \frac{N_{\mathrm{ex.}}}{N_{\mathrm{Tot}}} \tag{2.15}$$

Using Equation 2.13 and solving Equation 2.14 as before for a general temperature T, we get the condensate fraction for a gas in a box:

$$\frac{N_0}{N_{\mathrm{Tot}}} = 1 - \left(\frac{T}{T_c}\right)^{3/2} \tag{2.16}$$

2.1.4 Condensation Requirements in a Harmonic Trap

In most (if not all) ultracold gases experiments, the condensates are confined in a harmonic confinement potential: $V(x,y,z) = \frac{1}{2}m\left(\omega_x^2 x^2 + \omega_y^2 y^2 + \omega_z^2 z^2\right)$. The harmonic confinement geometry changes the conditions for condensation, as understood through Equation 2.5. However, the same procedure can be repeated as in the previous sections, the difference being that we calculate the density of states for the 3D harmonic oscillator. For a harmonic potential, the energy levels are $E = \hbar\omega_x(n_x + 1/2) + \hbar\omega_y(n_y + 1/2) + \hbar\omega_z(n_z + 1/2)$ with the integer $n_i \geq 0$. The harmonic oscillator is wonderful because the states are evenly spaced in energy, and the primary axes are not coupled together in a complex fashion. Calculating the density of states gives:

$$d(E) = \frac{E^2}{2\hbar^3\bar{\omega}^3}\,\mathrm{d}E \tag{2.17}$$

Where $\bar{\omega}^3 = \omega_x\omega_y\omega_z$, is the geometric mean of the harmonic potential frequencies. Following the method in Section 2.1.2, the critical temperature for condensation in the harmonic trap is:

$$T_c = \frac{\hbar\bar{\omega}}{k_{\mathrm{B}}}\left(\frac{n}{\zeta(3)}\right)^{1/3} \tag{2.18}$$

$$\approx 0.9405\frac{\hbar\bar{\omega}n^{1/3}}{k_{\mathrm{B}}} \tag{2.19}$$

The major difference here is that the critical temperature goes as the cube root of the density, not to the power 2/3. Similarly the condensate fraction is modified:

$$\frac{N_0}{N_{\text{Tot}}} = 1 - \left(\frac{T}{T_c}\right)^3 \tag{2.20}$$

The cubic power to the condensate fraction value for a harmonically confined condensate assists us in creating a large condensed fraction with less cooling. The intuitive explanation is that unlike a uniform gas in a box, the harmonic potential will have a region of high density at the center, helping the condensation process.

From performing the exercise of deriving the critical temperature twice for different geometry, a pattern emerges wherein the form of the critical temperature depends on the functional form of the density of states. Consider a generic density of states:

$$d(E) = c_d E^{p-1}\,\mathrm{dE} \tag{2.21}$$

Where c_d is a constant prefactor, and $p-1$ is the power law exponent of the density of states. It follows then, using the arguments as before, that the critical temperature for condensation is:

$$T_c = \left(\frac{n}{c_d \Gamma(p)\zeta(p)}\right)^{1/p} \tag{2.22}$$

This confinement agnostic form for the critical temperature shows the strong dependence between the type of confinement and the critical temperature required for condensation. This form is also helpful when calculating critical temperatures for condensation in different dimensional systems, as that information is contained in the density of states. For example, the density of states of a harmonic oscillator in an arbitrary number of dimensions can be calculated readily as the constant level spacing allows the system to be treated as a convolution of independent oscillators:

$$d_{\text{HO}}(E, l) = \frac{E^{l-1}}{(l-1)! \prod_{i=1}^{l} \hbar\omega_i}\,\mathrm{d}E \tag{2.23}$$

Where l is the number of dimensions[3] and ω_i is the harmonic oscillator frequency in the

[3] I would use a more intuitive n, but that is defined as the density

$\hat{\mathbf{e}}_i$ direction. So we can quickly calculate the critical temperature for an arbitrary number of dimensions as:

$$T_c = \left(\frac{n}{\Gamma(l)\zeta(l)(l-1)! \prod_{i=1}^{l} \hbar\omega_i} \right)^{1/l} \tag{2.24}$$

Note that for $l = 1$, a one-dimensional geometry, $\zeta(1) = \infty$ signifying that condensation cannot occur in such a system. In a two dimensional system (the far limit of 'pancake' style confinement geometry where $\omega_z >> \omega_{x,y}$) we get:

$$T_c \approx \frac{0.78}{\hbar} \sqrt{\frac{n}{\omega_i \omega_j}} \tag{2.25}$$

We can extend this exercise to higher dimensions although I cannot fathom why, but I will leave that as an exercise to the reader if they have an interest.

2.2 Condensation with Atomic Interactions

In Section 2.1, the requirements for condensation I discussed in terms of a non-interacting gas. However, atoms in a gas do interact and this effect provides a density dependent interaction potential. For the purpose of describing interactions between two atoms in the ultracold gas, I will attempt to side-step the details of deriving scattering theory from first principles and instead present the requisite information and resources to derive the origin of the interaction energy in a condensate. The principles of quantum mechanical scattering theory can be found in both [21] and [20]. Chapter 5 of [16] provides a detailed description of deriving the effective interaction energy for a cold, dilute gas based upon scattering theory, as well as [22].

2.2.1 Effective Atomic Interaction Potentials

To account for the interactions of particles in the system, a model is used that makes the approximation that the scattering processes between atoms is low energy process, valid for atoms in a low temperature condensed state. This approximation allows us to only consider spherically symmetric s-wave scattering effects to model the more complex interatomic potentials as an effective hard sphere scattering process, where each atom has an effective radius $a_{\text{scat.}}$, the scattering length. From the references listed previously, one can find that the presence of interactions in the condensate approximated by this model provides an energy proportional to the density of the atoms, specifically:

$$V_{int}(\vec{\mathbf{r}}) = \frac{4\pi\hbar^2 a_{\text{scat.}}}{m} n(\vec{\mathbf{r}}) = g n(\vec{\mathbf{r}}) \tag{2.26}$$

For ^{87}Rb, $a_{\text{scat.}} \approx 100\, a_{\text{B}}$, where $a_{\text{B}} = 5.3 \cdot 10^{-11}$m. Therefore the effective 'size' of the atoms in collision processes is much larger than the actual extent of the atom.

Atomic species can have either positive or negative values of the scattering. Condensates with particles that have attractive interactions ($a_{\text{scat.}} < 0$) such as the more isotopically abundant ^{85}Rb ($a_{\text{scat.}} = -23.44 a_{\text{B}}$) can exist, however after a critical number of atoms, the condensate will collapse [23, 24]. By comparison, condensates with repulsive interactions ($a_{\text{scat.}} > 0$) such as in ^{87}Rb are in a stable configuration, independent of particle number. In systems with spin degrees of freedom, the interaction between atoms in different spin states can have varying scattering lengths, as described in Section 5.1.1.

Scattering lengths are also important for evaporative cooling stages (Section 3.3.1), which rely on the interaction of the atoms to rethermalize the ensemble after ejecting the most energetic members. For atomic species with small scattering lengths, the evaporative cooling mechanism is less effective. To cool them down, a technique known as sympathetic cooling [25, 26] uses a two-species setup[4]: one that is easy to cool and one that is not. However, the interaction between the two elements is effective enough such that the second species cools off by interacting with the first.

[4] Either different elements or isotopes of the same element

2.2.2 The Gross-Pitaevskii Equation

In the regime where describing the inter-atomic interactions in the condensate by the scattering length is valid, the Schrodinger equation is modified with the interaction term to become what is known as the Gross-Pitaevskii Equation (GPE) [27, 28]. The equation has the form:

$$i\hbar\frac{\partial}{\partial t}\psi(\vec{\mathbf{r}},t) = \left(-\frac{\hbar^2}{2m}\nabla^2 + V(\vec{\mathbf{r}}) + g|\psi(\vec{\mathbf{r}},t)|^2\right)\psi(\vec{\mathbf{r}},t) \tag{2.27}$$

If we require the conditions that $\psi(\vec{\mathbf{r}},t)$ satisfies the mean-field approximation [16] as:

$$N = \int |\psi(\vec{\mathbf{r}},t)|^2 \tag{2.28}$$

$$\psi(\vec{\mathbf{r}},t) = \phi(\vec{\mathbf{r}})e^{-i\mu t/\hbar} \tag{2.29}$$

Then for a system in equilibrium, the time-independent form becomes:

$$\mu\phi(\vec{\mathbf{r}}) = \left[-\frac{\hbar^2}{2m}\nabla^2 + V(\vec{\mathbf{r}}) + gn(\vec{\mathbf{r}})\right]\phi(\vec{\mathbf{r}}) \tag{2.30}$$

2.2.3 The Thomas-Fermi Approximation

In a system in which the kinetic energy term in the GPE (Equation 2.27) is much less than both the confining potential and interaction energy, we can make the *Thomas-Fermi Approximation* to eliminate the kinetic energy term [29]. If we assume that we are in a time-independent configuration for the condensate, we get:

$$\mu\phi(\vec{\mathbf{r}}) = \left[V(\vec{\mathbf{r}}) + gn(\vec{\mathbf{r}})\right]\phi(\vec{\mathbf{r}}) \tag{2.31}$$

Note here that we are investigating the cases where $\psi(\vec{\mathbf{r}}) \neq 0$. Rearranging terms give us the density profile of the condensate in the trapping potential:

$$n(\vec{\mathbf{r}}) = \begin{cases} \frac{1}{g}(\mu - V(\vec{\mathbf{r}})) & : \mu - V(\vec{\mathbf{r}}) > 0 \\ 0 & : \mu - V(\vec{\mathbf{r}}) \leq 0 \end{cases} \tag{2.32}$$

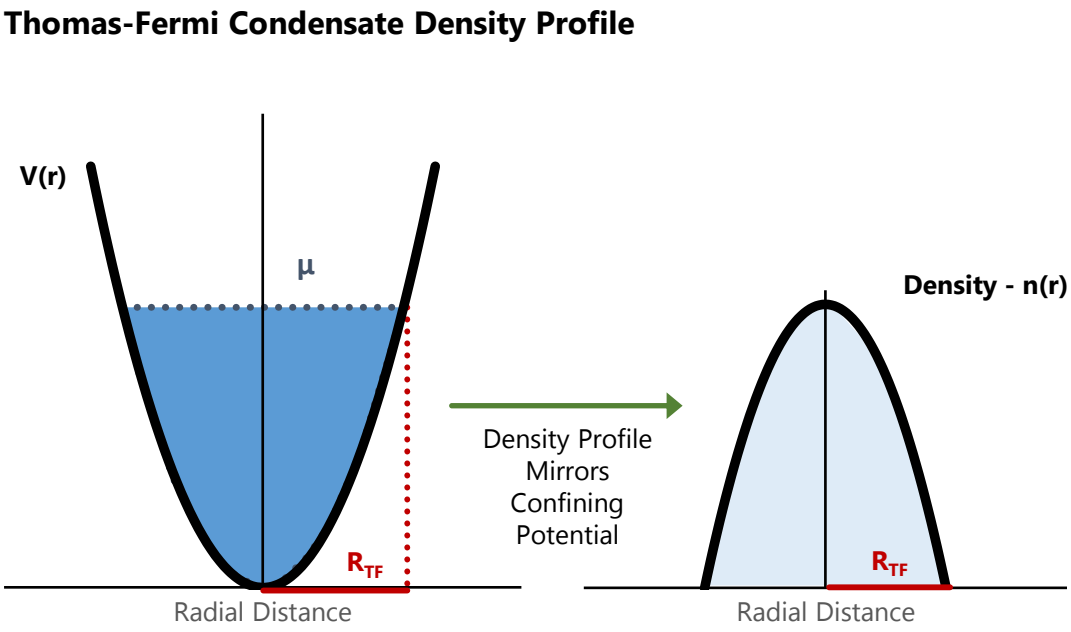

Figure 2.3: The Thomas-Fermi approximation for the BEC density, here shown in a 1D slice. The density profile of the atoms will mirror the curvatures of the potential which confines the atoms.

Therefore in the Thomas-Fermi limit, the shape of the density profile is a reflection of the trapping potential, scaled with the correct prefactors. For a harmonic confinement, we get an inverted parabola shape referred to as the Thomas-Fermi profile shown in Figure 2.3.

It is important to note that this is in fact an approximation, the discontinuity in the derivative at the edge of the Thomas-Fermi profile would make $\nabla^2\phi$ ill-defined. To account for this, we consider the length scale in which the derivative of the density should be non-zero.

We consider the energy scale associated with the chemical potential μ of the condensate to the kinetic energy term:

$$\mu = \frac{4\pi\hbar^2 a_{\text{scat}} n_0}{m} \sim \frac{\hbar^2}{2m\xi^2} \tag{2.33}$$

Where ξ accounts for the length scale units from the ∇^2 operator and n_0 is the peak density of the condensate. Solving for the length scale, we get:

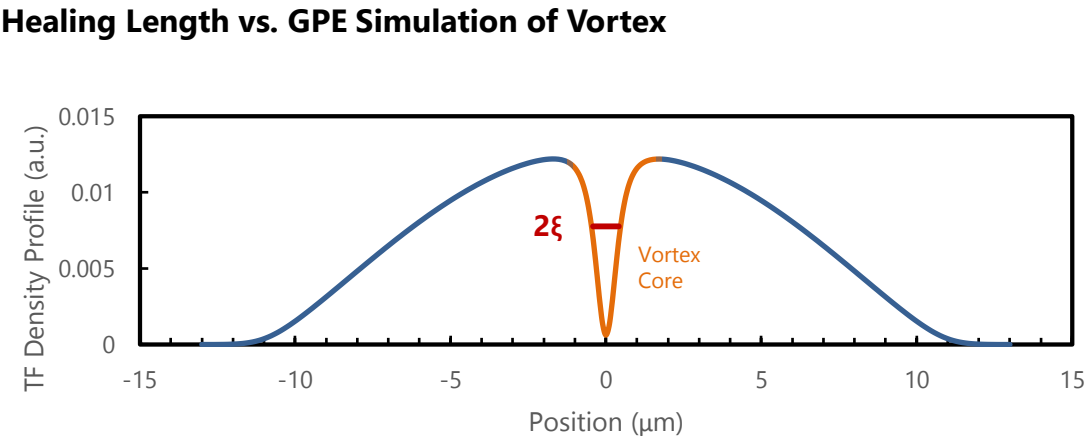

Figure 2.4: Illustration of the healing length ξ in a condensate. Here a simulated BEC density profile has a vortex in the middle of the cloud. The healing length roughly defines the spatial width of the vortex perturbation to the standard Thomas-Fermi profile.

$$\xi = (8\pi a_{\text{scat}} n_0)^{1/2} \tag{2.34}$$

Where we call ξ the healing length of the condensate. This length scale approximates the shortest distance over which perturbations can occur in which the density goes from zero to the bulk value. For instance, in the experiment with vortices in Chapter 8, the healing length sets the approximate radius of the vortex core.

2.2.4 Thomas-Fermi with a Harmonic Trapping Potential

In our experiment, and in many others, the condensate is confined in a harmonic trapping potential. By using the Thomas-Fermi approximation in Section 2.2.3, we can quantify many properties of the BEC, such as the chemical potential or atom number, as set by the geometry of the harmonic trap.

Knowing the density of the condensate from Equation 2.32, we can calculate the number of atoms within the condensate:

$$N = \int \mathrm{d}^3 r \, n(\vec{\mathbf{r}}) = \int \mathrm{d}^3 r \, \frac{1}{g}(\mu - V(\vec{\mathbf{r}})) \tag{2.35}$$

From the condition that the condensate must vanish when $\mu = V(R)$ in Section 2.2.3,

where R is the edge of the condensate, we can relate the harmonic oscillator frequencies, condensate radius and the chemical potential by:

$$\frac{1}{2}m\omega_i^2 = \frac{\mu}{R_i^2} \tag{2.36}$$

Where ω_i and R_i are the oscillator frequency and condensate radius along the $\hat{\mathbf{e}}_i$ direction respectively. Therefore we can calculate the atom number from:

$$N = \int \mathrm{d}^3 r \, \frac{\mu}{g}\left(1 - \frac{x^2}{R_x^2} - \frac{y^2}{R_y^2} - \frac{z^2}{R_z^2}\right) \tag{2.37}$$

If we define

$$n_0 = \frac{\mu}{g} = \frac{\mu m}{4\pi\hbar^2 a_{\mathrm{scat}}} \tag{2.38}$$

as the maximum density at the center of the condensate, we can define the spatial density as:

$$n(\vec{\mathbf{r}}) = n_0\left(1 - \frac{x^2}{R_x^2} - \frac{y^2}{R_y^2} - \frac{z^2}{R_z^2}\right) \tag{2.39}$$

If we integrate along one direction first, such as $\hat{\mathbf{z}}$, we can calculate the column density profile of the condensate, which is useful for absorption imaging purposes (see Section 3.5.1):

$$n(x,y) = 2\int_2^{R_z\sqrt{1-\frac{x^2}{R_x^2}-\frac{y^2}{R_y^2}}} n(x,y,z)\,\mathrm{d}z \tag{2.40}$$

$$= \frac{4R_z}{3}n_0\left(1 - \frac{x^2}{R_x^2} - \frac{y^2}{R_y^2}\right)^{3/2} \tag{2.41}$$

Therefore when a condensate is projected onto a two-dimensional surface, such as when imaging, the observed density profile is not a parabola, but instead goes as the power 3/2. Fully integrating over x and y gives the particle number in the condensate:

$$N = \frac{2}{5}n_0 \cdot \frac{4}{3}\pi R_x R_y R_z \tag{2.42}$$

Here I broke up the terms to illustrate that the result for the total atom number contains a effective uniform density term $2/5n_0$ multiplied by the volume of the ellipsoidal condensate. If we use the geometric mean of the radii (and therefore trap frequencies via Equation 2.36) to describe the average extent of the condensate:

$$N = \frac{8\pi m}{15g}\bar{\omega}^2\bar{R}^5 \tag{2.43}$$

Where $\bar{R} = (R_x R_y R_z)^{1/3}$ and $\bar{\omega} = (\Omega_x \Omega_y \Omega_z)^{1/3}$. The inverse of this equation, the radius as a function of number, has a 1/5 power law dependence - a little increase in measured radius means much more atoms in the condensate!

2.3 Density Profiles and Time-of-Flight Measurement

The measurement of density profiles of atomic ensembles is important as the atomic density reveals many other metrics relevant for calculations, such as atom number or temperature. Here I briefly discuss the density profiles for thermal and condensed clouds, at the extraction of information via time-of-flight (TOF) imaging.

2.3.1 Time-of-Flight (TOF) Imaging Measurement

To gain information in any of our experiments, we use absorption imaging techniques (Section 3.5.1) to image the column density of the atomic ensemble onto a CCD camera. We can either take an image when the atoms are still confined (an in-situ image) or take an image after abruptly turning off the trap, letting the ensemble expand (a time-of-flight image). In-situ imaging is difficult due to the high atom density (for absorption imaging) and the small target in which to image ($\sim$ μm). To image features in the condensate smaller than the radius, such as a vortex [30], complex techniques must be used. For this reason, we commonly default to using TOF imaging techniques. At the end of an experiment, we immediately remove the confining potential, after which the kinetic energy of the system causes an expansion of the gas. This rapid expansion effectively maps the

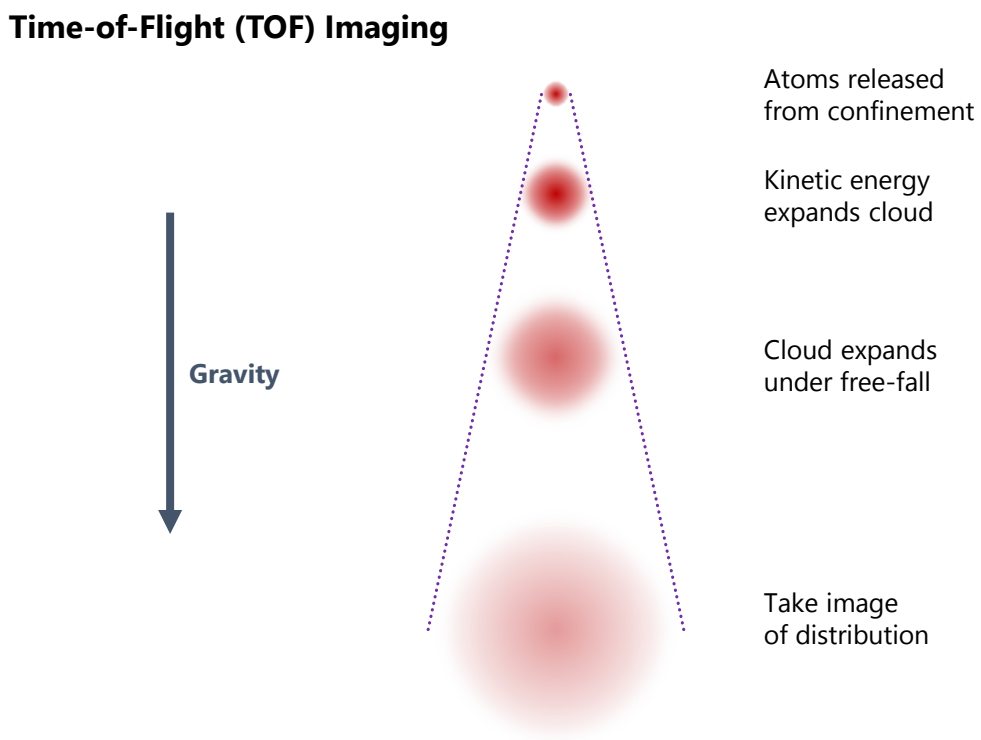

Figure 2.5: In Time-of-Flight (TOF) imaging, the atoms are suddenly released from their confining potential. As the gas falls, it expands due to the momentum of atoms within it. The distribution is then imaged after a free-fall time $t_{\mathrm{TOF}} \sim 20$ ms)

momentum distribution of the ensemble into position space.

2.3.2 Thermal Profiles

A confined thermal cloud will have a density profile of [31]:

$$n(x,y,z) = n_0 e^{-\frac{m}{2k_{\mathrm{B}}T}\left(\omega_x^2 x^2 + \omega_y^2 y^2 + \omega_z^2 z^2\right)} \tag{2.44}$$

Where n_0, the peak density can be calculated as:

$$n_0 = N\left(\frac{m\bar{\omega}^2}{2\pi k_{\mathrm{B}}T}\right)^{3/2} \tag{2.45}$$

With N being the total atom number. At the start of TOF, we release the confining potential, therefore, besides gravity, the system is described by free-particle physics. The velocity distribution after TOF for a thermal gas is governed by the Maxwell-Boltzmann distribution. For a sufficient TOF length, the thermal distribution:

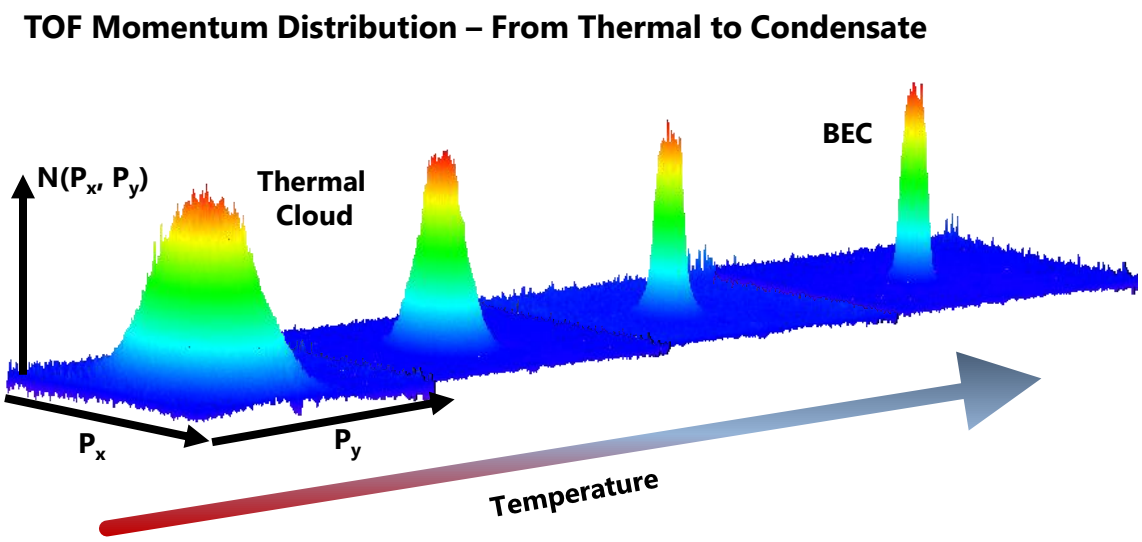

Figure 2.6: Momentum profiles of thermal clouds and condensates after TOF imaging. As the sample of atoms is cooled from a hot thermal cloud (left) to a condensate (right), the momentum becomes peaked around a single value.

$$n(x,y,z) = N\left(\frac{m}{2\pi k_{\mathrm{B}}T}\right)^{3/2} e^{-\frac{m}{2k_{\mathrm{B}}T}\left(v_x^2+v_y^2+v_z^2\right)} \tag{2.46}$$

is mapped to a spatial distribution:

$$n_{\mathrm{TOF}}(x,y,z) = Ae^{-\frac{m}{2k_{\mathrm{B}}T}\left(\frac{x^2}{\sigma_x^2}+\frac{y^2}{\sigma_y^2}+\frac{z^2}{\sigma_z^2}\right)} \tag{2.47}$$

However for imaging we project the vertical direction onto the two-dimensional image. So the thermal distribution on the camera will have the form:

$$n_{\mathrm{TOF}}(x,y) = Ae^{-\frac{m}{2k_{\mathrm{B}}T}\left(\frac{x^2}{\sigma_x^2}+\frac{y^2}{\sigma_y^2}\right)} \tag{2.48}$$

Where:

$$A = N\frac{m}{2\pi k_{\mathrm{B}}T} \tag{2.49}$$

$$\sigma_i = \sqrt{k_{\mathrm{B}}T/m} \tag{2.50}$$

By using a least-squares fit of the form above, we can extract the relevant information from the thermal distribution. Here I assert that given enough time, the distribution of the thermal cloud after TOF will become isotropic, unlike the TOF profile of a condensate, discussed in the next section.

2.3.3 Condensate Profiles

From Section 2.2.4, the density of a BEC in a harmonic trap is:

$$n_{\mathrm{TF}}(\vec{\mathbf{r}}) = \frac{\mu}{g}\left(1 - \frac{x^2}{R_x^2} - \frac{y^2}{R_y^2} - \frac{z^2}{R_z^2}\right) \tag{2.51}$$

The TOF density profile of a condensate is related to the harmonic trapping frequencies. For directions of tighter confinement, the BEC will 'explode' outwards with a higher momentum, thus expanding to a larger radius after a given amount of time. This is why condensates undergo anisotropic expansion in time of flight, unlike the uniform expansion that thermal clouds achieve. This anisotropy in expansion is considered the experimental signature to distinguish condensation from thermal ensembles.

From [32], we can calculate the anisotropic expansion according to a set of equations for the condensate radius as a function of time:

$$R_i(t) = \lambda_i(t) R_i(t=0) \tag{2.52}$$

$$\ddot{\lambda}_i(t) = \frac{\omega_i}{\lambda_i \lambda_i \lambda_j \lambda_k} \tag{2.53}$$

Where R_i is the condensate radius along the ith principal axes. These relationships, known as the Castin-Dum equations[5] can be used to both find the time of flight density profiles, or by measuring the TOF radii via absorption imaging, back-propagate what the original radii were when the condensate was confined. To extract the radii from the image, we do a least-squares fit to the column density in Equation 2.41 and extract the radii. Then we use the Castin-Dum equations to back propagate the density profile back to the start of TOF. Using the relationships in Section 2.2.4, we can calculate the atom number and

[5] Castin and Dum are the authors of [32], only fair they get an equation

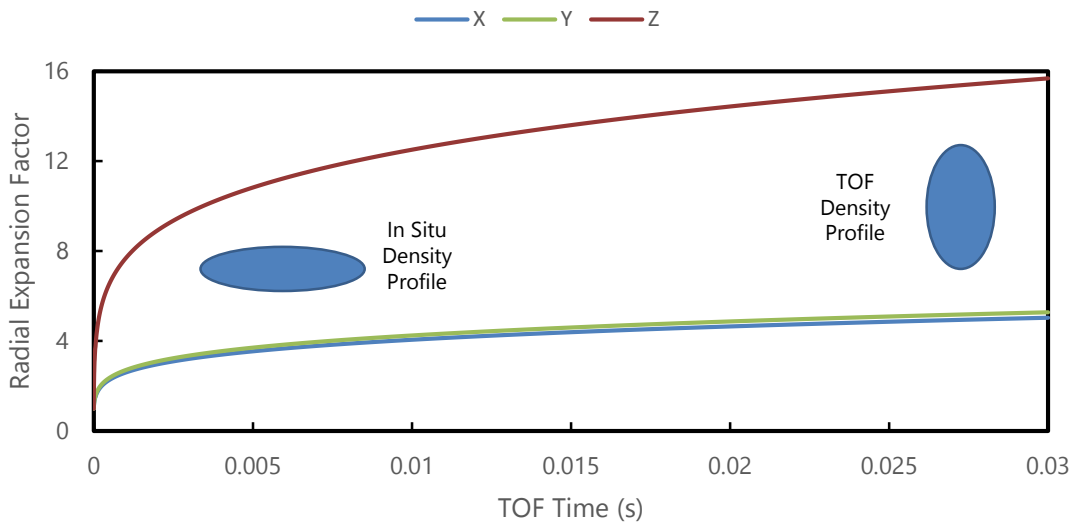

Figure 2.7: BEC expansion in TOF given a trap geometry of $(f_x, f_y, f_x) = (42.8, 43.3, 133)$ Hz. Due to the tight confinement along the $\hat{\mathbf{z}}$ direction, the Castin-Dum projection shows that the BEC will rapidly expand vertically. This more rapid expansion will invert the density profile from being extended along $\hat{\mathbf{x}}, \hat{\mathbf{y}}$ before TOF (left) to $\hat{\mathbf{z}}$ after TOF (right).

chemical potential.

2.3.4 Measurement of Trap Frequencies

From the previous sections, it is evident that the geometry of the confining potential is critical in determining the critical parameters of the system. Therefore, we characterize the system in terms of trap frequencies that describe the confinement in terms of a harmonic oscillator model.

To measure the trap frequencies, we excite the $n = 0$, $l = 0$ resonance of the trap and measure the modulation of the BEC. That is the fancy way of saying that we kick it with a magnetic force that causes the condensate to slosh in the trap. The periodicity of the slosh gives the trap frequency along the direction of the applied kick. A more detailed procedure is as follows. First, we prepare a condensate in a magnetically sensitive spin state. Next we apply a biasing field along a principal axis of the system[6]. We then pulse on a magnetic field gradient that imparts a force to the atoms along the biasing

[6]For the optical trap, the principal axes are $\hat{\mathbf{x}} \pm \hat{\mathbf{y}}$ as the beams intersect at 45° to the experiment axes defined in Section 4.1

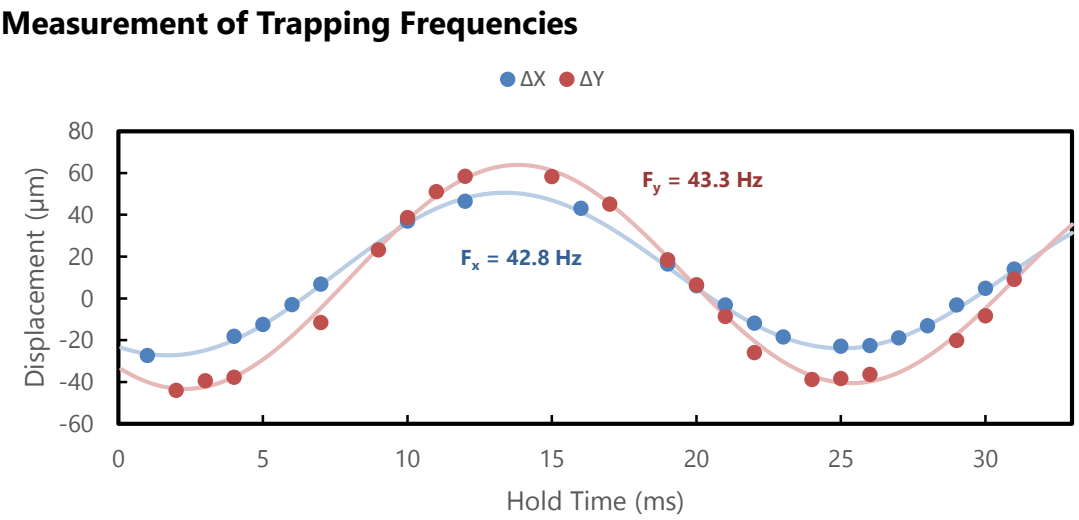

Figure 2.8: Measurement of trap frequencies in an optical dipole trap. The cloud is given a force impulse and allowed to slosh in the trap. The displacement as a function of time is measured, and the oscillation frequency extracted.

field direction. We time the length of this pulse to be approximately one-fourth of the estimated trap period, and the amplitude of the force is set to give a nice gentle push into oscillation, not a large shove that can push the condensate into higher oscillation modes, or into regions where the potential is no longer approximated by a harmonic trap. We then observe the motion of the condensate after varying hold times. The position of the condensate will oscillate at the trapping frequency, which can be then extracted by a least-squares fit of the position versus time dataset.

Chapter 3

Introduction to Laser Cooling and Trapping Techniques

Laser cooling was instrumental in being able to create Bose-Einstein condensates in the lab as the techniques developed were able to take a hot atomic beam and slow the atoms down in a trap with a temperatures of few millikelvin, comparable to the best cryogenic liquid Helium experiments. Magnetic trapping and optical trapping techniques to further cool down atomic gases also play a role in producing a condensate, and are also discussed here. This chapter is truly an overview of the physics and techniques for ultracold gases experiments. For readers interested in more in-depth discussions and derivations of the physics of laser cooling and trapping, I would suggest the atomic physics books by Metcalf [33] and Foot [22], or the multitude of theses from ultracold degenerate gases experiments in the past two decades.

3.1 Atoms and Magnetic Interactions

In ultracold atomic physics experiments, many of the laser cooling and trapping methods we use (Zeeman slowers, Magneto-Optical traps, and magnetic traps) take advantage of the Zeeman effect [34] to break the energy degeneracy between the various spin components (Figure 3.1). This energy shift comes from the interaction of the magnetic

field with the electronic magnetic moment and the nuclear magnetic moment. The limit of low magnetic field (where the applied field is much smaller than the internal field of the atom) is referred to as the linear Zeeman effect. In this regime, the system is best described by the hyperfine states $|F, m_F\rangle$. As the applied magnetic field strength is increased from zero, the energy splitting of the spin components goes linearly as $E_{\text{Zeeman}} = g_F \mu_B m_F B$ (Figure 3.1, bottom left). As the field is greatly increased, the strength of the internal magnetic field becomes a perturbation compared to the applied field in what is known as the Paschen-Back effect[1]. Here the spin-components are described in the $|J, m_J\rangle$ basis. In the intermediate regime of applied field, neither interaction can be described as a perturbation term. For J = 1/2 atoms (the alkalis) the energy of the spin components can be algebraically solved to give the Breit-Rabi equation:

$$\begin{aligned} x &= \frac{(g_j - g_i)\mu_B B}{\Delta E_{\text{HF}}} \\ \Delta E &= -\frac{1}{2(2I+1)} + \frac{\mu_B g_I m_F B}{\Delta E_{\text{HF}}} + \frac{1}{2}\sqrt{1 + \frac{4m_F}{2I+1}x + x^2} \end{aligned} \tag{3.1}$$

Where B is the applied field, μ_B is the Bohr magneton, g_j and g_j are the electronic and nuclear g-factors, I is the nuclear spin ($I = 3/2$ for ^{87}Rb), ΔE_{HF} is the energy splitting between the two hyperfine levels, and x is a dimensionless energy parameter dependent on the properties of the atom. The energy, ΔE, is given here in units of ΔE_{HF}. The Breit-Rabi equation (3.1) gives the energy splitting over all magnetic field values: the low and high field limits.

3.1.1 The Quadratic Zeeman shift

For low energies the Zeeman shift can be approximated as being linear for all spin components. However there is still a non-linearity in the low magnetic field strength regimes that causes a small, but measurable deviation. We call this small deviation from a linear function the quadratic Zeeman shift. In our ^{87}Rb experiment, we work primarily in the F=1 hyperfine states. Here we define the quadratic shift as $\epsilon = E_0 - (E_1 + E_{-1})/2$, where

[1] In our experiments, we go nowhere close to this regime

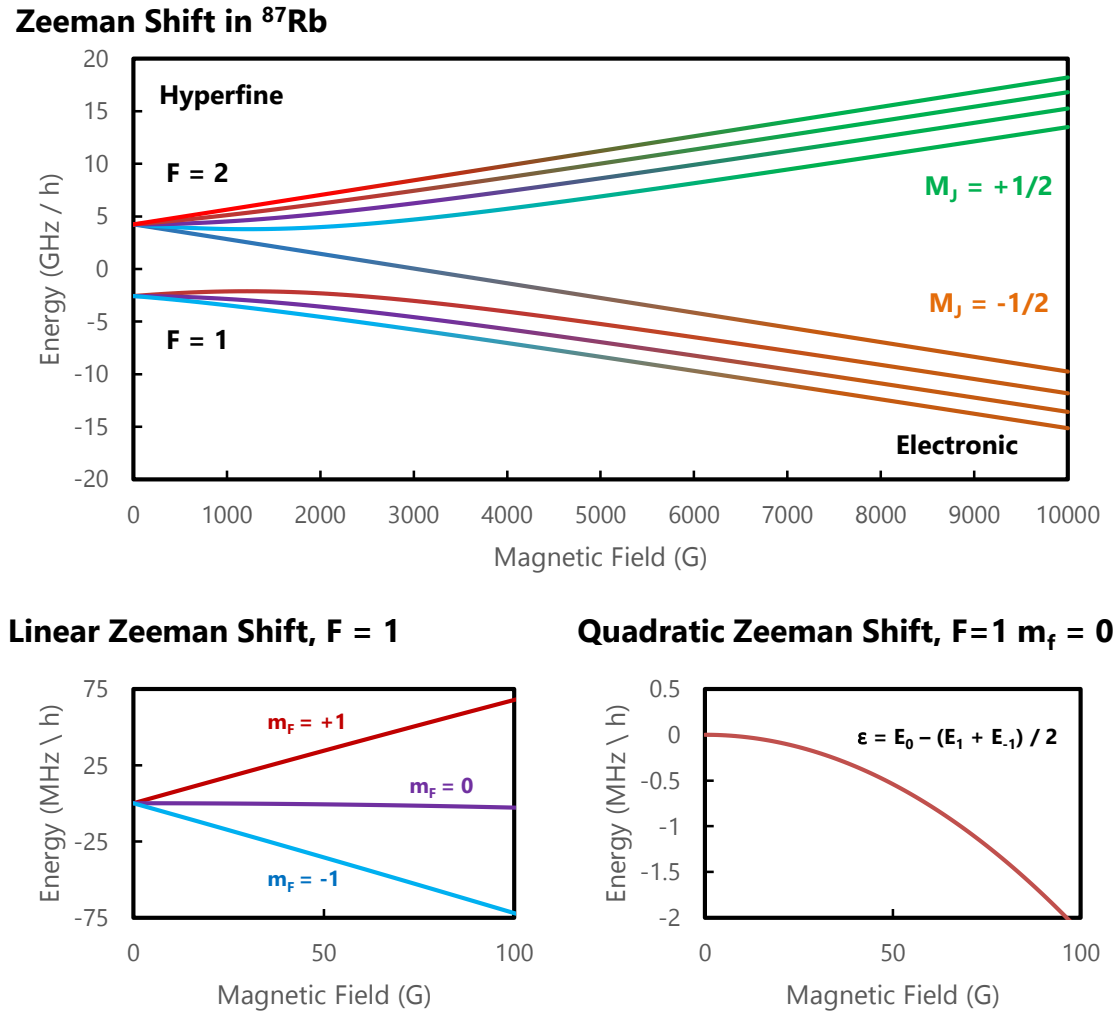

Figure 3.1: The Zeeman energy splittings in ^{87}Rb. The energy shift across arbitrary magnetic field strength is calculated using the Breit-Rabi formula (top). In our experiment we are mostly concerned with the linear Zeeman shift regime for small fields, and the effect of the quadratic Zeeman shift, a measure of the non-linearity as a function of the field strength.

E_{m_F} is the energy of the m_F state. The bottom right of (Figure 3.1) shows the quadratic shift in energy to the $m_F = 0$ state compared to the other states. This shift breaks the symmetry between the $m_F = \pm 1$ states, and allows us to isolate systems via optical or magnetic interactions to $m_F = 0, +1$ or $m_F = 0, -1$ only coupling schemes.

Helpful ^{87}Rb Breit-Rabi Parameters

Description	Symbol	Value
Nuclear g-factor	g_I	-0.0009951414
Electronic Fine Structure g-factor ($5S_{½}$)	g_J	2.00233113
Bohr Magneton	μ_B	1.399624604 MHz/G
Nuclear Spin	I	3/2
Hyperfine Energy Splitting	ΔE_{HF} / h	6.834682610904290 GHz

Figure 3.2: Magnetic properties of ^{87}Rb [35]

3.1.2 Oscillating Magnetic Fields a.k.a RF Coupling

In our experiment we commonly use oscillating magnetic fields (herein RF fields) to drive transition between the spin components of the BEC (the equipment is described in Section 4.4.5). The RF field is mathematically described as a simple field $\vec{\mathbf{B}}_{\mathrm{RF}}(t) = B_0 \cos(\omega_{\mathrm{RF}} t)$, which gives an interaction term in the Hamiltonian of the form $\hat{\mathbf{H}}_{\mathrm{RF}} = -\vec{\mu} \cdot \vec{\mathbf{B}}_{\mathrm{RF}} = \mu B_0 \cos(\omega_{\mathrm{RF}} t) \hat{\mathbf{F}}_x$. In matrix form we can write this as:

$$\hat{\mathbf{H}}_{\mathrm{RF}} = \hbar \begin{pmatrix} -\delta & \Omega_{\mathrm{RF}} \cos(\omega_{\mathrm{RF}} t)/\sqrt{2} & 0 \\ \Omega_{\mathrm{RF}} \cos(\omega_{\mathrm{RF}} t)/\sqrt{2} & \epsilon & \Omega_{\mathrm{RF}} \cos(\omega_{\mathrm{RF}} t)/\sqrt{2} \\ 0 & \Omega_{\mathrm{RF}} \cos(\omega_{\mathrm{RF}} t)/\sqrt{2} & \delta \end{pmatrix} \tag{3.2}$$

Where Ω_{RF} is the coupling strength of the RF filed (the Rabi frequency), $\delta = \omega_{\mathrm{RF}} - \omega_{\mathrm{Z}}$ is the detuning from RF resonance where $\hbar\omega_{\mathrm{Z}}$ is the energy splitting due to the linear Zeeman shift, and ϵ is the quadratic Zeeman shift. Transforming the matrix under rotation into the rotating frame at ω_{RF}, while ignoring terms going as $\omega_{\mathrm{RF}} + \omega_{\mathrm{Z}}$ we get:

$$\hat{\mathbf{H}}_{\mathrm{RF}} = \hbar \begin{pmatrix} -\delta & \Omega_{\mathrm{RF}} \cos(\omega_{\mathrm{RF}} t)/\sqrt{2} & 0 \\ \Omega_{\mathrm{RF}} \cos(\omega_{\mathrm{RF}} t)/\sqrt{2} & \epsilon & \Omega_{\mathrm{RF}} \cos(\omega_{\mathrm{RF}} t)/\sqrt{2} \\ 0 & \Omega_{\mathrm{RF}} \cos(\omega_{\mathrm{RF}} t)/\sqrt{2} & \delta \end{pmatrix} \tag{3.3}$$

This system can be solved for both the eigen energies and states, as shown in Figure 3.3.

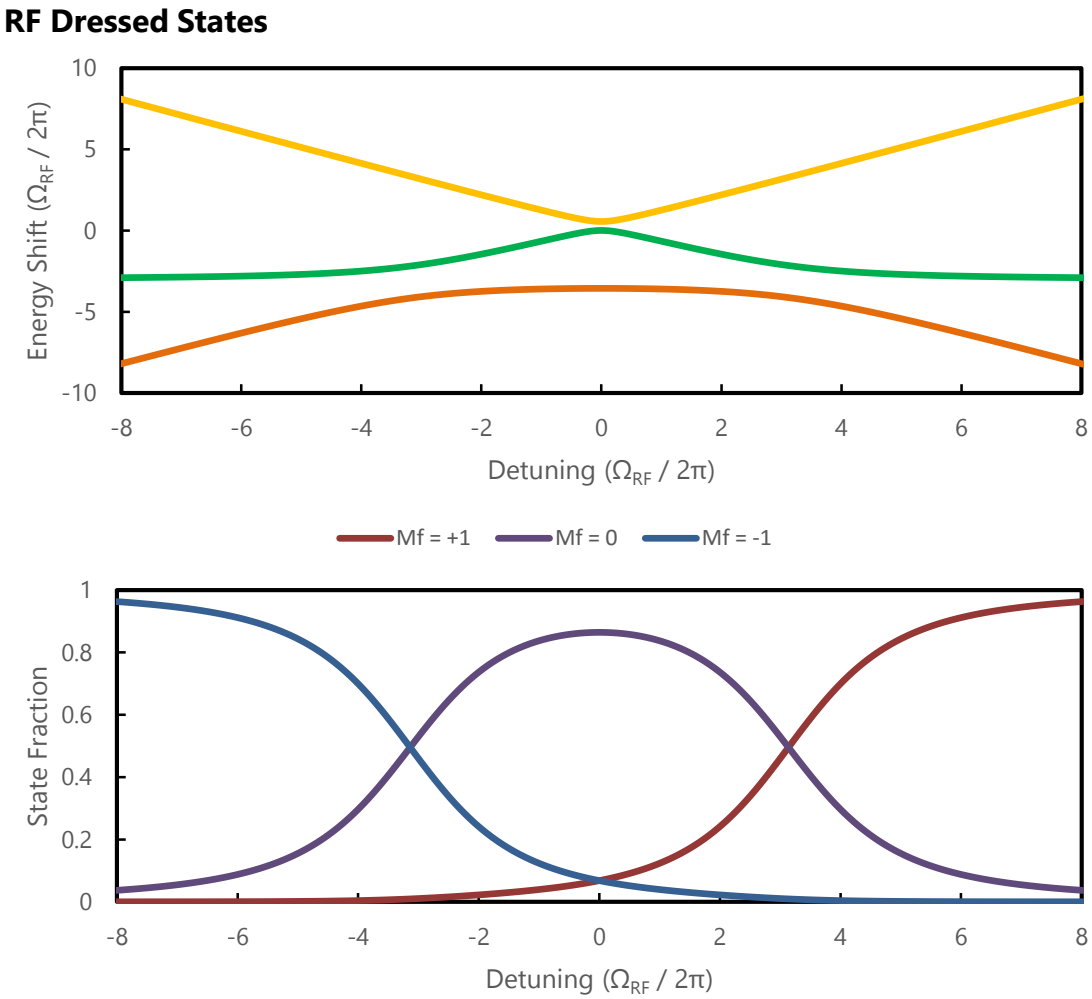

Figure 3.3: Top: The RF dressed state creates avoiding crossings in the energy levels as a function of the detuning from resonance. Bottom: The fractional composition of the lowest energy RF eigenstate with respect to the bare spin states. Both figures are simulated at $\Omega_{\mathrm{RF}} = 30$ kHz and $f_{\mathrm{RF}} = 25$ MHz, which implies for ^{87}Rb a quadratic Zeeman shift of $\epsilon_q \approx 90$ kHz.

Adiabatic Rapid Passage

The most common way we manipulate the spin characteristics in our experiment is through the Adiabatic Rapid Passage (ARP) technique. By ramping the detuning of the RF dressed state slowly with respect to the energy gaps between the dressed state bands[2], we can selectively transfer atoms between various spin compositions. The experimental process is as follows: First we prepare the BEC in the dipole trap in the $m_F = -1$ spin state. We then ramp on the biasing field slowly to set the value of the Zeeman splitting

[2] i.e. to avoid Landau-Zener tunneling

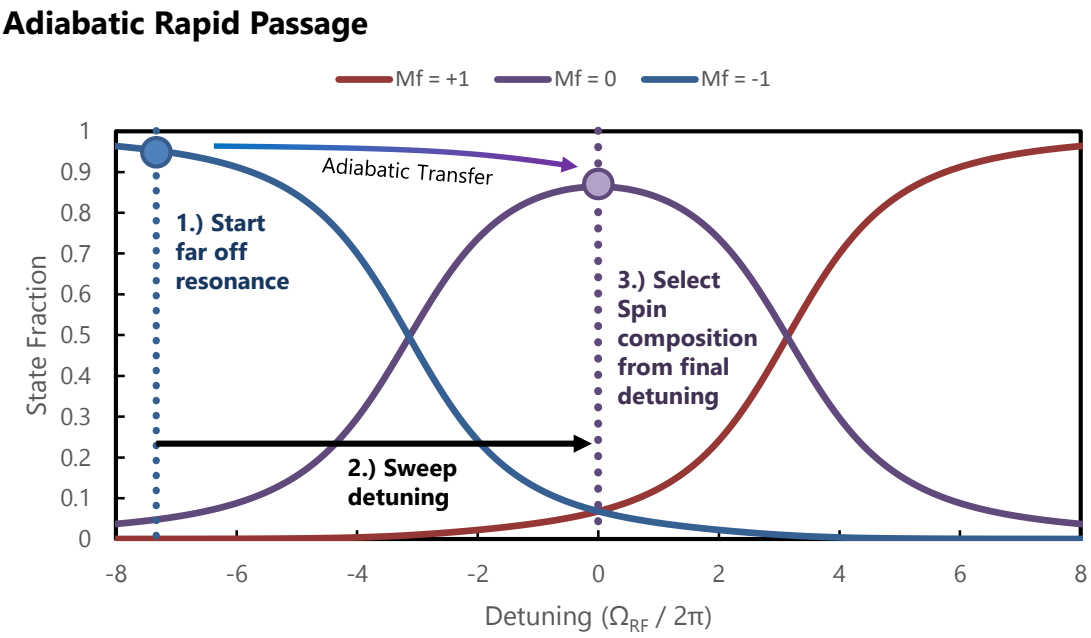

Figure 3.4: Adiabatic Rapid passage uses the eigenstates of the RF dressed state to select spin compositions via detuning dependent eigenstates.

$\hbar(\omega_Z - \delta_0)$ where δ_0 is a value that is far enough out of resonance that the dressed state spin fraction and bare state are effectively identical. We then slowly ramp up the RF frequency to $\omega_{RF} = \omega_Z$, while the magnetic field is still lower than resonance. We then slowly ramp the biasing field such that Zeeman shift $\omega_Z \to \omega_{RF}$. By selectively choosing the end point of the biasing ramp, we choose the value of $\delta = \omega_{RF} - \omega_Z$, and hence the spin state composition as shown in Figure 3.3, bottom. By slowly ramping off the RF, the system is brought back into the bare spin states with a spin fraction given by the final eigenstate.

3.2 Laser Cooling

In order to cool down our atomic gases to ultracold temperatures, we first use the properties of laser cooling to remove momentum from the atoms. Laser cooling processes use the momentum recoil of photons, caused by the atomic absorption and emission of photons, the generate a force upon the atoms. Many clever schemes can be used to

decelerate, trap, and drastically cool atoms using this force.

3.2.1 Providing a Force to Atoms From Light

An atom that absorbs and emits a photon will experience a shift in momentum and kinetic energy proportional to the wavelength of the light and the mass of the atom. This imparted momentum and energy is described by the recoil momentum $\hbar k_R = h/\lambda$, and the recoil energy $E_R = \hbar k_R^2/2m$. Consequentially, the force the atom will feel is simply the single photon recoil momentum multiplied by the photon scattering rate of the atom. In the case of a simple two-level atom model, the rate in which photons are scattered by the atoms is given as:

$$\gamma_{\text{scatter}} = \frac{\Gamma I/I_{sat}}{2\Gamma^2 + \Gamma I/I_{sat} + 4\delta^2} \tag{3.4}$$

Where I is the intensity of the light (Determined by the Rabi frequency Ω), δ is the detuning from atomic resonance and Γ is the spontaneous emission rate. If we drive the atomic transition as hard as possible, that is, provide a laser beam intense enough to provide non-stop atomic absorption and emission, we will reach an intensity known as the saturation intensity, $I_{sat} = 2\Omega^2/\Gamma^2$. The saturation intensity technically corresponds to the intensity of light required to place the two-level atom into an equal superposition of the ground and excited states, as we are instantly providing the next collision after any decay event occurs. The scattering rate and photon recoil momentum give the force imparted to the atoms as:

$$F_{\text{scatter}} = \hbar k \frac{\Gamma I/I_{sat}}{2\Gamma^2 + \Gamma I/I_{sat} + 4\delta^2} \tag{3.5}$$

If a very bright incident laser beam illuminates the atomic beam ($I >> I_{sat}$), the terms in the numerator and denominator of Equation 3.5 will approach unity such that the maximum scattering force the atoms feel is simply $F_{\text{scatter}} = \frac{1}{2}\hbar k\Gamma$.

3.2.2 Zeeman Slowers

One of the first methods to show laser cooling via the scattering force discussed in Section 3.2.1 was the Zeeman slower [1]. The idea is to use the scattering force from a laser to slow down an atomic beam of atoms by aligning the laser counter-propagating to the atomic beam.

To see how the scattering force can be used to slow down, or even stop, an atomic beam, consider the maximal acceleration that can be applied to an atom of mass m via the scattering force:

$$a_{\max} = \frac{F_{\max}}{m} = \frac{1}{2m}\hbar k\Gamma \tag{3.6}$$

Simple classical mechanics tells us that to slow down an atomic beam with an average atomic velocity of v_{beam}, we require a distance of $L_{\text{sl}} = v_{\text{beam}}^2/a_{\max}$ to bring the majority of the atoms to a stand-still.

One problem with using the scattering force to slow down the atoms is the detuning term in Equation 3.5. Even with a laser tuned to the correct resonance frequency, as the atoms slow down they experience a Doppler shift that will cause a detuning which in turn causes the force to drop off quickly. A cute idea was experimentally tested by Bill Phillips and Harold Metcalf [1] to spatially adjust the Zeeman effect to adjust the resonance of the atoms as they decelerated, therefore keeping the cooling light and the atoms in resonance until the atoms were at rest. This was accomplished with what we now call the Zeeman slower - a tapered solenoidal coil that has a variable magnetic field propagating along the atomic beam. The Doppler shift of kv is compensated by the field of the solenoidal coil, keeping the atoms in resonance during the length of the Zeeman slower, hence allowing the maximum acceleration during the whole flight of the atom.

In the case of a Zeeman slower of length L_{sl}, the maximal acceleration condition tells us that the velocity of the atoms will be:

$$v_{\text{beam}}\sqrt{1 - x/L_{\text{sl}}} \tag{3.7}$$

Where x is the distance from the start of the Zeeman slower. The Doppler shift of the

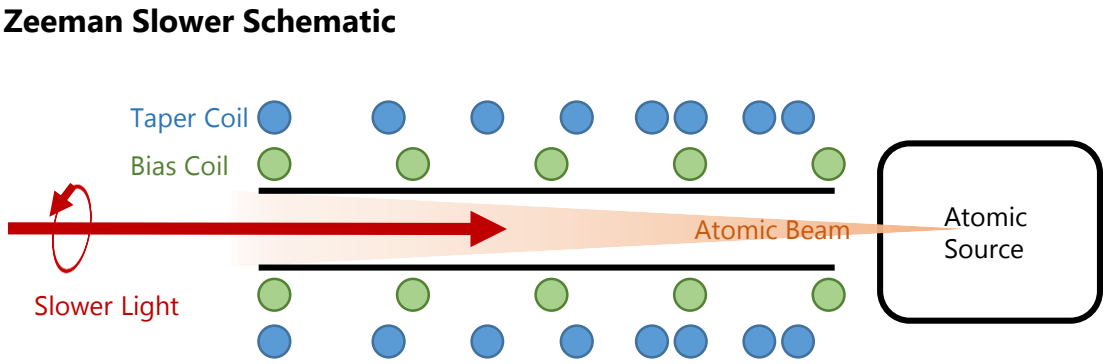

Figure 3.5: Schematic of a the RbLi Zeeman Slower. An atomic beam is sent in a linear path against a counter-propagating circular polarized slowing beam. The Taper coil provides a magnetic field that shifts the atomic resonance to balance the Doppler shift. The Bias uniformly shifts the resonance along the slower.

moving atoms needs to be considered however. The frequency of the laser the atoms see is $\omega_d = \omega + kv$, where k is the wavenumber of the laser, positive velocity is defined to be an atom traveling toward the counter propagated laser source. The Doppler shift of the atoms emerging from an atomic source is non trivial, for our oven at 120 °C (therefore atoms traveling at r.m.s velocity of 336 m/s), the detuning is a healthy 425 MHz. To compensate for the Doppler shift during the whole trajectory of the atoms down the Zeeman slower, the required field profile is:

$$B_{\mathrm{Sl}}(x) = \frac{h v_{\mathrm{beam}}}{\lambda \mu_B} \sqrt{1 - \frac{x}{L_{\mathrm{sl}}}} \tag{3.8}$$

A coil that matches these requirements can be designed using magneto-static computations (i.e. a lot of Biot-Savart). In our experiment, we have both a taper and bias coil on our Zeeman slower in the RbLi experiment (Section 4.4.1 for the design and measurements). The magnetic field profile along both of these coils was optimized numerically for the coil spacings and currents. The bias coil is a solenoid made from uniformly spaced current windings, and as such provides a uniform field along the Zeeman slower. This field allows us to offset the taper field to choose the velocity of atoms at the end of the slower.

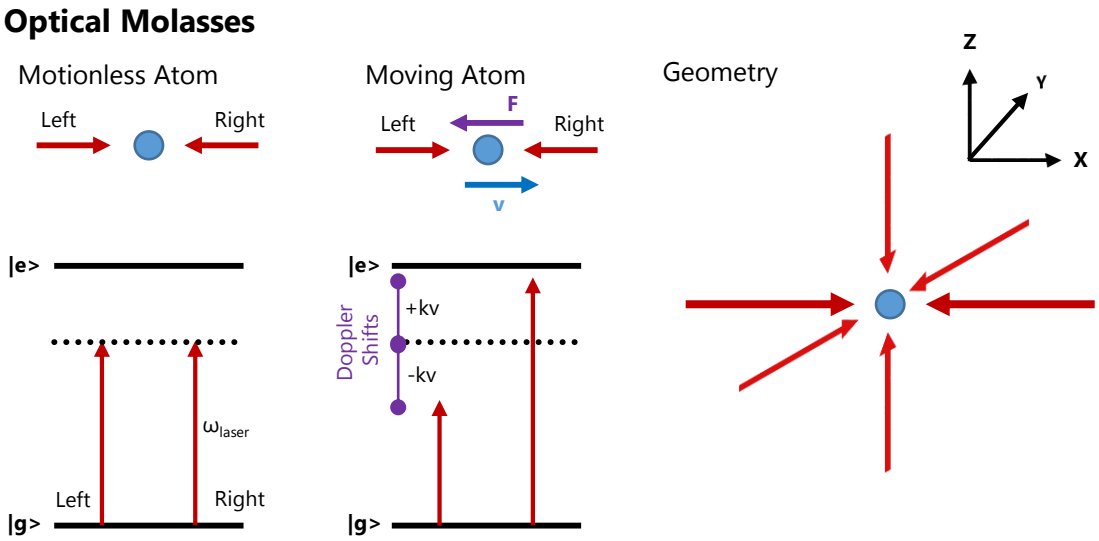

Figure 3.6: Simple model of the optical molasses cooling technique. By red-detuning the beams, atoms with higher velocities will have a Doppler shift that brings them into resonance, increasing the optical scattering force.

3.2.3 Optical Molasses

While the slowing technique with the Zeeman slower can cool an atomic beam with a single velocity direction, the atoms after the slower still will posses velocity (therefore kinetic energy) in the other two Cartesian directions. To cool down the atoms in all directions, a set of three counter-propagating beam pairs aligned on each Cartesian axis is used in what is known as the optical molasses. For an atom with zero velocity, the symmetry of the system would demand that all of the scattering forces from each of the beams cancel, imparting no net force. However, for an atom not at rest, the Doppler shift breaks this symmetry, causing a larger scattering force to occur in the direction that opposes the motion of the atom. If we set the frequency of the laser beams to be below resonance, one of the beams will become resonant with the light, causing a scattering force that increases with the velocity of the atom. In fact, the optical molasses name relates to the fact that the scattering force increases with the velocity of the atom, like motion through a viscous fluid.

Mathematically, one a single direct the scattering force imparted onto the atom via the molasses is the sum of the scattering force in Equation 3.5 for an atom that sees a red

and blue shifted laser via the doppler shift:

$$F_{molasses} = F_{-kv} - F_{+kv} \tag{3.9}$$

$$= F_{sc}(\omega - \omega_0 - kv) - F_{sc}(\omega - \omega_0 + kv) \tag{3.10}$$

Where k is the laser wavenumber (or the recoil momentum of the photon), and v is the velocity of the atom. When evaluating using Equation 3.5, the force can be cast into the form $F = -\alpha v$, a dissipative force with α equal to:

$$\alpha = 4\hbar k^2 \frac{I}{I_{sat}} \frac{-2\delta/\Gamma}{(1 + (2\delta/\Gamma)^2)^2} \tag{3.11}$$

when the assumption is made that the atoms have slow velocities (such that $kv << \Gamma$) and $I << I_{sat}$. In order to give a damping force, we require α to be negative, hence the laser beams need to be red-detuned from the atomic resonance.

3.2.4 The Doppler Cooling Limit and Sub-Doppler Cooling

Although the optical molasses provides a damping force (Equation 3.11), the minimum possible velocity (and therefore temperature) is determined by the Doppler Cooling Limit. The optical molasses provides a net damping force to the atoms, however during each photon scattering event, the atom gains 2 E_{R} of energy.

By assuming a steady state situation where the input energy (heating) from the photon recoils matches the energy dissipation (cooling) from the optical molasses:

$$4E_{\mathrm{R}}\gamma_{\mathrm{scatter}} = F_{\mathrm{mol.}}v \tag{3.12}$$

By relating the recoil energy to the kinetic energy of the atoms ($E_{\mathrm{R}} = 1/2m\langle v\rangle^2$), plugging in the cooling from the molasses, and recalling the equipartition theorem relating temperature and kinetic energy, we get:

$$T_D = \frac{\hbar\Gamma}{4k_{\mathrm{B}}} \frac{1 + (2\delta/\Gamma)^2}{-2\delta/\Gamma} \tag{3.13}$$

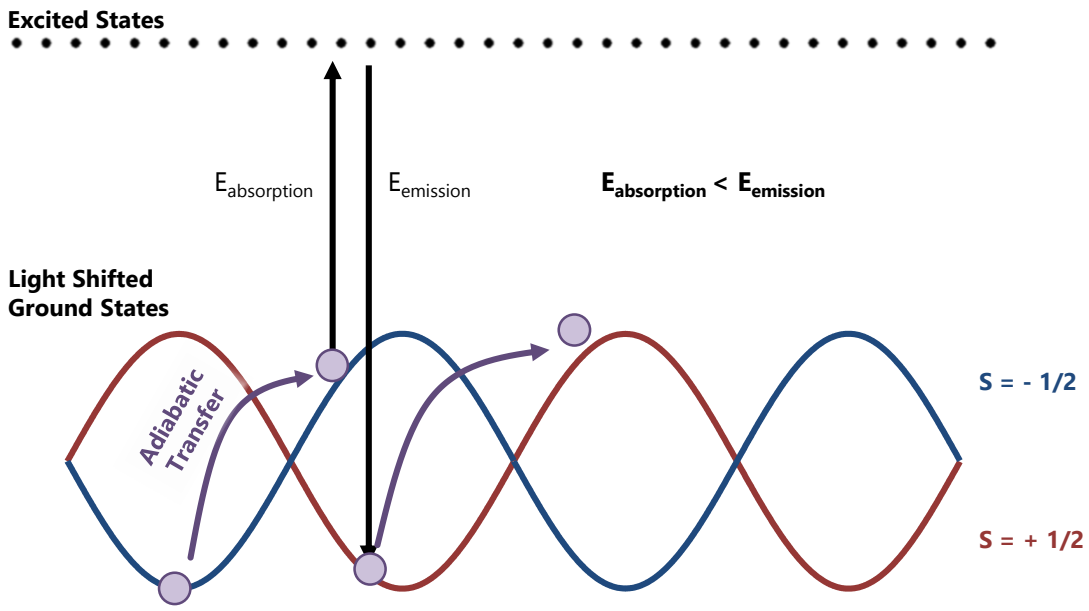

Figure 3.7: In polarization gradient cooling, the atom adiabatically transfers to a higher energy state while traversing along the spatial polarization gradient. The optical interaction can cause the atom to cycle between the excited and ground states, where the emitted photon has more energy than the absorbed one.

The minimum of this function occurs when $\delta = -\Gamma/2$, giving:

$$T_D = \frac{\hbar\Gamma}{2k_{\mathrm{B}}} \tag{3.14}$$

For the $\Gamma = 2\pi \cdot 6.066$ MHz lifetime in ^{87}Rb, this leads to a minimum molasses temperature of $\approx 150\mu$K. Nice and cold, but not enough to reach condensation.

To get cooler than this, a technique known as Sub-doppler cooling, Polarization gradient cooling, or Sisyphus cooling, is used to get beyond this limit. This effect was experimentally discovered [36] as an unexpected result, and was theoretically explained later [37]. Here I will describe an extremely simple model[3] or flavor of the mechanism at work. In the optical molasses one-dimensional geometry, we have a pair of counter propagating lasers at the same frequency, but with different helicities of circular polarization. The superposition of these two beams forms an optical lattice type structure, where the

[3]The title of Reference [37] says 'simple theoretical models', however is 10+ pages of math.

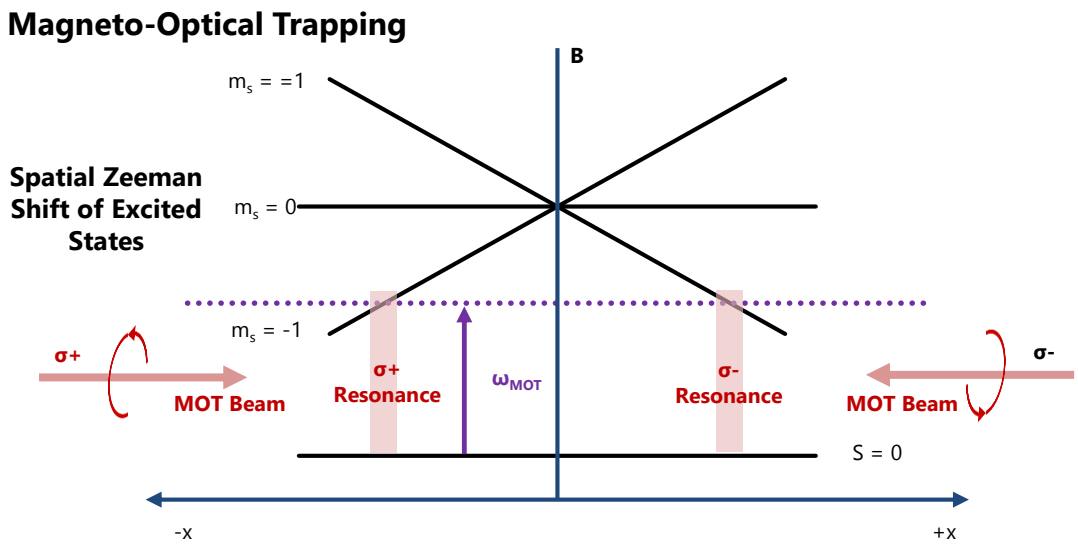

Figure 3.8: Simple spin-0 to spin-1 model of magneto-optical trapping. The magnetic field gradient shifts the energy of the atomic spins states in space. Appropriately circular polarized counter-propagating laser beams have a spin-dependent and spatial dependent resonance that provides a restoring force to the atoms.

polarization changes in space from left circular → horizontal linear → right circular → etc. over a period length equal to the laser wavelength. Specifically the polarization has a rotating field form of $\hat{\mathbf{e}} = \cos(kz)\mathbf{e}_x - \sin(ky)\mathbf{e}_y$ with $k = 2\pi/\lambda$. In an atom more complex than a two-level atom model, where the ground and excited states have Zeeman sublevels with different spin angular momentum, the polarization gradient in space will break the symmetry between the levels. Along the polarization 'wave', the sublevels will have a spatially oscillating light shift. An atom moving along this direction can adiabatically transfer from being in the low energy sublevel to the high energy level without changing spin. The atoms can then absorb a photon and decay into the lower state again, causing a reduction in energy. This technique can in theory cool atoms down to the recoil limit: $T_{\mathrm{R}} \approx E_{\mathrm{R}}/k_{\mathrm{B}}$.

3.2.5 Magneto-Optical Trapping (MOT)

The Magneto-Optical Trap (MOT) is the workhorse of the atomic physics world. MOTs are commonly the first stage of laser cooling and trapping in cold atom systems. The operation of a Sodium MOT was first experimentally shown by Raab, et. al. [3] back in

1987. The MOT collects the slowed atoms from the exit of the Zeeman slower by providing both a trapping force and a dissipative force (as an optical molasses) to cool the atoms further.

The classic example of the MOT mechanism is the case of hypothetical atom with a spin-0 ground state and a spin-1 excited state with three sub levels (Figure Figure 3.8). Using a quadrupole magnetic field (Section 3.3), we can generate a spatially dependent Zeeman shift that grows linearly from the coil's geometric center. Considering a one-dimensional geometry for simplicity, we illuminate the atoms with a pair of counter-propagating beams along $\pm\hat{\mathbf{x}}$: one with $\sigma+$ and the other with $\sigma-$ polarization. If the laser light is detuned below the non-shifted atomic resonance frequency, atoms at $x > 0$ will absorb more $\sigma-$ photons than $\sigma+$ photons and as such will feel an average force toward $x = 0$. By symmetry, an atom at $x < 0$ will feel a force that similarly pushes the atom to $x = 0$. In summary, the magnetic field helps to provide a restoring force that traps the atoms within the magnetic field. To make a MOT in our experiment, we replicate the geometry (polarization, magnetic field) along all three Cartesian axes. Similarly although ^{87}Rb is not a simple atom as described in Figure 3.8, we can use the cooling transitions between the $F = 2$ to $F' = 3$ states in the same way. Similar to the Zeeman slower, the MOT also needs to have repumping light as well along all 6 laser beams (see Section 3.2.6) to keep the atoms within the cooling transitions.

In our ^{87}Rb MOT, we can collect billions of atoms out of the Zeeman slower within 3-7 seconds, and they are cooled to order milliKelvin in temperature, cold enough for other cooling techniques to be used on the way to condensation. Naturally the larger amount of atom flux out of the Zeeman slower translates to more atoms in the MOT steady-state as well. The atom number loaded into the MOT is highly complex, depending on: the alignment of the six MOT beams, the polarization of the beams, the frequency of the MOT cooling and repump beams, the atomic oven temperature, the alignment of the atomic beam axis with the MOT center[4], the slower performance (slower currents, frequencies, and alignment), and the strength of the magnetic field gradient. Needless to say, getting a MOT can sometimes be a chore.

[4]The alignment of the MOT to the atomic beam path can adjusted with the bias coils (Section 4.4.3)

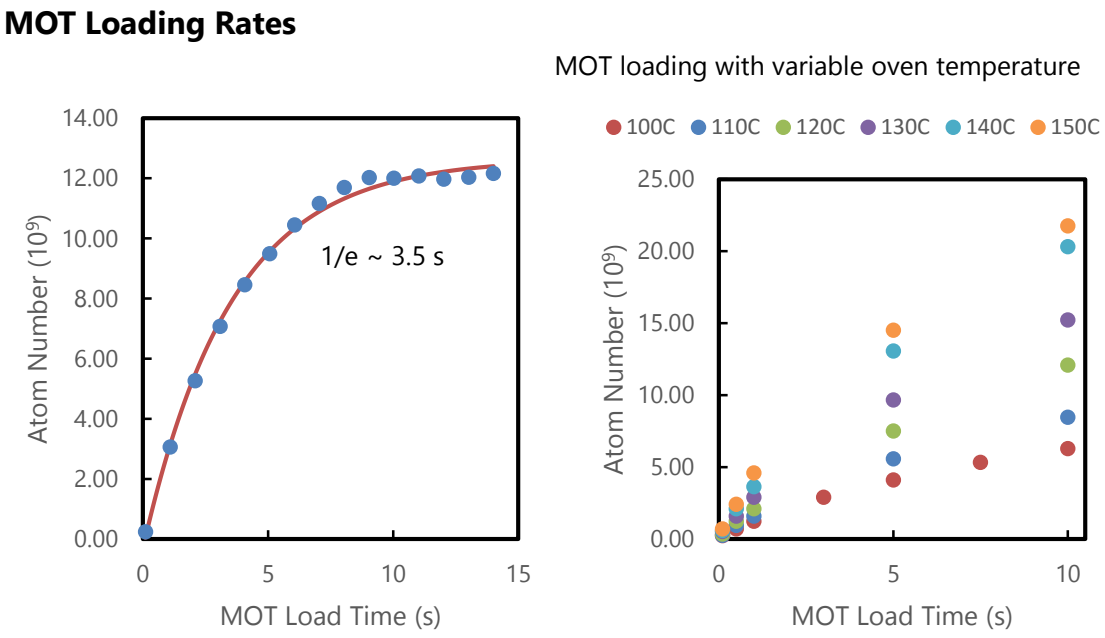

Figure 3.9: Measured MOT loading rates as a function of time. Our MOT captures order a billion atoms within 3.5 seconds (left). As the temperature of the atomic oven is increased, the flux of atoms in the slower atomic beam increases, allowing more atoms to be captured in a steady-state configuration.

3.2.6 Atomic Repumping

In this discussion of light induced forces I described laser cooling processes happening in an effective two level atom. In most cases we are exciting atoms, in ^{87}Rb we are driving a transition between the $F = 2$ to $F' = 3$ state. Unlike simple models, Rubidium is a multi-level atom with closely-spaced hyperfine energy levels. However a laser of finite line-width could drive off-resonant transitions to other nearby hyperfine states, which have a possibility of decaying into the $F = 1$ ground state. The large splitting in the hyperfine ground states (6.8 GHz) causes the cooling light to become decoupled from these 'lost' atoms. If the cooling procedure is continued, eventually all atoms will be pumped into the inaccessible F = 1 state. To prevent this a second laser is used simultaneously with the cooling laser, a repump laser, that is set to drive transitions between the $F = 1$ to $F' = 2$ states. This laser repopulates atoms into the laser cooling transitions, allowing laser cooling to continue.

to move the center of the quadrupole field

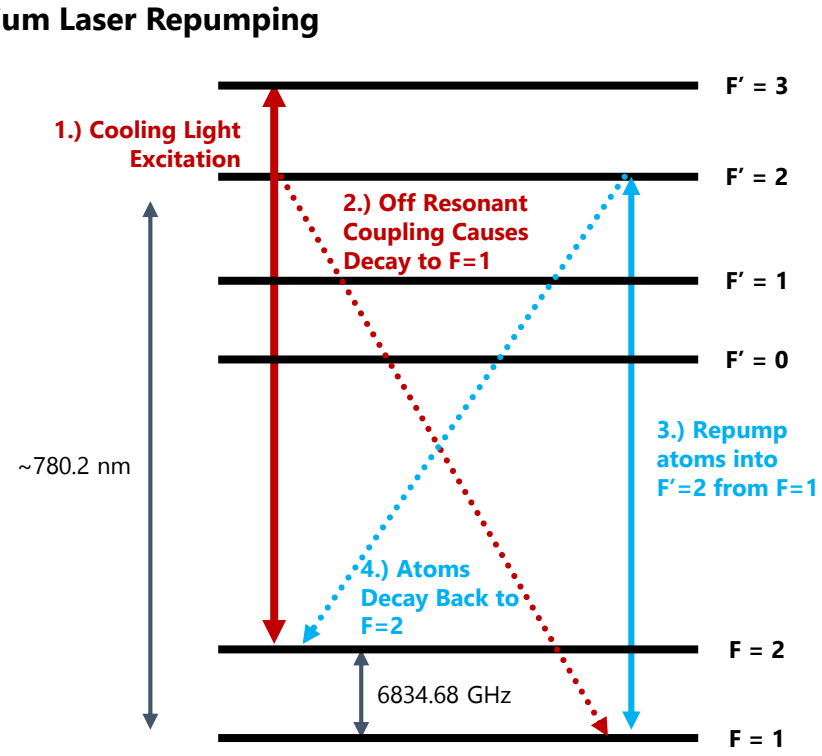

Figure 3.10: Repumping for laser cooling in ^{87}Rb. Because light on the $F = 2$ to $F' = 3$ transition can off-resonantly couple to $F' = 2$, atoms can reach the $F = 1$ ground state and become uncoupled from the cooling process. The repumping scheme optical pumps these atoms back into the cooling transition

3.3 Magnetic Trapping

Magnetic trapping of cold atomic gases is a common next stage after performing laser cooling techniques. Magnetic trapping operates via a magnetic dipole interaction with the atoms. The atom in a magnetic field will experience a shift in energy $V = -\vec{\boldsymbol{\mu}} \cdot \vec{\mathbf{B}}$ where $\vec{\boldsymbol{\mu}}$ is the magnetic moment of the atom. For an atom in a non-zero magnitude spin state, this will generate a Zeeman shift energy $V = g_F \mu_B m_F B$, where g_F is the gyromagnetic ratio, μ_B is the Bohr magneton and m_F is the spin of the atom. It follows for any potential that there is a force such that $\vec{\mathbf{F}} = -\vec{\nabla} V$, hence the atoms will feel a force:

$$\vec{\mathbf{F}}_{mag} = -g_F \mu_B m_F \left(\frac{\partial B}{\partial x}\hat{\mathbf{x}} + \frac{\partial B}{\partial y}\hat{\mathbf{y}} + \frac{\partial B}{\partial z}\hat{\mathbf{z}}\right) \tag{3.15}$$

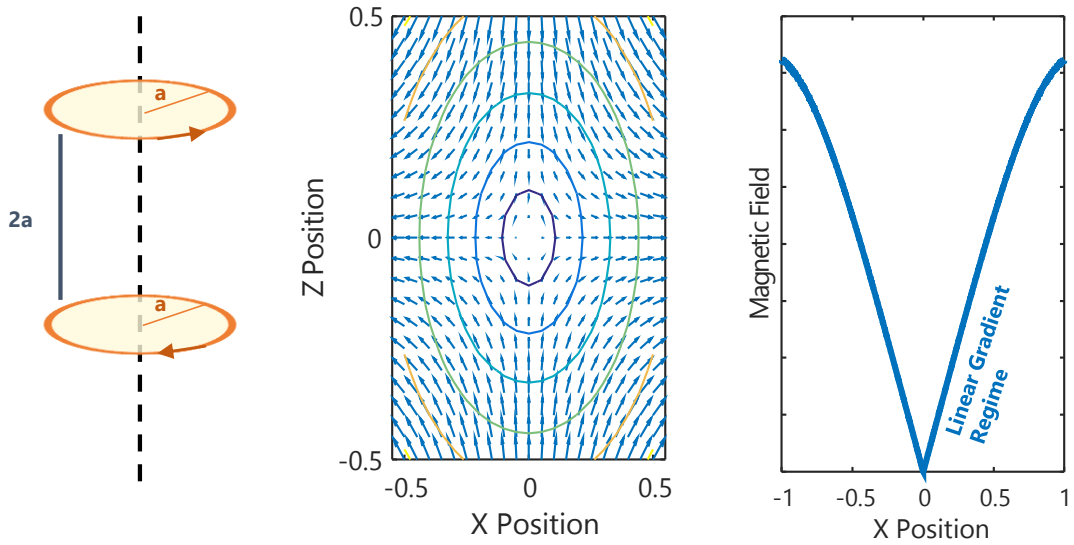

Figure 3.11: Quadrupole magnetic field geometry. A pair of anti-Helmholtz coils (left) generate a cylindrically symmetric magnetic field profile (center), which near the geometric center has a linear increase in magnitude as a function of position (right). This linear region allows us to make the magnetic trapping approximations in Equation 3.19.

Thus to have a restoring force, we need to have a magnetic field that varies in space such that the atoms experience a restoring force to a central point.

This requirement can be met by using a pair of Helmholtz coils with opposite current flow directions, the same geometry required for the Magneto-Optical trap. By using a pair of the anti-Helmholtz or quadrupole coils, we can achieve the restoring force to create a magnetic trap. For small displacements from the center of the coil geometry, the magnetic field has the form:

$$\vec{\mathbf{B}} = B'(x\hat{\mathbf{x}} + y\hat{\mathbf{x}} - 2z\hat{\mathbf{z}}) + B_0 \tag{3.16}$$

Where B' is the strength of the quadrupole magnetic field, and B_0 is any spatially uniform magnetic fields. For a geometry where the coil axis is along the $\hat{\mathbf{z}}$ direction (which is true in our experiment), the potential energy in the absence of uniform fields becomes:

$$V(\vec{\mathbf{r}}) = g_F \mu_B m_F B' \sqrt{x^2 + y^2 - 4z^2} \tag{3.17}$$

If we add a background uniform field with strength B_0 along the $\hat{\mathbf{z}}$ direction, we get:

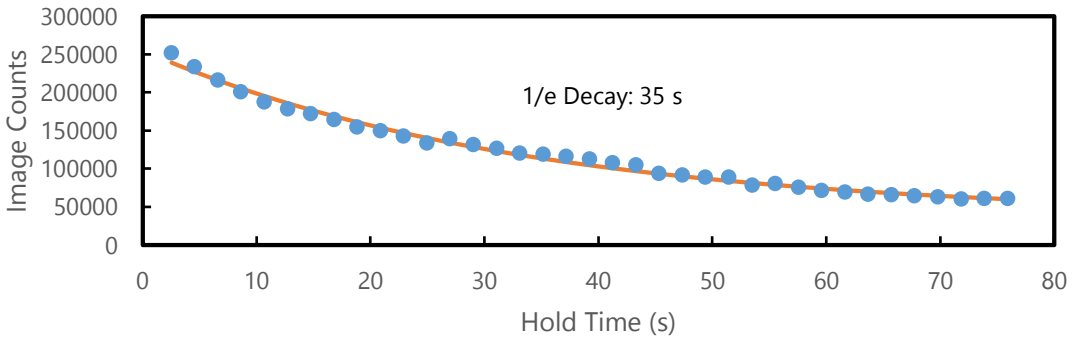

Figure 3.12: The measured lifetime of atoms in RbLi experiment's magnetic trap

$$V(\vec{\mathbf{r}}) = g_F \mu_B m_F B' \sqrt{x^2 + y^2 - 4(z + \frac{B_0}{B'})^2} \tag{3.18}$$

For very near the center of the coil geometry (which is valid for small atomic clouds versus the 10 cm length scales of the coils), the potential becomes linear in all directions, and radially symmetric along the coil axis:

$$V(\vec{\mathbf{r}}, z) = g_F \mu_B m_F B' (r - 2|z - \frac{B_0}{B'}|) \tag{3.19}$$

It is important to note that for atoms to be trapped we need $g_F \mu_B m_F > 0$. For the ^{87}Rb $F = 1$ states, this results in the $m_F = -1$ state being magnetically trappable, the $m_F = 0, +1$ states will either feel no force or explode outward respectively. For this reason, before loading our magnetic trap, we quickly optically pump the atomic cloud into the $m_F = -1$ state. The magnetic trapping potential is quite robust and only limited by the quality of the vacuum system we have. In our experiment we see $1/e$ atom number lifetimes in our trap of about 35 seconds.

3.3.1 Evaporative Cooling

Evaporative cooling is used to cool atoms down further after the laser-cooling stages of our experiment. Evaporative cooling works by selectively removing the hottest atoms in the cloud, which carry away large amounts of energy. This is done by lowering the strength of the trapping potential in which the atoms are confined. As the trap depth gets lower,

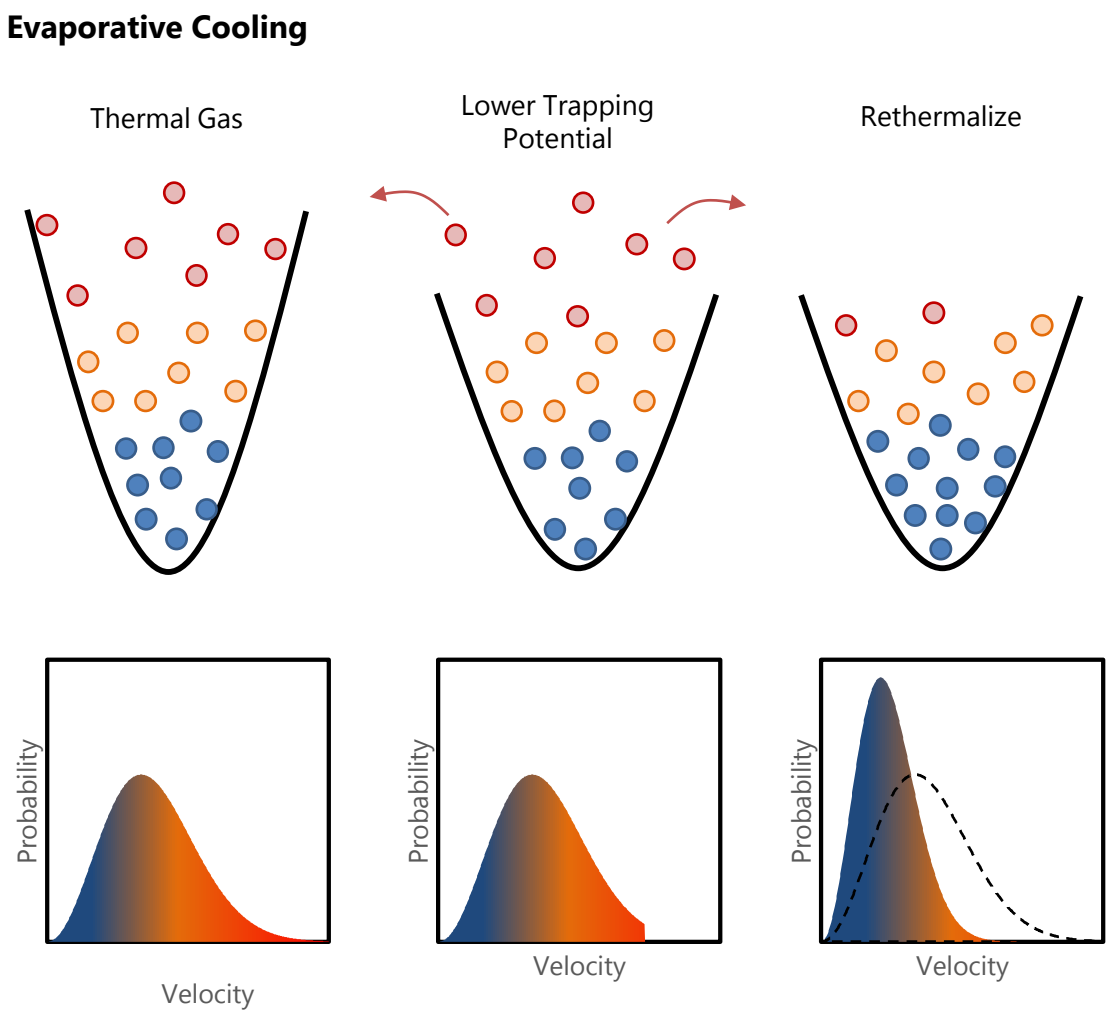

Figure 3.13: Evaporative cooling in a gas occurs when the potential of the trap is lowered, allowing the atoms with the most energy to escape. The loss of the atoms removes energy from the system, and the remaining atoms rethermalize through collisions to a lower temperature. This process can be repeated to further cool the sample.

the population of atoms that have a sufficient velocity (and kinetic energy / temperature) can escape the trap. As these atoms leave the trap, the population of atoms left in the cloud rethermalize with each other through scattering processes. The result is that the average temperature of the remaining atomic cloud, by selectively ejecting hot atoms, is lowered. This process can be extended to continuously and adiabatically (with respect to rethermalization) lowering the trapping depth until the desired temperature is reached.

3.3.2 RF Induced Evaporation

In magnetic traps, evaporation is done via a forced RF evaporation scheme. Instead of lowering the trapping potential and allowing the atoms to escape, an RF field with a large frequency is applied to the atoms. Due to the Zeeman effect, there exists a distance away from the trap center such that the atoms are on resonance, specifically where $\hbar\omega_{\mathrm{RF}} = \mu_B g_F B' r$, where B' is the strength of the magnetic field gradient of the magnetic trap. An atom within this region of space will be transfered from the magnetically trappable to untrappable states, and ejected from the cloud. By beginning the RF at a frequency far beyond the atomic distribution's radial extent, and similarly adiabatically lowering the frequency, the hottest atoms will be ejected, allowing the atomic cloud to undergo evaporation. In our experiment we typically ramp the RF frequency from 22 MHz down to 5 MHz in 3 seconds to give us a thermal cloud at $\approx 30\mu K$, cold enough to efficiently load the atoms into our optical dipole trap.

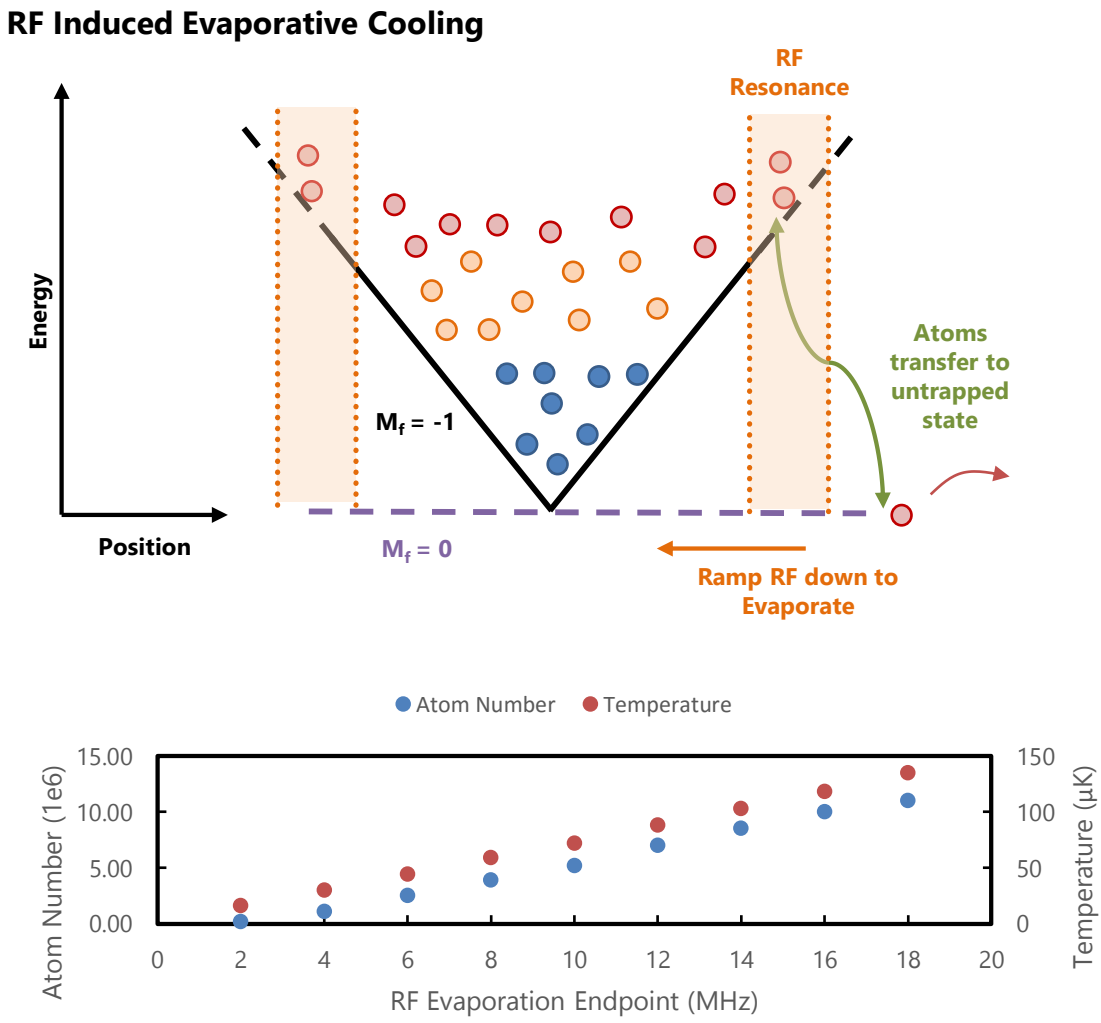

Figure 3.14: Top: In RF evaporative cooling in a magnetic trap, the potential is held constant while a resonant RF field is used to eject hot atoms into an untrappable spin state. Because of the magnetic field gradient, the resonance condition for the RF becomes a function of space, allowing the selective removal of atoms at high temperatures. Reducing the RF frequency will progressively select cooler and cooler populations to eject. Bottom: Measured temperature and atom number as a function of the end point of the RF frequency sweep.

3.4 Optical Trapping

A light-field that illuminates an atomic system can perturb the energy level structure of the atoms. This effect, known as the a.c. Stark shift or the light shift, is used within

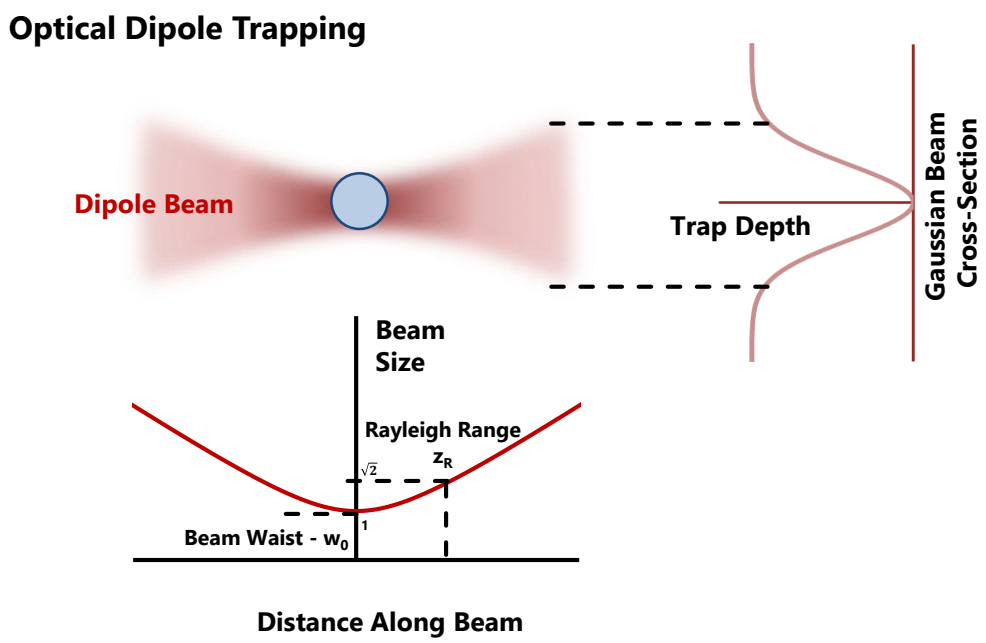

Figure 3.15: Trapping atoms using an optical field. The red-detuned light creates an intensity dependent attractive potential. The geometry of the optical trap is determined by the size and focus of the optical trapping beam.

degenerate gas experiments to confine the atomic clouds or condensates in space without a magnetic field component [38]. The confinement of condensates in a purely optical trap is advantageous as this opens up the study of spinor dynamics within the system [39, 40], as with magnetic traps only the magnetically trappable states can be studied.

The origin of the dipole force due to an electric field at an atom can be understood from the classical 'electron on a spring' harmonic oscillator model of the interaction of light with atoms. Using the assumption that the nucleus acts as a point charge and the electron is a uniform charge cloud of radius[5] R, we can write the internal electron-nucleus force as:

$$F = -m\omega_0^2 \vec{\mathbf{x}} \tag{3.20}$$

Where:

$$\omega_0^2 = \frac{e^2/mR^3}{4\pi\epsilon_0} \tag{3.21}$$

[5] s orbital spherical electron distribution

Where e is the electron charge, m is the electron mass, and ϵ is the Electric Constant. Including a perturbing electric field we get the equation of motion for the displacement of the electron-nucleus:

$$\frac{d^2}{dt^2}\vec{\mathbf{x}} + \omega_0^2\vec{\mathbf{x}} = \frac{e}{m}\vec{\mathbf{E}}(\vec{\mathbf{r}}, t) \tag{3.22}$$

Typically as a fudge factor to account for absorption, scattering and other lossy processes, a dissipative term is added, yielding the Lorentz Model of the atom:

$$\frac{d^2}{dt^2}\vec{\mathbf{x}} + 2\beta\frac{d}{dt}\vec{\mathbf{x}} + \omega_0^2\vec{\mathbf{x}} = \frac{e}{m}\vec{\mathbf{E}}(\vec{\mathbf{r}}, t) \tag{3.23}$$

Solving this equation using a plane wave oscillating electric field ($\vec{\mathbf{E}} = \vec{\mathbf{E_0}}e^{-i\omega t}$) gives the complex polarizabilty of the atom:

$$\alpha(\omega) = \frac{e^2}{2m\omega}\frac{(\omega_0 - \omega) + i\beta}{(\omega_0 - \omega)^2 + \beta^2} \tag{3.24}$$

Where:

$$\vec{\mathbf{p}} = \alpha(\omega)\vec{\mathbf{E}} \tag{3.25}$$

We can calculate the dipole energy using $V = -\hat{\mathbf{p}} \cdot \vec{\mathbf{E}}$. Calculating this horrid expression and averaging over the oscillation cycles we get:

$$V = \frac{-e^2|E_0(\vec{\mathbf{r}})|^2}{4m\omega}\frac{\omega_0 - \omega}{(\omega_0 - \omega)^2 + \beta^2} \tag{3.26}$$

Using the relationships between potential energy and forces, we can define the force:

$$\vec{\mathbf{F}}_{dipole}(\vec{\mathbf{r}}) = -\vec{\nabla}V = \frac{e^2\nabla|E_0(\vec{\mathbf{r}})|^2}{4m\omega}\frac{\omega_0 - \omega}{(\omega_0 - \omega)^2 + \beta^2} \tag{3.27}$$

If we recast this in terms of a Rabi frequency and take the limit $\delta = \omega_0 - \omega >> \beta$, we can achieve a substantial dipole force operating on the atoms with minimal absorption effects. In this limit, we get:

$$V_{light} = \frac{\hbar\Omega^2}{4\delta} \tag{3.28}$$

Where Ω is the Rabi frequency and δ is the detuning from resonance. For a negative

detuning, this will create a downward shift in energy, causing the state to become more preferable to an atomic system. Because the shift depends on Ω^2, a more intense light field will create a larger shift in energy. To use this effect to create a trapping potential, a spatially dependent intensity is used, specifically in the form of a Gaussian laser beam. A Gaussian beam propagating in the $\hat{\mathbf{z}}$ direction has the intensity profile:

$$I(x,y,z) = \frac{2P}{\pi w^2(z)} \exp(\frac{-2(x^2+y^2)}{w^2(z)}) \tag{3.29}$$

Where P in the power in the beam and w is the waist of the beam (the beam radius orthogonal to the propagation direction):

$$w(z) = w_0\sqrt{1+\frac{z^2}{z_r^2}} \tag{3.30}$$

Where w_0 is the beam waist (the 1/e radius of the beam at focus) and the Rayleigh range $z_r = \pi w_0/\lambda$ is the measure of the distance along the beam propagation direction in which the radius increases to $\sqrt{2}w_0$. In the limit for a far detuned laser beam, the energy shift from the a.c. Stark shift takes the form:

$$V = \frac{\hbar\Gamma^2 I}{8\delta I_{sat}} \tag{3.31}$$

When the detuning is positive ($\delta > 0$) the presence of the laser beam causes a positive gain in energy that repels the atoms (sometimes used on purpose to blow holes through condensates [41]). In the case of negative detuning ($\delta < 0$), the potential becomes attractive, and the atoms will seek locations of high intensity. For a laser beam with a tight focus placed by the atoms, they will feel a confining potential at the location of minimum beam waist (highest intensity).

For a laser beam with a Gaussian profile (Equation 3.31), the trapping potential can be calculated as:

$$V = \frac{\hbar\Gamma^2}{8\delta I_{sat}} \frac{2P}{\pi w^2(z)} \exp(\frac{-2(x^2+y^2)}{w^2(z)}) \tag{3.32}$$

If we approximate the potential as a harmonic oscillator, i.e. take a series expansion, we

find a potential of the form:

$$V(x,y,z) = \frac{1}{2}m(\omega_x x^2 + \omega_y y^2 + \omega_z z^2) \tag{3.33}$$
$$\omega_x^2 = \frac{4V_0}{mw_0^2}$$
$$\omega_y^2 = \frac{4V_0}{mw_0^2}$$
$$\omega_z^2 = \frac{2V_0}{mz_R^2}$$

Where V_0 is the depth of the trap, and ω_i are the characteristic trapping frequencies in each Cartesian direction. A single laser beam provides a tight radial confinement potential. The Rayleigh range of the focused beam is typically much larger then the beam waist therefore the axial confinement will be small by comparison. To provide tight confinement along both directions, a pair of optical dipole trapping beams can be used to form what is known as a crossed dipole trap. In this scheme, two trapping beams are intersected at the atoms (typically at 90 degrees) such that there is tight confinement along all three axes of the trap. The trapping potential of the two potentials are superimposed together in space. The geometry of the crossed dipole trap can be experimentally adjusted by shaping each of the two beams via optical elements, or altering the ratio of power between the two beams. In our experiment, we have altered the optical dipole trap geometry to give both quasi one dimensional trapping potentials (Figure 5.3) and cylindrically symmetric traps (Chapter 7).

3.5 Measurement of Cold Atoms

The most critical portion of any experiment is the measurement. The goal of most experiments is to apply a controlled evolution of the system and measure the effects upon the atomic ensemble. In order to retrieve the information in the ensemble, we as the experimenters need a method to probe and measure the state of the system. With ul-

tracold atomic systems, most measurement techniques involve capturing an image of a laser beam that has passed through the atoms. The workhorse method of measurement, absorption imaging, illuminates the condensate with on resonance laser light and images the beam to extract information via the absorption behavior of the atoms. Other techniques can also be used that focus on the dispersive properties of the atoms, including phase-contrast imaging [42], which provides a non-destructive imaging method. During my tenure the RbLi experiment has exclusively used absorption imaging, and as such is discussed primarily.

3.5.1 Absorption Imaging

Absorption imaging is the standard method of imaging in ultracold atomic experiments. The measurement process is destructive, as the protocol involves on resonance light that provides momentum to the atoms. This is a large limitation of the method, however from a single image we can obtain the density profile of the atoms which allows us to calculate parameters such as temperature or momentum when combined with time-of-flight imaging.

To describe the processes used in absorption imaging and use it as a measurement technique, we need to understand the basic processes of atomic absorption. To model the absorption process, we consider a laser beam with intensity I propagating along $\mathbf{e}_z$ through a gas of atoms with density n in a rectangular volume $A{\cdot}\Delta z$. The atoms themselves have an optical absorption cross section, σ, which characterizes the probability of the absorption process occurring. The fraction of the light that is absorbed is the volume density n multiplied by the thickness of the sample Δz and the effective area of each atom: $\sigma n \Delta z$. The cross section σ is frequency dependent with the functional form of Lorentzian centered around the atomic resonance. Therefore the rate in which the beam is attenuated as it propagates through the atomic sample is:

$$\frac{dI}{dz} = -n\sigma(\omega)I \tag{3.34}$$

Which is readily solvable to give the intensity as a function of distance through the atomic sample:

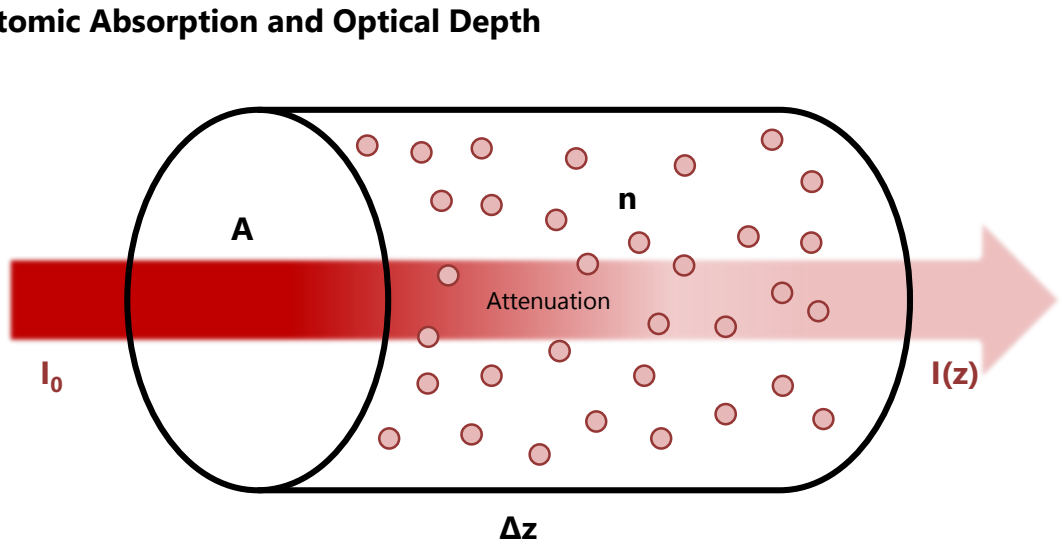

Figure 3.16: A sample of atoms with density n is intersected by a beam of cross-sectional area A for a length Δz. The absorption of light from the atoms causes an attenuation in the beam related to n and Δz given by Beer's law.

$$I(\omega, z) = I_0 \exp(-n\sigma(\omega)z) \tag{3.35}$$

Equation 3.35 is known as Beer's law [43]. In the context of absorption imaging, we define the optical depth of the atomic gas OD such that $OD = n\sigma(\omega)z$. Making this substitution and rearranging Equation 3.35:

$$OD = \ln(\frac{I}{I_0}) \tag{3.36}$$

Helpful ^{87}Rb Absorption Imaging Parameters

Description	Symbol	Value
Saturation Intensity $\|F=2,m_F=\pm2\rangle$ to $\|F=3,m_F=\pm3\rangle$, $\sigma_\pm$	I_{sat}	1.662 mW / cm^2
Peak Optical Cross-Section	$\sigma_0=3\lambda_0^2/2\pi$	2.9 x 10^{-9} cm^2

Figure 3.17: Parameters used in calculating atom number from absorption imaging.

This equation is at the heart of absorption imaging. By taking an image of the resonant light passing through the image, we obtain the information about $I(x, y)$ (the absorption image, Figure 3.18). By taking a second image of the probe beam with no atoms, we obtain the initial intensity of light, $I_0(x, y)$ (the probe image, Figure 3.18). Because we do not have some sort of three-dimensional camera, the optical depth OD represents the integration of the atomic density along the probe beam direction, that is: $OD_{meas} = \sigma(\omega) \int_0^{\Delta z} n(x, y, z)\, \mathrm{d}z$. By knowing the value of the optical cross-section $\sigma(\omega)$, we can directly measure the atom density. To make the numbers easier, we always use circularly polarized light that we keep on resonance, giving a straight forward calculation of the cross section (Figure 3.17).

Experimentally, we also take a third shot in each sequence to measure the background light incident on the camera (the background image, Figure 3.18). For this shot we disable all of the lasers, allowing only the ambient light to be measured. We subtract this image from both the absorption and probe images, thus our experimentally measured optical depth is:

$$OD = \ln\left(\frac{I_{\mathrm{abs}} - I_{\mathrm{bg}}}{I_{probe} - I_{\mathrm{bg}}}\right) \tag{3.37}$$

For ^{87}Rb we address the $|F = 2, m_F = \pm 2\rangle$ to $|F' = 3, m_F = \pm 3\rangle$ transitions for absorption imaging. Because we work with the F=1 manifold when doing BEC experiments, we first use the repump laser to transfer atoms out of the F=1 states to F=2 in a 100 μs pulse, and then image with the probe beam for approximately 20 μs.

3.5.2 High Intensity Absorption Imaging

In the previous section, the formalism assumed the case where the intensity of light was much less than the saturation intensity of the atomic transition ($I << I_{sat}$), leading to the approximation that most of the atoms in the sample were in the ground state. In the case of very dense atomic samples (such as BECs), a weak probe beam incident on the atomic sample may be completely absorbed. In this case, a ratio of the absorption imaging intensity to the solely probe beam intensity is not sufficient all light is attenuated.

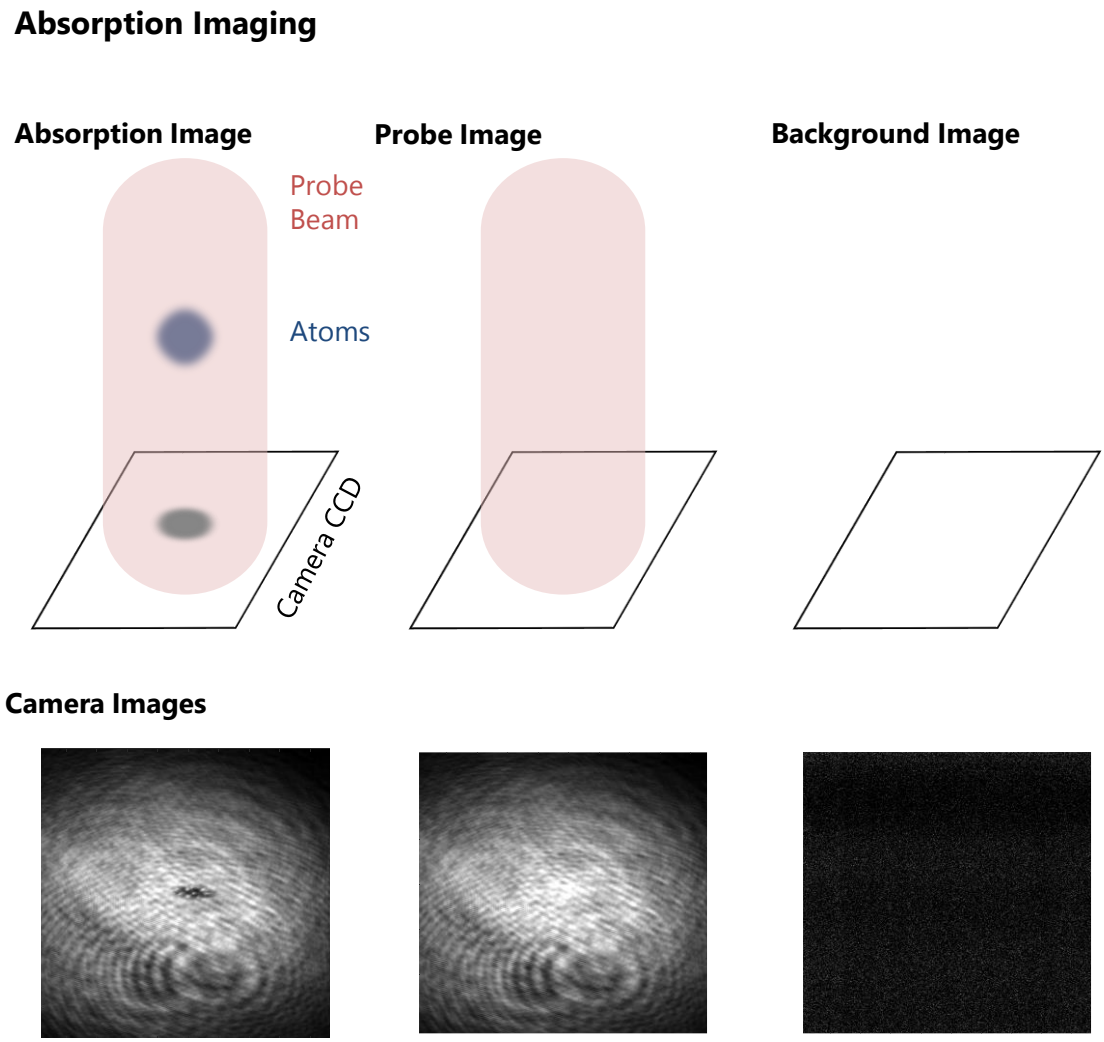

Figure 3.18: For absorption imaging, three separate images are taken. First, the atoms are illuminated by the probe beam and the CCD camera detects the shadow in the beam from the atomic absorption (left, absorption image). Next an image of the beam without the atoms is taken (center, probe image). Lastly an image of the background with no light is taken to account for stray light hitting the camera (right, background image).

The solution at first glance is to increase the amount of power in the probe beam to the point where the flux of photons through the atomic sample is greater than the rate in which they can be scattered at peak density. This approach can lead to problems. First, our Beer's law approximation that most of the atoms in the ground state fails, and the different populations of atoms in both the excited and ground states must be considered. Secondly, with a high intensity probe beam, the CCD camera used for imaging can saturate. A solution to this problem is to decrease the probe pulse time. Note that

this time cannot be reduced arbitrarily. There is a lower limit on the system given by the linewidth of the transition being used for absorption - the atoms have to at least have time to scatter photons!

To avoid approximations of low power, we need to consider a modified Beer's law where atoms can be in either the ground or excited states (see Reference [44] for a wonderful description):

$$\frac{dI}{dz} = -n\frac{\sigma_0}{\alpha^*}\frac{1}{1 + I/(I_{sat}\alpha^*)}I = -n\sigma(I,\omega)I \tag{3.38}$$

Where α is an empirically determined value that accounts for polarization impurities and corrections to the two-level atom model. Solving this differential equation for the optical depth yields:

$$OD(x,y) = \sigma_0 \int n(x,y,z)\,\mathrm{d}z \tag{3.39}$$

$$= -\alpha^* \ln(\frac{I_{\mathrm{abs}} - I_{\mathrm{bg}}}{I_{probe} - I_{\mathrm{bg}}}) + \frac{I_{\mathrm{probe}} - I_{\mathrm{abs}} - I_{\mathrm{bg}}}{I_{\mathrm{sat}}} \tag{3.40}$$

The result is an extra term that includes a direct subtraction of the probe and absorption images, instead of just a ratio. This process can introduce noise into the images due to the linear term, however at large optical depths, such as those in BECs, we can recover the atom density correctly. Reference [44] describes a calibration procedure for α^* and I_{sat}.

Chapter 4

The RbLi Experimental Apparatus

4.1 The RbLi Apparatus

The RbLi experimental apparatus was constructed to facilitate the laser cooling and trapping of both ^{87}Rb and ^{6}Li (Figure 4.1). The design contains a traditional (tried and true) Zeeman slower atomic source combined with a magneto-optical cooling and trapping stage. For the experimental geometry used throughout this chapter, I define $\hat{\mathbf{x}}$ to be along the Zeeman slower axis, with $+\hat{\mathbf{x}}$ defining the vector from the experimental cell towards the atomic source. Similarly $\hat{\mathbf{y}}$ is the direction orthogonal to the $\hat{\mathbf{x}}$ direction and $+\hat{\mathbf{z}}$ is the direction opposite of gravity.

4.1.1 Experimental Layout

The science within the RbLi apparatus takes place within a glass cell under ultra-high vacuum. To create an atomic source a pair of ovens, loaded with Rubidium and Lithium, are heated to create an atomic vapor of each element. The hot atomic vapor is collimated through an aperture and enters the Zeeman slower. The Zeeman slower, using a slowing

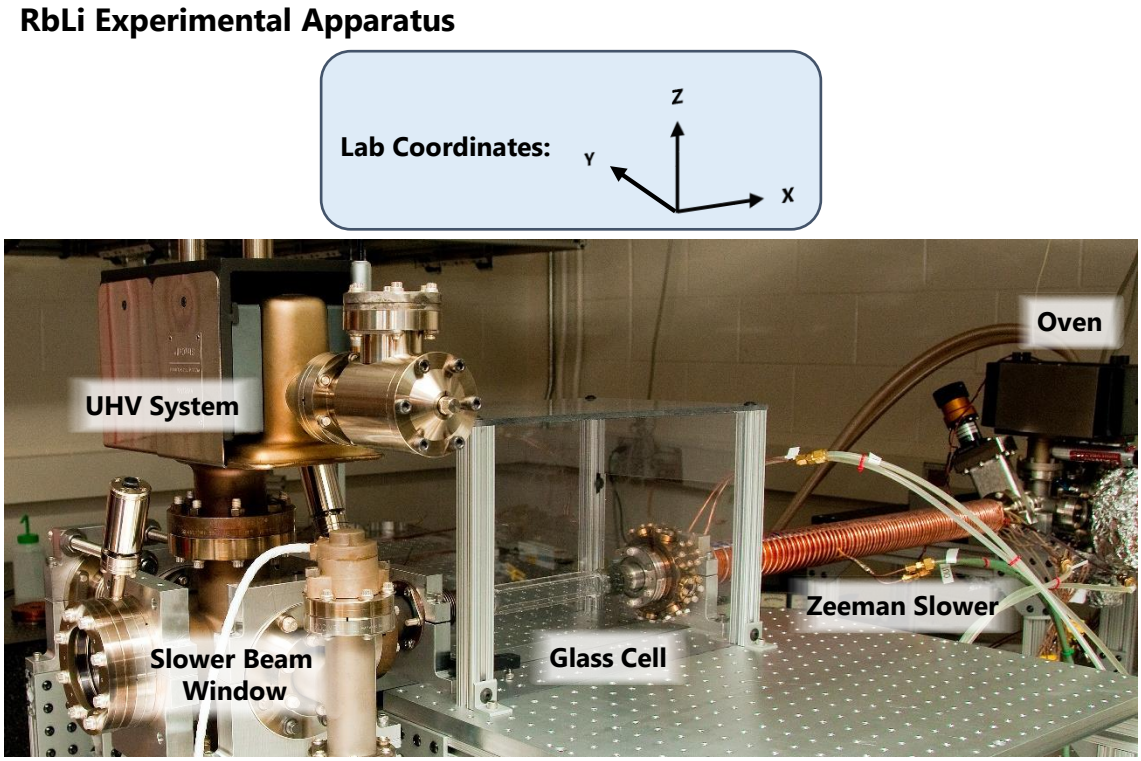

Figure 4.1: The RbLi Experimental Apparatus, prior to installation of cooling and trapping optics. An atomic oven is connected to the experimental glass cell via a Zeeman slower.

beam and a solenoidal current wrapped around the slower, is able to cool the atomic beam to within the capture velocity of the MOT at the experimental cell. For the MOT, six cooling and repump beams, following paths along $\pm\hat{\mathbf{x}} \pm \hat{\mathbf{y}}$ and $\pm\hat{\mathbf{z}}$ overlap at the center of the experimental cell. Above and below the experimental cell are a pair of anti-Helmhotz coils that provide a magnetic field gradient used for creating the MOT, magnetic trapping and generic magnetic field gradient creation. Figures 4.5 and Figure 4.45 show the XY and XZ layouts of the system respectively.

On the $+\hat{\mathbf{y}}$ side of the experimental optics is the arrangement for the optical dipole trapping laser. The dipole provides the trapping potential for confining atoms when at degeneracy. The dipole beams propagate along the $\hat{\mathbf{x}} - \hat{\mathbf{y}}$ and $-\hat{\mathbf{x}} + \hat{\mathbf{y}}$ directions, however slightly rotated within the xy plane so as to dodge the MOT optics. The entire system is enclosed by a box of 1/4" black plexiglass. This enclosure helps to keep out stray light, keep temperatures stable, but most importantly, provide a barrier of safety between the

lab and the high power laser for optical dipole trapping.

4.1.2 Oven Vacuum System

The RbLi apparatus has a dual species oven chamber design. The Rubidium and Lithium ovens come into the apparatus in series. As the Rubidium is heated up in the rear chamber, it flows through narrow and slightly angled nozzle port into the Lithium oven, which also serves as a mixing chamber for both species.

The Rubidium and Lithium reservoirs and nozzles are wrapped in heater tape. To generate a large enough vapor pressure to create an atomic beam of Rubidium to load our MOT, the Rubidium and Lithium ovens need to be heated to 120 °C and 160 °C respectively. The nozzles are also heated to prevent buildup from occurring in the narrow passages. The Rubidium nozzle is heated to 400 °C, while the Lithium nozzle is kept at 240 °C. The Lithium setup is kept warm, but because we are not actively doing experiments involving Lithium, we keep the oven quite cool compared to the temperature require to make a Lithium atomic beam (≈350 - 400 °C). The entire region of reservoirs and nozzles is wrapped in aluminum foil to better insulate and spread the heat. Each region is separately

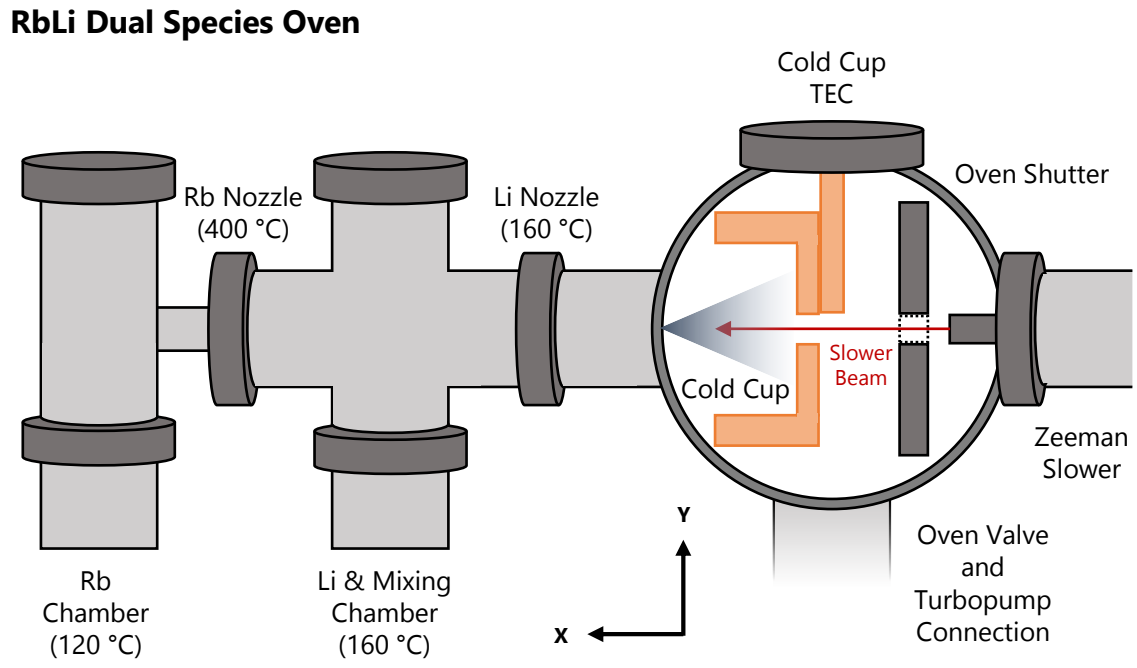

Figure 4.2: Schematic of dual species oven.

temperature stabilized by using heater tape, an individual thermocouple, and an Omega CNI 3233 temperature controller unit to regulate each region. The controllers each drive an Omega high voltage solid state relay that connects power from an AC power source, that we controller with variable transformer units, to the heater tape.

Both species then travel out of the heated oven units into a main chamber that contains a cold cup and an oven shutter. The cold cup is a cylindrical copper unit that is thermo-electrically cooled, via a copper bar connection to outside of the chamber, to approximately -30 °C. The head depositing side a thermo-electric cooler (TEC) providing the cooling is connected to a closed loop water chiller unit. The cold cup design helps to capture excess atomic deposition in the oven chamber instead of damaging our ion pumps.

The portion of the atomic beam that travels past the cold cup traverses the oven shutter region. The oven shutter is used to block the atomic beam when not loading the MOT as the atomic beam causes unwanted heating in the later stages of cooling our atomic clouds. The shutter is constructed from a disassembled hard disk drive actuator arm with a metallic flag at the end. By sending this device current, via vacuum-friendly kapton sealed wires connecting to outside of the oven chamber, this makeshift shutter can be actuated to enable or disable the atomic beam. From the shutter the atomic beam travels down the Zeeman slower, which acts as both a collimator for the beam and a differential pumping stage between the oven vacuum chamber and the experimental vacuum chamber.

4.1.3 Experiment Side Vacuum System

The experimental vacuum system consists of the glass cell where we perform our BEC experiments, as well as Titanium-sublimation (Ti-Sub) pump and ion pump units. At the end of the apparatus is a vacuum window in which the slower beam is passed down the $\hat{\mathbf{x}}$ direction of the apparatus, all the way back to the oven. The glass cell is 1.25" wide square diameter and 8" along the slower ($\hat{\mathbf{x}}$) axis. The cell is made from 1/8" uncoated Pyrex glass. The cell center is the geometric center of our experiment, and as such all electromagnetic coils, except the slower units, have their geometry fixed by design with this point in the enter.

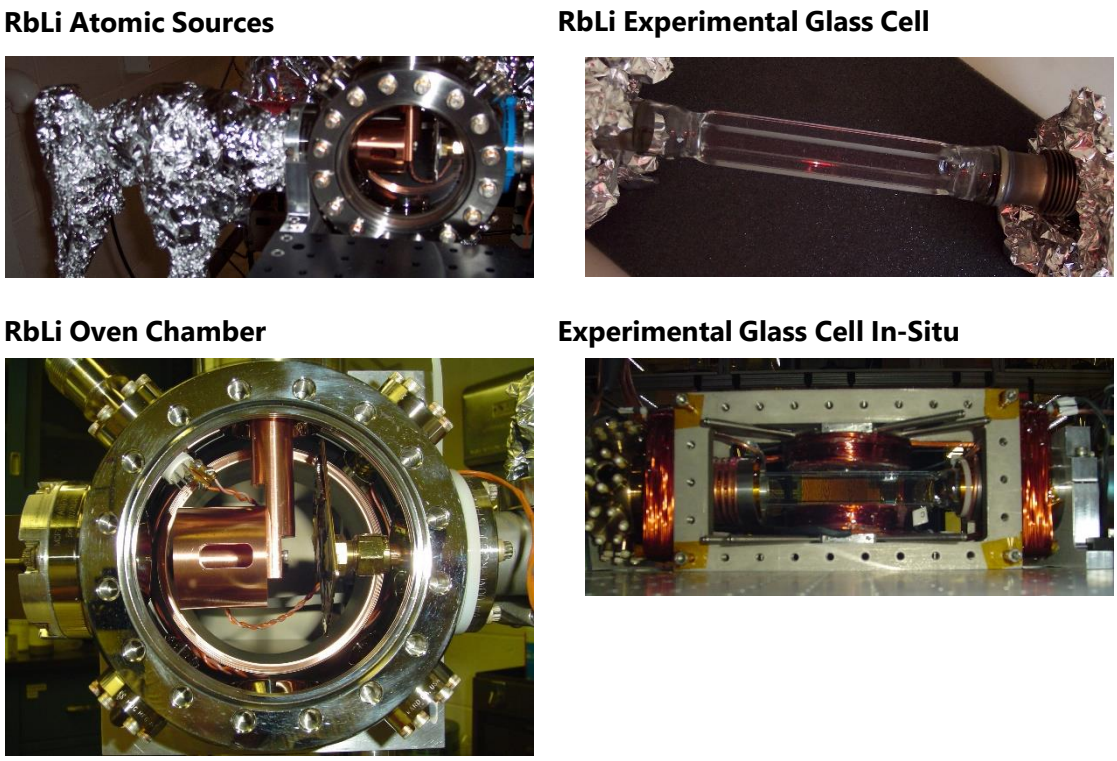

Figure 4.3: RbLi Apparatus vacuum system components when being installed.

4.1.4 RbLi Experimental Cooling Sequence

Our apparatus is designed to rapidly generate ^{87}Rb BECs that are loaded into a crossed optical dipole trap. As absorption imaging is a destructive measurement technique, we have to generate a new condensate per measurement. The cycle to take atoms from our experimental ovens to a trapped condensate is described here in an overview.

First, we heat our Rubidium atomic source to 120 °C, creating a collimated atomic beam that travels down our Zeeman slower. These atoms are slowed and captured into our MOT. In order to have enough atoms at the condensate, after all losses, we continue the MOT loading process for 7 seconds. We then turn off the magnetic gradient field for the MOT, and perform an optical molasses cooling stage for a brief ≈15 ms. Within milliseconds after the molasses cooling stage, we optically pump the atoms into the $|1, -1\rangle$ state, which are magnetically trappable. We then snap on the magnetic trap to capture the atoms. We then compress the atomic cloud by adiabatically increasing the depth of

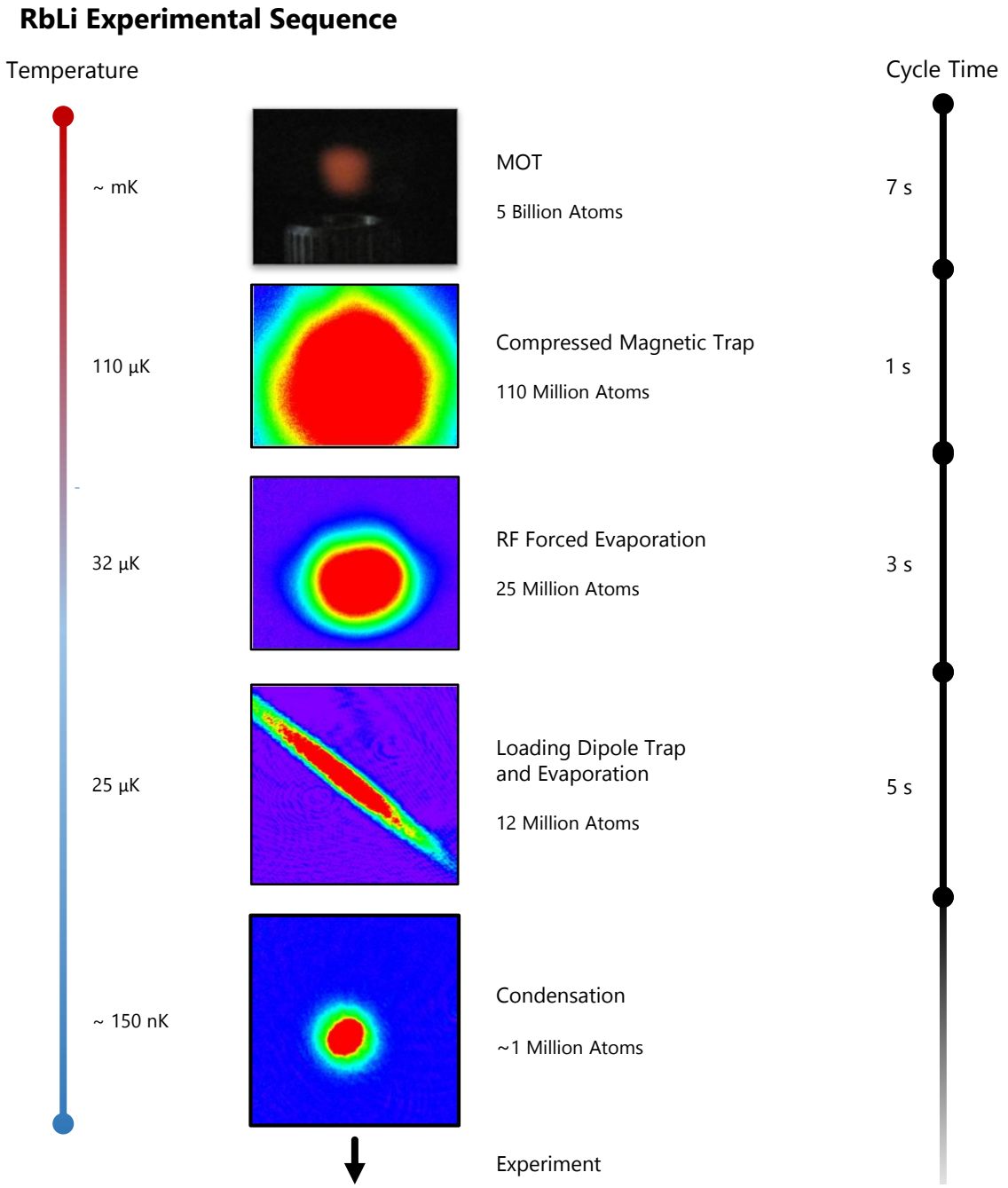

Figure 4.4: Cooling sequence for the experiment. The process to reach BEC requires multiple laser cooling and evaporative stages. Images show representative absorption images at the various stages.

the trap, and then perform an RF forced evaporation stage for 3 seconds to further cool the cloud.

After the evaporation stage, we relax the trap while simultaneously transferring atoms into a single optical dipole trap. Here we reduce the strength of the magnetic trap

such that the combined optical and magnetic trap will still confine the atoms against gravity. Next we transfer to a crossed optical dipole trap and slowly remove any magnetic trapping. The transfer to a pure optical dipole trap acts as a preliminary evaporation stage. To reach condensation, we further relax the optical dipole trap by lowering the intensity in the beams, causing more evaporative cooling to take place. Once we have a condensate, we commonly use an adiabatic rapid passage technique to prepare the BEC in a preferred spin configuration before performing an experiment.

4.1.5 Experiment Side Optical Setups

Slower Optics

The slower optics are at the end of the apparatus, on the far side from the ovens. The optics are build in a vertical cage mounted structure that reflects into a viewport at the end of the apparatus, down the glass cell, Zeeman slower and into the oven. The slower repump and slower cooling light are brought over to the experiment and combined in fiber optics. Traditionally we have aligned the slower beam by viewing the oven with an infrared camera, and adjusting the alignment and focusing until we see maximal florescence.

MOT Optics

The experiment has a set of six MOT beams that intersect at right angles at the center of the glass cell. Both the MOT cooling and repump light are combined in fiber optics from the laser boards, then multiplexed into 6 separate fiber lines. Each of these fiber lines terminates at a fiber launch on the experiment side. Each of these launches are identical in construction. Primarily the units consist of fiber collimation optics, a telescope to enlarge the MOT beams to approximately one inch in diameter, and a $\lambda/4$ waveplate to create the circular polarization necessary for the MOT. The light from each MOT fiber launch is reflected via gold mirrors[1] and through a two mirror periscope consisting of two elliptical one inch gold mirrors. The light then crosses the glass cell.

[1] Gold mirrors help preserve the circular polarization of the beams

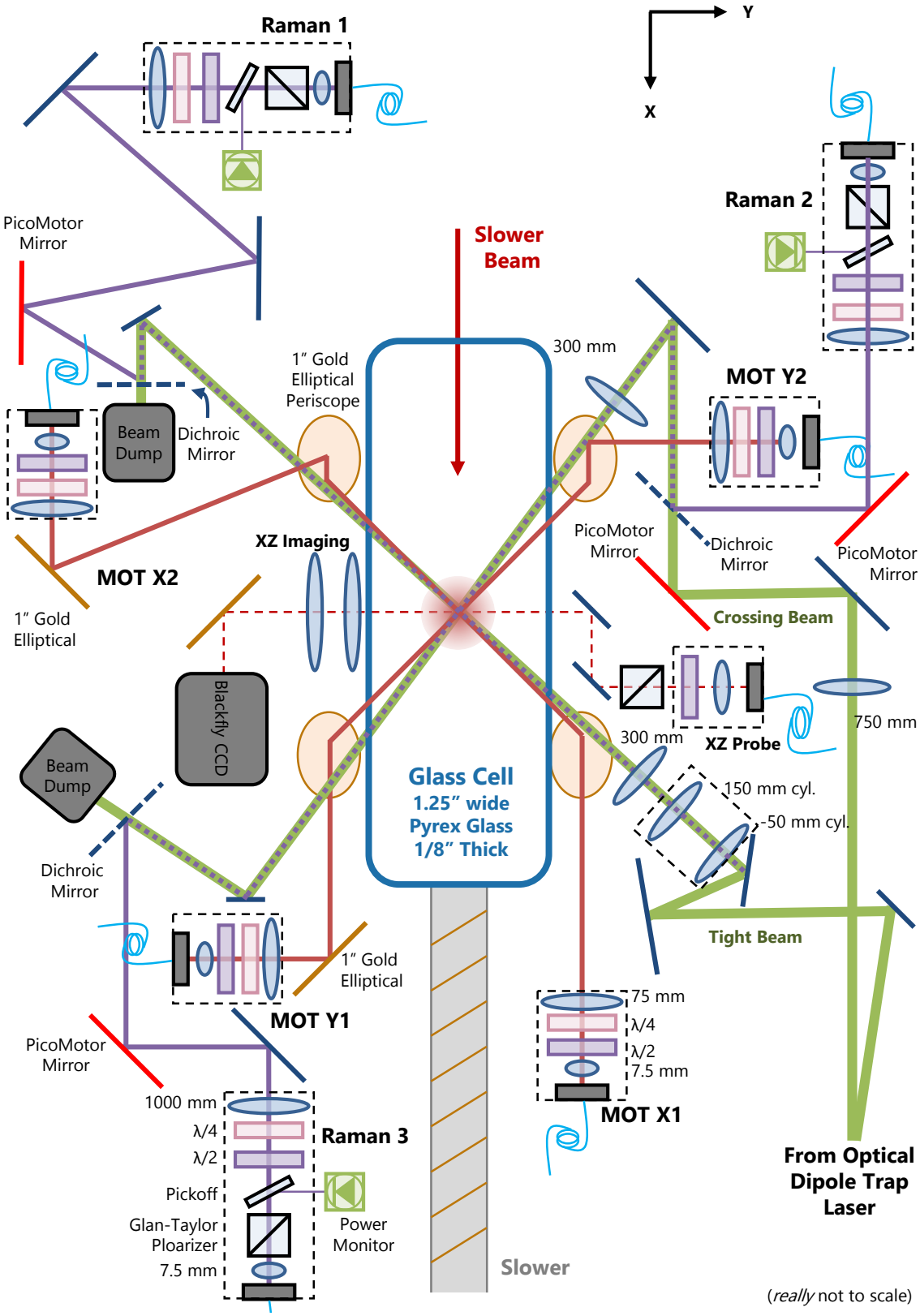

Figure 4.5: RbLi Experimental Side Optics. Items in dashed boxes represent cage mounted opto-mechanical units.

Originally the last gold mirror on the telescope was connected to a flipper mirror unit, so when the MOT stage was complete, the large mirrors could be rotated out of the way, allowing more optical access for later experimental stages. However in the early years of the experiment, these flipper mirrors repeatedly malfunctioned (both slowly and instantly), ruining our MOT alignment. After the nth time of repairing these units, we switched the MOT periscopes in plane with the glass cell with static mirror mounts, and we have had no issues since. However the price we pay is now we have all other optical beams coming in at non 45 degree angles to dodge the MOT mirrors. Summary to anyone who reads this: **do not use flipper mirrors in new designs**.

To align these beams, we used optical cage assembly that could be attached to our quadrupole coil holders above and below the glass cell. The connection points for the optomechanics and the coil holders ensured 90 degree intersections. Using cage based alignment tools, we can, with great effort, get all the MOT beams orthogonal.

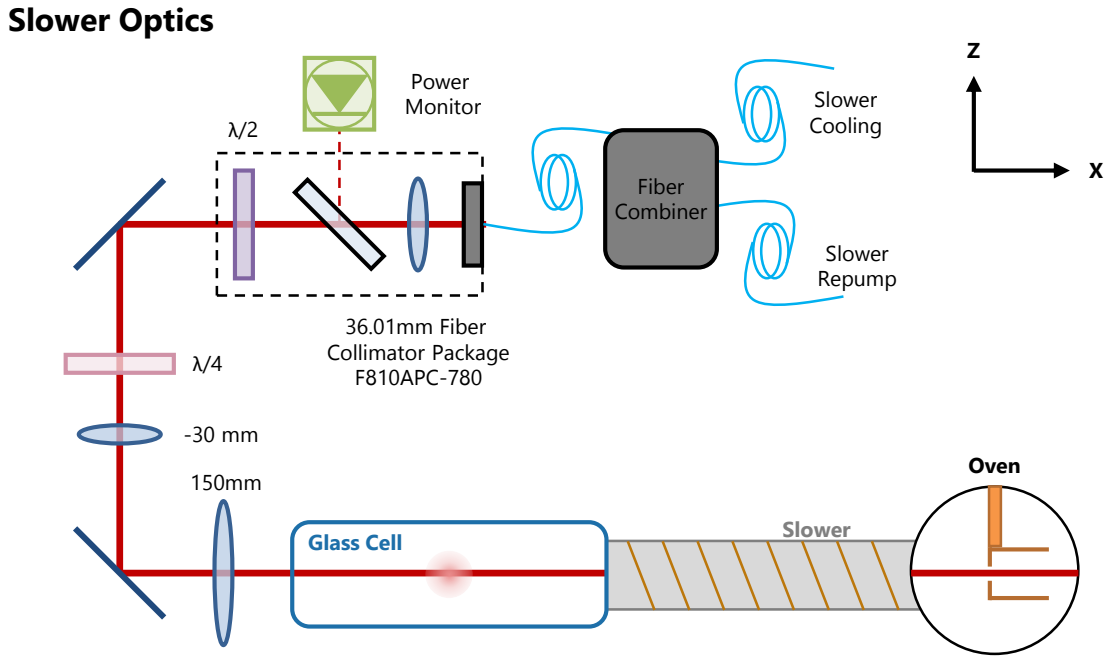

Figure 4.6: RbLi Experiment slower optics and geometry

Optical Dipole Trap Optics

The optical dipole trap optics intersect the glass cell and atoms at nearly the same $\hat{\mathbf{x}} \pm \hat{\mathbf{y}}$ trajectory as the MOT beams. However, because of issues with the MOT mirrors and geometry (see last section), the optical dipole traps beams were rotated slightly in plane from the more natural $hatx \pm \hat{\mathbf{y}}$ geometry. The optical dipole beams, unlike other systems, are not brought to the experiment side via fibers, but in free space optics adjacent to the main experimental optics (Figure 4.23). The tight and crossing beams originate from the $+\hat{\mathbf{y}}$ side of the experiment. Both beams have telescope systems to reshape the beam geometry before a final lens near the glass cell that focuses the dipole beam at the atoms. Current, and for most of the work we have done, the lens systems produce a 67 μm waist for the tight beam, and a 300 μm waist for the crossing beam at the atoms.

Because of the intense amount of light involved, the ODT beams after propagating through the atoms need to be reflected into high power beam dumps to avoid burning through any nearby objects, wires or surfaces. In the later stages of the experiment (circa Spring 2015), the Raman beams were overlapped with the ODT beam optical path via dichroic mirrors, making alignment of both systems more straight forward.

Raman Optics

The Raman beams are used in our synthetic gauge field and spin-orbit coupling experiments. On the experiment side they are ported in from fiber lines into specialized fiber launches. We use a 7.5mm aspheric lens to collimate the beam, followed by a Glan-Taylor polarizer as the exact polarization matters with the Raman coupling scheme. The light then traverses a pickoff into a power detector that is used for intensity stability. The light then goes through both a $\lambda/4$ and $\lambda/2$ waveplate to give full polarization control. Lastly the light is focused down at the atoms with a 1000 mm lens at the end of the launch. All three beams propagate with the ODT beam lines via dichroic mirrors added to the system. When setting the polarization, the measurement with the polarimeter is done after the glass cell itself instead of after the launch, given the polarization distortion effects from dielectric mirrors.

Picomotor Mirrors

The Picomotor mirrors from New Focus Optics are computerized stepper mirrors whose deflection angle can be electronically incremented on the order of mircoradians. Given the precision down to microns we need to align critical beams, such as the ODT beams or the Raman beams, this form of alignment vastly reduces alignment time and day-to-day stability of the system. Currently all of the Raman beam lines have a Picomotor mirror on the last tunable mirror before the atoms. The crossing ODT beam also has a Picomotor mirror for ease of alignment. The tight direction ODT beam will be upgraded as well, however as of writing it currently is aligned well, and we wait for a better opportunity to switch out the optics.

Vertical Optics

The optics on the upper and lower tiers of the experiment primarily are for the vertical MOT beams and our XY imaging system. A side on view showing the verical optics systems is shown in Figure 4.46. To combine the vertical probe path and vertical MOT beams, we used a pair of flipper mirrors that can rotate out of the way. We shine the MOT beams on these mirrors, and rotate them out after the MOT stage.

4.1.6 Ultraviolet LEDs and Preventing Lithium Buildup

In the original design of the system, both Rubidium and Lithium were going to be present within the vacuum system. More importantly, Lithium was going to be heated out of the oven and shot down the Zeeman slower into the ultra high vacuum region of the apparatus. Lithium is problematic in a vacuum system as it can be absorbed into glass, reducing (or blocking) the transmission of laser light. The thesis from Claudiu Stan at MIT (reference [45], section 2.2.4) covers the woes of Lithium quite well. The end solution to avoid absorption of Lithium was to heat the windows to prevent the Lithium from sticking onto the windows.

Given our apparatus design, we decided to forgo a heated window system and instead were going to use an array of UV light sources to prevent the Lithium from sticking. The mechanism, light-induced atomic desorption, is related to the physics of the photoelectric

effect. An incoming photon can be absorbed by an atom on a surface, gaining the kinetic energy to eject from the surface. This method has been used previously to increase vapor pressures enough to load MOTs from background atoms [46].

The design I made uses a set of 3W UV LED spotlight units from Mightex. Two of these units are placed at the end of the apparatus, aimed at the vacuum window where the slower beam enters. Another unit is placed by the glass cell, and another placed to illuminate the oven window. These units can be toggled on and off with a digital TTL signal (DO2-12) so the LEDs can be turned on in between cycles, or overnight[2]. Although we do not plan to run Lithium in the near future, the LEDs can also prevent any Rubidium from depositing within the vacuum system as well.

4.2 Computer Control Systems

For modern ultracold atomic physics experiments, precise timing and control of experimental parameters is of extreme importance. In order to go from a hot jet of thermal atoms out of an oven to a nanokelvin cooled BEC, there are many parameters in the systems, such as laser frequencies and intensities, currents in electromagnetic coils, and radio frequency fields that are parameterized at exactly the right moment (down to microseconds precision) in order to effectively capture and cool the atoms down to degeneracy. In order to coordinate the myriad of electronic components and instruments through out the lab that are required to reach our experimental goals, we use a computer control system that marshals all of the other instruments via analog and digital signaling. Our lab utilizes two separate computers in order to control and monitor the experiment, the 'Control' and 'Imaging' computers.

4.2.1 Control System

The control computer is tasked with sending the correct signals to all of the various instruments throughout the experiment. The control computer utilizes National Instrument's

[2] a practice that should be enforced more

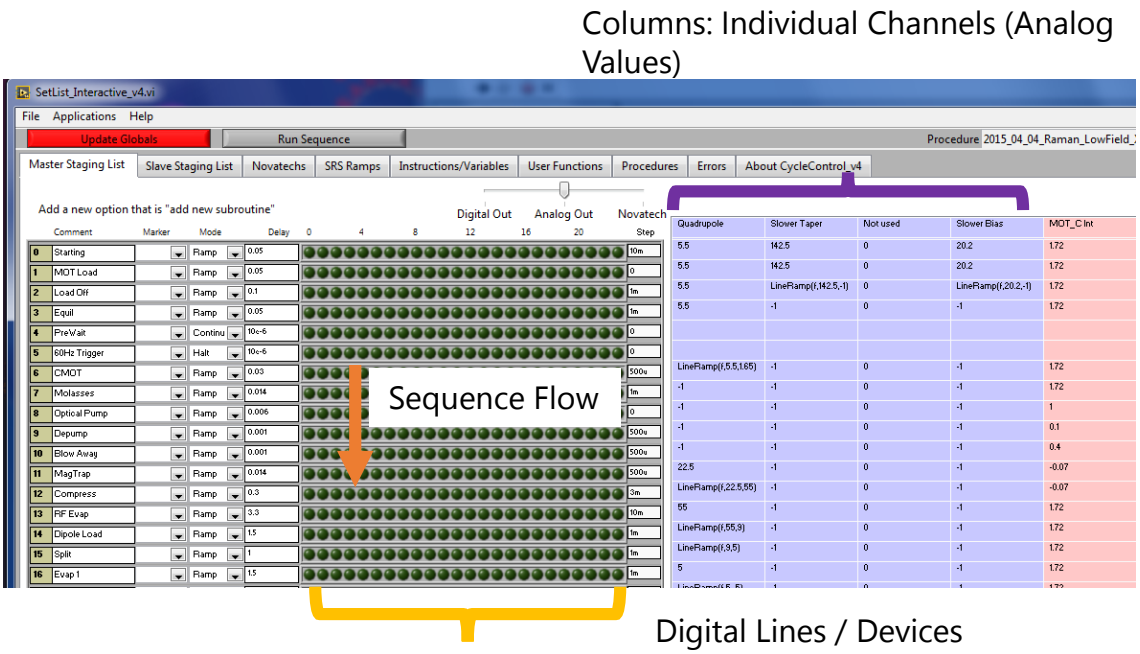

Figure 4.7: Computer control program example. Rows in the program represent steps within the cycle, and columns represent digital 5V signal toggling or analog voltages sent to laboratory equipment.

LabView software and the 'SetList' custom code widely used (in one version or another) throughout the JQI ultracold atom physics groups. This code is the front end for the user/experimentalist to input the sequence of commands that can be then translated as signals sent to various instruments in the lab.

The software acts as very large linear state machine that increments in steps through a predefined cycle that is programmed by the user. At each stage, each variable (whether it be a signal that sets a certain amount of current in a coil to produce a given magnetic field, or the frequency of an AOM) is updated as output by the system. To translate the computer commands to electronic signals that the experimental hardware can interface with, we have deployed 6 National Instruments USB-6229 Analog-Digital conversion adapters. These devices are tasked with three purposes. First, outputting both digital TTL signals used for precise timing of state toggling of devices, like optical shutters, flipping mirrors or RF switches. Second, the USB-6229 devices output analog signals to control experimental equipment such as electromagnetic current control or laser beam intensity, both variable and continuous values. The analog output channels allow us to command voltages of

	Device 1	Device 2	Device 3	Device 4	Device 5	Device 6
AO_0	Quadrupole Current	MOT Cooling AOM	X Bias Current	RF Mixer (Amplitude)	Raman 2 (A) Intensity	XY Gradient Shim
AO_1	Slower Current	MOT Repump AOM	Y Bias Current	ODT Power AOM	Raman 3 (B) Intensity	YX Gradient Shim
AO_2	Quad Fine	Slower Cooling AOM	Z Bias Current	ODT Cross AOM	Raman 1 (C) Intensity	Z Gradient Shim
AO_3	Slower Biasing	Probe AOM	Fine Current		Raman 4 (D) Intensity	
DO_0		Slower Repump Shutter	XY Probe Fiber Switch	ODT Power AOM	Raman 2 (A) Switch	
DO_1		Slower Repump AOM	Y-Z Fine Bias Toggle	ODT Cross AOM	Raman 3 (B) Switch	
DO_2	Quad Softscope Trigger	Slower Cooling Shutter			Raman 1 (C) Switch	
DO_3	Quad Coil Disable	Slower Cooling AOM		Dipole Shutter	Raman 4 (D) Switch	
DO_4	Quad Fine Command Only	MOT Repump Shutter			Raman 2 (A) Shutter	
DO_5		MOT Repump AOM			Raman 3 (B) Shutter	
DO_6		MOT Cooling Shutter			Raman 1 (C) Shutter	
DO_7		MOT Cooling AOM			Raman 4 (D) Shutter	
DO_8		XZ Probe Shutter				
DO_9		XY Probe Shutter				
DO_10		Probe AOM				
DO_11		Master Laser Shutter				
DO_12		UV LEDs				
DO_13		Atomic Oven Shutter		Flux Gate Power		
DO_14		Flipper Mirror Toggle		RF Coil, Chan. 2		
DO_15		XY Camera Trigger		RF Coil, Chan. 1		

Figure 4.8: Mapping of the analog and digital signals from the computer control software to the laboratory equipment.

± 10 V to the various instruments in the lab with approximately 2.5 μs updates. Lastly, these devices also allow for data acquisition on analog to digital lines which we have used to record analog waveforms within the experiment. The NI devices are also electrically isolated from the control computers via fiber optic USB extenders and hubs. The goal of this setup was to effectively isolate the ground on each device and prevent electrical ground loops (which act as antennas and pick up noise on a wire) from being formed on our signal lines.

Pulse Blaster Channel		Pulse Blaster Channel	
PB_0	Oscilloscope Trigger	PB_16	NovaTech Com2 Trigger
PB_1	Flux-Gate Sampling	PB_17	Dev 5 Trigger
PB_2	AI Lines Sample	PB_18	NovaTech Com4 Trigger
PB_3		PB_19	Dev 3 Trigger
PB_4		PB_20	NovaTech Com3 Trigger
PB_5		PB_21	Dev 3 Trigger
PB_6		PB_22	Dev 2 Trigger
PB_7		PB_23	Dev 1 Trigger
PB_8		PB_24	
PB_9		PB_25	
PB_10		PB_26	
PB_11		PB_27	
PB_12		PB_28	
PB_13		PB_29	
PB_14		PB_30	
PB_15	Dev 6 Trigger	PB_31	

Novatech	COM 2	COM 3	COM 4
Channel 0	Raman 2 (A)	RF Coil	Repump Laser Beatnote
Channel 1	Raman 3 (B)	RF Channel 2	Cooling Laser Beatnote
Channel 2	Raman 1 (C)		
Channel 3	Raman 4 (D)		

Pico Devices	Channel	Mirror
9742-11975 (R1XY-R3XY)	1	Raman 1 X
	2	Raman 1 Y
	3	Raman 3 X
	4	Raman 3 Y
9742-11974 (R2XY-CrossXY)	1	Raman 2 X
	2	Raman 2 Y
	3	ODT Cross X
	4	ODT Cross Y

Figure 4.9: Mapping of other devices in the lab from the computer control software.

The NI devices we use cannot drive large electrical loads on the analog outputs, such as 50 ohm terminated inputs found in many instruments using BNC cabling. In many cases, these signals are fed through a buffering circuit based around the Texas Instruments BUF-634P amplifier IC. This IC has a high response bandwidth (≈30 MHz) and is able to drive large amounts of current with wide voltage rails, much more than the NI devices themselves can provide.

Our experiment also deploys a set of three Novatech 409B direct-digital synthesizer (DDS) modules to generate frequency precise RF waveforms. These devices provide stable

frequency sources used in our RF coil when addressing atomic samples and for AOMs used in the lab. The frequency accuracy and stability of these devices, order Hz out of MHz as measured against a Rubidium atomic clock, allows for a high degree of control when targeting atomic resonances within our system.

In order to properly time all these state/signal updates, at the core of the experiment lies a Spin Core PulseBlaster USB TTL pulse generator, a programmable digital pulse generator. This device is programmed to send out update pulses to all other sequenced devices to synchronize all cycle steps between devices. The computer staging software downloads a series of pulses on this device that correspond to when various devices in the lab need to update an output signal. To do so, the PulseBlaster device sends a TTL trigger signal to NI-6229 AO/AI devices or Novatech 409B devices signaling to output the next value in the sequence on each channel. In the end, these devices translate the bulk of information between the experimental staging on the computer and the instruments required to do the experiment. Any other information is either hand coded, in the case of programmable stepper mirrors, or through grad student coding (i.e. turning a knob).

To prevent ground loops across the lab, we electrically isolate the computer systems from the devices in the lab. We use a set of USB to optical fiber adapters to break ground between the computers and the rack mounted equipment. At the equipment side, the optical fiber terminates into a USB hub unit, allowing us to connect instrumentation to the USB bus remotely. Recently we have also begun deploying devices, such as cameras, over Gigabit Ethernet connections, as the connection are transformer isolated.

4.2.2 Acquisition System

The data acquisition computer is used within the experiment to collect images from the CCD cameras within the experiment and to record any analog signals captured during a run of the experiment (the CCD camera systems we use are further described in Section 4.5). The cameras are connected to the imaging computer via an optically isolated FireWire connection or via a Gigabit Ethernet connection. This computer similarly uses LabView code to communicate with the control computer and the CCD cameras so that it captures and downloads the images at the correct time wthin the experimental cycle. The

acquisition computer, after capturing the images, saves the images in a RAW format to the hard disk for later analysis, and/or passes the RAW info to our custom image analysis written the Wavemetrics Igor data analysis program. The custom program provides, in real time after each shot, the calculation of the optical depth from each image, and along with the calibration of OD and magnification, uses the calculations from Chapter 2 and 3 to determine the various parameters of the atomic cloud in real time, such as: the atom number, temperature, optical depth, and relative position.

4.3 Laser Systems

We have a few main laser systems in the RbLi experiment. For laser cooling, we have separate cooling and repump lasers that are ≈ 6.8 GHz apart in frequency. To frequency stabilize these lasers, we have a separate master laser and saturated absorption spectroscopy setup that provides a reference to the other Rubidium laser cooling lasers. For creating an optical dipole trap for the condensate, we have a high power (30W) 1064 nm fiber laser. We also have a laser system to create optical Raman coupling in our experiment, as well as a lithium laser cooling setup.

All of the laser systems in the RbLi experiment (with the exception of the high power optical dipole trap laser) are on separate optical tables from the main experiment. All light is ported over in polarization maintaining fibers to the experimental optics. This design allows for independence between the alignment of the laser boards and the alignment of the experiment side optics. Each laser is also kept on its own optical breadboard, allowing the laser unit to be transported easily if needed.

4.3.1 Rubidium Laser Cooling Scheme

For laser cooling and trapping Rubidium, we used three separate laser systems: one to address the $F = 2$ to $F' = 3$ cooling transitions; one to repump atoms from the $F = 1$ ground state; and one that provides a reference frequency lock to a saturated absorption spectroscopy cell. We conveniently name these laser systems the cooling, repump, and

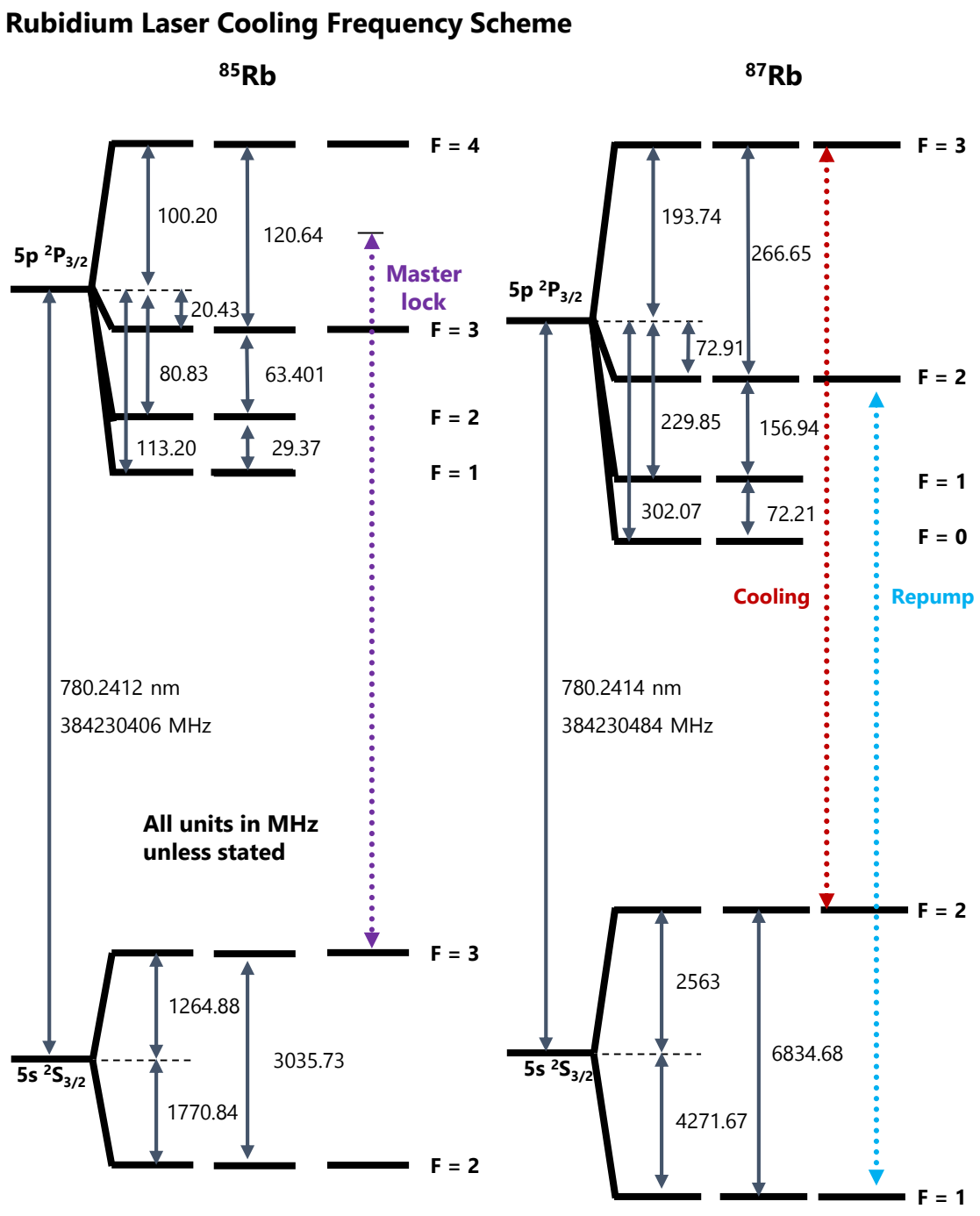

Figure 4.10: The hyperfine structure of Rubidium. Colored lines indicated the set frequencies of the cooling lasers.

master lasers respectively.

In the RbLi experiment, both the cooling and repump lasers for Rubidium are beat-note locked to the master laser which itself is frequency stabilized, via saturation

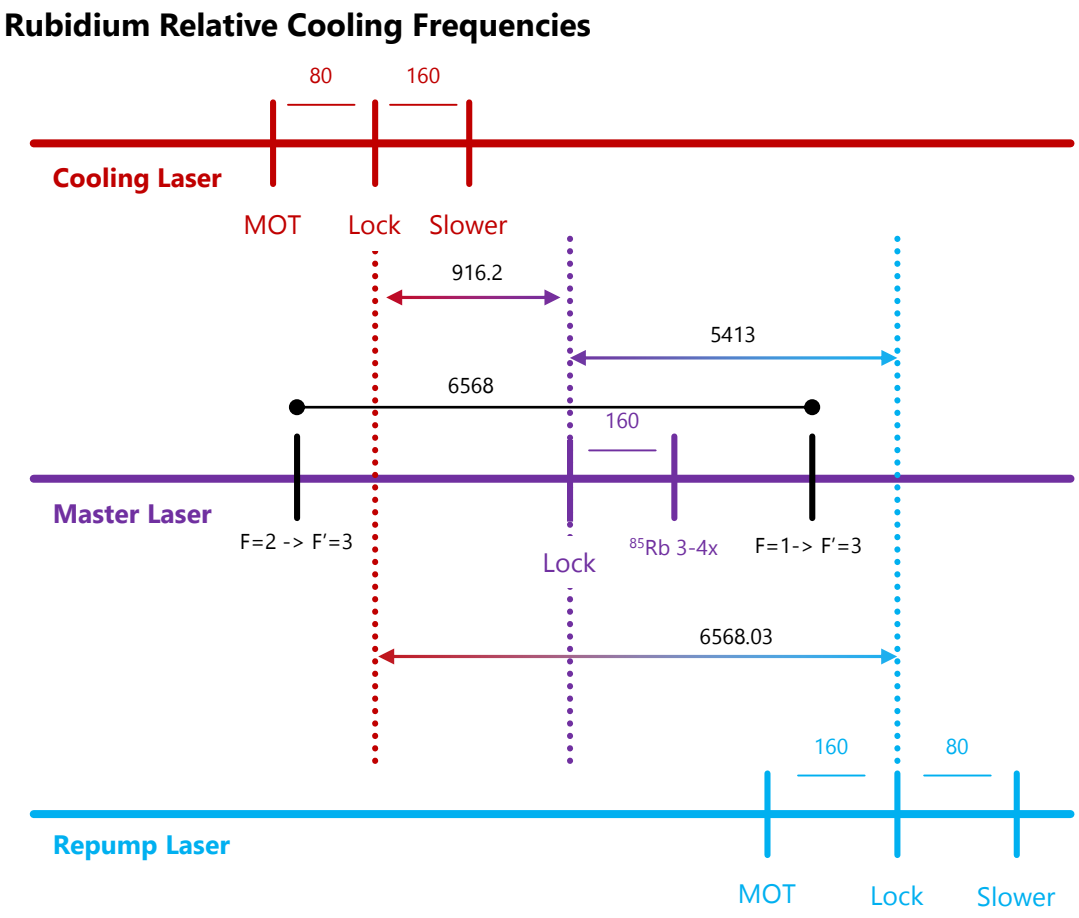

Figure 4.11: Relative locking frequencies between the Rubidium cooling lasers. All units in MHz.

absorption spectroscopy, to the $F = 3$ to $F' = 3$ and $F = 3$ to $F' = 4$ cross over transition in the $P_{3/2}$ state of ^{85}Rb. Light from the master laser, cooling laser and repump laser is injected into optical fibers and combined in a Font Canada 4x4 fiber combiner and multiplexer. One port of the fiber multiplexer is tapped off to a EOT GaAs ET-4000AF high speed amplified photodiode. The photodiode has a frequency bandwidth up to 9 GHz, thus is able to resolve a range of frequencies spanning between the ^{87}Rb $F = 1$ to $F = 2$ 6.8 GHz hyperfine splitting. All three frequencies combined onto the single photodiode creates multiple beat frequencies at the differences between the three lasers.

To use this to beat-note lock the lasers, we high pass filter the photodiode signal to get a beat note between the master laser and repump. Similarly we low pass filter the photodiode signal to get the beat note between the master and cooling laser. To generate

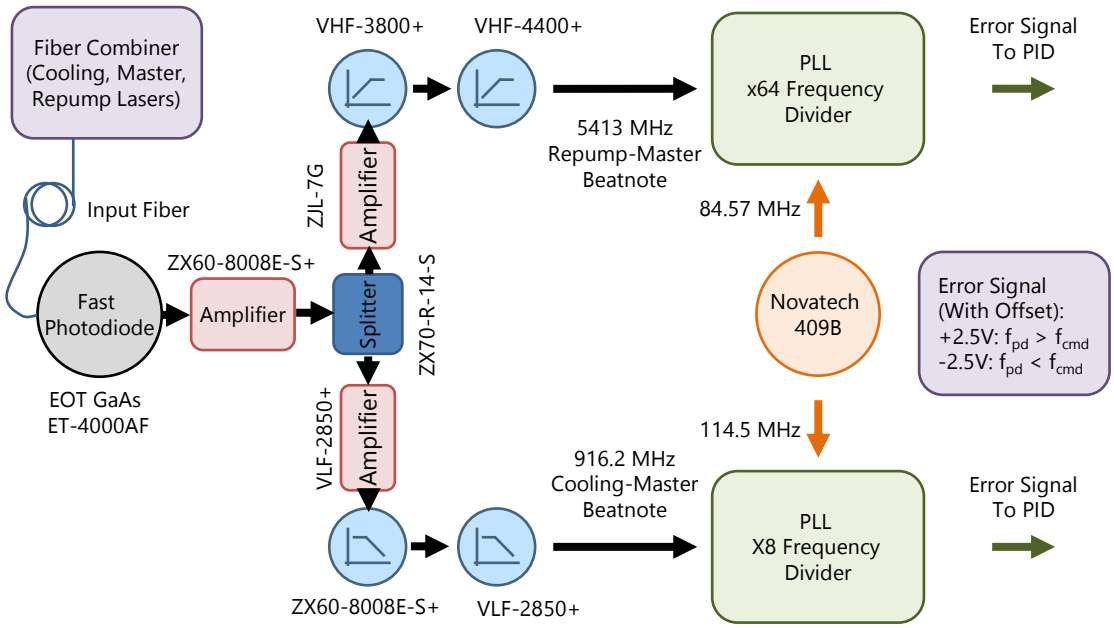

Figure 4.12: Schematic of the Rubidium laser beat-note locking electronics

an error signal for both the repump and cooling lasers, we use a PLL device to first frequency divide the beat-note signal from microwave frequencies to RF frequencies, then we use a frequency comparator that compares the frequency between the particular beat note signal and a DDS generated target frequency. The frequency comparator outputs a positive 5 Volt signal when the laser frequency is too high, and 0 Volts when the frequency is too low. This signal, while not perfectly continuous, is used as an error signal fed into a PID controller.

Both the cooling laser and repump laser use the PLL generated error signal to frequency lock via a Precision Photonics LB1005 PI controller (Figure 4.13). We use the error offset feature on the PI controllers to set the error signal to +2.5 Volt signal when the laser frequency is too high, and -2.5 Volts when the frequency is too low. The controller outputs a correction signal to feed back to the frequency of the laser. We take it and both high pass and low pass the signal into two signals. The low frequency signal is connected to the laser cavity piezo, which has a response time on the order of kHz. The high frequency signal is used to modulate the laser diode current. This modulation is connected to the DC current port on the DL Pro laser unit. For optimal performance, it is important to

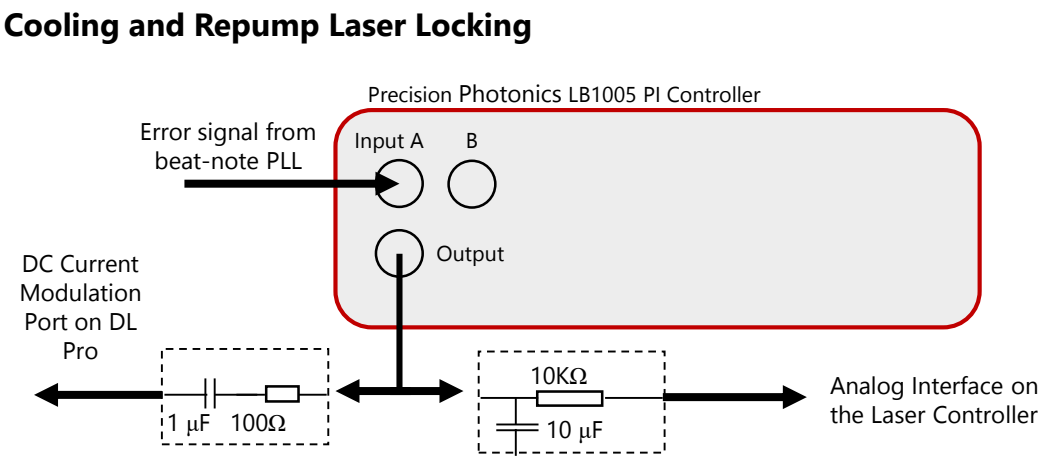

Figure 4.13: Frequency locking electronics configuration for the Cooling and Repump lasers

tune the PI controller gain and frequency cutoff, as well as the current feed forward gain on the piezo command (see Toptica Dl Pro manual) to extend the mode-hop free range of the laser.

4.3.2 Rubidium Master Laser

The Rubidium master laser system for the RbLi experiment was built to provide a stable frequency reference for the other laser cooling systems. The system consists of a New Focus Vortex II TLB-6900 extended cavity diode laser used for frequency locking via a saturated spectroscopy setup. The light from the master laser is passed through a pick-off plate to generate the pump and probe beams. The pump beam is then passed through a $\lambda/2$ waveplate and a polarizing beam cube, with the waveplate to control the ratio of light that is reflected or passed through the cube. The light that is passed through the cube is fiber coupled into the beat note locking system. Light that is reflected through the cube is passed through an AOM at 82 MHz and $\lambda/4$ waveplate, then is retro-reflected. The modified pump beam is then passed counter-propagating with the probe beam through a Rubidium vapor cell that has been magnetically shielded. The two beams have a frequency difference of twice that of the AOM drive, which addresses atoms moving at a specific velocity, via the Doppler shift. The probe beam is then passed onto a photodiode, which measures the absorption of the light by the Rubidium atoms, giving

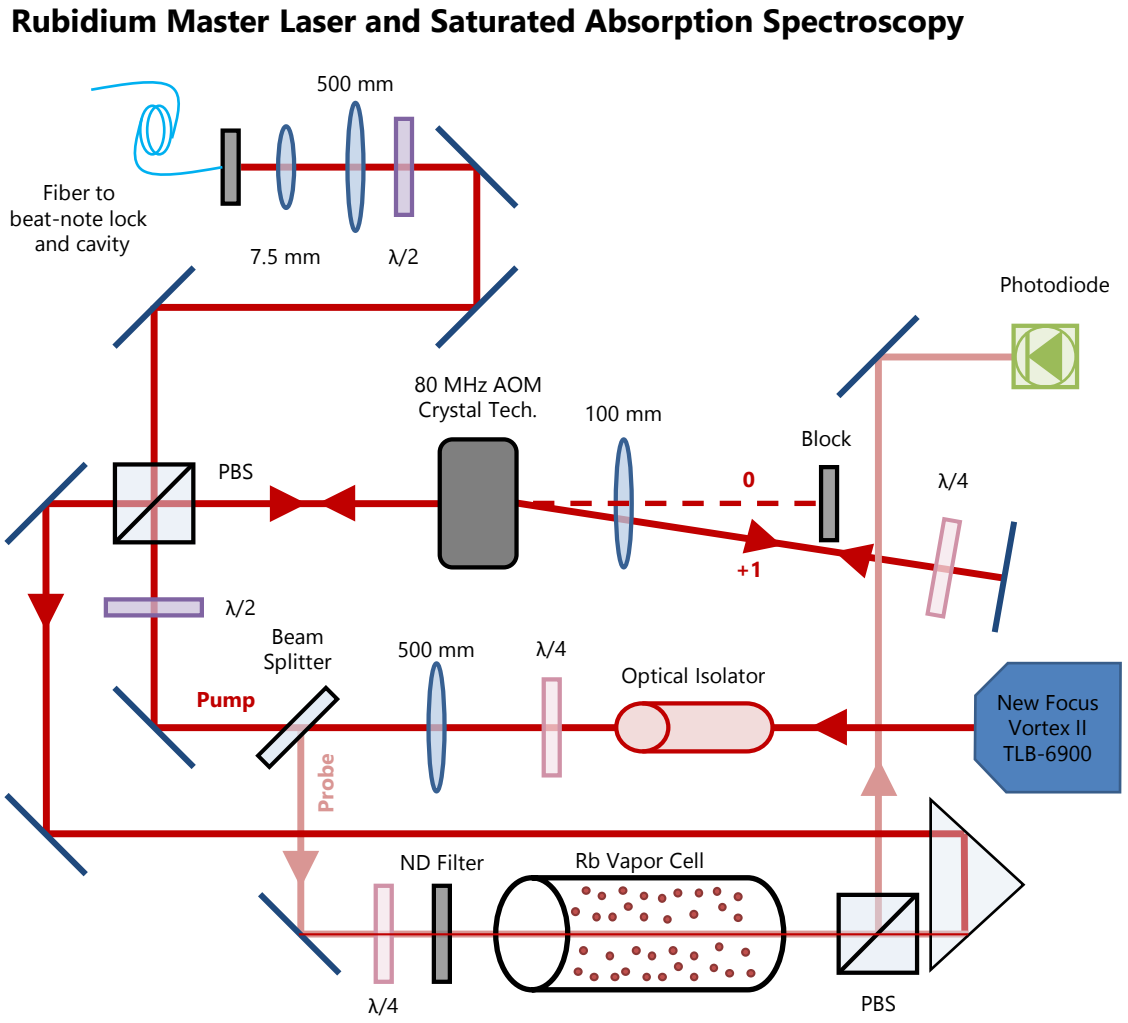

Figure 4.14: Layout of the Rubidium master laser optics for saturated absorption spectroscopy.

our frequency reference.

To lock the frequency of the master laser, we use an FPGA based lock-in amplifier and PID controller combination (For hardware description of the FPGA LockBox, see Appendix **??**). The FPGA system generates a $\approx$ 100 kHz, $2V_{pk-pk}$ sine wave that is coupled into the frequency modulation port of the AOM driver. The small oscillations in frequency cause an amplitude modulation, at the same $\approx$ 100 kHz frequency, in the absorption / probe signal.

The absorption signal from the home-built amplified photodiode is sent into the FPGA based lock-in amplifier. The lock-in amplifier digitally multiplies the reference

signal versus the photodiode signal to extract the amplitude and phase of the signal at the modulation frequency. The amplitude of the signal is a measure of the slope / derivative of the absorption spectrum at a given center frequency (Figure 4.15). The phase of the signal extracted by the lock-in amplifier reports if the absorption modulation signal is in phase (indicating a positive derivative) or out of phase (a negative derivative). By modulating the signal while scanning the center frequency across an atomic absorption feature, the lock-in amplifier will generate a derivative signal with a zero crossing at the zero-velocity atomic absorption frequency. This zero crossing provides the error signal measurement for the PID controller. By engaging the PID controller, the system will stabilize around the absorption feature center. By knowing which absorption feature we have locked the laser to (in our case we lock to the $F = 3$ to $F' = 3$ and $F = 3$ to $F' = 4$ cross over transition in the $P_{3/2}$ state of ^{85}Rb), we produce an absolute frequency measurement and source to which we can lock other lasers to via a beat-note scheme.

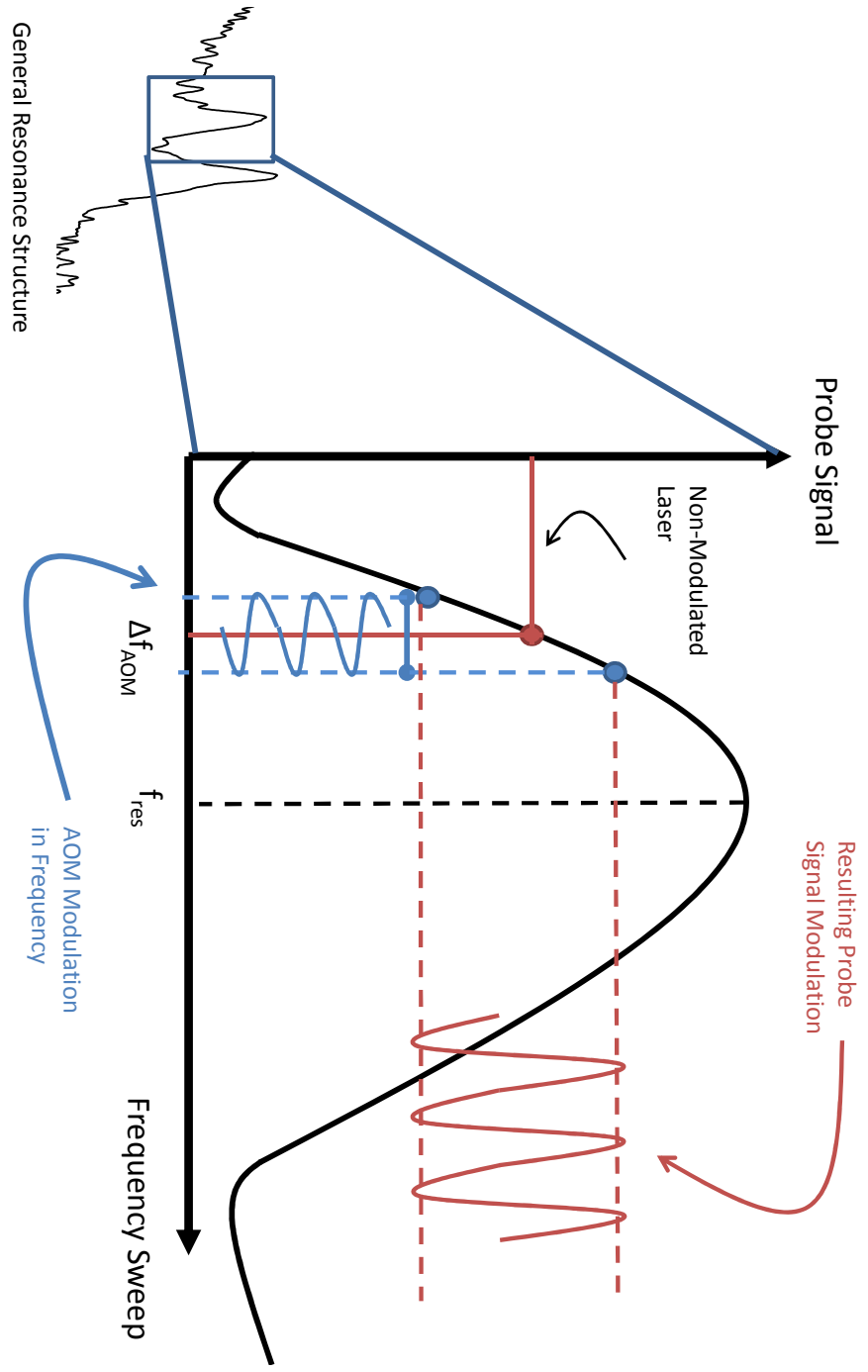

Figure 4.15: Frequency modulation of the absorption signal and the resulting modulation on the probe signal at the photodiode. The phase and amplitude of the probe oscillation with respect to the original frequency modulation at the AOM gives the derivative of the absorption signal.

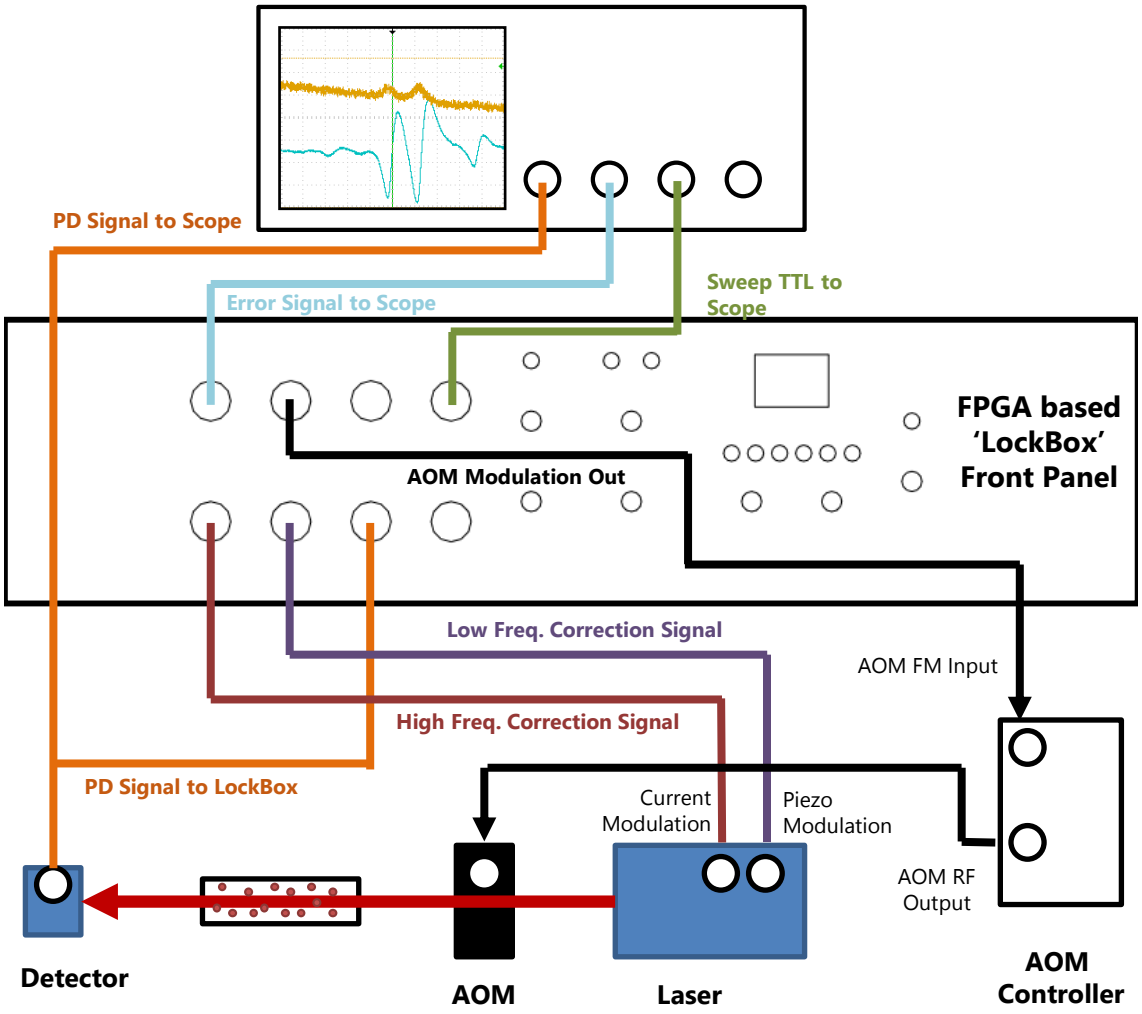

Figure 4.16: Schematic of the FPGA based frequency locking electronics for the Rubidium master laser. The FPGA device generates the AOM frequency modulation signal, calculates the derivative of the absorption features from the photodiode signal, and sends a correction signal to the laser.

4.3.3 Rubidium Cooling Laser

The Rubidium Cooling Laser system is primarily designed to provide laser light for the $F = 2$ to $F' = 3$ cooling transitions in both the MOT and slower stages. This system also provides the resonant light used in the absorption imaging of our atoms. The system is based on light from a Toptica DL Pro extended cavity laser system, with a laser diode chosen to operate near 780 nm. The light from the laser is, right after exiting the laser unit, split into two beams. The first beam goes to both the fiber coupler used for the beat-note lock, and is also split into a pair of probe beams for the XY and XZ absorption imaging systems.

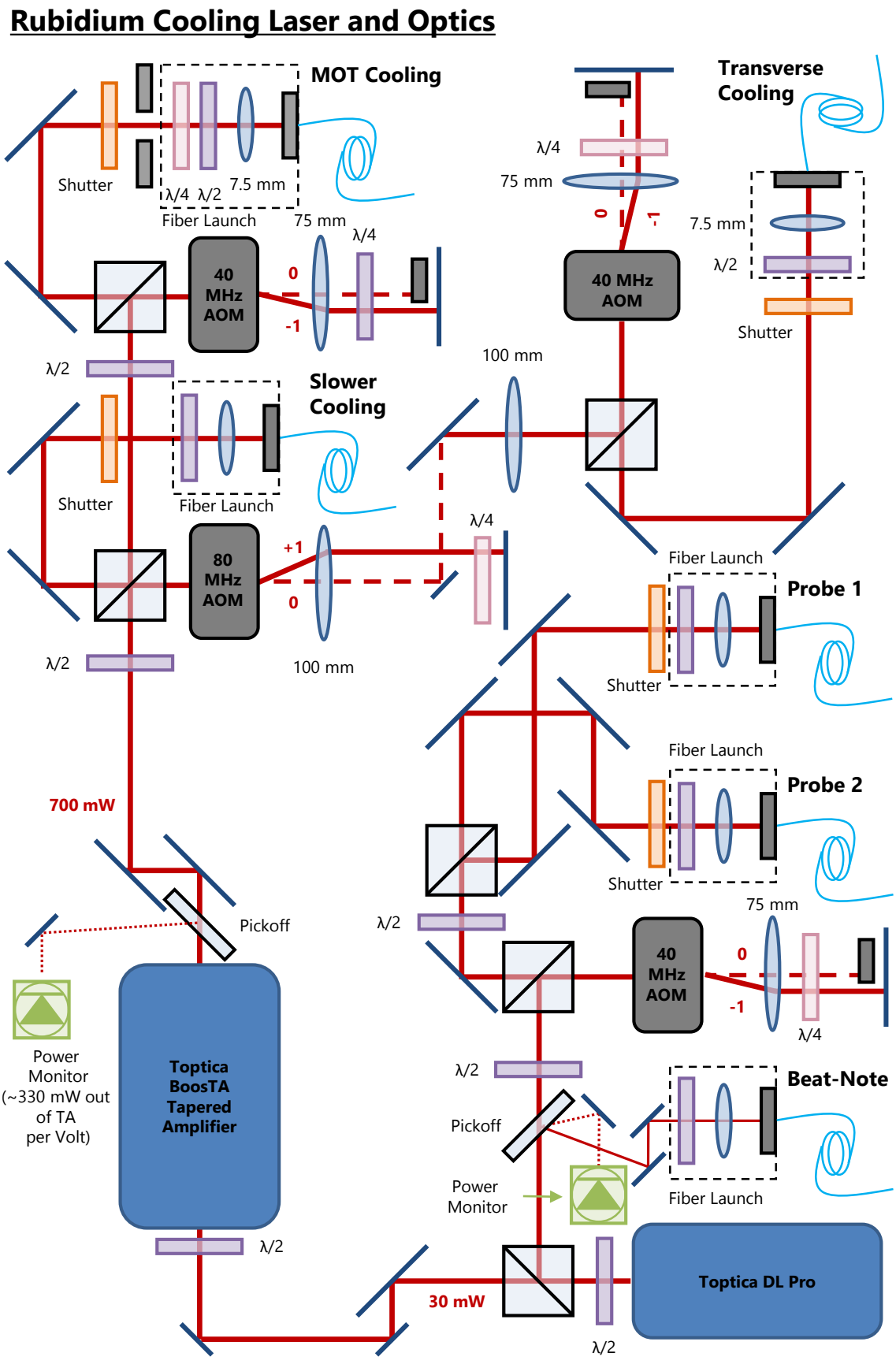

Figure 4.17: Rubidium Cooling laser optical setup

The rest of the light from the laser is sent into a Toptica BoosTA tapered amplifier giving approximately 650 mW of power, out of the specified 1 W. The light out of the tapered amplifier is broken off into subsections of double passed AOMs for the the MOT and slower cooling light. Both of these systems used the double passed AOM configuration to allow frequency and intensity control of the MOT and slower cooling light. Both beams are then injected into optical fibers, where they are combined with the repump light and multiplexed on the experiment side. The cooling board also has a transverse cooling unit that uses light from the zeroth order of the slower cooling AOM to provide transverse cooling on the experiment side. We rarely use this line for transverse cooling, but more often as a fiber coupled light source for diagnostics elsewhere. Figure 4.17 shows the cooling board setup in finer detail. Settings for the Cooling laser are in Figure 4.18

Rubidium Laser System Properties

Setting	Value
Cooling Laser Current	96 mA
Cooling Laser Temperature	21.9 °C
Cooling Laser Piezo	350 - Knob
BoosTA Current	1600 mA
BoosTA Output Power	~ 650 mW
Repump Laser Current	202 mA
Repump Laser Temperature	20.4 °C
Repump Laser Piezo	250 - Knob
Master Laser Current	84.6 mA
Master Laser Piezo	74 V

Figure 4.18: Parameters for the various Rubidium cooling lasers

4.3.4 Rubidium Repump Laser

The Rubidium Repump laser is designed to provide laser light to repump atoms back into the cooling transitions for the MOT and slower stages of the experiment. The system uses a Toptica DL Pro 100 extended cavity laser system, with a laser diode chosen to operate near 780 nm, similar to the cooling laser. This system does not have a tapered amplifier as the diode itself generates approximately 100 mW of laser light. We pass this light through a 3:1 telescope to improve our efficiency when aligning through AOMs and fiber injecting the light. This light is picked off via polarizing beam cubes and $\lambda/2$ waveplates into a MOT repump unit, a slower repump unit, and the remaining light is fiber coupled into the beat note lock system. The Slower repump light is put through a double passed AOM at 40 MHz, and we counter-propagate the +1 order. Similarly the MOT repump unit uses a double-passed 80 MHz AOM where we counter-propagate the -1 order of the AOM. Settings for the Repump laser are in Figure 4.18

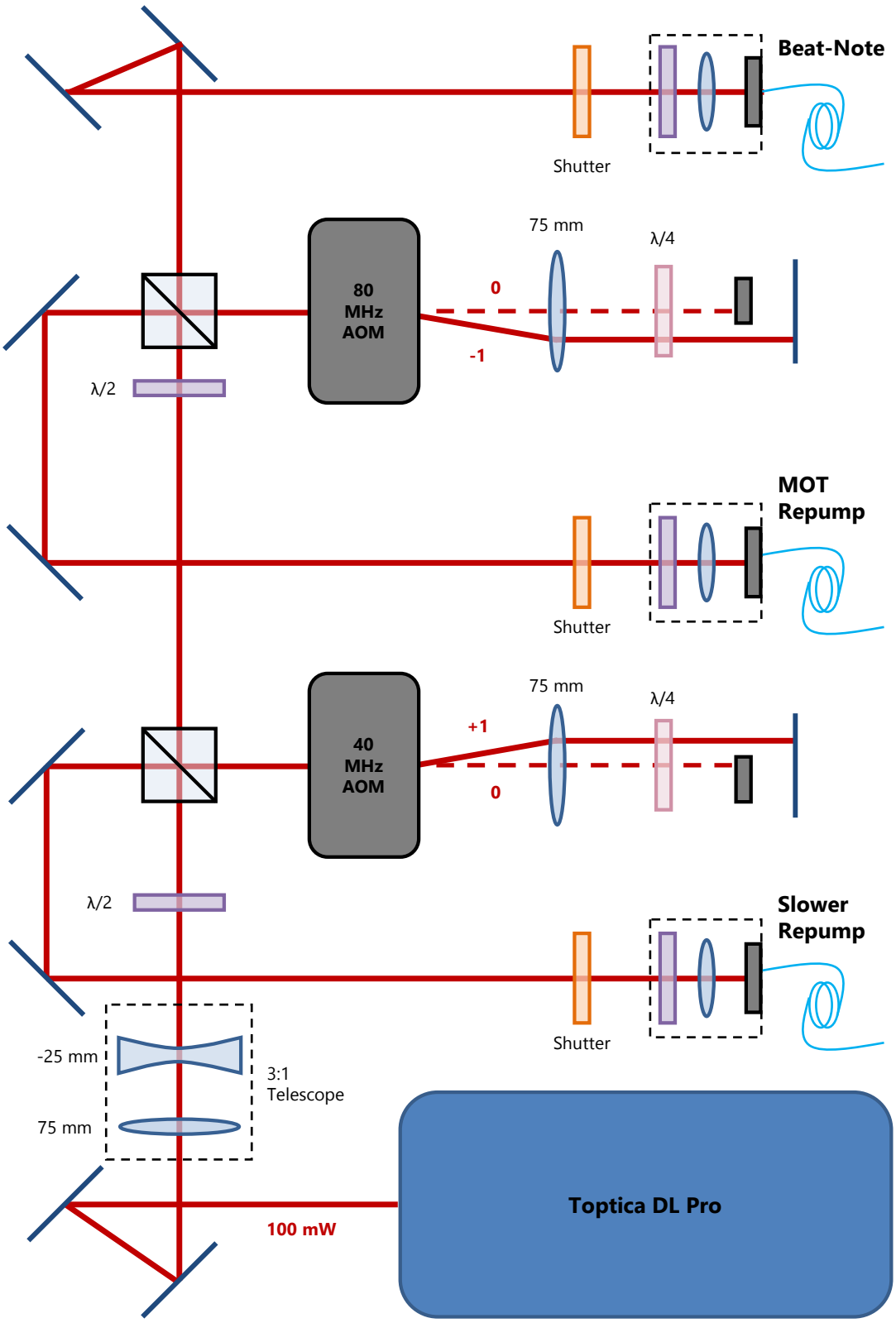

Figure 4.19: Rubidium Repump laser optical setup

4.3.5 Lithium Saturated Absorption Spectroscopy

Before Rubidium and Lithium mixtures were abandoned, I had spent a fair amount of time designing and assembling the Lithium saturated absorption spectroscopy oven and optics. Given the Lithium oven and optics sit cleanly on an optical breadboard, and the Lithium light used to lock is fiber coupled in, this board as a unit is complete and can be easily integrated into any future Lithium experiments by picking it up and moving it. That said, the following is a description of the Lithium oven, the optical setup and the absorption properties.

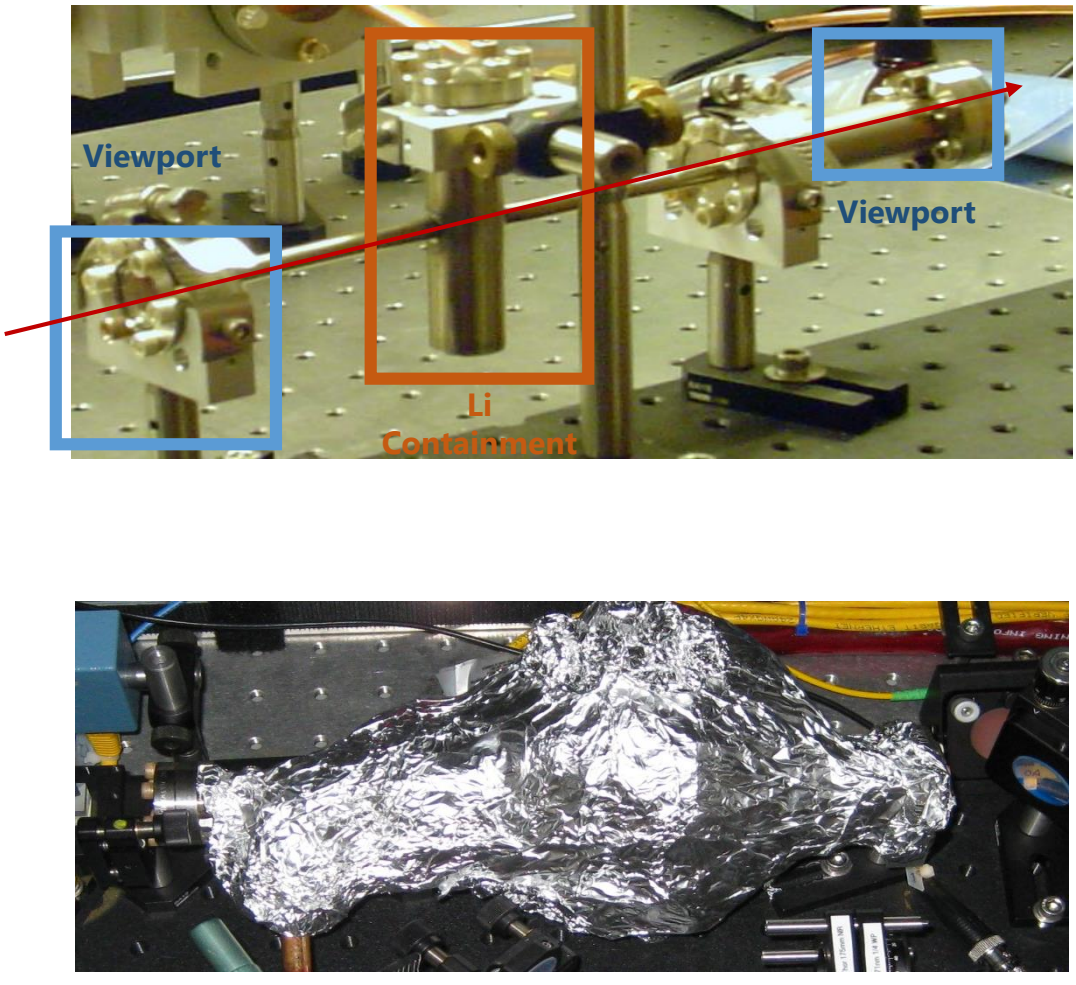

Figure 4.20: Top: Lithium saturated absorption spectroscopy cell during construction. Bottom: The Lithium cell in the optical setup, with heat insulation materials applied.

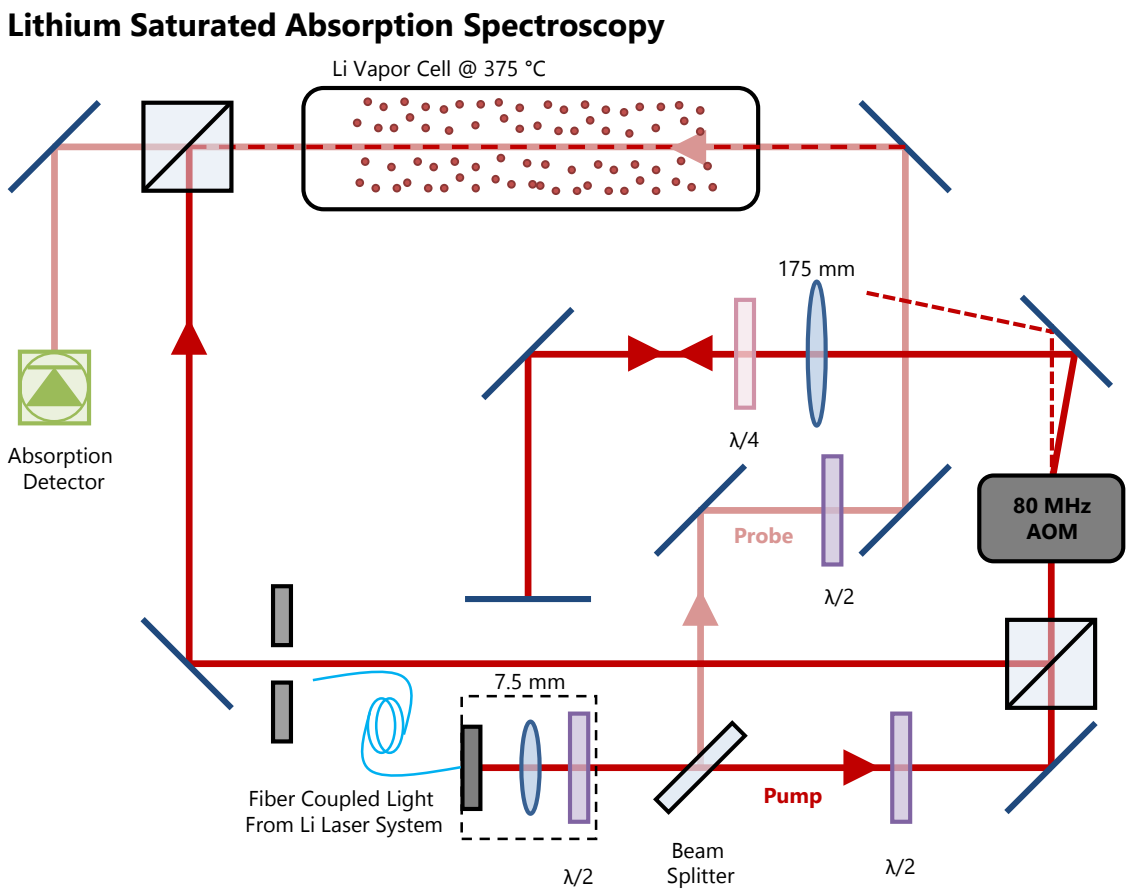

Figure 4.21: Lithium saturated absorption spectroscopy optical setup

Due to the poor vapor pressure of Lithium, it needs to be heated up to a range of $350 - 400\,^{\circ}\mathrm{C}$ to produce an optically thick vapor so that absorption can be measured. To create these conditions, I built a stainless steel cell to house the Lithium sample when heated[3]. The design of the cell is straightforward: There are two view ports that provide a laser path towards an internal steel bucket housing the Lithium (Figure 4.20). Because Lithium wants to oxidize, the cell is pumped down to vacuum, and the view ports are a large distance away from the Lithium housing to help prevent any 'caking on' of the Lithium. To further protect the view ports from being contaminated with Lithium, I back flowed the chamber with Argon gas to a pressure of approximately 10 mTorr. To heat the cell, I wrapped the entire unit with heating tape in two specific sections: one to heat the cell (and Lithium atoms) up, and another to heat the view ports, to prevent Lithium from

[3]The cell design credit goes to Subhadeep De and Ian Spielman

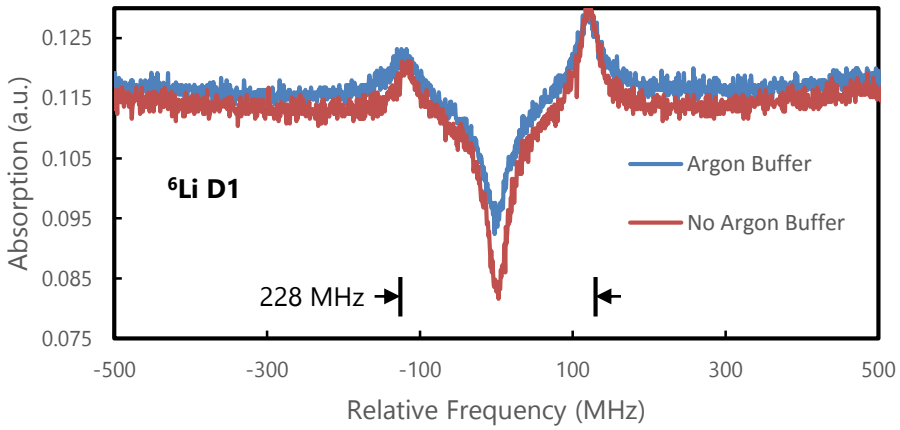

Figure 4.22: Measured absorption signal from the ^{6}Li D1 transition using the Lithium cell

sticking onto the windows. The entire unit was then wrapped, excessively, with aluminum foil to insulate the heat within the cell and to prevent large amounts of heat from reaching the nearby optics.

The saturated spectroscopy optical setup is very similar to that for Rubidium: in general a pump and probe beam are sent counter-propagating through the Lithium vapor and a photodiode captures the absorption signal (Figure 4.21). In this setup, the light from the (now defunct) Lithium laser system is fiber coupled onto the board. This light proceeds through a simple beam splitter to create the pump and probe beams. A $\lambda/2$ waveplate before the beam splitter helps to adjust the ratio of power between the two beams. The pump is double passed through an 80 MHz AOM, then retro-reflected against the probe beam in the Lithium vapor cell. The probe is aligned onto a photodiode to measure the absorption.

In this setup, I used isotropically enriched ^{6}Li in the vapor cell, as this is also what is loaded into the main apparatus. With the saturated absorption optics in place, we measured the absorption signal from the atoms at the ^{6}Li D1 line and were able to measure the 228 MHz hyperfine splitting in the ground state of Lithium. This setup was also used to determine the amount of Argon buffer gas to place in the cell. I allowed the Argon to flow until I begun to measure pressure broadening of the hyperfine states (Figure 4.22). I found that the best temperature for the cell was at about 380 °C as it gave the

best contrast in the absorption features before saturating.

4.3.6 Optical Dipole Trap Laser

Our optical dipole trapping laser system uses a 30 W IPG Photonics 1064 nm fiber laser. While the unit can provide 30 W we only set the laser to 11 W normally, with the extra trapping power initially planned for including Lithium into the design. The light from the laser head is highly Gaussian, making optical systems more manageable. The light from the laser is passed through a 4:1 telescope, decreasing the beam waist to 0.5 millimeters. The light then passes through a 80 MHz AOM used to control the intensity of the beam. The zeroth order of the beam is deflected into a beam dump. The first order out of the AOM is propagated further to a pickoff, where a small sample of light is targeted onto an InGaAs photodiode unit. We previously used a common Si photodiode for this purpose, but we begun having large intensity stabilization issues owing to the Si photodiode having

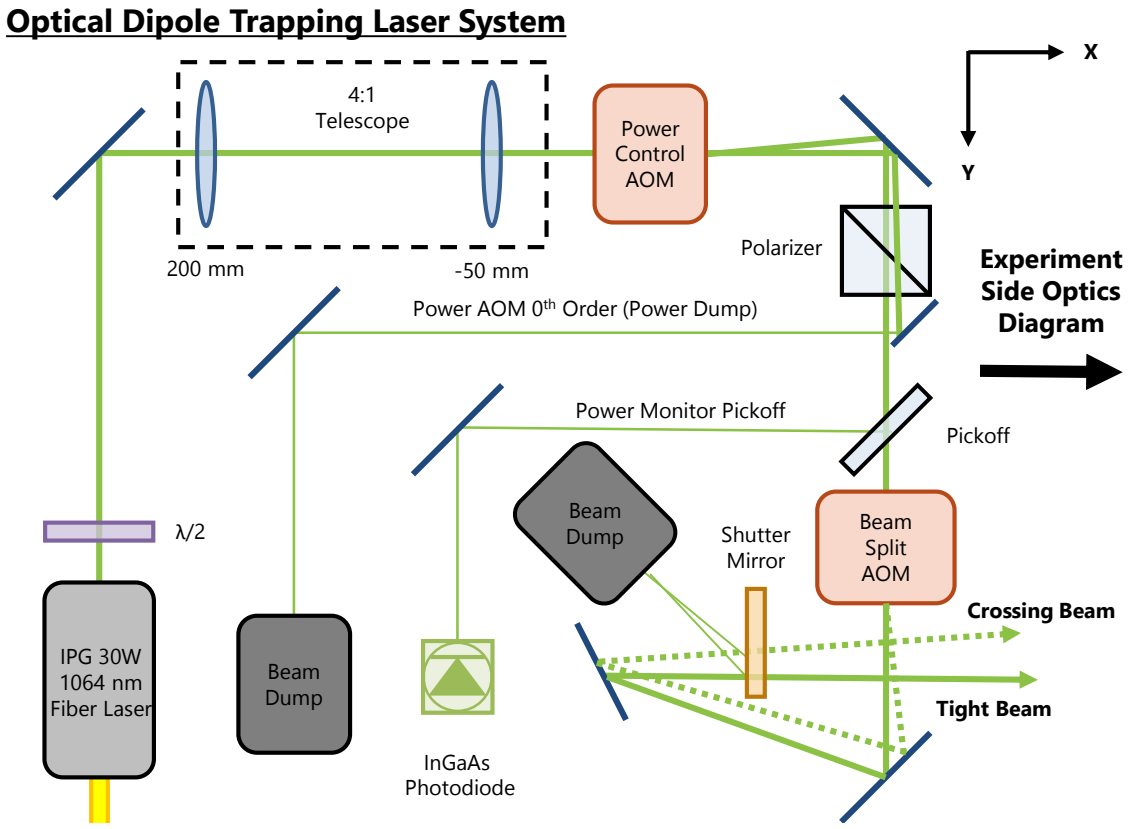

Figure 4.23: Optical dipole trap fiber laser optical setup.

both poor response at 1064 nm and temperature drifts as well. With a more stable detection system, we use this signal with a PID controller to feed back to the amplitude of the power AOM RF signal, hence controlling the laser intensity. This intensity controlled beam is passed through a second AOM, which generates two separate beams for our crossed optical dipole trap: a tight primary beam (1st order), and the crossing beam (0th order). These beams are reflected towards the experimental optics setup in Figure 4.5. A shutter that has a mirror attached to it is placed in line with both beams. When the shutter is powered down (its default state), the two trapping beams are deflected into a beam dump. This setup was originally fiber coupled to the experiment like all other laser systems, however after burning out multiple fibers on accident, we decided to put this laser on the experimental optics table. Post-fibers exploding, we have purchased new fibers with high power connectors and internal design. We have not implemented this because: 1) If it ain't broke don't fix it 2) The lab will move soon anyway, let us do it then.

4.3.7 Raman Coupling Laser System

The Raman laser system is used within our research to generate synthetic gauge fields and spin-orbit coupling in our condensates. This laser system provides the means to do the experiments in both Chapters **??** and 8. The diagram in Figure **??** shows the setup for our Raman laser system. The alignment of these beams into the atoms at the experimental apparatus is depicted in Figure 4.5.

To get large amounts of power, this system uses a pair of tapered amplifiers, with a 1 W capability each. Originally the seed beam from the DL Pro was passed through a 50/50 beam splitter into both amplifiers. However, the mode out of the DL Pro was not coupling well with the TA chips. The solution was to inject light into the TAs in serial, one TA seeding a second. In between the two TAs we placed an optical fiber connection. On the output port of the fiber, the mode is very Gaussian, allowing for great coupling to the second TA.

Because we use one tapered amplifier to seed another, there is the obvious failure mode of too much power being passed from the first to the second, causing a broken second

amplifier. To prevent this, we have placed a power monitor at the output of the fiber from the first TA to the second. This value is monitored by an interlock system implemented on a microcontroller. If it detects too little power (the TA chips need minimum power), or too much power, it will send an interlock signal to both of the TA power supplies.

When initially using this system, we found that the amplified spontaneous emission (ASE) light from the TAs was large enough in intensity that it heated up our BECs. To solve this we put a Semrock laser line filter after the amplifiers, and adjust their incident angle with the laser beam until we maximize power.

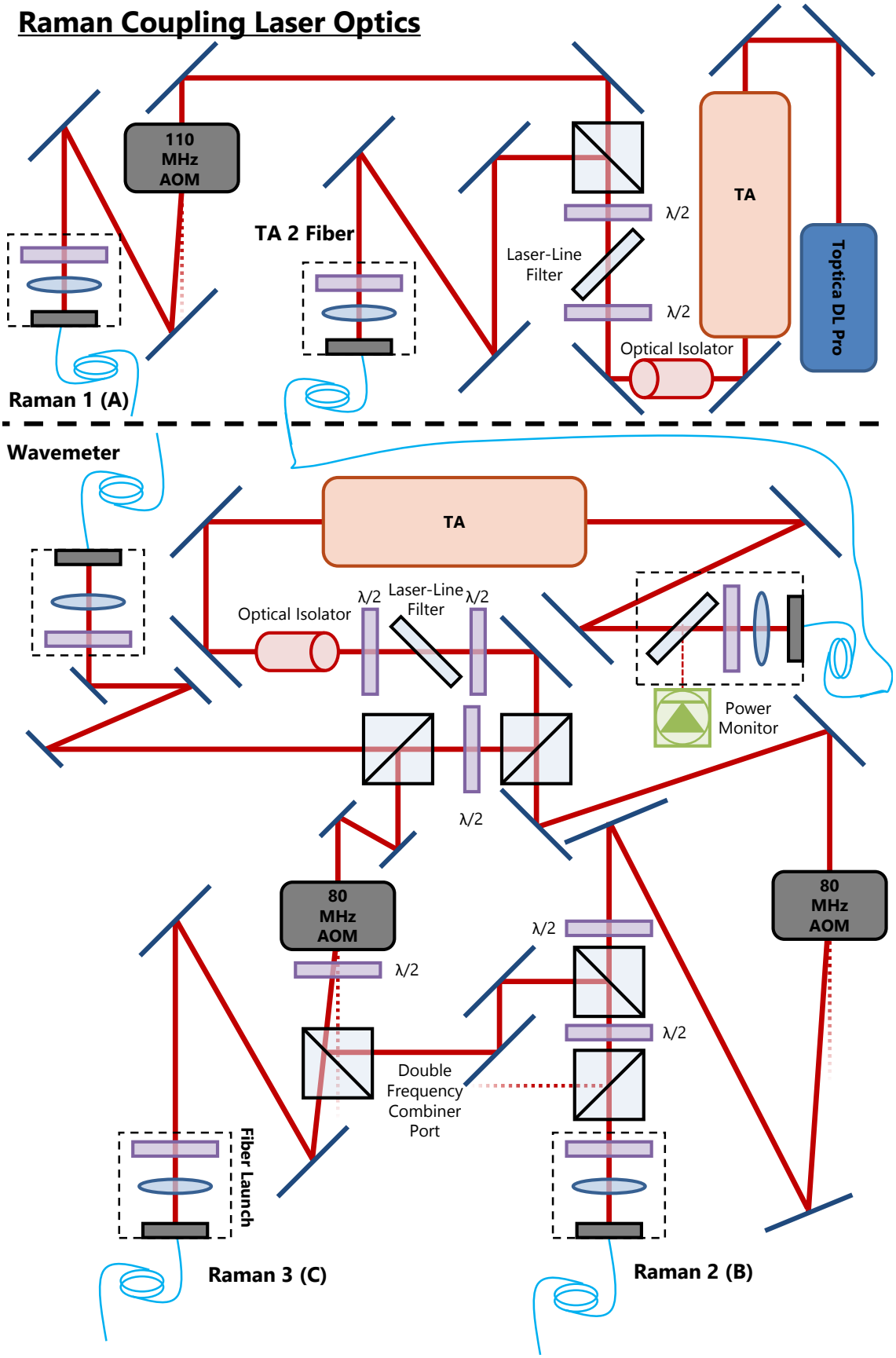

Figure 4.24: Raman laser system optical setup.

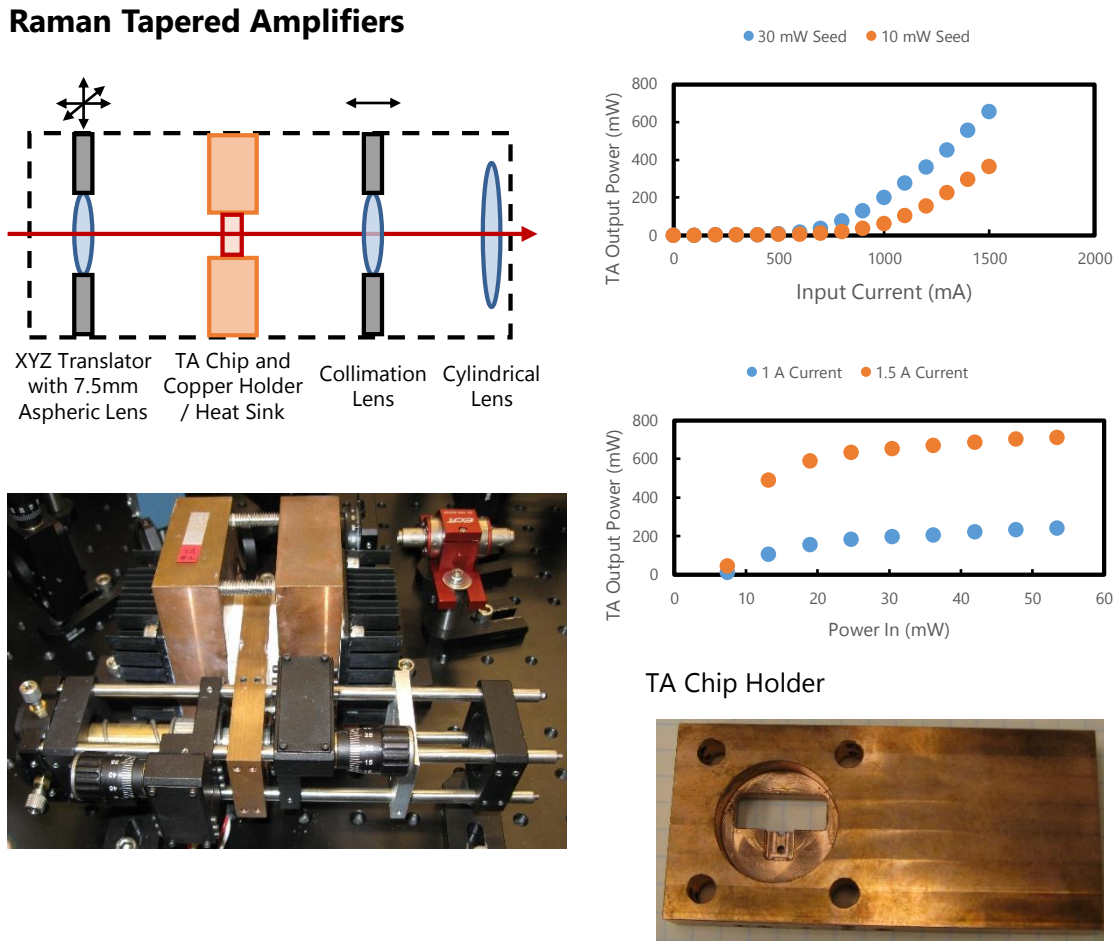

Figure 4.25: Custom tapered amplifiers constructed for the Raman laser system. A TA chip is mounted into a custom machined piece of copper which is thermally regulated.

The tapered amplifiers are designed and constructed in house. The design uses a small TA chip (which we have gotten from both vendors Eagle Yard and M2) that is mounted into a custom milled copper plate to house it. The copper plate is thermo-electrically cooled to regulate the temperature of the TA chip. Light being injected into the TA passes through a short focal length lens mounted in a full XYZ translator so that the alignment can be fine adjusted. On the output of the TA there is a cylindrical lens to account for the asymmetric divergences of the elliptical beam. The entire system is mounted into a ThorLabs optics cage assembly in order to put the optics on axis with one another.

To generate the double frequency beam in our spin-1 spin orbit coupling experiment

(Chapter 7), the light on the Raman 3 beam line can be diverted, by a $\lambda/2$ and polarizing beam cube combination, to a path that combines with the Raman 2 beam line via polarization optics. In this scheme, the Raman 2 and 3 beams are combined on a beam cube with orthogonal polarizations. Another polarizing beam cube then acts as a polarizer, combining the two frequencies, but rejecting half the power. We originally generated the two Raman frequencies on a single AOM via combing two RF signals prior to the AOM, however there were unwanted higher harmonics and beat tones that introduced noise and heating into our Raman experiments and measurements. We forwent this method, and went with what we knew had no noise issues.

All of the AOMs on this board are controlled via RF electronics that we designed and built, versus the commercial drivers on the laser cooling systems. The schematic of the system for each AOM is effectively the same as our RF antenna for interacting with the atoms (Figure 4.37), except the AOMs only require a 2 W amplifier. In this method, we use a Novatech 409B to precisely set the frequencies of the Raman AOMs. This digital precision of the frequencies is what allowed us to perform the first-order transition measurements down to Hertz in width in our spin-1 experiment (Chapter 7).

Power Calibrations

To calibrate the power of the Raman coupling, we first find RF resonance in the system via an RF field and a biasing magnetic field. Next we pulse on the Raman beams (with frequency difference equal to that of the RF frequency) for a variable amount of time (typically order tens of microseconds) and measure the population fraction. By measuring the fraction in the $f = 1$ state as a function of time, it becomes straight forward to use the governing physics in Equation 6.9 to extract the coupling strength Ω_{R}.

By doing this measurement while recording the Raman beam intensity at the experiment side via photodiodes (Figure 4.5) we can calibrate the power in the beams to the photodiode signal and to the Raman coupling strength. Given a daily calibration of the photodiode measurement to the coupling strength measured from the pulsing data, we can use the photodiode signals to measure the shot-to-shot coupling strength in the Raman beams. This calibration and photodiode measurement is also used to implement

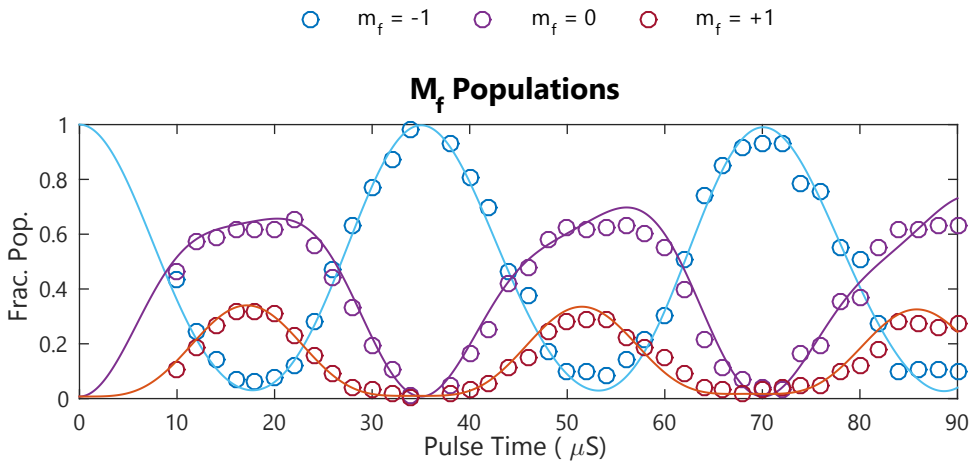

Figure 4.26: Measuring the oscillation of spin population after pulsing on the Raman coupling. The form of the oscillations can be fit to the Raman Hamiltonian (Section 6.1.3) to give a calibration of the coupling strength.

intensity control via FPGA based PI controllers (see Appendix B). While in most cases the photodiode signal is constant during calibration, for experiments where we have two frequencies on a single beam (Chapter 7) the beat tone of the two frequencies arrives at the photodiode. To measure the coupling strength, we measure the amplitude of the beat signal, and divide the amplitude by 2 (as the photodiode records intensity, not the electric field!).

4.3.8 Laser Wavemeters

To monitor the output of the Rubidium cooling lasers (the Cooling, Repump and Master lasers), we use both a wavelength meter to measure the absolute wavelength of each laser, as well as the mode profile of the beams. To do this, we inject light from each system into fiber, then combine and multiplex it out to a fiber coupled Bristol 521 wavemeter, and a Thorlabs SA200 Fabry-Perot interferometer (an optical cavity). The wavelength meter allows us to tune each of the laser wavelengths coarsely to the desired value used for locking. The wavemeter is traditionally used when the laser parameters have drifted such that the locking region of the respective laser is no longer evident. Because the wavemeter receives all three wavelengths of light over fiber, we have to block off[4] all lasers except the one of interest so as to get a reliable wavelength measurement.

Similarly, we use the optical cavity to monitor the mode of each laser. For laser

[4] i.e. card in front of the fiber launches

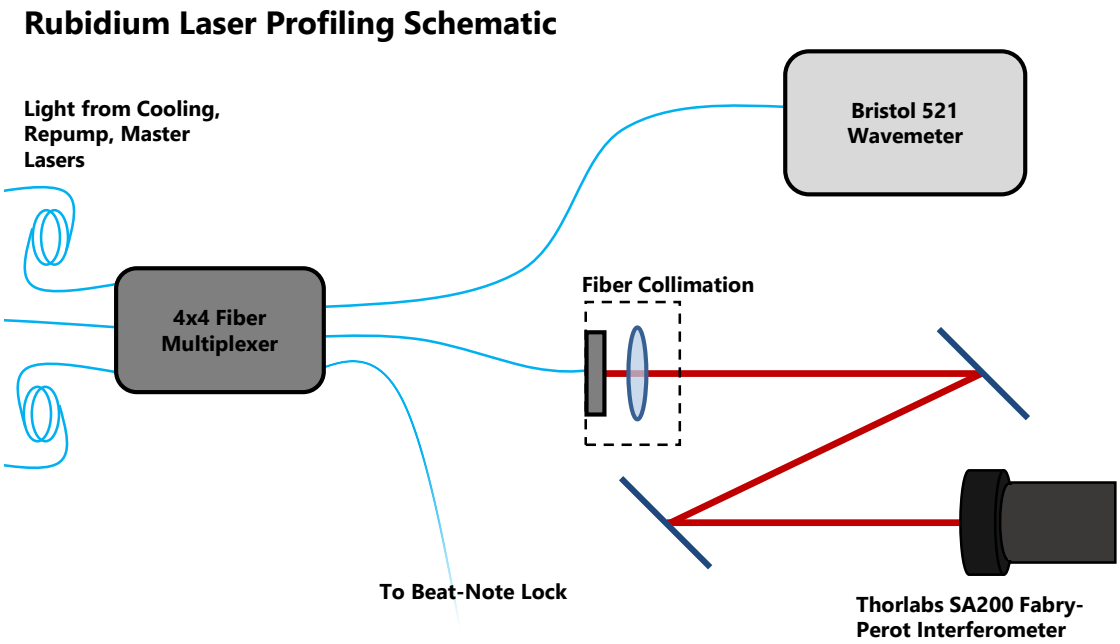

Figure 4.27: Light from the Cooling, Repump, and Master laser setups are fiber coupled into a fiber multiplexer, which provides light for wavelength measurement at the wavemeter, and observation of laser mode at the interferometer.

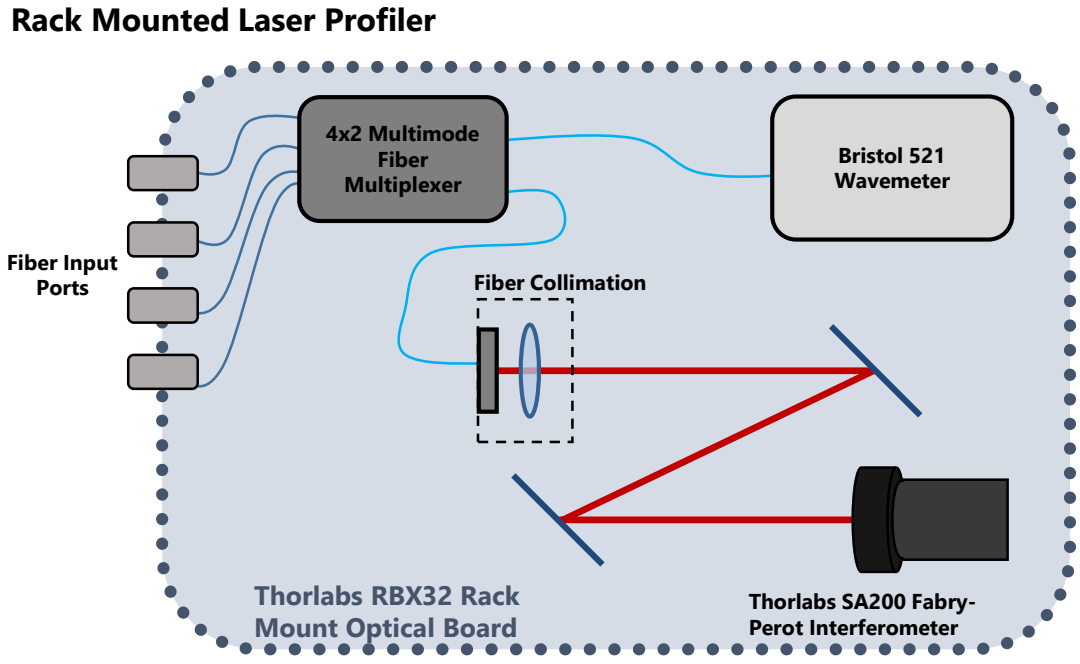

Figure 4.28: Schematic of the 19" rack mounted laser profiler.

cooling purposes, we require each laser to be operating in a single mode configuration, which appears on the optical cavity output signal as a single peak. By comparison, if

the laser is in a parameter regime that produces multi-mode behavior, the wavemeter will show a forest of peaks representing all of the lasing frequencies present. Similar to the wavemeter, to identify a single laser signal, the two other laser inputs must be blocked off. In most operating conditions, the observation of three peaks, corresponding to three single-mode lasers, represents correct system operation.

For the Raman and other laser systems, I built a wavemeter setup similar to that used for the cooling setup, however I designed it to be both rack mounted and independent of target wavelength[5]. To save space and make the system effectively act as a 'black box' that profiles the lasers, I built the optical cavity optics into a Thorlabs RBX32 rack mounted slide out optical breadboard. The front panels of the box has a set of four fiber inputs that are multiplexed in fiber into both the cavity and the wavemeter. This unit provided the space inside to place the multimode fiber multiplexer units, the free space optical cavity optics and the Bristol 521 wavemeter in a single package, freeing up space on the optical tables.

4.4 Magnetic Field Control

Magnetic fields generated from electromagnetic coils are an important tool within the RbLi experiment. Because ^{87}Rb has a non zero hyperfine spin ground state (specifically $F = 1$), magnetic fields break the degeneracy of the spin states of the atoms via the linear Zeeman effect. Therefore magnetic fields are instrumental in the control of the spin degree of freedom for laser cooling or quantum manipulation of a BEC.

4.4.1 Zeeman Slower

The Zeeman slower in our experiment connects the oven region of the apparatus to the experimental glass cell. The slower is a 0.71 meter long stainless steel tube that the atomic beam travels down with two coils wrapped around it: a taper coil and the biasing coil. Both coils are made from copper tubing, allowing internal water flow to help dissipate the

[5]The plan was to hook up any 1064 nm lasers or unknown future lasers as well

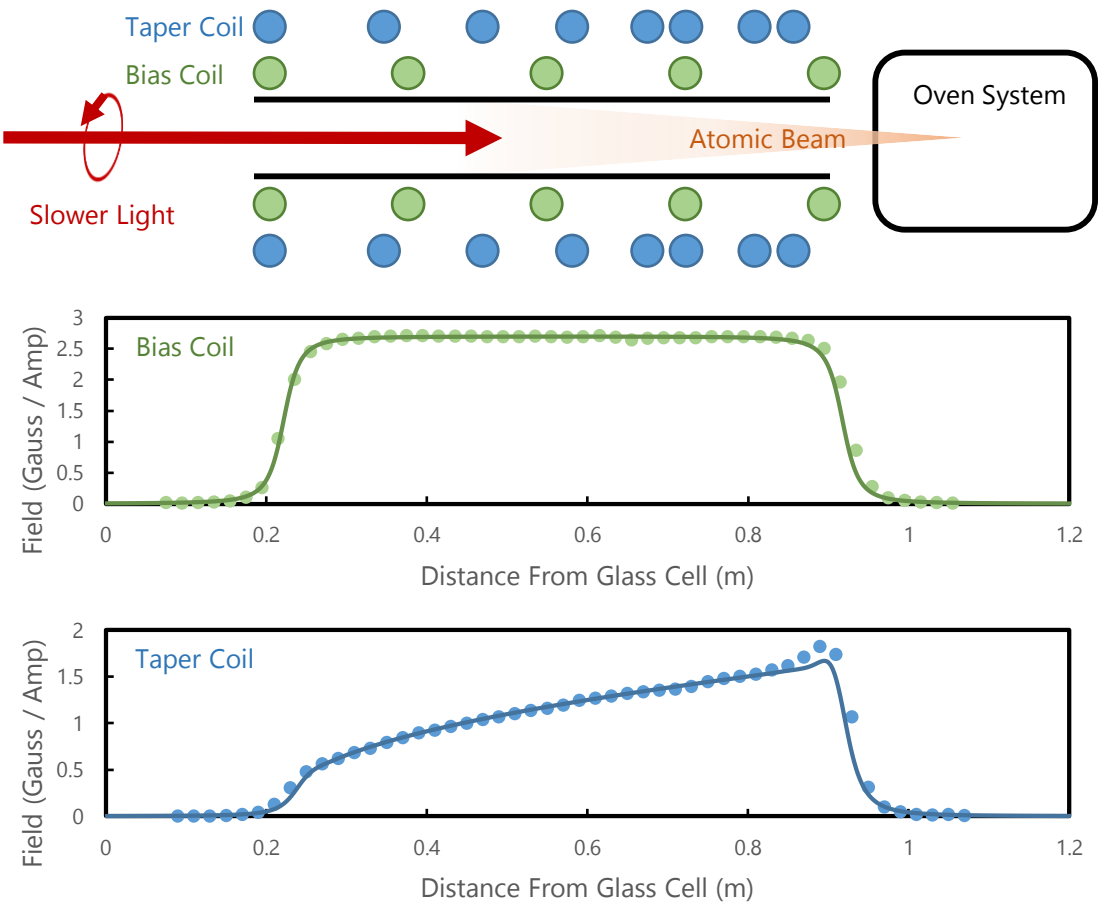

Figure 4.29: Top: Schematic of the Zeeman slower, including the uniformly spaced Bias coils and the Doppler compensating Taper coil. Bottom: Measured and calculated field profiles of the Bias and Taper coils along the slower axis.

large amount of heat generate from ohmic losses.

The taper coil is a solenoidal electromagnet with variable coil spacing, giving a non-uniform field profile that varies along the slower length. The spacing of the coils is designed to counteract the decreasing Doppler shift of the slowed atoms, thereby keeping the slower laser beam on resonance for maximum slowing efficiency. In our loading procedures, this coil runs at approximately 135 A yielding a maximum field of 240 G at the oven side of the slower.

The bias coil is similarly a solenoidal electromagnet with uniform windings, giving a uniform field profile down the entire slower. The uniform field is used to shift the resonance of the atoms across the entirety of the slower. In our MOT loading procedures, this coil

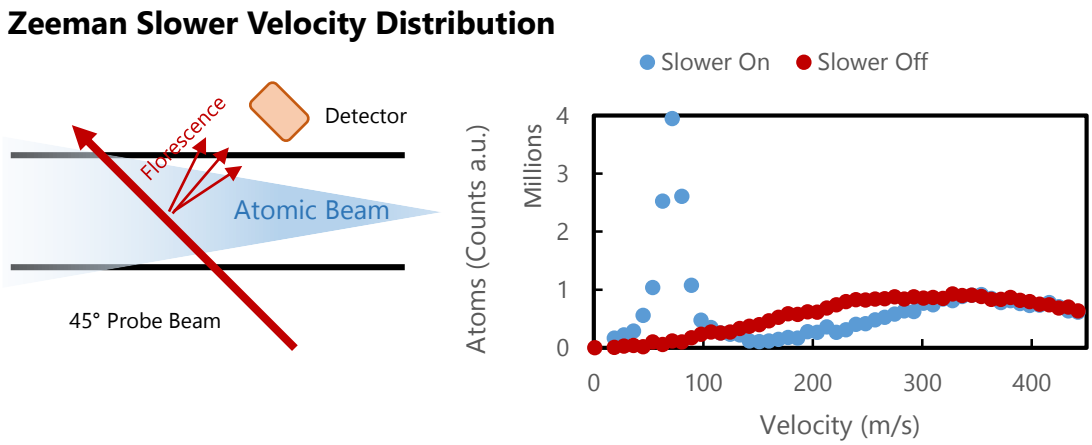

Figure 4.30: Characterization of the Zeeman slower. We measure the velocity of the atoms as a function of atomic resonance and see a large profile of slowed atoms after the slower compared to background.

runs at approximately 20 A, yielding a 54 G field uniformly down the slower.

The slowing laser beam is counter propagated against the atomic beam. Both the slower light from the cooling and repump laser systems are combined in an optical fiber combiner before being aligned into the slower. The laser light is passed through a $\lambda/4$ waveplate in order to create the circular polarization for the slower operation.

Measuring Atomic Velocities

To measure the performance for MOT loading, we used a probe beam to measure the velocity profile of the slowed atoms. Because the linewidth of the atomic transition is small compared to the Doppler broaden width of the thermal atoms, measuring the frequency dependent absorption is proxy for measuring the velocity itself. For ^{87}Rb, this gives approximately 1.28 MHz/m/s. By passing a probe beam through the atoms and measuring the absorption as a function of frequency, we reclaim the velocity profile (Figure 4.30). To measure both the longitudinal and transverse velocities, we intersected the probe and atomic beams at a 45° angle. Because of the large frequency range required for this scan ($\approx$ 500 MHz), we had to borrow fiber coupled light from another experiment with a separate laser system, in addition to our own cooling and repump lasers. We can measure that our slower, when optimized, can shift the velocity profile at the glass cell from 300 m/s to 50 m/s.

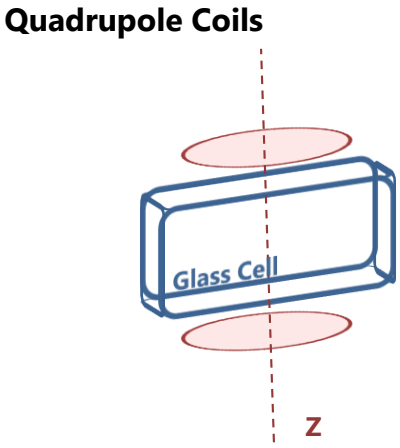

Field Gradient Strength (KHz / um / A)	0.1 (in plane) 0.2 (vertical)
Field Gradient Strength (G / cm / A)	1.42 (in plane) 2.84 (vertical)
Resistance (mΩ)	17.5
Turns	40 each
MOT Capture Current (A)	5.5
Magnetic Trap Compression (A)	60
Magnetic Trap Gravity Balance (A)	10.5

Figure 4.31: Geometry of the quadrupole coils. The coils are mounted in an anti-Helmholtz configuration immediately above and below the glass experimental cell.

4.4.2 Quadrupole Coils

The quadrupole coils in the RbLi experiment are an anti-Helholtz coil pair mounted immediately above and below the glass experiment cell. The coils are wound with 40 turns of square copper tubing (allowing for water cooling) in a configuration of 8 layers of 5 turns each. The current for the coils is provided by an Aglient 6690A power supply that operates at maximum 15V and 440A of current.

The current in the quadrupole coils is regulated by a bank of 20 MOSFETs in parallel that all share a common gate voltage that is controlled by a PI servo. The large number

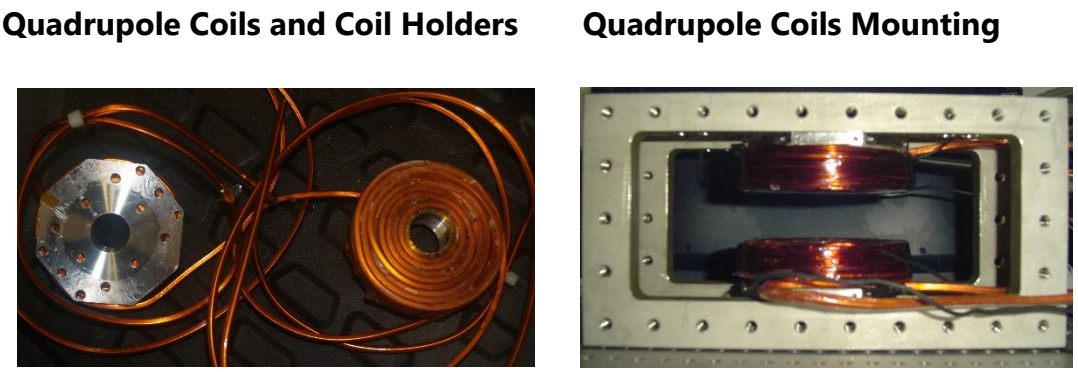

Figure 4.32: Left: Construction of the quadrupole coils from copper tubing. Right: Installation of the coils into the apparatus.

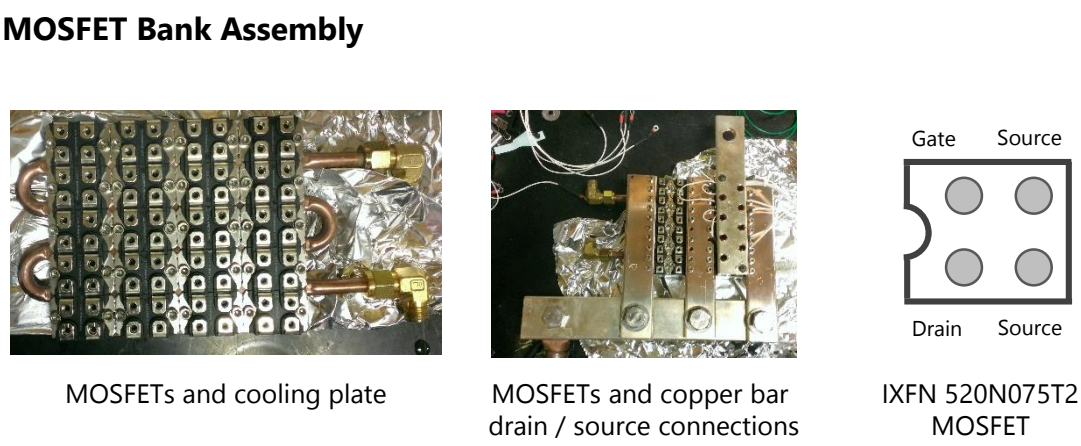

Figure 4.33: Quadrupole MOSFET bank used for current regulation. Due to the high currents and heat dissipation involved, the bank consists of 20 MOSFETs on a water cooled plate. This allows for both high and low currents at a constant power supply voltage.

of MOSFETs, along with water cooling, allow us to run large currents with the voltage on the power supply held constant at 15 V. Due to the low resistance of the quadrupole coils, the majority of the voltage drop, and thus power dissipation, occurs at the MOSFETs, which creates the requirement for water cooling and large number of parallel units to share the power load. The advantage of this configuration is that it allows us to quickly change field values on the quadrupole as the larger available voltage helps counteract the large inductive kickback from the coils to snap-on commands. This configuration reduced the turn on time of the coils from approximately 100 ms to 5 ms, allowing for much more repeatable Stern-Gerlach spin separation pulses, or magnetic trap turn ons.

However, because of the high inductive voltages generated during a quick snap on of current, a variety of elements were put in parallel with the MOSFET bank to prevent reverse currents that can cause the MOSFETs to: pop, catch fire, silently stop working and destabilize your system. To combat these problems we put a set of varistors in parallel to prevent large voltages from building up. Because these varistors still failed under various conditions, causing failed MOSFETs, we placed a set of diodes to allow current from source to drain so that reverse currents could bypass the MOSFETs. Through trial and error we found that having diodes rated for different situations put together in parallel, i.e. rapidly responding diodes with low current rating plus large current diodes with a

slow response, provided a sufficient amount of protection.

The strength of the gradient was measured using the position of condensates after time of flight imaging. The condensates were prepared in pure $m_F = \pm 1$ states. The current was ramped to a variable value with a biasing field along one of the principal axes of the experiment, allowed time to relax, and the condensate was released for time-of-flight with the current still constant. By watching the position of the condensate as a function of quadrupole current, we can measure the acceleration, thus force and magnetic field gradient, due to the coils. By repeating this in all directions, with both $m_F = \pm 1$ condensates (which will feel equal magnitude and opposite direction forces), we can calibrate the magnetic field gradient from the coils in all directions. We find that the coils have, in ^{87}Rb centric units, 200 Hz/ μm in the vertical direction and 100 Hz/ μm in plane, matching the 2:1 geometry of the anti-Helmholtz coils.

4.4.3 Bias Coils

The bias coils in the RbLi experiment are used to generate uniform magnetic fields across the atomic cloud (Figure 4.34). There are three sets of Helmholtz aligned coil pairs, each set along one of the principal axes of the experiment. The coils are created from 15 turns of 16-gauge magnet wire. All coils are driven on independent Kepco BOP ±20 A power supply units with hall probe based PID servo electronics that give a precision (not

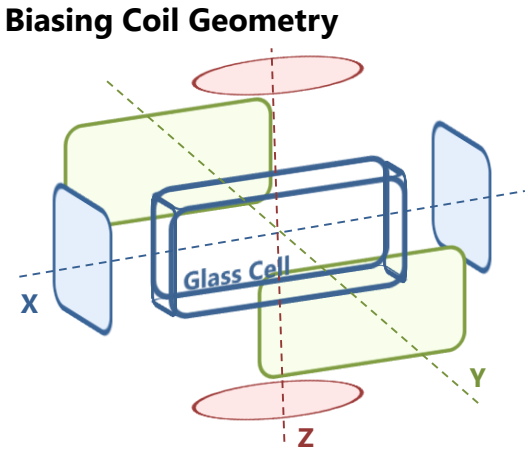

	X Coil	Y Coil	Z Coil
Field Strength (MHz / A)	0.144	0.828	1.685
Resistance (mΩ)	0.56	0.43	0.211
Inductance (mH)	24.6	25.3	21.9
Background Magnetic Field Cancellation Current (A)	1.040	0.062	0.303

Figure 4.34: Geometry of the biasing coils used in the experiment to provide spatially uniform magnetic fields along the primary experiment axes.

accuracy) of approximately 100 μA control over the ± 20 A output range.

The X and Y coils are mounted on rectangular aluminum structures that are parallel to the glass cell. The Z coil pair is mounted on top of the quadrupole coils, and are the closest coil pair and produce the largest magnetic field per Ampere. As such, the Z bias coils are the primary biasing coils used in experiments that require high (+10 MHz) biasing fields. The Y coil is used as the primary biasing coil where the field must be in plane. The X coil, owing to its distance from the atoms and weak field strength, is exclusively used to cancel background magnetic fields.

Each of the coils is calibrated in field strength by performing an experiment to measure the linear Zeeman shift generated by each of the coils at various currents. We subject the BEC to an RF field that we adjust to find resonance with the linear Zeeman shift at a given coil current. We repeat this measurement for various RF frequencies and current combinations to develop a proportional relationship between the current and Zeeman shift. By knowing the gyromagnetic ratio for ^{87}Rb (≈ 0.7 MHz/G) we can compute the magnetic field strength as a function of current. By repeating this measurement on each coil, for both positive and negative currents, we gain information on the field strength of each coil. This measurement process also gives the background magnetic field within the experiment. By measuring resonance while varying the current, hence magnetic field strength, across a wide range we find the value which minimizes the RF frequency that brings the system to resonance. In Figure 4.35, this corresponds to the zero crossing of the linear fits.

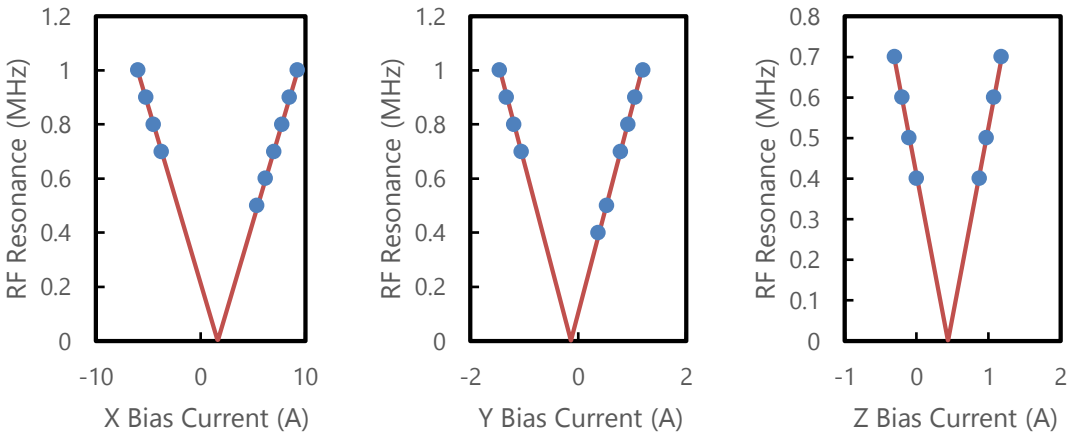

Figure 4.35: Calibration of coil field strength and background field via RF spectroscopy.

4.4.4 Gradient Shim Coils

Above and below the glass cell, mounted onto the far side (from the cell) of the quadrupole coil holders, are three sets of coils that produce magnetic field gradients. These coils, named the 'Gradient Shim Coils' are arranged on top in bottom in a clover-leaf pattern, with opposing coils being in pairs. Each set, top and bottom, has a center coil which together form a classic anti-Helmholtz coil configuration. The other directions, XY and YX, have two coils on the top and the bottom that together form a magnetic field gradient along the $\hat{\mathbf{x}}+\hat{\mathbf{y}}$ and $\hat{\mathbf{x}}-\hat{\mathbf{y}}$ respectively. The coils are placed along these axes because they match the principal axes of the optical dipole trap. Another set of gradient shim coils were used in our spinor domains experiment (Section 5.2.1), but have since been removed in favor of the design here.

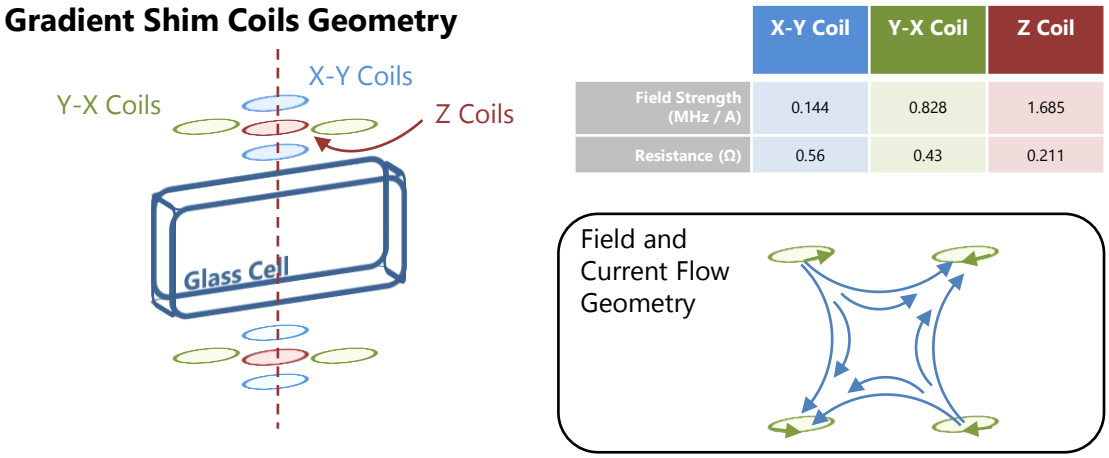

Figure 4.36: Geometry of the gradient shim coils, used to cancel out background magnetic field gradients at the atoms.

4.4.5 RF Coil

To interact with the atoms using RF fields, with frequencies on the order of MHz, we have a set of coils printed onto a thin PCB that is placed snuggly between the top of the glass cell and the quadrupole coils. The multi-coil design allows us to generate linearly polarized RF fields in either the $\hat{\mathbf{x}}$ or $\hat{\mathbf{z}}$ directions, depending on the geometry of the magnetic biasing field. We use a Novatech 409B direct-digital synthesizer to provide a computer controlled signal generator. To control the amplitude of the RF waveform, we can use both a digitally stored command in the Novatech, or for faster amplitude changes we can use a RF-mixer (a mini-circuits ZAD-3+) connected to a dc voltage source. The RF waveform amplitude can be adjusted, non-linearly, by adjusting the dc voltage that couples into it. We also use a digital switch (a mini-circuits ZYSWA-2-50DR), under computer control via a digital line, to enable and disable the RF signal from being propagated to the coil. The RF signal is then passed through a 10W RF amplifier and then onto the coil. After the coil, we place a high-power attenuator and 50 Ω coupled termination onto the line to prevent reflections of the signal. To measure the coupling strength of the RF coil, we perform an on resonance Rabi pulse and measure the fractional populations of atoms in the spin states, and compare to theory (similar to calibrating the Raman coupling strength, as described in Section 4.3.7). For our RF coil setup, our maximum power described as a Rabi frequency is approximately $\Omega_{\mathrm{RF}} \sim 2\pi \cdot 35$ kHz.

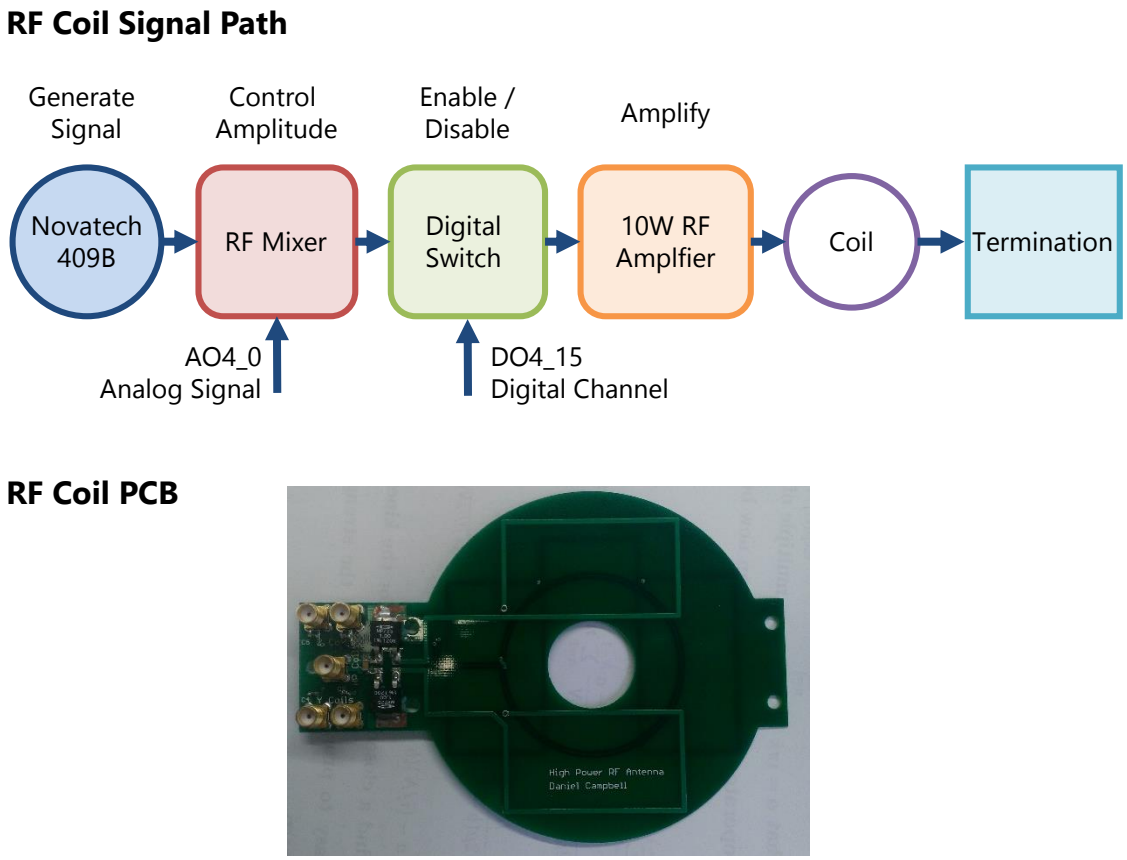

Figure 4.37: Top: Schematic of the RF coil signal path. Bottom: PCB printed RF coil placed immediately above the experimental glass cell.

4.4.6 Table Coils

The 'Table Coils' are two large single coils along both the Y and Z directions. These coils are used primarily for generating a small uniform biasing field at the atoms for calibrating and deploying our magnetic field stabilization system (see Section 4.4.7). Both are single coils, therefore they do not make magnetic fields as uniform as the Helmholtz biasing coils. However the diameters of the table coils (meters) compared to the condensate (microns) makes the uniform field approximation valid.

The Y table coil consists of 10 loops of magnet wire along a square 80-20 aluminum structure enclosing the apparatus. By design of the enclosure structure, the Y table coil is close to being centered on the atoms and glass cell. The Z table coil is 20 turns of magnet wire looped along the side of the $4' \times 8'$ optics table.

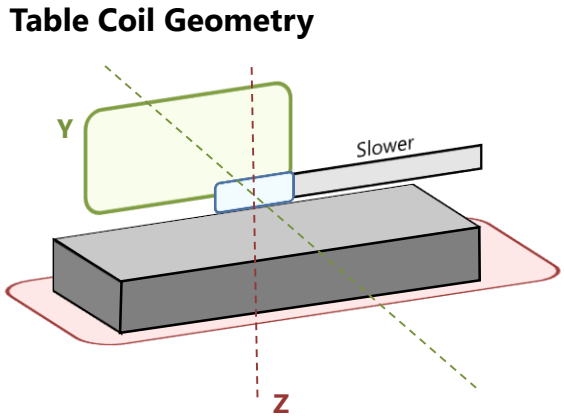

	Y Table Coil	Z Table Coil
Field Strength (mG / A)	30.73	64.3
Field Strength (MHz / A)	0.0215	0.045
Resistance (Ω)	1.6	11.4
Coil Windings	10	20

Figure 4.38: Geometry of the table coils. These coils are used primarily for background magnetic field cancellation.

4.4.7 Magnetic Field Stabilization

Magnetic field control in spinor condensate experiments is important as any stray field can cause an unwanted linear Zeeman effect that can cause energy shifts larger than those characteristic to the system. These can be slowly drifting fields throughout the day, or radiated 60 Hz line noise coming from laboratory electronics. In ^{87}Rb experiments in the $F = 1$ ground manifold, any stray fields break the symmetry between the $m_F = \pm 1$ states, causing a preference that may be unwanted. In our experiment, we have gone through extensive measures to characterize and combat these unwanted sources of noise.

Measuring Magnetic Field Stability

To measure the magnetic field noise in the system, we use RF coupling to create a combination of the $F = 1$ spin states. We typically use an Adiabatic Rapid Passage scheme to take a $m_F = -1$ BEC and create an equal mixture of $m_F = 1, 0$. In measurements, we go to a high enough linear Zeeman shift such that the $m_F = 1$ state does not become involved, thus simplifying the measurement for us. To measure the magnetic field, we first find the command on the bias coils to create a 50/50 mixture of the two spins. Next we let the system run, collecting information about the relative populations of the spins as a function of time.

By knowing the power and frequency of the RF field, we can calculate the relative

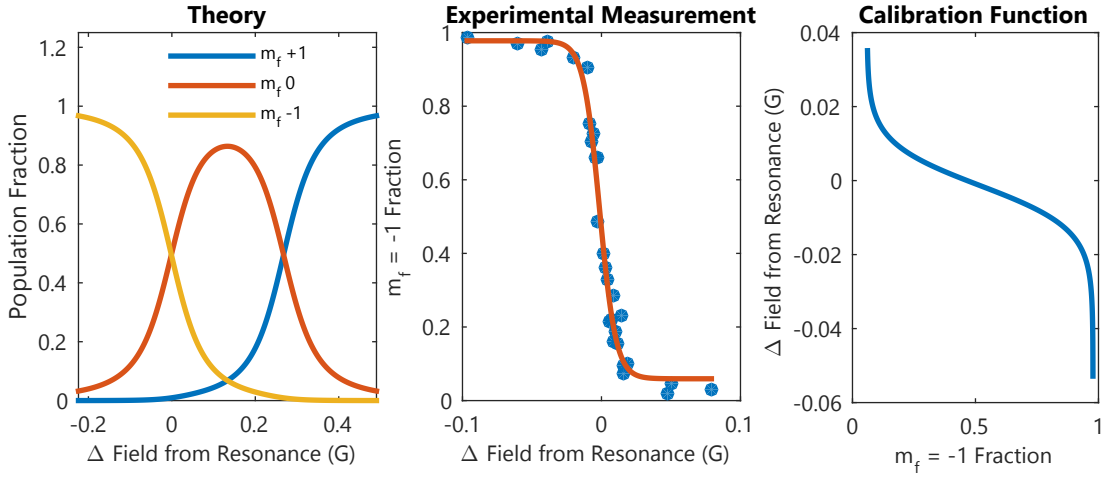

Figure 4.39: Left: Calculation of the spin populations for the dressed state of a 18 MHz RF field. Center: Experimental measurement of the population as a function of the field difference from resonance. Right: Conversion of population information to magnetic field value, from either experimental measurements or theoretical calculations

populations that should be appearing as a function of detuning. If we invert the relationship, we have a function of detuning as a function of measured population fraction. Because we have the RF field set precisely, the detuning drift measured must be due to the magnetic field and Zeeman effect.

More empirically, we can also use a measurement of the fractional population as a function of the magnetic field (and hence detuning) that we command on the bias coil. This also gives a similar fractional population versus detuning dataset that can be inverted to give the shift in the field as a function of fractional population. It is also important to note that the power of the RF field, in terms of Rabi frequency, can broaden or narrow the resonance, giving a measurement across large or narrow detuning ranges.

Background Stability

Using the methods described in the previous section, we can measure the field noise in our experiment. The field noise measured in both the Y and Z directions is shown in Figure 4.40. Both directions have approximately a milligauss shot-to-shot variability. However, the Z direction also shows a long term drift, on the scale of an hour or so, where the field can drift by a few milligauss. This is problematic as our typical data collection scans requires such an amount of time to perform, without time in between to find resonance.

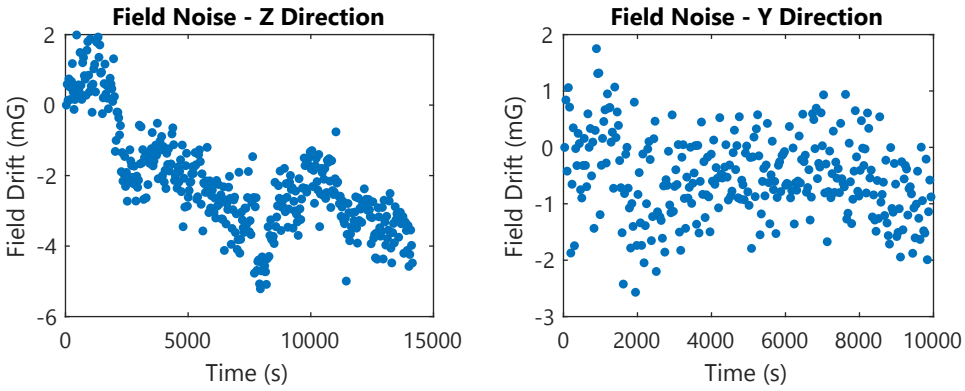

Figure 4.40: Measurement of the magnetic field drift in the Y and Z experimental directions as a function of time.

Flux Gate Feed Forward System

In order to improve the magnetic field environment of our system, I developed a magnetic field stabilization system based on a pair of flux gate magnetic field sensors place near the experimental cell. The system measures the ambient magnetic field environment, then through calibrations, feeds a signal forward to the bias control servo to cancel the variation in the magnetic field.

The flux gate system successfully removes the slowly drifting background magnetic field in the experiment. However, shot-to-shot noise still remains within the system that could be related to many factors due to the method of measuring the field with the atoms. Any uncertainty in the condensate preparation and measurement, such as the repeatability of our RF adiabatic rapid passage scheme, or the variation in the imaging and measurement performance, could limit our ability to measure beyond this limit.

The flux gate system, with both the DC and 60 Hz magnetic field sensing and removal mechanisms, is described in detail in Appendix A.

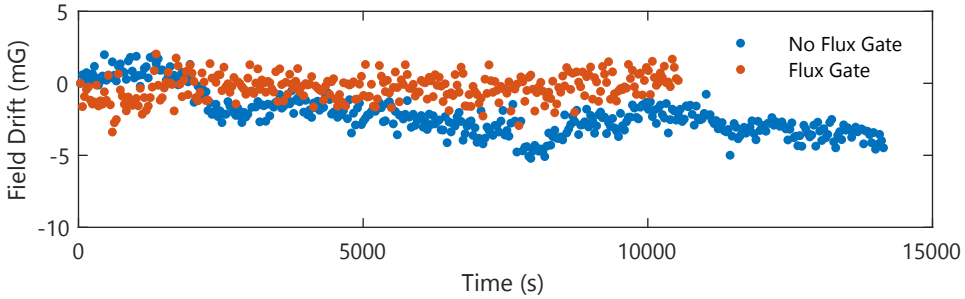

Figure 4.41: Magnetic field drift in the Z direction without and with the flux gate correction system.

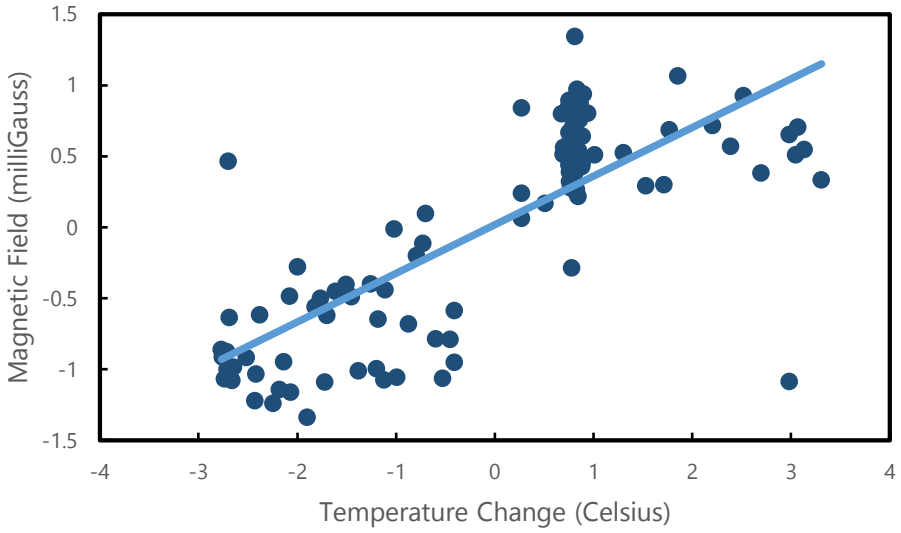

Figure 4.42: Correlation between lab temperature and magnetic fields as measured by the atoms. The measurements give an approximately 0.34 mG/V effect.

Magnetic Fields and Lab Temperature

In many experimental systems, there is a substantial effort to keep the lab temperature stable. For atomic physics experiments, temperature stability is necessary due to the sensitivity of laser diode mode behavior, the alignment of optics, and the polarization stability of optical fibers. However, for those who work with sensitive atomic resonances in the RbLi experiment, it is to be noted that magnetic fields also depend on the lab temperature as well.

Given the slow background magnetic field drift measured in the lab, attention turned to other possible sources of error that operate on long time scales. One possible source of field drift was due to not the background fields necessarily, but that our electronics could have temperature dependent effects that cause slight resistance or gain shifts. To test and see how large of an effect this is, a set of temperature transducers, based on the precision AD590 temperature-to-current device, were constructed[6] and placed in the lab near the experimental cell and near the bias coil servo electronics. The temperature was recorded simultaneously along with atomic resonance data to make a correlation between

[6]Credit for this project belongs to two undergraduate students under my guidance, Doug Hockey and Brendan Van Hook, for their project designing the temperature sensors and performing the following measurements

the two. To help get a wider range of temperatures in the lab to correlate against, the lab thermostat, in perhaps poor judgment, was blasted with a hot air gun to cause a large influx of cold air into the lab.

From these measurements, the trend of the correlations show there is an approximately 0.34 mG/V effect. Whether this is due to the control electronics or some other temperature dependent correlation is still undetermined.

4.4.8 High Power Op Amp Current Sources

Given the need to reduce magnetic field noise at the atoms, as described in Section 4.4.7, another source of noise we investigated was the Kepco bipolar power supplies we use on our bias coils. Given their tendency to radiate 60 Hz noise, we needed an alternative high current source. Unlike the quadrupole, and slower coils, the bias coils require a bipolar current source, therefore our MOSFET based current stabilization schemes would not be effective.

To get a bipolar current source that we could control, we opted to build a current source based on a bank of Apex PA05 High Power Operational Amplifiers[7]. These amplifiers are designed to be standard operational amplifiers that can operate at high power voltages from ± 50 V at up to 30 A output. The idea was to have very quiet DC power supplies that provide a $< \pm 50$ V source with high current capabilities that act as the power source for the PA05 op amps.

By making a standard and simple non-inverting op amp circuit with the PA05, a command voltage at the op amp input determines the output current (for a fixed load). The circuit is designed with two resistors that set the voltage gain across the op amp. Considering that most voltage command signals in our lab are ± 10 V signals, a non-inverting gain allows voltage commands that can utilize the full ± 50 V output range of the power source if needed. The circuit includes op amp bypassing capacitors arranged for a 30 A output (330 μF, as given by the Apex application notes pages). The circuit design also has a connection to the shutdown pin of the op amp, allowing a TTL disabling

[7]Credit for this project belongs to two undergraduate students under my guidance, Smita Speer for the design of the operational amplifier circuit and box construction, and Ben Cannon for installing the hall probe sensors within the box and integrating it within our experiment.

Apex PA05 High Current Op Amp

Specifications	
Voltage	± 50 V
Current	30 A
Slew Rate	100 V / µs
Bandwidth	3 MHz
Power Dissipation	250 W

Water Cooling System

Op Amp Circuit Board

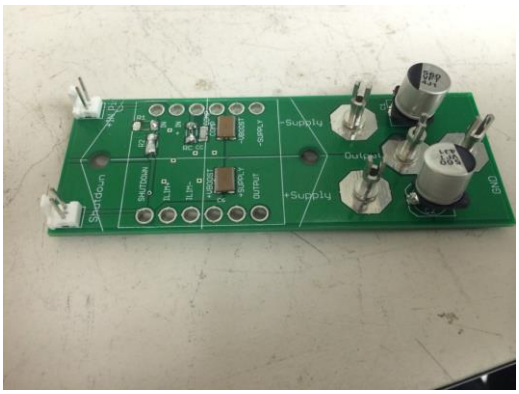

Populated Circuit In-Situ

Figure 4.43: PA05 high power op amp current supply box. The PA05 high power op amps are mounted into custom PCBs, then mounted onto water cooled heat sink units. The entire assembly contains cooling for four op amps.

mechanism, useful for quick snap offs or interlock operation.

The high power ability of the PA05 op amps means that the op amps themselves will dissipate an enormous amount of heat when pushed to their maximum limits. For this reason, the op amps are mounted into custom heat sinks, available from Apex, that fits the proprietary connectors of the PA05, allowing the underside of the PA05 to be flush against the heat sink with the pins poking through. During assembly, we placed thermal conductive paste between the op amp and heat sink to ensure good thermal conduction. To go to the extreme, the heat sink itself is mounted onto water cooled plates. However, due to the geometry of the heat sink, the op amp is at the bottom, with the fins on top. The water cooling plates, due to these restrictions, are placed in contact with the op amp

side of the heat sinks with as much area overlap as possible. In a test where 115 W of heat were constantly dissipated at the op amps, the unit measured a maximum temperature of only 120 °F, with effectively[8] no water cooling.

Again due to the geometry restrictions of the heat sinks, any connections to the op amp must be made at the pins, which poke up in a flat region between the fins of the heat sink. The circuit for controlling the current was printed onto a PCB which fit into the slot between the fins of the heat sink. The op amp connects to a socket soldered onto the PCB (the socket, again, is a special part available from Apex), allowing separation between the PCB and heat sink / op amp unit.

The entire current supply box duplicates the op amp and cooling setup four times, providing current control on the four separate op amp blocks. Each block also has a hall probe in line to measure the current at the output of the op amp. The output of the box has a voltage input that goes to the input pin of the op amp, a hall probe measurement voltage output, a red banana jack connector for current out of the op amp, and a black banana jack connector that goes to ground[9].

Sadly, as of writing, the noise performance of this system has not been tested as we have not yet acquired a quiet DC power supply, and interest in the project has waned. However, the system has been faithfully powering our gradient shim coils without incident.

4.4.9 Water Cooling for Electromagnetic Coils

In order to dissipate the heat due to ohmic losses in our high current systems, like the quadrupole coil and Zeeman slower, we installed a water cooling system in the experiment. The major electromagnetic coils, such as the Zeeman slower, quadrupole coils and slower biasing coils, are wound with copper tubing[10] that has cooling water flow inside. The water in these coils flows in a contained loop, with a chiller to cool the water and hold a reservoir, a booster pump to increase the water pressure up to 170 psi before the coils, a set of valves to control flow to individual systems, and flow meters to electronically detect

[8] The chiller unit running the water to the cooling plates hardly had the pressure to push water through the test coil and the water plates

[9] The box assumes you *always* want to connect one side of the coil to ground

[10] We specifically used refrigerator tubing when possible as the standard to be clean enough for drinking water meant these would be more free of particulates and oils

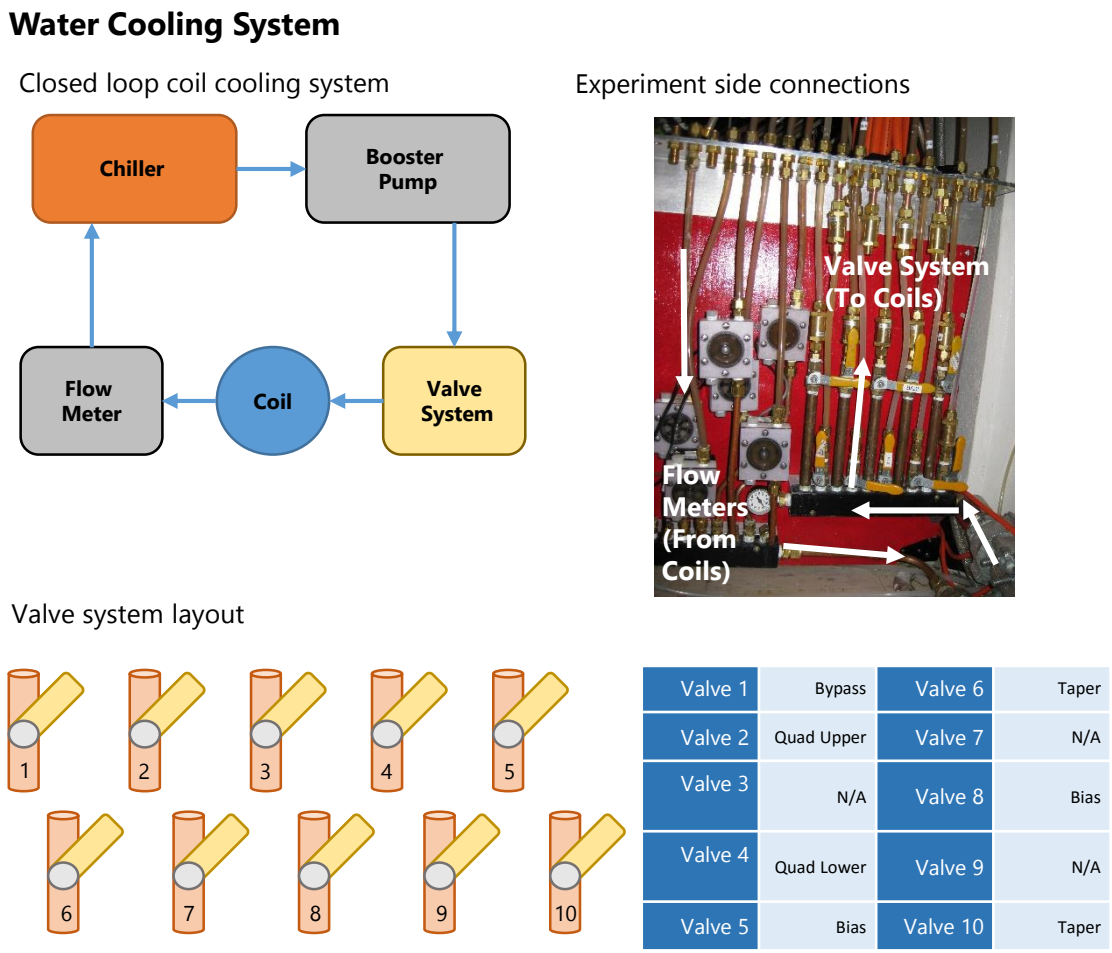

Valve 1	Bypass	Valve 6	Taper
Valve 2	Quad Upper	Valve 7	N/A
Valve 3	N/A	Valve 8	Bias
Valve 4	Quad Lower	Valve 9	N/A
Valve 5	Bias	Valve 10	Taper

Figure 4.44: Top: Schematic of the RbLi water cooling system. Bottom: Mapping of flow control valves to the associated electromagnetic coil.

the flow of water in the experiment. The flow meters act as an interlock to the high current systems: if the flow meters do not detect flow in the water cooling system, a set of interlock electronics will disable the high current power supplies, thus preventing an overheating (or other) catastrophe. Similarly, an advantage of using a closed loop water cooling system is that it has a finite amount of water contained within in so that if any large leaks occur, the flooding can be minimized. To cool the large amount of heat generated at the MOSFET regulation banks in our experiment, we used water cooled aluminum plates connected to the water system supplied by the building facilities.

4.5 Imaging System

While everything else in this chapter has been about the design of the different elements of the RbLi experiment to trap and cool atoms, the imaging systems are the only setups we have to directly measure the state of the atoms. We have two imaging setups within the experiment. The first system images in the XZ direction: we use this system mostly for images of large atomic clouds, such as magnetically trapped atoms, and other diagnostics. The second imaging system is the XY system which views the atoms from below. The XY system is the primary imaging system used to measure the system when at the BEC stage of an experiment.

4.5.1 XZ Imaging Setup

The XZ imaging system looks at the atomic cloud 'side-on', with gravity being along the vertical axis of the image. This imaging direction is used primarily for diagnostics as its low magnification is able to image all stages of creating a condensate, from MOT to BEC, also with variable times of flight without the need to refocus the camera. The design of the XZ imaging system is depicted in Figure 4.45.

The system uses probe light that comes from a fiber coupled line on the cooling laser board. The light is collimated into a wide ($\approx$ 1") beam waist, and by using a polarizing beam splitter and $\lambda/4$ waveplate, the beam is made circularly polarized. The probe beam is then passed through the atoms, then through a two element telescope, with a 50 mm 1" spheric lens and a 125 mm plano-convex lens, giving a designed 2.5 magnification and experimentally measured 2.54 magnification. The image is then focused onto a Point Grey Blackfly PGE-50H5M-C CCD camera. The camera is on both a translation stage to find focus, and a rotation mount that allows us to precisely align the vertical of the camera with the direction of gravity.

The Blackfly camera has a 2448 $\times$ 2048 pixel array with 3.45 μm per pixel, which yields a 3.36 mm $\times$ 2.8 mm field of view of the atomic cloud with a 1.38 μm/pixel resolution. The field of view and resolution together allow the XZ imaging system the ability to

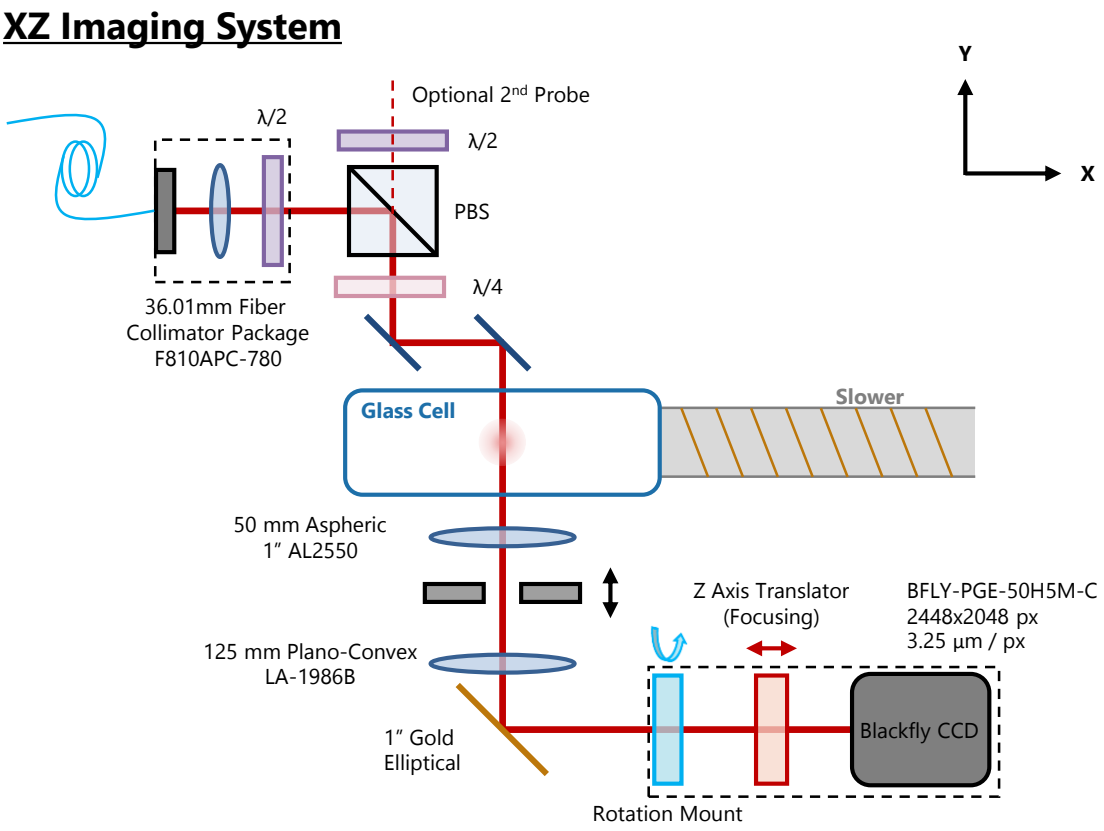

Figure 4.45: XZ imaging system optical setup

view both large magnetically trapped clouds and BECs with resolution equal to the primary, XY, imaging system. The disadvantage of the camera, however, is that the Gigabit Ethernet connection requires ≈ 300 ms per image to transfer, causing a long delay between the three shots for absorption imaging. The images at full resolution are large, causing issues with computation speed while doing analysis. For this reason, it is recommended to use Region of Interest (ROI) modes to take smaller images when possible.

4.5.2 XY Imaging Setup

The XY imaging system is the primary measurement method used in the experiment. The system starts with fiber coupled light from the cooling laser system. This light is collimated through a 7.5 mm aspheric lens to give a beam waist of approximately 300 μm at the atoms. The probe beam is then passed through a Glan-Taylor polarizer and a $\lambda/4$ waveplate to ensure a nearly pure circularly polarized beam. The beam then traverses off of two gold mirrors (to maintain polarization qualities), then vertically toward the glass

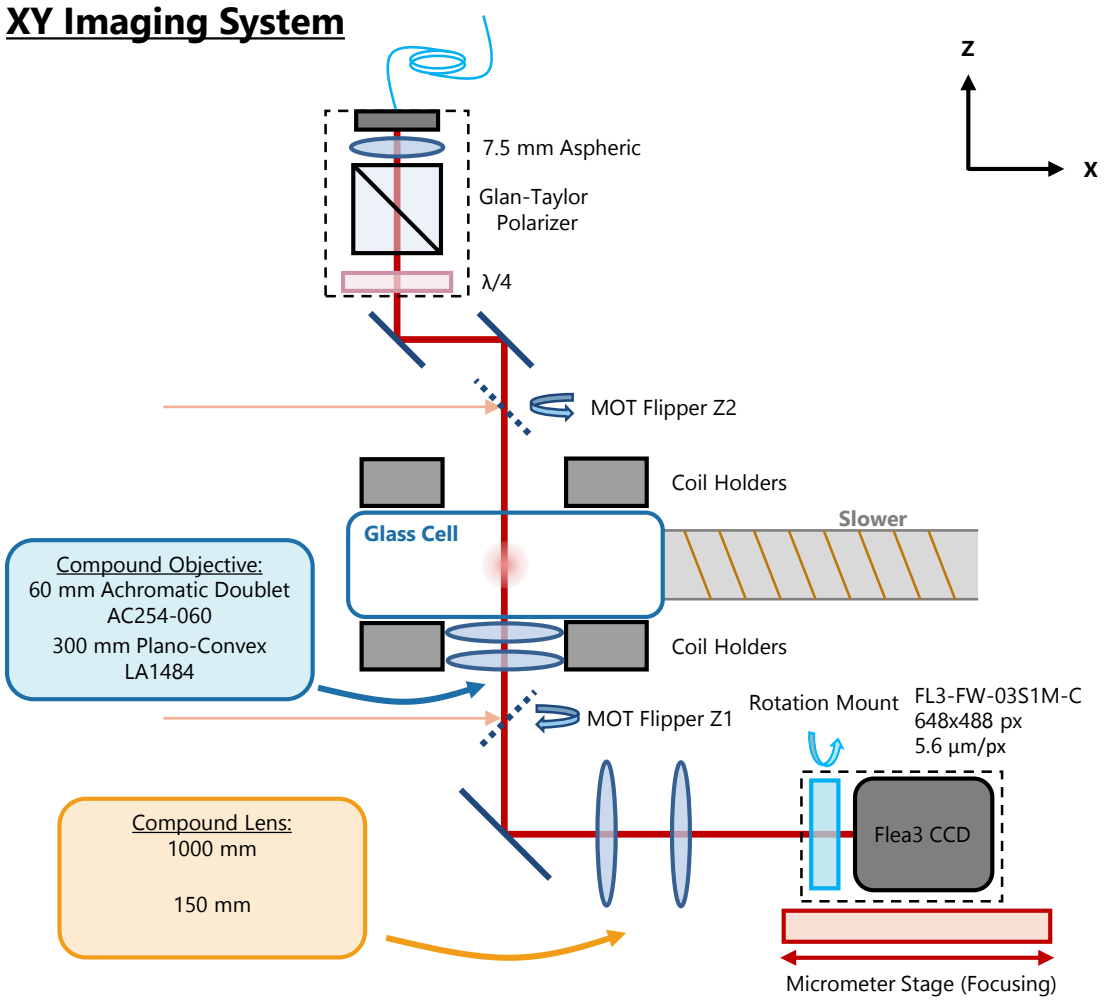

Figure 4.46: XY imaging system optical setup

cell and atoms. Because the MOT also requires vertical beams, the imaging probe and MOT beams must share the same vertical trajectory. We remove the MOT light (and downward pointing mirror) by using a pair of flipper mirrors that are removed from the vertical beam path when we image, allowing the probe beam full access.

After the light has passed through the atomic sample, the beam passes through a two lens compound objective and a second compound lens pair to give a magnification to the system. Lastly, this light is passed onto the Point Grey Flea3 CCD camera for imaging. The camera is mounted on a micrometer stage so we can precisely focus the image. Similarly the camera is mounted on a rotation mount so we can align the camera axes, typically to either the optical dipole trap coordinates $(\hat{\mathbf{x}} \pm \hat{\mathbf{y}})$ or the experiment coordinates $(\hat{\mathbf{x}}, \hat{\mathbf{y}})$.

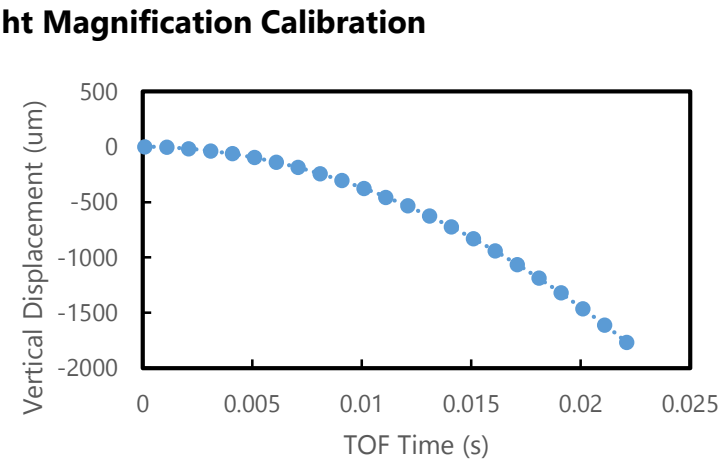

Figure 4.47: Gravitational displacement of BEC versus variable TOF time. Measuring the acceleration in pixels/s^2 and comparing to $g = 9.81m/\text{s}^2$ gives the magnification

4.5.3 Calibrating the Magnification

We use two methods for calibrating the magnification of our imaging systems. The first is to measure the free fall acceleration of the BEC during time-of-flight imaging. The technique is simple: We prepare a $m_F = 0$ BEC (because of the insensitivity to magnetic forces), release it in TOF, and vary the time until we take the image of the BEC. By measuring the vertical displacement of the BEC (in pixels!) compared to the time of free-fall, we can use the standard $\Delta Y = \frac{1}{2}at^2$ to find the acceleration in pixels/s^2, and compare to standard gravitational free-fall of $\approx 9.8\text{m/s}^2$ and the camera pixel size:

$$M = \frac{a_{meas.}}{g}\Delta\text{Px} \tag{4.1}$$

Where $a_{meas.}$ is the measured acceleration in pixels/s^2 and ΔPx is the size of the pixel on the camera chip. This calibration method is useful as it makes no assumptions about the system other than the gravitational field.

This measurement naturally is performed for the XZ imaging. As such, we align the vertical axis of the image with the direction of gravity prior to the magnification measurement by rotating the camera until the horizontal displacement of the BEC in the image is invariant under different TOF times.

This method can be extended to calibrate the magnification in the XY imaging

direction as well. After the XZ imaging is calibrated, we can perform an experiment where we prepare an $m_F = -1$ BEC and apply a constant gradient along the $\hat{\mathbf{x}}$ direction (the horizontal axis of the XZ camera) during TOF, while varying the TOF again. The cloud, due to the constant acceleration due to the magnetic force, will again move across the image. Doing this scan using the XZ imaging measures the calibrated acceleration due to the magnetic force in m/s^2. By comparing this value to the acceleration, in pixels/s^2, measured from the same scan using XY imaging, the magnification can once again be measured.

Another method we use to calibrate the magnification of the imaging system is through lattice diffraction. We use a Raman coupling pulse to impart different momenta populations to the condensate. Because the momentum is well defined in units of $k_{\mathrm{R}} = 2\pi/\lambda_R$ where λ_R is the laser wavelength, we know the velocity of the atoms during TOF, and hence can calculate the distance they should move in a given time period. By measuring the displacement in pixels and comparing, we have another metric for magnification.

4.5.4 Calibrating the Focus

To focus our imaging systems, we use density-density correlations in images of BECs. This technique, which we stumbled upon during our spinor domains experiment (Chapter 5), allows us to set the focal plane to within microns of the correct location. The method relies on a BEC that has spatial density modulations across a large swath of frequencies, such as spinor BECs with domains, BECs with vortices, or other atomic interference pattern effects. When passing probe light through the condensate, modeled as a set of random scatterers, a set of fringes appear in the power spectral density (PSD) of the image. The wavevector that the fringes in the PSD occurs at diverges when the focal plane is at the center of the scatterer distribution (see Figure 4.48, left panel). The detailed theory of this method is discussed at length[11] in Reference [47], from here I will discuss the practical implementation within our experiment.

[11]Theory data and fits presented here, and moreover the work of developing the theoretical model of this method goes to lab colleague Andika Putra

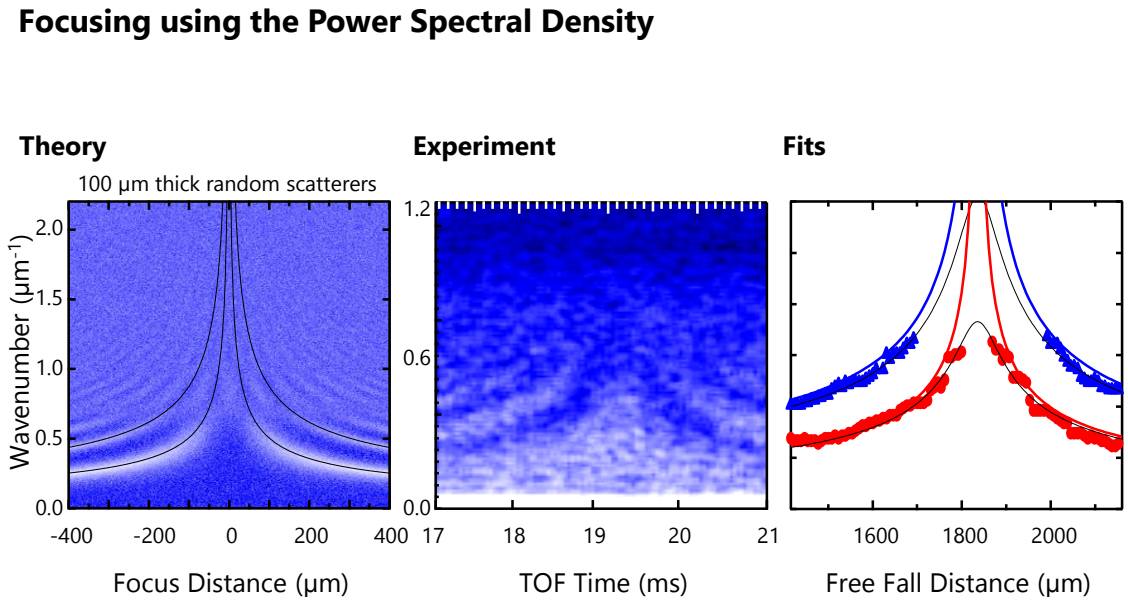

Figure 4.48: Left: A simulated set of random scatterers will have voids in the power spectral density (PSD) as a function of the distance from focus. The voids asymptote to infinite frequency when in focus. Center: Observation of the voids in the PSD from experimental imaging. Right: Fits of the features in the center plot give the location of ideal focus.

To find focus, we create a BEC with spatial noise at higher wavenumbers so as to give contrast in the PSD between signal and the fringes. Next to scan the focal plane we vary the TOF time before imaging the condensate. By taking a one-dimensional PSD measurement[12] at each TOF time (hence distance from focus), we can observe the fringe pattern in the PSD and locate the diverging point as a function of the focal distance (Figure 4.48, center panel). The fringe locations in the experimental data can be located and fit according to the theory in Reference [47], giving us the optimal focal distance, and similarly TOF time (Figure 4.48, right panel). When using the TOF time as a variable focus adjustment, we must account for the quadratic increase in focal distance as a function of time. This effect otherwise leads to asymmetric distributions, as shown in Figure 4.48.

[12] slices for our 1D spinor experiment, later radial averages when using vortices

Chapter 5

Domain Formation in Crossing the Miscible-Immiscible Transition in a Spinor BEC

The establishment of out of equilibrium domains formed by quenching through a phase transition is ubiquitous in physical systems ranging from grain formation in minerals [48], domain nucleation in magnetic systems [49], to Kibble-Zurek phenomena such as structure growth in the early universe [50], and spontaneous vortex formation in quenched BECs [51].

Here we study a similar quantum quench in a two component spinor BEC, where the spin degree of freedom is initialized in a maximally excited state where the spin distribution is uniform across the BEC. Because of the spin dependent interactions in ^{87}Rb, the $m_f = \pm 1$ states will gain energy by spatially separating. We follow the resulting dynamics during which spin domains rapidly form, and subsequently slowly relax towards equilibrium as the domain size increases and the domain number decreases.

5.1 Background and Theory

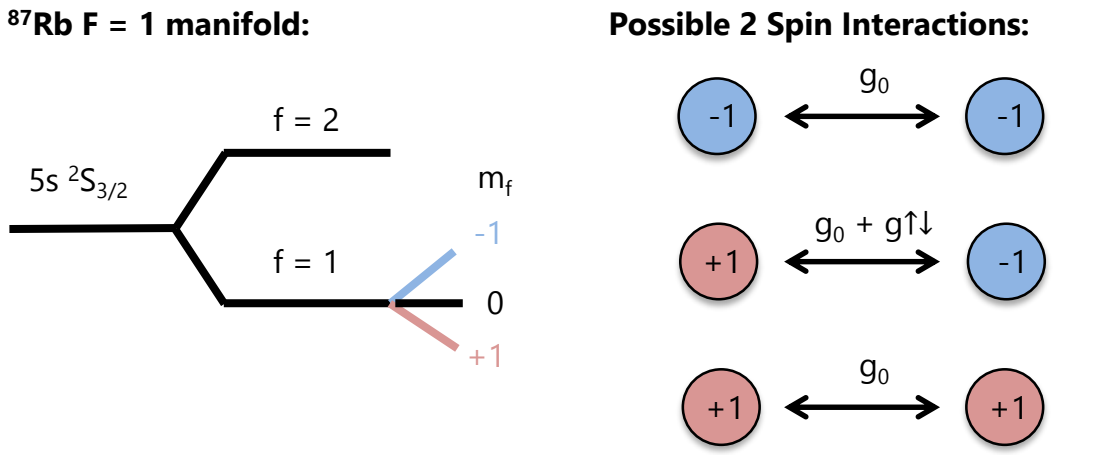

Figure 5.1: Interactions in the ^{87}Rb $F = 1$ ground states. The $m_F = \pm 1$ states have different interaction energies when interacting in a different-spin configuration than a same-spin interaction.

5.1.1 Spin-dependent Interactions and Miscibility

In our system we utilize ^{87}Rb in the $F = 1$ ground state and hence focus on the $m_f = 0, \pm 1$ magnetic hyperfine states. Here there are two s-wave scattering channel lengths a_0, a_2 due to the two possible total angular momentum states of $F = 0, 2$ from two spin 1 particles interacting. For ^{87}Rb, $a_0 = 101.8\, a_B$ and $a_2 = 100.4\, a_B$ where $a_B = 5.29 \times 10^{-11}$m is the Bohr radius. We can calculate the spin-dependent interaction coefficients c_0, c_2 as

$$c_0 = \frac{4\pi\hbar^2}{m}\frac{a_0 + 2a_2}{3} = 100.84 a_B \frac{4\pi\hbar^2}{m} \tag{5.1}$$

$$c_2 = \frac{4\pi\hbar^2}{m}\frac{a_2 - a_0}{3} \approx -4.7 \times 10^{-3}\, c_0 \tag{5.2}$$

For our ^{87}Rb BECs the c_0 term determines the spin-independent interaction strength, and contributes a term in the Hamiltonian that only depends on the total density of ^{87}Rb atoms. However, the c_2 term is present when the density of both $m_f = \pm 1$ atoms is non-zero at any given location in space. This spin-dependent interaction energy is weak compared to the spin-independent energy ($\approx 0.5\%$), however the sign of the spin interaction is negative. The spins gain energy when densities overlap, and is the source of

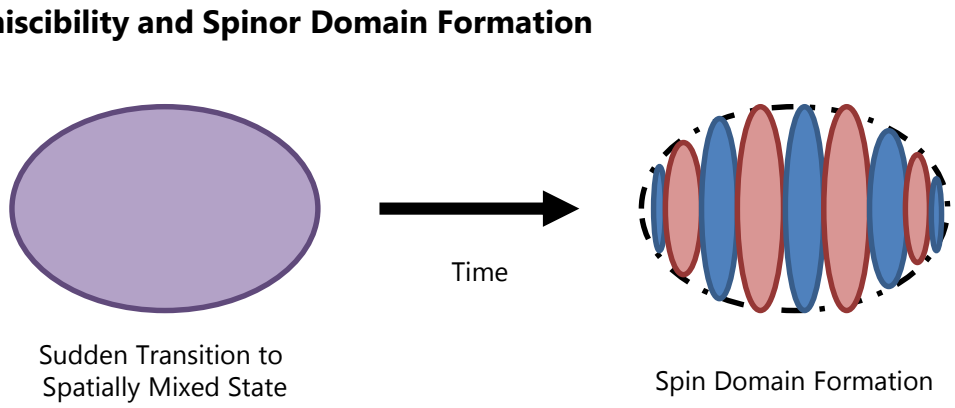

Figure 5.2: Spinor immiscibility occurs when the same-spin interaction energy is less than that of interaction with differing spins. The transition between these conditions causes the formation of spin domains, in which the opposite spins repel each other to minimize energy.

immiscibility in our system. When a spatially uniform mixture of the $m_f = \pm 1$ state is made, the c_2 term drives an interaction that is ferromagnetic, causing spin domains to form within the condensate.

5.1.2 Spinor BEC Hamiltonian

This experiment explores the time-evolving magnetization of two-component ^{87}Rb BECs in the $5S_{1/2}$ electronic ground state. Our BECs are well described in terms of a spinor wavefunction $\Psi(\mathbf{r}) = \{\psi_\uparrow(\mathbf{r}), \psi_\downarrow(\mathbf{r})\}$, where the $|\uparrow,\downarrow\rangle$ pseudo-spins label the $|f=1, m_F=\pm 1\rangle$ atomic spin states. The dynamics are governed by the spinor Gross-Pitaevskii equation (sGPE)

$$i\hbar\partial_t\psi_{\uparrow,\downarrow}(\mathbf{r}) = \Big[-\frac{\hbar^2\nabla^2}{2m} + V(\mathbf{r}) + (c_0 - c_2)\, n(\mathbf{r}) + 2c_2 N\,|\psi_{\uparrow,\downarrow}(\mathbf{r})|^2\Big]\psi_{\uparrow,\downarrow}(\mathbf{r}) + \frac{\Omega_\perp}{2}\psi_{\downarrow,\uparrow}(\mathbf{r}), \tag{5.3}$$

a continuum analog to the transverse field Ising model. $n(\mathbf{r}) = N\left[|\psi_\uparrow(\mathbf{r})|^2 + |\psi_\downarrow(\mathbf{r})|^2\right]$ is the total density; m is the atomic mass; $V(\mathbf{r})$ is a spin-independent external potential (here a harmonic potential from an optical dipole trap); $\Omega_\perp$ describes the Zeeman shift of a transverse magnetic field; and $c_{0,2}$ are the spin-independent and spin-dependent interaction coefficients [52, 53]. This Hamiltonian has a Z_2 symmetry describing a reversal of $|\uparrow\rangle$ and

$|\downarrow\rangle$, which is absent in most binary mixtures [54–57].

Because the typical $c_0 n(\mathbf{r})$ spin-independent energy vastly exceeds the $c_2 n(\mathbf{r})$ spin-dependent energy scale, we make the conventional Thomas-Fermi approximation for the overall density distribution $n(\mathbf{r})$ characterized by a chemical potential μ, and a minimum healing length $\xi = \hbar/\sqrt{2m\mu}$. This gives $n(\mathbf{r}) = [\mu - V(\mathbf{r})] \,/\, \left[c_0 + c_2 M_z^2(\mathbf{r})\right]$, which depends very weakly on the z component of the local magnetization vector, $\mathbf{M}(\mathbf{r}) = \{M_x(\mathbf{r}), M_y(\mathbf{r}), M_z(\mathbf{r})\} = \Big\{2\mathrm{Re}[\psi_\uparrow^*(\mathbf{r})\psi_\downarrow(\mathbf{r})], 2\mathrm{Im}[\psi_\uparrow^*(\mathbf{r})\psi_\downarrow(\mathbf{r})], |\psi_\uparrow(\mathbf{r})|^2 - |\psi_\downarrow(\mathbf{r})|^2\Big\}$.

The spin degrees of freedom vary almost exclusively with axial, not radial, position [58] because our extremely anisotropic condensate's $\approx$3.9 μm radial extent is comparable to the minimum spin healing length $\xi_s = \xi|c_0/c_2|^{1/2} = 3.20(4)$ μm (see Figure 5.3). Theoretically, we may describe the spin degree of freedom as a 1D spinor [59] with components $\chi_{\uparrow,\downarrow}(z) = |\chi_{\uparrow,\downarrow}(z)|\, e^{i\phi_{\uparrow,\downarrow}(z)}$; retaining terms through first order in c_2/c_0, we obtain an effective 1D sGPE

$$i\hbar\partial_t \chi_{\uparrow,\downarrow} = \left[-\frac{\hbar^2\partial_z^2}{2m} - g_{1\mathrm{D}}(z) + 2g_{1\mathrm{D}}(z)\,|\chi_{\uparrow,\downarrow}|^2\right]\chi_{\uparrow,\downarrow}. \tag{5.4}$$

The 1D interaction strength $g_{1\mathrm{D}}(z) \propto c_2$ is related to a 1D healing length $\xi_{1\mathrm{D}} \approx \sqrt{3/2}\xi_s$. These two 1D sGPE's are coupled by the local constraints $|\chi_\uparrow(z)|^2\partial_z\phi_\uparrow(z) + |\chi_\downarrow(z)|^2\partial_z\phi_\downarrow(z) = 0$ (i.e., no mass currents in our experiment). To make the analogy explicit, we dropped terms quadratic in $|\chi_{\uparrow,\downarrow}|^2$ resulting from integrating out the transverse dimensions. These repulsive terms do not affect the dynamics at short times after the quench, but must be included at long times.

5.2 Experimental Setup and Execution

In our experiment, we prepare a transversely magnetized two component spinor BEC described by a U(1) order parameter, and observe the formation and spatial expansion (coarsening) of domains following a quench into a phase with a $\mathrm{U}(1)\times\mathrm{Z}_2$ order parameter [60, 61], unexplored by previous studies with binary condensates (miscible [54, 55] or

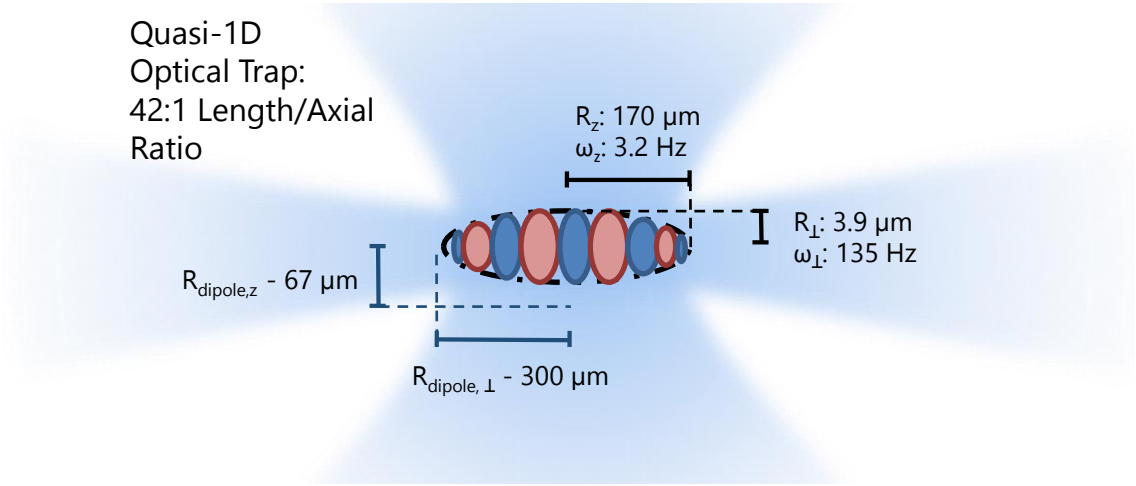

Figure 5.3: Experimental trap geometry for the spinor domains experiment. The optical trapping beams were configured to make a quasi-1D trap in order to restrict domain formation to a single direction.

immiscible [56, 57]). As compared with three component systems [58, 62–67], the relative simplicity present here allows us to identify an intriguing analogy between our spin system and a single-component *attractive* BEC as it collapses [59, 68–70].

We produce $N = 7.0(5)\times10^5$ atom ^{87}Rb BECs in the $|f=1, m_F=0\rangle$ hyperfine state, originating from cold $|f=1, m_F=-1\rangle$ thermal clouds formed in a hybrid magnetic/optical trap [71]. To initially transfer atoms to the $|f=1, m_F=0\rangle$ state from $|f=1, m_F=-1\rangle$, we applied a RF field while off of resonance and used an adiabatic rapid passage technique to transfer atoms while in the dressed RF state. These BECs are subject to a uniform magnetic field with magnitude $B_0 = 107.0(2)$ μT and are confined in the extremely anisotropic crossed optical dipole trap depicted in Figure 5.12a. Our dipole trap is formed from a pair of axially symmetric 1064 nm laser beams intersecting at right angles with $1/e^2$ radii ≈ 67 μm and ≈ 300 μm. The radial ($\mathbf{e}_r$, i.e., in the $\mathbf{e}_x - \mathbf{e}_y$ plane) and axial ($\mathbf{e}_z$) trap frequencies are $\omega_r/2\pi = 135(3)$ Hz and $\omega_z/2\pi = 3.1(2)$ Hz respectively. Our $T = 90(8)$ nK condensates have radial and axial Thomas-Fermi radii of $R_r = 3.9(1)$ μm and $R_z = 170(7)$ μm. The BECs' 170 μm axial radius is not small compared to the dipole laser's 300 μm waist along the axial direction; as a result, we expect small deviations from the conventional inverted parabola density profile, explicitly the introduction of quartic trapping terms.

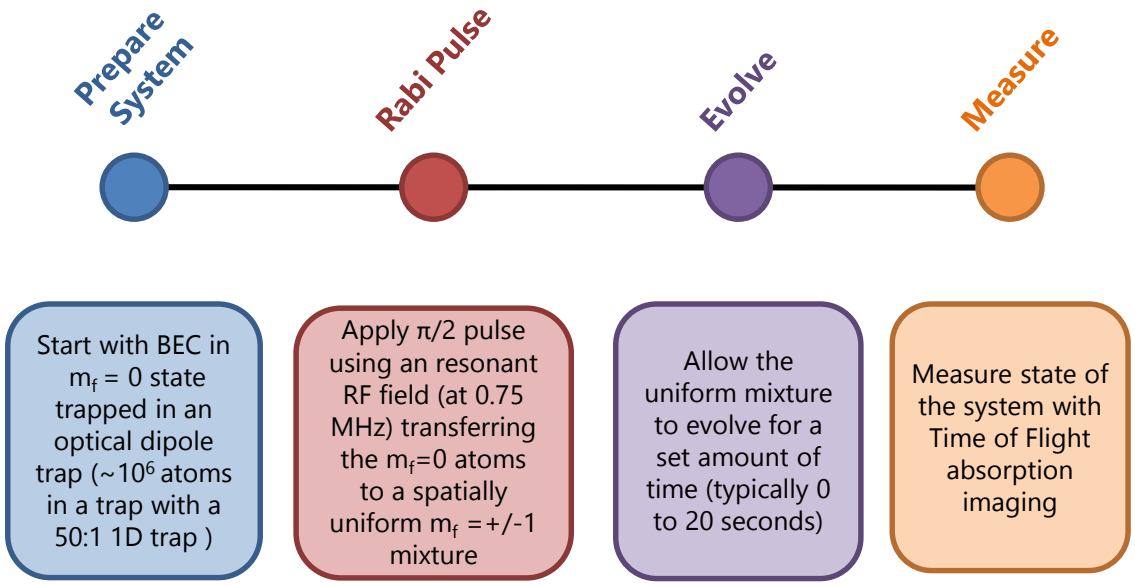

Figure 5.4: Experimental sequence used to prepare, evolve, and measure the spinor system.

The spinor experiment is initiated by a 34 μs RF-pulse that puts each atom into an equal-amplitude superposition of the $|\uparrow,\downarrow\rangle = |m_F = \pm 1\rangle$ spin states, the ground state when $\Omega_\perp$ is large; the system then evolves according to Equation 5.3 with $\Omega_\perp = 0$. This procedure is equivalent to rapidly quenching $\Omega_\perp$ to zero: the ground state goes from breaking a U(1) symmetry to breaking a *different* U(1) symmetry along with a Z_2 symmetry. While a conventional BEC breaks just a single U(1) symmetry associated with a wave function's overall phase (generated by the identity), our spinor Hamiltonian adds a U(1) symmetry associated with the relative phase of the spin (generated by the Pauli matrix $\check{\sigma}_z$), as well as a discrete Z_2 symmetry. Post quench, the formation of spin domains corresponds to breaking the Z_2 symmetry, while within a specific domain, a new U(1) symmetry is broken. This is generated by a combination of the overall and relative phases: each spin domain has a broken generator $(\check{1} \pm \check{\sigma}_z)/2$, leaving behind a "sneaky" unbroken U(1) symmetry generated by $(\check{1} \mp \check{\sigma}_z)/2$.

The quenched binary mixture is held for a variable duration t_{hold}, up to 20 s, while spin structure forms and evolves. Spin mixing collisions are suppressed because the relatively large 82 Hz quadratic Zeeman shift greatly exceeds the $c_2 n(\mathbf{r}) \approx 6$ Hz spin dependent energy [62]. As a result, we observe no population in $m_F = 0$ for the entire duration of our

experiment.

After t_{hold}, we remove the confining potential and allow the atomic ensemble to expand for 19.3 ms, during which time we Stern-Gerlach [72] separate the spin components and measure the density distributions with absorption imaging.

5.2.1 Magnetic Field Gradient Calibrations

To help remove the effects of background magnetic field gradients, which themselves can cause spin domains and spin-flow, we used an RF π-pulse (≈ 16 μs long) to rapidly (compared to the domain dynamics) flip the two populations between $m_F = \pm 1$. This pulse, when placed at the midpoint of the quench hold time, causes each spin state to experience an equal force-impulse along the gradient in both directions that effectively cancel out. This method helped to remove large scale spin separation in our BEC due to gradients while leaving the spinor dynamics, which occur at a shorter periodicity, unaffected.

Along each principal axis we also deployed three gradient shim coils - coil pairs in an anti-Helmholtz configuration - in order to compensate for background magnetic field gradients in our system. The field gradients from the ambient and coil sources were measured using time-of-flight imaging. Knowing the mass of ^{87}Rb and the duration of the time-of-flight procedure, we can measure the distance the atoms move during this time and calculate the force that the atoms felt due to the magnetic field gradient while falling.

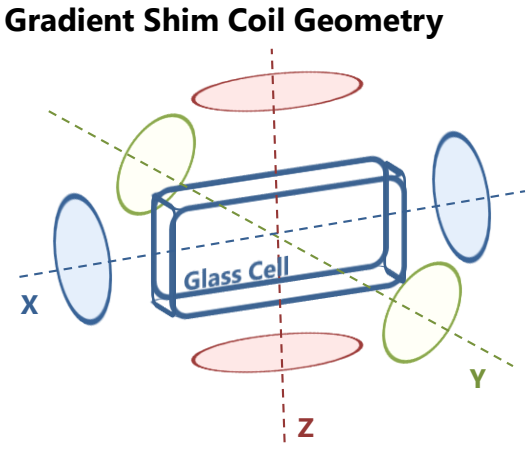

Quantization Direction	X Field Gradient (mG/cm)	Y Field Gradient (mG/cm)	Z Field Gradient (mG/cm)
+X	4.8	-1.6	-0.9
-X	-5.5	2.0	--
+Y	1.7	-4.9	0.5
-Y	1.8	3.5	--
+Z	1.2	0.5	2.9
-Z	1.3	0.5	-1.3
None	1.2	2.1	-3.2

Figure 5.5: First generation gradient shim coil geometry and the measured magnitude of background gradients at the atoms

We perform this measurement using both pure spin ±1 BECs, exploiting the symmetry between the states to increase our measurement efficiency. To determine the strength of the magnetic field gradient in a given direction, we apply a sizable biasing field (≈ 3 MHz) to provide a well defined quantization axis. By repeating this measurement over many bias field, spin state, and gradient coil configurations[1] , we can calculate the ambient magnetic field gradients, and know how to compensate correctly for them. In later experiments, these coils were disabled and were replaced with the cloverleaf coils described in Section 4.4.4.

5.3 Measurement and Reconstruction

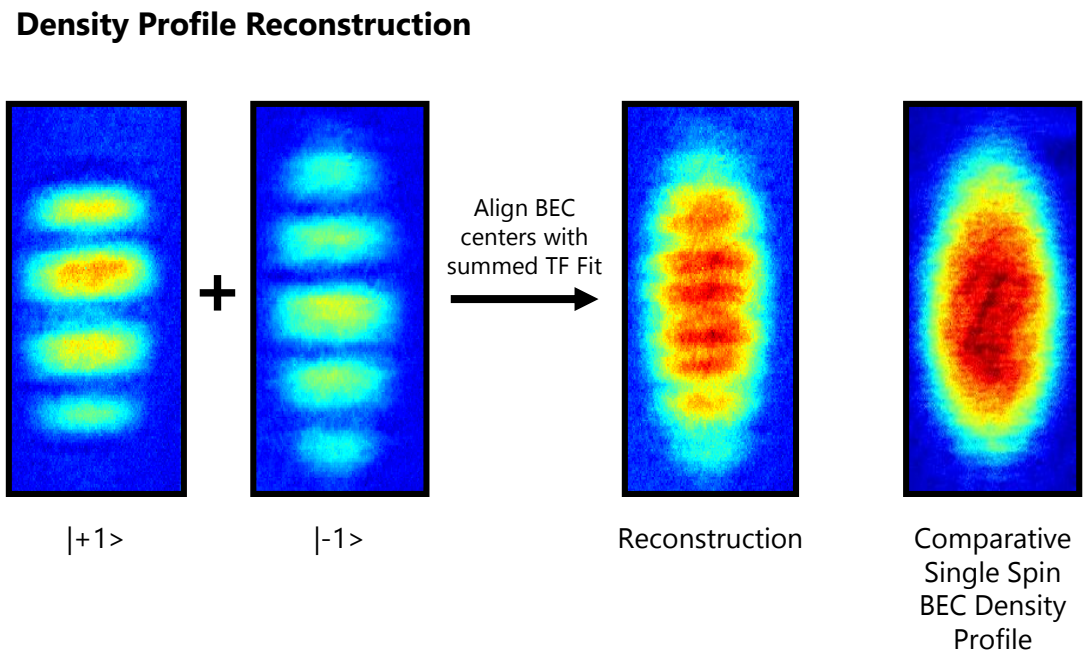

Figure 5.6: Reconstruction of the BEC density profile from the spin-separated distributions.

5.3.1 Reconstruction

We detect the resulting density distribution by absorption imaging. By using a Stern-Gerlach pulse during time of flight, we spatially separate the spin components on different regions on the image. In order to retrieve the full density distribution of the BEC, along with the fractional populations, we used a least-squared fitting approach to optimize reconstruction of the profiles into a single Thomas-Fermi profile (Figure 5.6). First, the locations of the two spin distributions was cropped into two equally sized regions of interest, with the centers of the regions being fit parameters. Next the two regions we summed together and a Thomas-Fermi fit was performed. The overlapping fit was optimized by minimizing the fit residuals of the total Thomas-Fermi profile. In addition to varying the center coordinates of the two regions, a scale factor parameter was added to resize one region versus the other. We found that our Stern-Gerlach procedure asymmetrically affected the $m_F \pm 1$ states, causing the two resulting distributions to vary in expansion size on the order of $\approx 3\%$

5.3.2 Extracting M_z and M_x Simultaneously

By obtaining the population fraction of each spin state, we were able to reconstruct both $M_x(x,z)$ and $M_z(x,z)$, projected onto the $\mathbf{e}_z - \mathbf{e}_x$ imaging plane. A brief RF pulse lasting 9.4 μs just before TOF can partially re-populate $|m_F = 0\rangle$. Following TOF expansion and Stern-Gerlach separation, the distribution of all three spin states contains sufficient information to obtain M_x and M_z simultaneously.

By knowing both the power of the RF pulse, Ω_{RF} and the pulse duration $t_{\mathrm{pulse}} = \Omega_{\mathrm{RF}}/4$, we can calculate M_z:

$$M_z = \frac{|\psi_\uparrow|^2 - |\psi_\downarrow|^2}{\cos(t_{\mathrm{pulse}}\Omega_{\mathrm{RF}})} \tag{5.5}$$

Similarly by observing the fraction of atoms that are measured in the $m_F = 0$ state, we can extract M_x simultaneously:

[1] credit to colleague Dan Campbell for doing this 'fun' task

$$M_x = \frac{|\psi_0|^2}{\sin^2(t_{\text{pulse}}\Omega_{\text{RF}})} \tag{5.6}$$

We can use these relations to reconstruct the full magnetization profile of the BEC, such as the shots in Figure 5.12.

5.3.3 Flirting with Spin-Selective Imaging

Initially in order to measure the spin domains, we used a spin-selective imaging technique to measure the population of either the $m_F = \pm 1$ spin state. Due to the absence of microwaves to selectively pulse atoms out of the $F = 1$ hyperfine ground states to the $F = 2$ manifold, we opted to try a polarization and frequency dependent method using our repump laser before absorption imaging (Figure 5.7). The idea was to create a sizable magnetic field that would, by the linear Zeeman effect, create a large energy shift between individual states in the $F = 1$ and $F' = 1$ manifolds. By also using a circularly polarized repump beam, we could further restrict the transitions that could occur. We could reverse the direction of the biasing field to switch between the spin states.

Figure 5.9 shows the imaging efficiency as a function of our repump detuning. We were able to identify peaks corresponding to the $F' = 2$ and $F' = 1$ hyperfine manifolds, measured to be 153 MHz apart, compared to the actual 156 MHz. This allowed us to

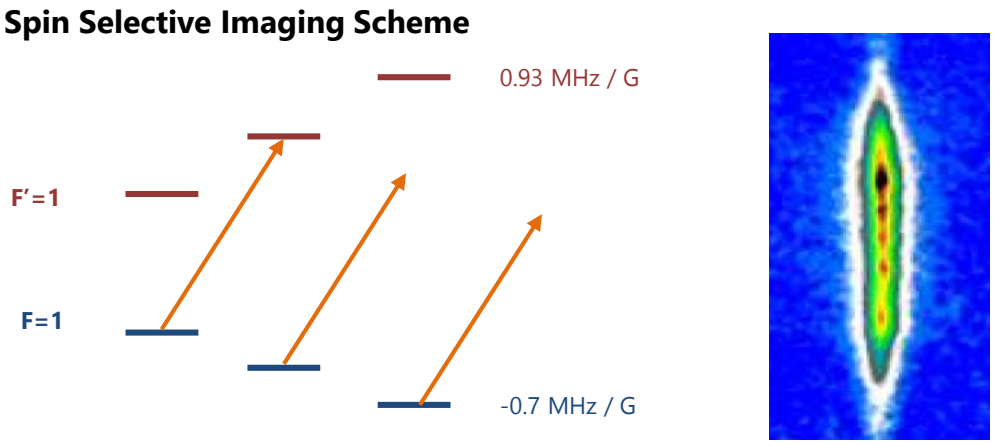

Figure 5.7: Left: Targeting atomic transitions for imaging using an offset repump laser pulse. Right: In-situ image of a spinor BEC.

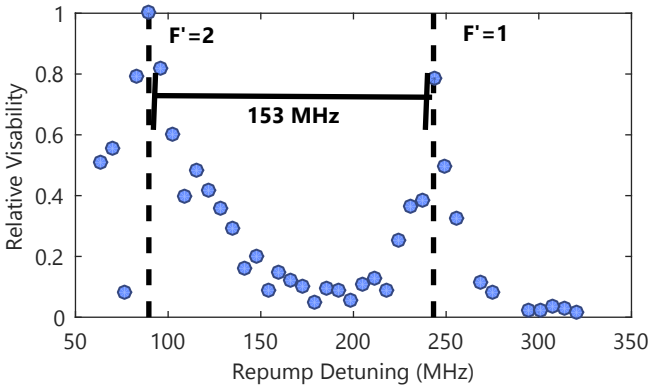

Figure 5.8: Measurement of atomic transitions for spin selective imaging by scanning the repump laser frequency

confidently set the transition to the $F' = 1$ transition.

When using this technique on a simple system with 2 large separated spin domains, we saw a contrast between the states on the order of 5 at maximum. For large domains (Figure 5.9), the contrast was sufficient to identify the spin domains. However with smaller domain size (Figure 5.7), the low contrast began to make differentiating separate domain difficult. The time of flight imaging technique clearly had an advantage in resolving small domains in the elongated BEC (for example, Figure 5.17, and with reconstruction techniques were superior. Thus the in-situ imaging work was abandoned.

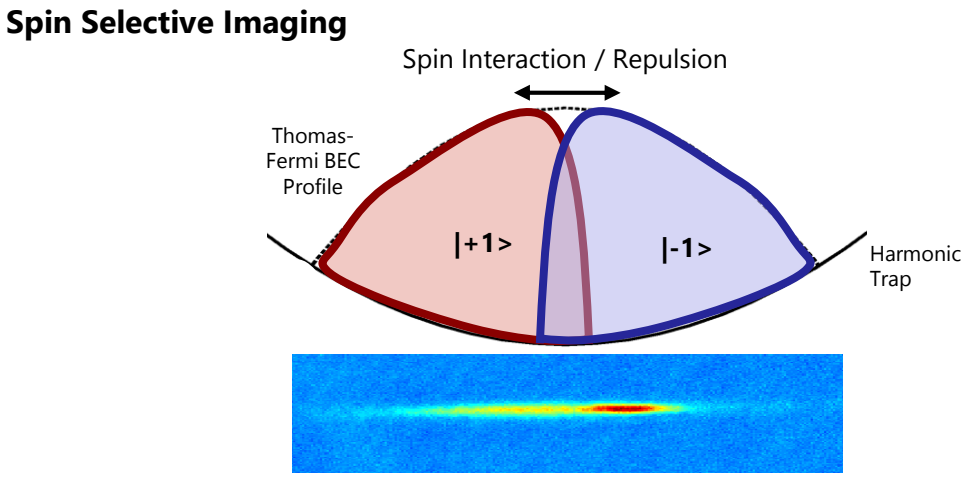

Figure 5.9: Spin-Selective imaging example illustrating the low contrast between the states.

5.3.4 Upgrade to Higher Resolution Imaging

For this experiment, we switched our primary imaging system to a higher magnification of approximately 6.25 in order to image the in-situ spinor domains. Although in the end we used time of flight measurements and reconstructed the in-situ spin densities, this higher magnification was still in place as the expanded BECs after the measurement procedure optimally fit into the imaging plane. Later this system would be switched out for an imaging solution with a magnification of 3.

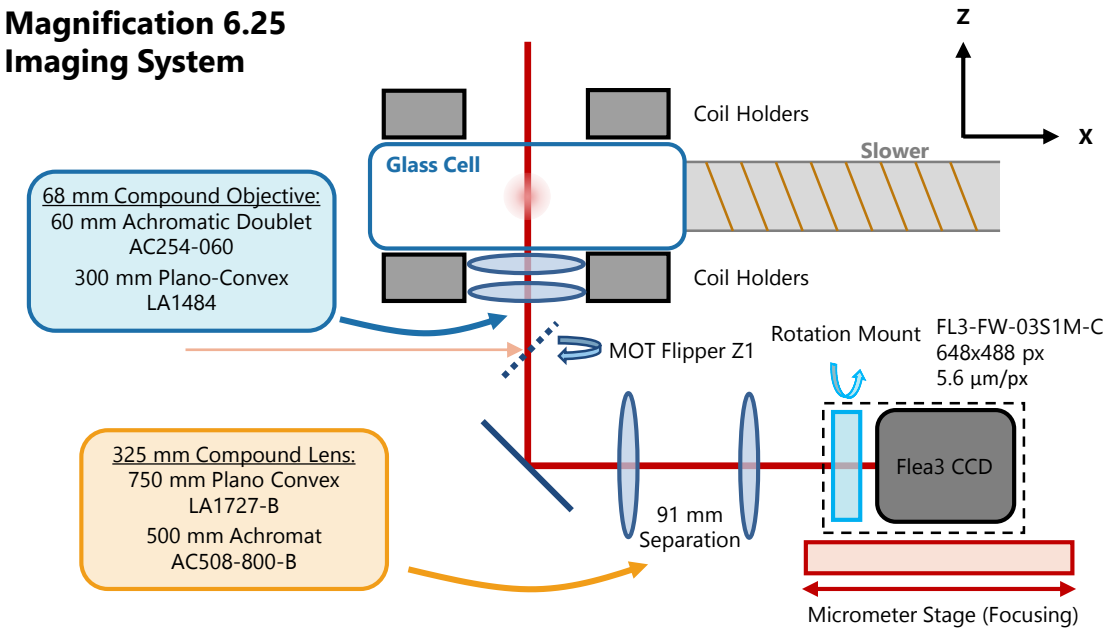

Figure 5.10: Upgraded imaging system for higher resolution imaging of the spinor domain BECs.

5.4 Results

The initially ($t_{\text{hold}} = 0$) uniform $\boldsymbol{\chi}(z) = (|\uparrow\rangle + |\downarrow\rangle)/\sqrt{2}$ spin superposition is dynamically unstable, as indicated in Figure 5.12b's snapshots. At this unstable point, small spin-wave excitations have an $(\hbar\omega/\mu_{1D})^2 = (k\xi_{1D})^2\left[(k\xi_{1D})^2 - 2\right]$ energy spectrum [67], where $\mu_{1D} = \hbar^2/2m\xi_{1D}^2$ is a typical 1D spin interaction energy. When $\hbar\omega$ is imaginary – for $k\xi_{1D} \in \left(0, \sqrt{2}\right)$ – the associated modes grow exponentially with peak gain at $k = 1/\xi_{1D}$, amplifying any existing spin fluctuations, classical or quantum. Figure 5.13 depicts the magnetization $M_z(z)$, showing the initially unmagnetized condensate developing visible structure after about 200 ms. The experimental data plotted in Figure 5.13a is in qualitative agreement with a stochastic-projective GPE (SP-GPE) simulation [73], with parameters nearly matched to our experiment, Figure 5.13b. In what follows, we make several

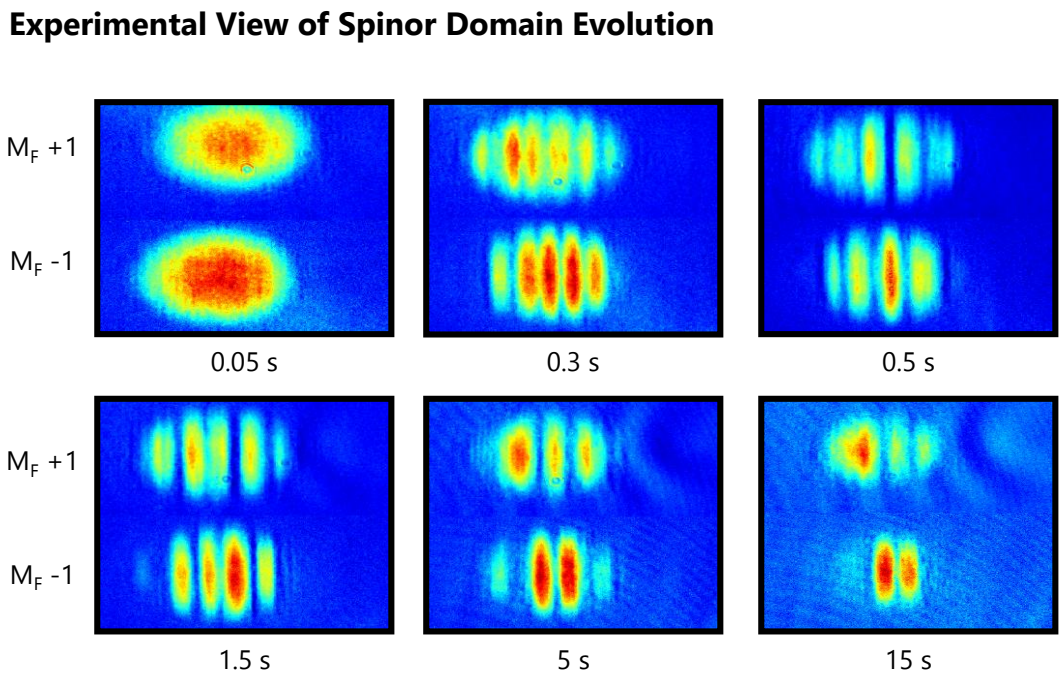

Figure 5.11: Spinor domain experimental evolution in raw images from domain onset through the coarsening stages.

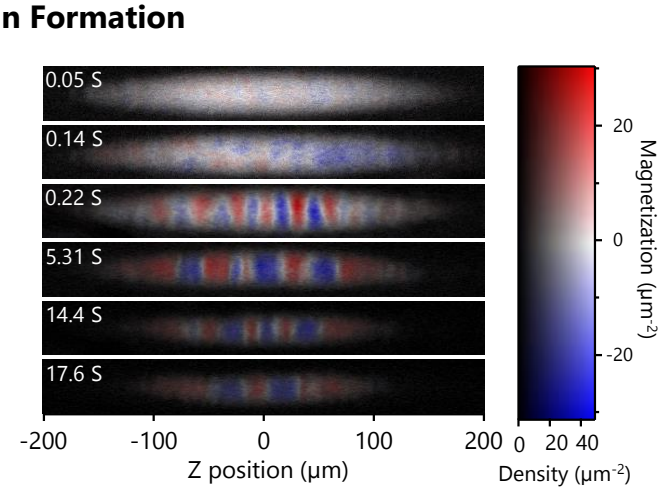

Figure 5.12: Images showing the progression from a uniformly magnetized condensate (short times) in which domains appear (intermediate times), and then grow spatially (long times). During this process the condensate slowly decays away

quantitative comparisons between the two. The SP-GPE's stochastic noise term was chosen to match the experimentally observed temperature, and was not tuned to match the onset-time for domain formation. While the amplitude of these spin waves grow with an exponential time constant $\tau(k) = 1/\mathrm{Im}(\omega(k,z))$ [minimum at $\tau(z) = 2m\xi_{1\mathrm{D}}^2(z)/\hbar \approx 42$ ms], Figure 5.13a shows that no structure is visible until $t_{\mathrm{hold}} \approx 200$ ms. Representative reconstructions of $M_z(x,y)$ at six hold times are depicted in Figure 5.12.

Our simulations predict that structure begins to grow immediately, however the domains that have formed directly after the quench cannot be detected due to the magnetization $M_z(z)$ at the beginning of the exponential formation process being smaller in magnitude than the technical noise (primarily due to shot noise in density fluctuations across the BEC) in the system. The methodology of detecting a spin domain in the BEC is based upon detecting the number of modulations in $M_z(z)$ that are larger in amplitude than the measured noise in $M_z(z)$. After the quench when the magnetization of the domains grows rapidly in amplitude, there is a threshold once domains will become statistically measurable in the analysis. This measurement effect is evident in the rapid increase of domains we experimentally detect in Figure 5.14 at ≈ 200 ms.

Figure 5.13 also shows that spin structure forms more slowly in the lower density periphery of the system where $\xi_{1\mathrm{D}}$ and τ are larger. To quantify this effect, Figure 5.14

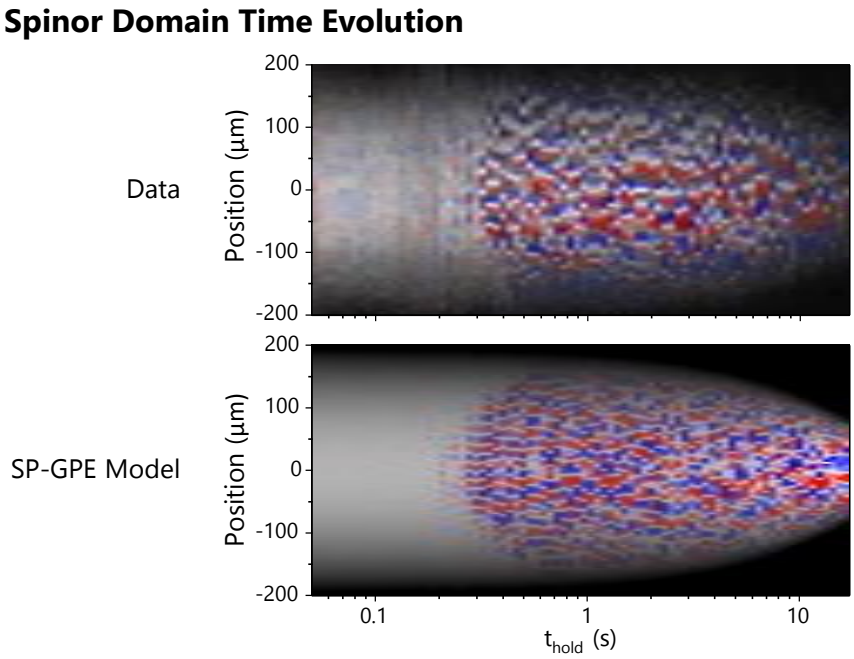

Figure 5.13: Time evolution of magnetization $M_z(z)$. (a) Experimental data and (b) finite temperature simulation using the SP-GPE method. In both simulation and experiment, the spatial structure of $M_z(z)$ coarsens after an initial growth period as domains coalesce.

plots the number of spin-regions visible above the noise, along with the results of our SP-GPE simulations, and a local density approximation (LDA, accounting for our systems inhomogeneous density profile) prediction for the expected pattern of domain growth. This number increases for short times because spin-regions become visible in the system's center before its edges, and does not initially reflect a change of their spatial size.

The spin modulations continue to grow in amplitude until, at $t_{\rm hold} \approx 300$ ms, they form fully spin polarized domains of $|\uparrow\rangle$, and $|\downarrow\rangle$, with a spacing set by the dynamic growth process, not by the system's equilibrium thermodynamics. After this period of rapid growth, the polarized spin domains evolve slowly, equilibrating, for the remaining 20 s duration of our experiment.

Our BEC has a $\tau = 10(1)$ s lifetime, implying that the domain pattern *must* evolve in time as the BEC slowly contracts. The simplest model – in which the domain pattern contracts together with the dwindling BEC (where each domain simply contracts) – is obviated by Figure 5.14, that shows the number of domains decreasing after $t_{\rm hold} \approx 1$ s. Indeed, once a domain becomes smaller than $\approx 2\xi_{\rm 1D}(z)$, it can no longer reach full spin-

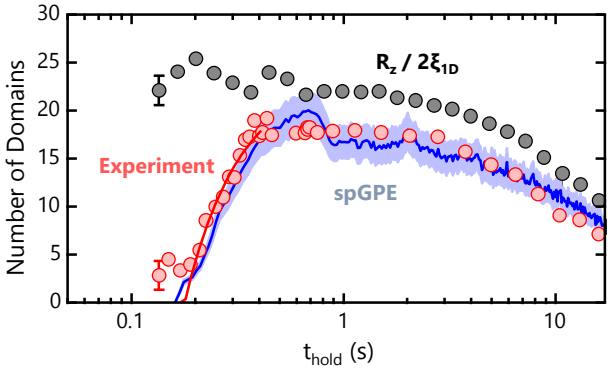

Figure 5.14: Number of domains as a function of t_{hold}. The red symbols depict the experimentally observed number of domains (typical uncertainty plotted on the leftmost point) and the blue curve plots the results of our SP-GPE simulation (uncertainties denoted by the blue band). In both cases, the uncertainties reflect the standard deviation over many realizations. In addition, the red curve fits the data to a model assuming exponential growth along with a non-zero observation threshold, in the LDA. The grey symbols correspond to the ratio $R_z/2\xi_{1\mathrm{D}}$: an estimate of domain number, assuming the system with length $2R_z$ is partitioned into domains of local size $\pi\xi_{1\mathrm{D}}(z)$ (the size at which domains initially form); the weighted average of this over our system is about $4\xi_{1\mathrm{D}}$.

polarization in its center, and it ceases to be a barrier for the hydrodynamic flow of the other spin state. As a result, small domains de-pin and can move freely until they coalesce with another domain of the same spin.

While Figure 5.13 and Figure 5.14 qualitatively suggest that the domains gradually expand as t_{hold} increases from 300 ms to 20 s, it is difficult to obtain a quantitative measure of domain size from data in this form. Indeed, the data show that while measurements at neighboring times have similar domain sizes, the exact domain pattern has a significant element of randomness – primarily in the form of phase shifts – likely resulting from subtle differences in the initial conditions, as amplified by the subsequent exponential gain process. To mitigate these effects, we turn to the power spectral density $\mathrm{PSD}_{x,z}(k) = \left|\int M_{x,z}(z)\exp(ikz)\mathrm{d}z\right|^2$ obtained from these data. With the PSD, we can compare different realizations even in the presence of spatial phase shifts of the domain structure.

Figure 5.15a shows $\mathrm{PSD}_z(k)$ derived from $M_z(z)$ shown in Figure 5.13. For short times ($t_{\mathrm{hold}} \lesssim 300$ ms), a narrow peak associated with the growing spin modulations

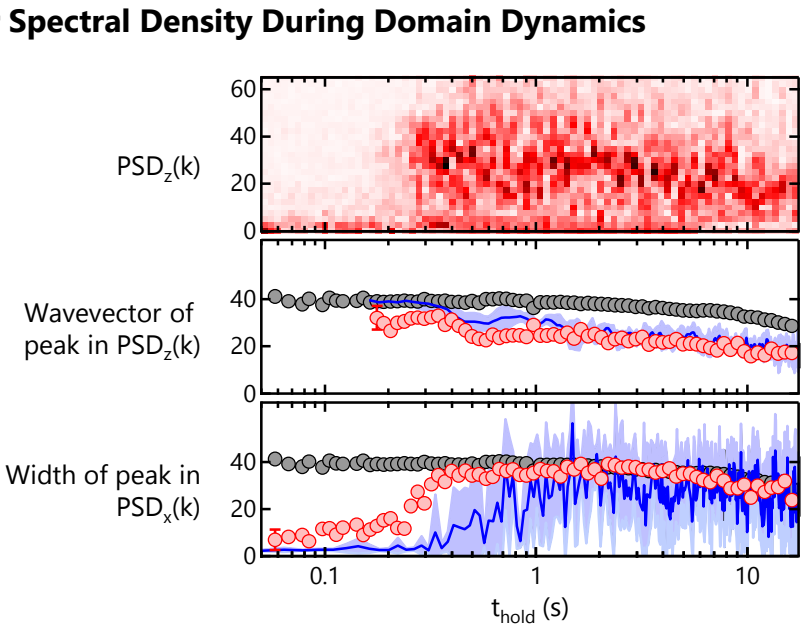

Figure 5.15: Power spectral density. (a) $\mathrm{PSD}_z(k)$ as a function of t_{hold} showing the formation of a peak at finite wave-vector k, followed by the gradual movement of that peak to smaller k as the spin domains expand. Each vertical slice represents a single experimental realization, i.e., no averaging. The color scale depicts increasing spectral power with darker color. (b) Wavevector of $\mathrm{PSD}_z(k)$'s peak. (c) Width of $\mathrm{PSD}_x(k)$, which always peaked around zero. In (b) and (c), the red symbols depict the experimentally observed peak location (typical uncertainty plotted on the leftmost point) and the blue curve plots the results of our SP-GPE simulation (uncertainties denoted by the blue band). In these three cases, the uncertainties reflect the standard deviation over eleven realizations, i.e., (b) and (c) are averaged data. The grey symbols mark $1/\xi_{1\mathrm{D}}$, the homogenous-system wave-vector of maximum gain (the uncertainties are comparable to the symbol size).

develops. Once the spin domains reach unity polarization, the magnetization's magnitude saturates and the boundaries between domains – domain walls – sharpen, broadening $\mathrm{PSD}_z(k)$ starting at $t_{\mathrm{hold}} \approx 250$ ms. At longer times, the broad peak drifts to smaller wavevectors, indicating an increasing typical domain size. Figure 5.15b compares this peak location for both experiment and theory against $1/\xi_{1\mathrm{D}}$. Figure 5.15 plots experimental data with red symbols and SP-GPE simulation with the blue curve. Our analytical model predicts maximum gain at this wave-vector and indeed our SP-GPE simulation shows peak gain at $1/\xi_{1\mathrm{D}}$. By contrast, the peak in $\mathrm{PSD}_z(k)$ for the experiment is at slightly smaller k.

Because the $\approx 2\xi_{1\mathrm{D}}(z)$ minimum domain size increases as the condensate depletes away, it is plausible that the increase in domain-size results exclusively from an increasing

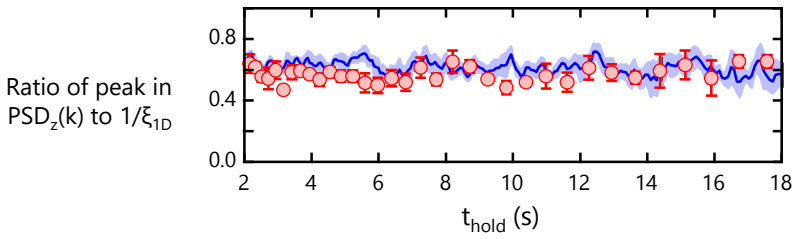

Figure 5.16: Ratio of peak in $\mathrm{PSD}_z(k)$ over $1/\xi_{1\mathrm{D}}$ plotted on a linear time scale. We use only the seven data runs that include $t_{\mathrm{hold}} > 6\,\mathrm{sec}$. The red symbols depict the experimentally observed peak location and the blue curve plots the results of our SP-GPE simulation (uncertainties denoted by the blue band).

cutoff in the minimum domain size. If we assume a proportional relationship between $1/\xi_{1\mathrm{D}}(z)$ (Figure 5.15, grey symbols) and the peak in $\mathrm{PSD}_z(k)$ such that the ratio of one over the other would hold constant we see in Figure 5.15b that for $t_{\mathrm{hold}} > 2\,\mathrm{sec}$ this theory could describe the data. To highlight this possible relationship, we display the ratio between $\mathrm{PSD}_z(k)$ and $1/\xi_{1\mathrm{D}}(z)$ – essentially constant – on a linear time scale in Figure 5.16 (the uncertainties reflect the standard deviation of the mean at each t_{hold}).

Unlike $\mathrm{PSD}_z(k)$, $\mathrm{PSD}_x(k)$ is peaked about zero; this is because $M_x(z)$ is only appreciable in the domain walls where the gas is not fully polarized: it consists of a series of narrow peaks. By showing that the width of the peak in $\mathrm{PSD}_x(k)$ tracks the inverse spin-healing length, Figure 5.15c demonstrates that the domain walls are sized according to $\xi_{1\mathrm{D}}$ (grey symbols).

For $c_2 < 0$, as in ^{87}Rb, Equation 5.3 and Equation 5.4 describe our system's spin degree of freedom as a single component attractive BEC (the overall density follows the conventional Thomas-Fermi profile). The process of domain formation is a spinor analog to the "chain of pearls" pattern that forms in 1D BECs quenched from repulsive to attractive interactions [68, 69]. In that case, the growth of structure results from a modulational instability with peak gain at $k = 1/\xi$ set by the conventional healing length. Attractive Bose systems are intrinsically unstable against collapse [70], however for spinors, any eventual collapse is stymied by an effective hard core interaction resulting from the bounded individual spin wavefunctions, and higher order interaction terms omitted from Equation

5.4.

5.4.1 Forced Counterflow

As an extra interest, we examined the effects of a system that was not only quenched from a miscible to immiscible state, but also gave the system a 'kick' to induce dynamics in the system. Contrary to the gradient cancellation schemes of Section 5.2.1, in this system we purposely introduced a gradient to cause spins to flow. In these data runs, we followed the same experimental sequence to create BECs and the immiscible system as described in Figure 5.4. However, to introduce the kick, we created a pulse on the y pair of magnetic field gradient shim coils (Figure 5.5). This pulse was shaped to be a one period long sine wave, with a period of 160 ms, and with extra terms to create a continuous derivative at the start and end of the pulse for a smooth transition. The oscillatory nature of the kick imparts momentum in both directions for both spin populations, causing the small unformed domains to slosh into one another.

The forced counterflow, as one may expect, generates more domains in the system than an unperturbed method. In Figure 5.17, the short term and long term behavior of the domains shows that the induced flow system generates more domains, but also they do not coarsen to larger domains as rapidly as the unperturbed case. When comparing the

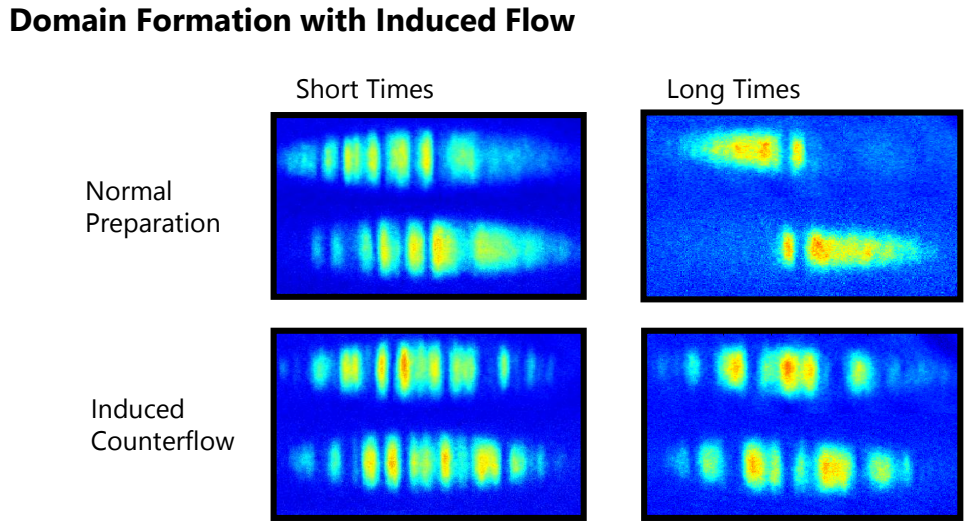

Figure 5.17: Spinor domain formation with and without induced flow

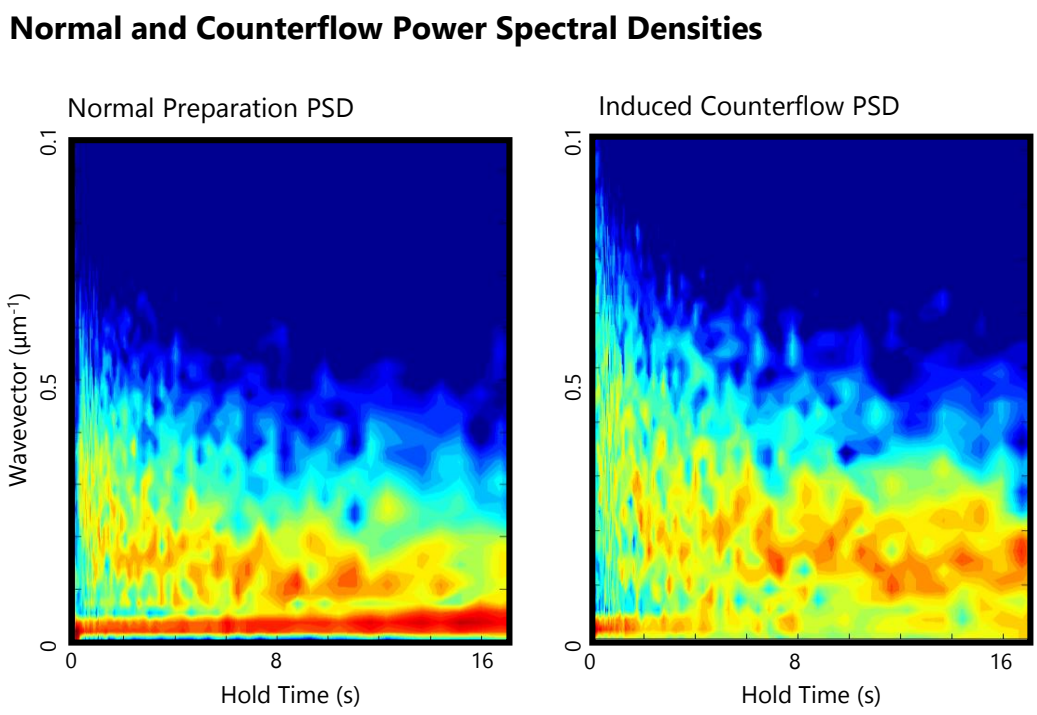

Figure 5.18: Power spectral density (PSD) of spinor domain formation with and without induced flow

power spectral density (Figure 5.18), the induced counterflow has domains that begin to appear slightly earlier than normal (≈ 50 ms), with higher spatial frequency on average, suggesting the generation of smaller, but less energetically favorable, spin domains.

5.5 Conclusion

We observe the full gamut of time scales starting with the dynamical generation of spin-domains from an initially non-equilibrium system followed by their subsequent relaxation to progressively larger domains, i.e., coarsening. However, for times > 2 sec this coarsening occurs with the only other relevant length scale: the spin healing length ξ_{1D}.

Chapter 6

Creating Artificial Gauge Fields via Optical Raman Interactions

While ultracold degenerate gas systems lend themselves well to acting as quantum simulators due to the high degree of control provided, there are many systems in physics that cannot be accessed this way due to the inherent charge neutral property of our condensates. This is problematic as many topics in physics involve electromagnetic phenomena, and hence cannot be realized in a standard degenerate gas system.

Many experiments [74–76] have exploited the equivalent mathematical form of the electromagnetic Lorentz force and the Coriolis force present in rotating systems. In these systems, rotating the condensate within a confining trap creates an energy term in the Hamiltonian analogous to a condensate of charged particles with a uniform magnetic field present[1]. These systems exhibit properties similar to other 'super' systems - superconductivity and superfluidity - namely the signature creation of quantized vortices of rotation[2]. The disadvantage of this method is that only one analogous system can be created - a uniform magnetic field. For other geometries, or to simulate an electric field, one needs to be able to engineer a more complex vector potential. A Raman coupling scheme provides this ability by using the connection between a geometric phase (a Berry's phase [77]) and the form of the vector potential in quantum mechanics [20]. Using such a Raman coupling

[1] Without the more complex issue of electromagnetic atomic interactions beyond the usual

[2] for much more detail on this topic, skip on ahead to Chapter 8

scheme, the engineering of light induced artificial electric [78] and magnetic [79] fields have been created through modifying the dispersion relation in a controllable manner.

Here I describe the basic physical principles involving Raman coupling as it forms the basic of the theory for Chapter 7 and Chapter 8. The first part of this chapter provides the framework for Raman coupling schemes and generating artificial fields, relevant for the non-uniform magnetic fields described in Chapter 8. The second half of this chapter describes our Raman coupling scheme that couples all of the $F = 1$ states of ^{87}Rb simultaneously, and forms the basis for the exploration of magnetic phases in Chapter 7.

6.1 Artificial Gauge Fields and Raman Coupling

6.1.1 Electromagnetism in Quantum Mechanics

In classical physics, the electromagnetic field is primarily described by the physical electric and magnetic fields ($\vec{\mathbf{E}}$ and $\vec{\mathbf{B}}$), mathematically represented by two vector fields in space. These fields, through the Lorentz force $F = q(\vec{\mathbf{E}} + \vec{\mathbf{v}} \times \vec{\mathbf{B}})$ for particle of charge q with velocity $\vec{\mathbf{v}}$, can describe the motion of any particle. Furthermore, the evolution of the electromagnetic fields are governed by Maxwell's equations, themselves only reliant on the electromagnetic fields.

In quantum mechanics, we typically deal with energies, not forces. To account for the electromagnetic fields, we instead use a formalism with the introduction of a scalar potential ϕ and vector potential $\vec{\mathbf{A}}$ such that: $E = \vec{\nabla}\phi - \frac{\partial \vec{\mathbf{A}}}{\partial t}$ and $\vec{\mathbf{B}} = \vec{\nabla} \times \vec{\mathbf{A}}$. The Hamiltonian for a particle in an electromagnetic field is given by:

$$\vec{\mathbf{H}} = \frac{\hbar^2}{2m}(\vec{\mathbf{p}} - q\vec{\mathbf{A}})^2 + q\phi \tag{6.1}$$

By using a Raman coupling scheme, described in the next section, we can optically induce terms in the Hamiltonian for our BECs that have the same form as Equation 6.1.

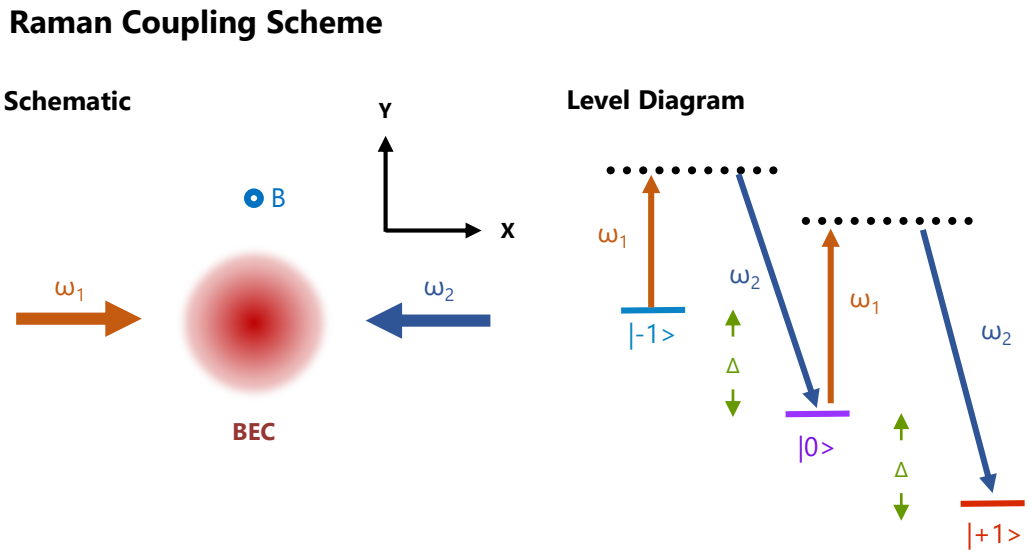

Figure 6.1: Left: Geometry of the Raman coupling scheme. Right: Raman coupling between the $F = 1$ states of ^{87}Rb.

6.1.2 Raman Coupling Scheme

In our system, we created a Raman coupled system with the following setup (see Figure 6.1). First, we create our ^{87}Rb condensate in our optical dipole trap and subject it to a biasing magnetic field along the $\hat{\mathbf{y}}$ direction, which by the linear Zeeman effect breaks the degeneracy between the ^{87}Rb $F = 1$ states, separating them by an energy[3] $\hbar\omega_Z$. We then subject the BEC to two Raman beams, with their frequency difference $\omega_1 - \omega_2 = \omega_R \approx \omega_Z$, that intersect the condensate.

Within this setup, we consider the case of two counter propagating Raman beams as in Figure 6.1. These beams have oscillation frequencies ω_0 and $\omega_0 + \Delta\omega$ where $\omega_0 \gg \Delta\omega$. Given the geometry, the electric fields produced by the two laser beams can be written as:

$$\vec{\mathbf{E}}_1 = E_1 \hat{\mathbf{e}}_\mathbf{i} \exp(i(kx - \omega_0 t)) \tag{6.2}$$

$$\vec{\mathbf{E}}_2 = E_2 \hat{\mathbf{e}}_\mathbf{j} \exp(i(-kx - \omega_0 t - \Delta\omega t)) \tag{6.3}$$

Where E_1, E_2 are the field amplitudes, $k = 2\pi/\lambda_R$ is the wavevector and $\hat{\mathbf{e}}_i$, $\hat{\mathbf{e}}_j$ are the

[3] I am assuming the quadratic Zeeman effect is negligibly small for now

polarizations of the two laser beams. It follows through the principle of superposition that the total field seen by the atoms is the sum of the two fields:

$$\vec{\mathbf{E}} = \exp(-i\omega_0 t)\{E_1\hat{\mathbf{e}_\mathbf{i}}\exp(ikx) + E_2\hat{\mathbf{e}_\mathbf{j}}\exp(-ikx - i\Delta\omega t)\} \tag{6.4}$$

We are interested in the vector light shift $\vec{\mathbf{E}}^* \times \vec{\mathbf{E}}$ of the total electric field. The vector light shift term is proportional to an effective magnetic field $\hat{\mathbf{B}}_{\text{eff}} \propto \vec{\mathbf{E}}^* \times \vec{\mathbf{E}}$ which then interacts with the atoms according to $-\vec{\mu} \cdot \hat{\mathbf{B}}_{\text{eff}} = -g_f m_F \hbar \hat{\mathbf{F}} \cdot \hat{\mathbf{B}}_{\text{eff}}$ with g_f being the gyromagnetic ratio, m_F being a particular spin state (note the spin dependence, hence the 'vector' nature of the interaction) and $\hat{\mathbf{F}}$ being the spin-1 spin projection operator [80]. We compute this and find

$$\vec{\mathbf{E}}^* \times \vec{\mathbf{E}} = 2E_1E_2(\hat{\mathbf{e}_\mathbf{i}} \times \hat{\mathbf{e}_\mathbf{j}})\cos(2kx + \Delta\omega t) \tag{6.5}$$

Giving an interaction term:

$$\hat{\mathbf{H}}_{\text{Raman}} = -2g_f m_F \hbar E_1 E_2(\hat{\mathbf{e}_\mathbf{i}} \times \hat{\mathbf{e}_\mathbf{j}}) \cdot \hat{\mathbf{F}}\cos(2kx + \Delta\omega t) \tag{6.6}$$

If we set the polarizations $\hat{\mathbf{e}}_i$, $\hat{\mathbf{e}}_j$ equal to $\hat{\mathbf{y}}$, $\hat{\mathbf{z}}$, then we get a projection of the interaction with the $\hat{\mathbf{F}}_x$ operator:

$$\hat{\mathbf{H}}_{\text{Raman}} = -2g_f m_F \hbar E_1 E_2 \hat{\mathbf{F}}_x \sin(2kx + \Delta\omega t) \tag{6.7}$$

If we scrunch numerical coefficients into an interaction strength Ω_{R}, we get:

$$\hat{\mathbf{H}}_{\text{Raman}} = \frac{\hbar\Omega_{\text{R}}}{\sqrt{2}}\cos(2kx + \Delta\omega t)\hat{\mathbf{F}}_x \tag{6.8}$$

6.1.3 The Raman Coupled Hamiltonian

Using the result in Equation 6.8, we make a transformation into the rotating frame at $\Delta\omega$ and into the momentum basis. Due to the non-commutative position and momentum terms in the Raman coupling Hamiltonian, we get a Hamiltonian which has a spin-dependent momentum offset:

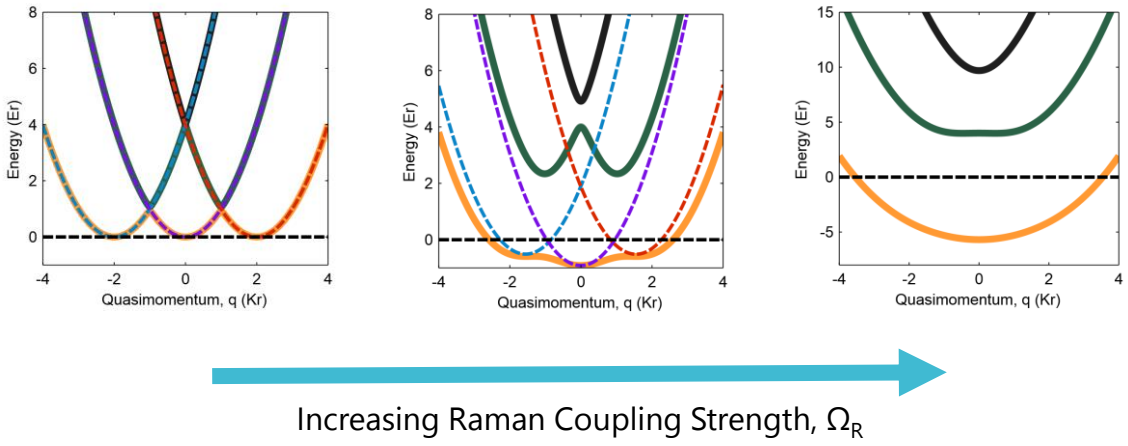

Figure 6.2: The effect of Raman coupling on the atomic dispersions. As the coupling strength Ω_{R} is increased, the eigenenergies of the system form a band structure owing to avoided crossing in the system.

$$\hat{\mathbf{H}}_{\mathrm{Raman}} = \begin{pmatrix} \frac{\hbar^2}{2m}(p-2k)^2 - \delta & \Omega_R/\sqrt{2} & 0 \\ \Omega_R/\sqrt{2} & \frac{\hbar^2 p^2}{2m} + \hbar\epsilon & \Omega_R/\sqrt{2} \\ 0 & \Omega_R/\sqrt{2} & \frac{\hbar^2}{2m}(p+2k)^2 + \delta \end{pmatrix} \tag{6.9}$$

Where the terms δ and ϵ are the Raman detuning from resonance and the quadratic Zeeman shift (Section 3.1.1) respectively. We define the characteristic energy of the system in terms of the recoil energy $E_L = \hbar^2 k_L^2/2m$ and the recoil momentum $K_L = 2\pi/\lambda_R$.

Here I focus on the transformation of the kinetic energy in the $\hat{\mathbf{x}}$ direction (the Raman direction defined by the polarizations of the Raman beams) as the $\hat{\mathbf{y}}$ and $\hat{\mathbf{z}}$ directions are unchanged. The Raman interaction Hamiltonian in Equation 6.9 governs the physics behind Chapter 7 and Chapter 8.

The eigenstates for the Raman Hamiltonian consist of three separated energy-momentum dispersion bands (Figure 6.2) that arise from the avoided crossing of the offset bare state dispersions ($\hbar^2(k \pm 2)^2/2m$, dashed curves in Figure 6.2) as Ω_{R} is increased. For the experiments presented within the rest of this thesis, I am only concerned with the lowest energy band of the Raman Hamiltonian - we make the good assumption here that we load atoms adiabatically into the lowest band (ground state) and they like to stay there.

6.1.4 The Scalar and Vector Light Shifts

For our Raman processes, we want the two-photon transition caused by the two laser beams to be off resonance. However, when operating at a wavelength away from resonance, we must contend with other effects. From the arguments in Section 3.4 about optical trapping, an optical field applied to an atomic system will cause a shift in the energy levels of the system. Here we refer to this field as the scalar light shift, or scalar polarizabilty. This effect is highly undesirable in our system as the presence of the Raman beams will affect the trap geometry, and any alignment drifts will move the trapping potential as well[4]. For the scalar light shift, as in Equation 3.28, in the limit of large detuning from resonance the light shift goes as:

$$\Delta V_{light} \propto \frac{\Omega^2}{\delta} \tag{6.10}$$

Where Ω, as usual, is the Rabi frequency proportional to the intensity of the light, and δ is the detuning.

In a hand-waving argument, we can say then that for blue shifted light ($\delta > 0$) the field will raise the energy of the system making an anti-trap, and for red-shifted light ($\delta < 0$) we get an attractive trapping potential. Consider the case where we have two resonances in the system, in our case the ^{87}Rb D1 and D2 lines. For frequencies of light that are in between the two resonances, there is both an effective trapping and anti-trapping potential. Some form of the intermediate value theorem then says that there must be a frequency in between these two resonances such that their effect cancels, leaving no energy shift. We call this frequency the *magic wavelength* [81, 82], and in ^{87}Rb, $\lambda_{\text{magic}} = 790.024$ nm. For this reason, our Raman laser is set (but not locked) to 790.024 nm when we perform experiments.

For systems where $\vec{\mathbf{E}}^* \times \vec{\mathbf{E}}$ is non-zero, we also are concerned with the vector light shift, which shifts the different Zeeman sublevels with different energies. I measured this effect in the lab by measuring the shift in an RF resonance when only one of the Raman beams is present in the sample. By scanning for resonance with no beams on, and each of

[4]This can be used as an alignment technique when setting $\lambda_R \neq 790$ nm and moving the condensate with the Raman beams

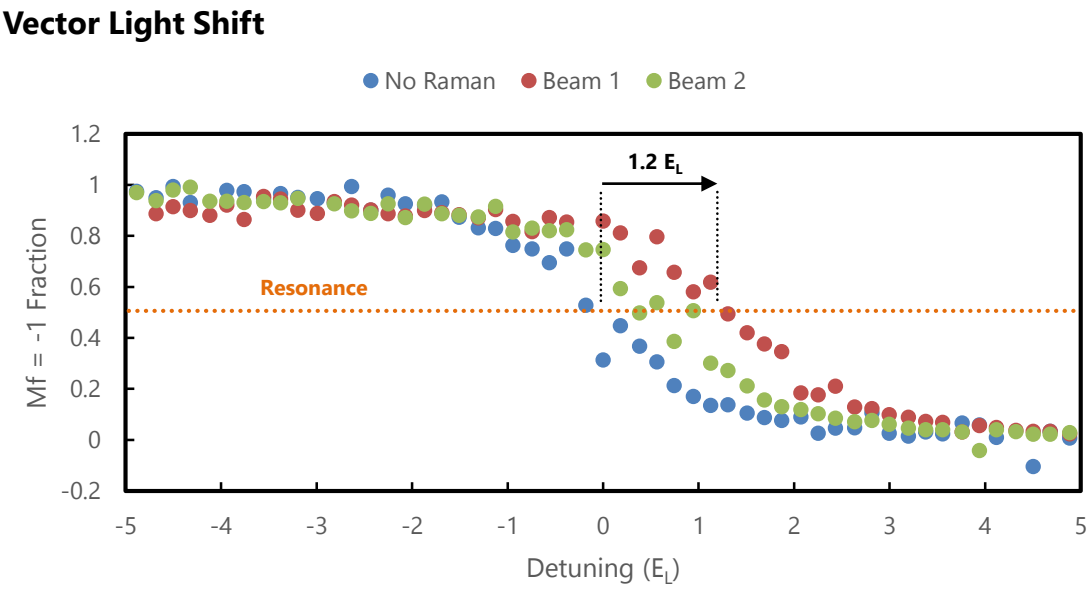

Figure 6.3: Shift in resonance due to the vector light shift. The resonance was first measured with no Raman beams present (blue) and the presence of a Raman beam, one at a time, shifted the resonance, signifying a state-dependent energy shift.

the two Raman beams on, we can visually see the shifting resonance in Figure 6.3. Here the measure of resonance is related to measuring the relative fractions of atoms in the $m_F = -1, 0$ states, as described in Section 4.4.7.

Polarization of the Raman beams strongly influences the magnitude of the vector light shift. While holding the system at resonance, one beam at a time was sent toward the atoms while a $\lambda/4$ waveplate was rotated, therefore adjusting the polarization of the Raman beam. The data in Figure 6.4 show that the atomic resonance of the system changes on the order of the recoil energy E_L as the polarization changes. This measurement can help optimize the polarization in the beams at the atoms, including any effects of the Raman beams traversing the glass experiment cell.

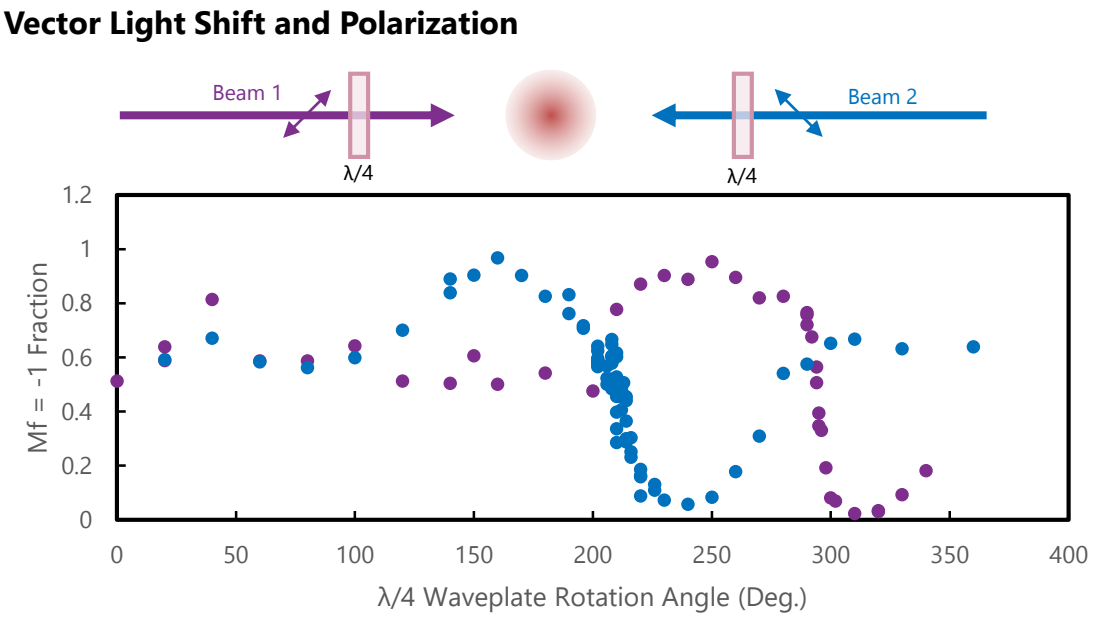

Figure 6.4: Measurement of the vector light shift effect on atomic resonance as a function of the polarization in each Raman beam. A $\lambda/4$ waveplate on each Raman beam was rotated through 360°, and the resonance shift measured.

6.1.5 Synthetic Magnetic and Electric Fields From Raman Coupling

Definition of the Synthetic Vector Potential A_x

Once the atoms are adiabatically loaded into the Raman dressed state, their dispersion is defined by the curvature of the lowest band. In general, we describe this dispersion engineering by:

$$E(k_x) = \frac{\hbar^2(k_x - A_x(\Omega_\mathrm{R}, \delta))^2}{2m^*(\Omega_\mathrm{R}, \delta)} \tag{6.11}$$

Where $A_x/\hbar = k_\mathrm{min}$, the momentum corresponding to the lowest energy possible, and $m*$ is the effective mass, which is to account for the correction of the dispersion curvature compared to the parabolic free-particle dispersion. Figure 6.5 shows how the value of the vector potential is determined in the dispersion curve.

It is important to note that the properties of the Raman dispersion, A_x and $m*$, can be adjusted directly via the Raman coupling strength Ω_R and the detuning δ. The detuning plays a large role in shaping the dispersion, as the detuning can break the

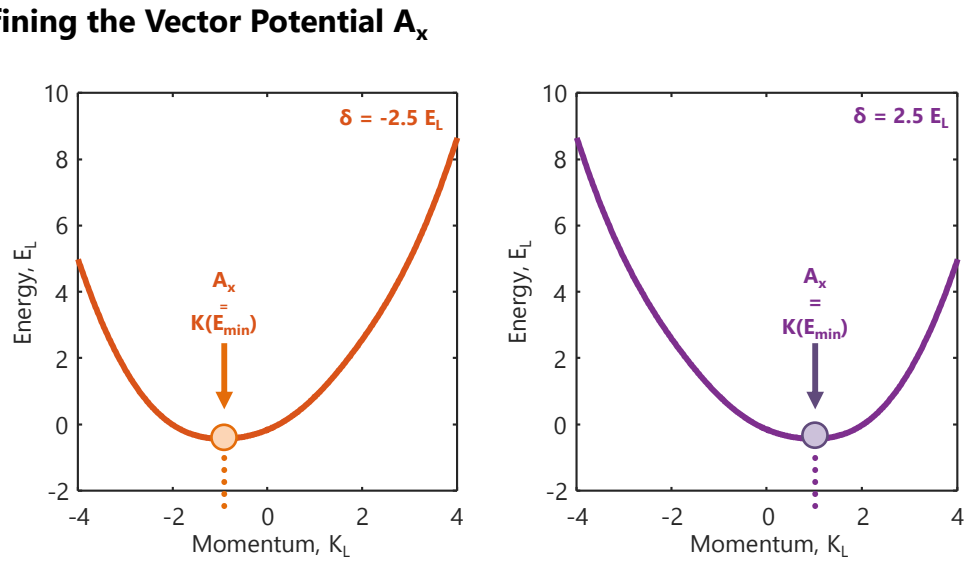

Figure 6.5: The definition of the Vector Potential A_x is given by the momentum value associated with the minimum energy in the Raman dispersion. The change of the vector potential as a function of the detuning δ from resonance is shown at negative values (left) and positive values (right).

symmetry of the $m_F = \pm 1$ states, causing a preference for one state, and accordingly shifting A_x as well. Figure 6.6 shows how the dispersions change as a function of δ. As the detuning from resonance is increased, the dispersion curve will 'tilt' in such a way that the minimum in the momentum dispersion (defined as A_x above) is no longer zero (shown by the solid light-blue curve). Furthermore, as the detuning is increased, the zero energy of the dispersion will decrease as well.

If we measure the vector potential as a function of detuning, we get the relationship shown in Figure 6.7. For large values of δ, the vector potential A_x will asymptote to $\pm 2k_{\mathrm{L}}$.

Creating Synthetic Magnetic Fields

In the context of vector potentials, the magnetic field $\vec{\mathbf{B}}$ is defined as $\vec{\mathbf{B}} = \vec{\nabla} \times \vec{\mathbf{A}}$. Previously we applied a real magnetic field (a constant biasing field)[5] of $B_0\hat{\mathbf{y}}$ as described in Section 6.1.2, which for our spatially uniform one-dimensional vector potential A_x, $\frac{\partial A}{\partial x_i} = B_{\mathrm{eff}} = 0$. However if we apply a real magnetic field profile of $B(y) = B_0 + B'y$, a linearly dependent field strength along the $\hat{\mathbf{y}}$ direction, this will create a linearly depen-

[5] We purposely balance the biasing Zeeman field such that at the center of the BEC, $\delta_0 = 0$

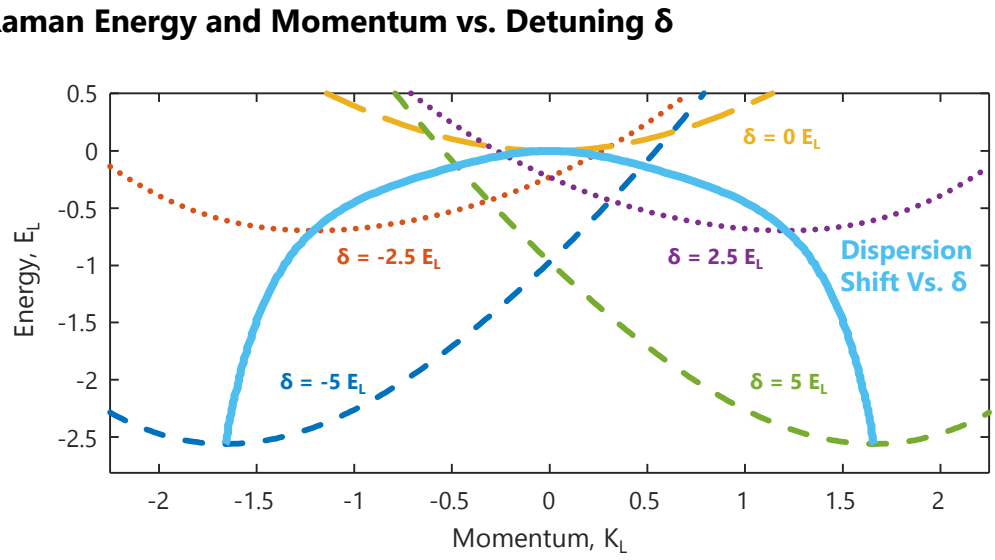

Figure 6.6: The detuning δ in the Raman system shifts the location of the minima in momentum (the value of the vector potential A_x) and provides a negative scalar energy shift. Dashed curves show the Raman dispersion at various detunings. The solid light blue curve shows a continuous trajectory of the minimum energy and the associated momentum as a function of detuning. This example is at $\Omega_{\mathrm{R}} = 5E_{\mathrm{L}}$

dent detuning $\delta(y) = \delta_0 + \delta'(y)$. From looking at Figure 6.7 and Equation 6.11, we note that the vector potential now becomes a function of y as well: $A_x(y)$. In this case the term $B_{\mathrm{eff}} = \frac{\partial A}{\partial y} \neq 0$, yielding an effective magnetic force on the atoms. For calculations of

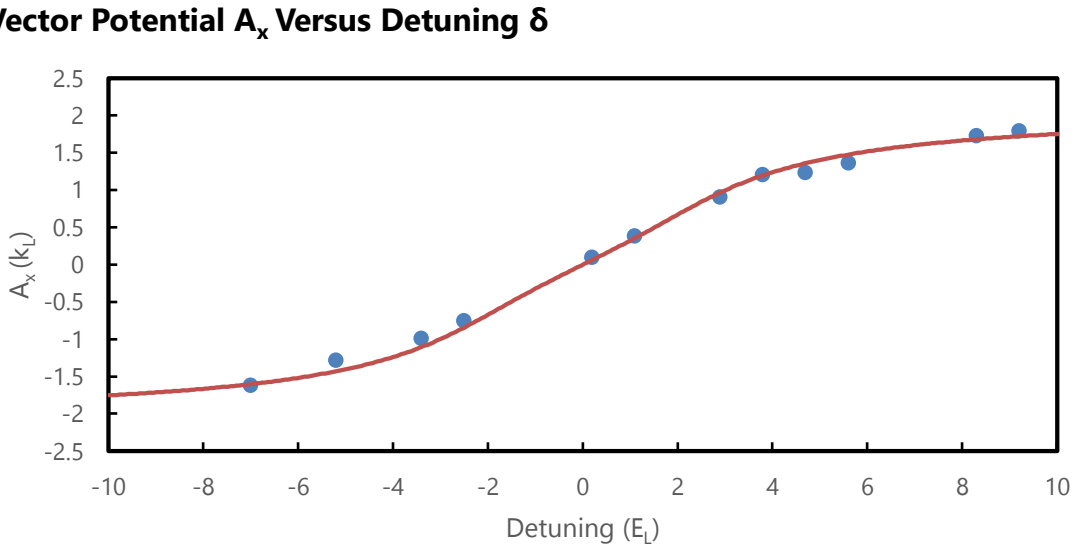

Figure 6.7: Calculation and measurement of the vector potential as a function of detuning at $\Omega_{\mathrm{R}} = 7E_{\mathrm{L}}$. A_x asymptotes to $\pm 2k_{\mathrm{R}}$ for large Ω_{R}.

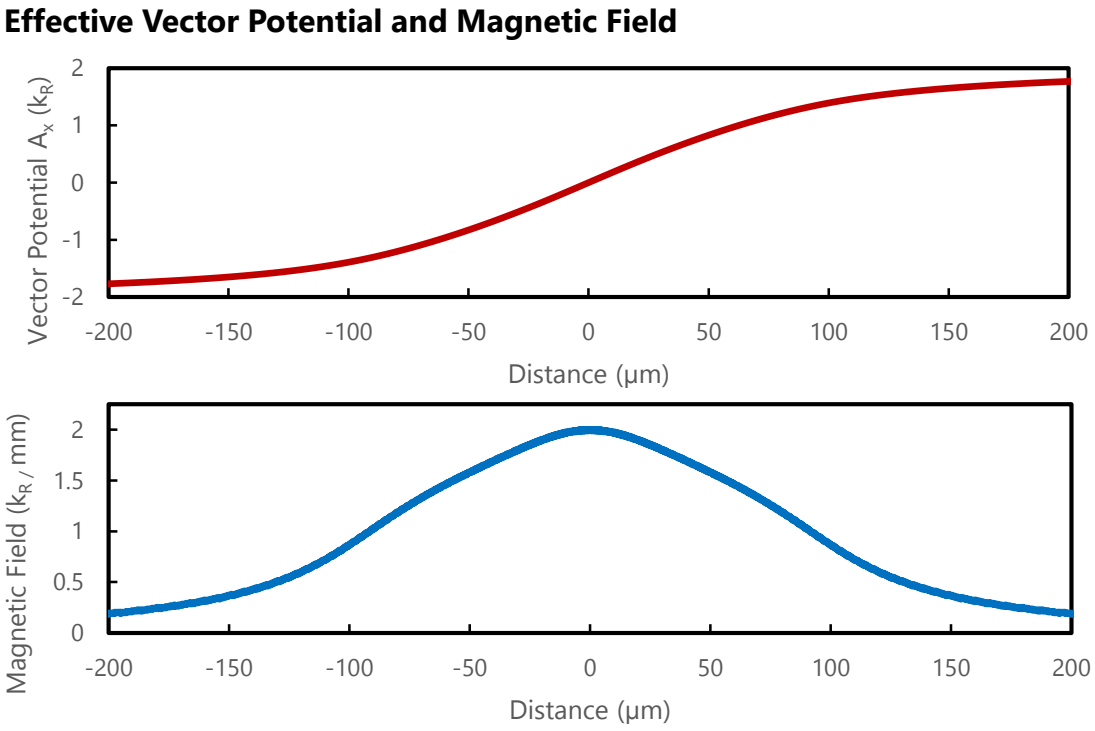

Figure 6.8: For a spatially dependent vector potential $A_x(y)$ (created by a real magnetic field gradient), there exists a non-zero effective magnetic field. Example at at $\Omega_{\mathrm{R}} = 7E_{\mathrm{L}}$.

magnetic field strength, we define the effective "charge" of atoms to be that of the electron charge e.

For schemes with $\Omega_{\mathrm{R}} > 4E_L$ (a single dispersion minima) and $\delta' > 0$, this yields a quasi-linear region near $y = 0$, giving a B_{eff} that is constant. If Ω_{R} and δ' are tuned such that the majority of the condensate is within this region of constant magnetic field, the system becomes equivalent to the original rotating trap experiments that first created vortex lattices in BECs [74–76]. The physics of this system is extended further to examine the effects of non-uniform fields across the condensate in Chapter 8, and the consequences on vortex nucleation when crossing a transition between a non-uniform to uniform field configuration.

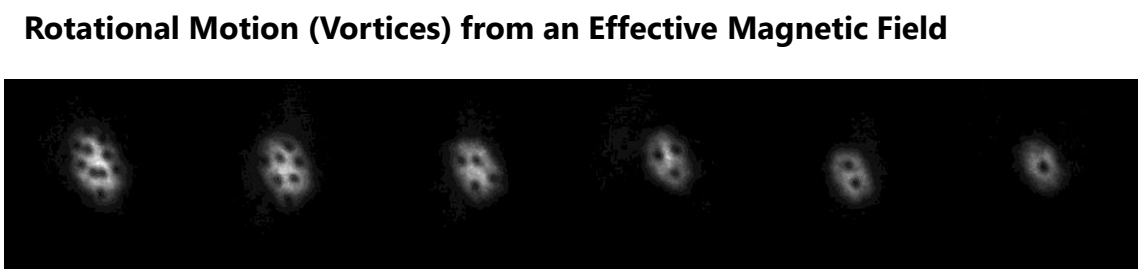

Figure 6.9: Observed vortex formation in a BEC subject to a synthetic magnetic field. A uniform synthetic field induces a Lorentz force to the 'charged' particles, causing cyclotron (rotational) motion

Creating Synthetic Electric Fields

The electric force is related to the rate in which the vector potential changes in time, that is: $\vec{\mathbf{E}} = \frac{\partial A}{\partial t}$. This effect has been previously studied [78], and here I want to point out our application of the synthetic electric field in the experimental apparatus. Because the value of A_x depends on Ω_{R}, it follows that a time dependent change in Ω_{R}, effectively the intensity of the Raman laser beams, will cause a synthetic electric field. We commonly need to increase the Raman coupling in slow ramp ups to avoid large momentum transfers via the electric effect. We also use the electric field to our advantage when doing TOF imaging. When we release the condensate from the optical dipole trap before imaging, we also suddenly switch off the Raman beams. The rapid change imparts momentum to the different components (spin and momentum) of the condensate, which after the TOF free-fall, have become spatially separated. This separation is what allows us to measure the momentum states of the BEC (see Section 6.1.6).

6.1.6 Measuring Raman Coupled Systems in TOF

To measure the spin in momentum states of the condensates, we have two methods available, a snap-off method and an adiabatic deloading method.

The snap-off method is a projection of the Raman dressed state into the bare spin-momentum basis. In this method we turn off the Raman coupling instantly at the start of TOF (hence the snap-off name) and allow the atoms to free-fall. The projection to the bare states will cause the states with differing momentum to be spatially displaced

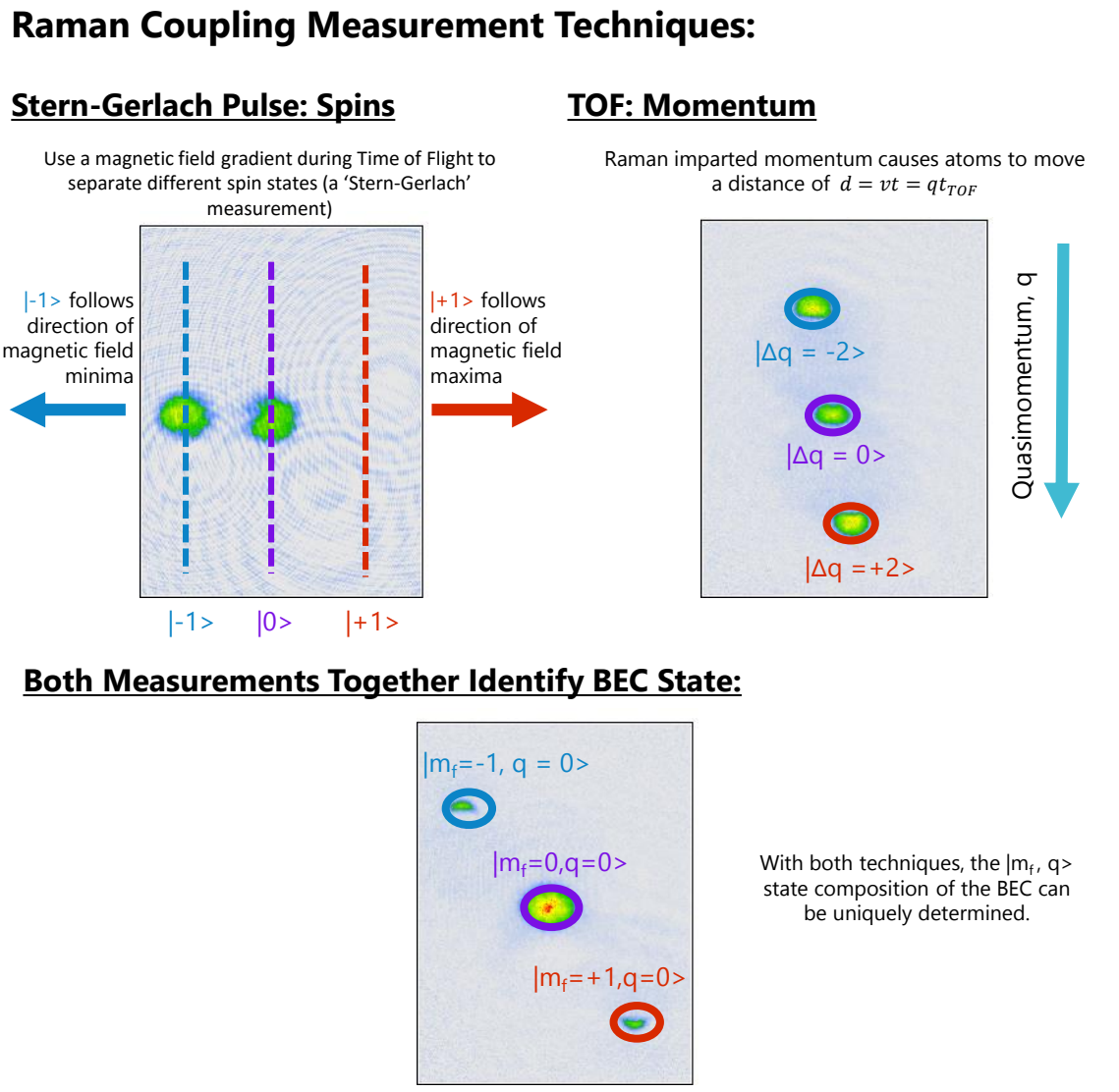

Figure 6.10: Measurement of Raman coupled system after time-of-flight (TOF).

after having time to expand (this is essentially the argument of TOF being a mapping of momentum to position space in Section 2.3.1). To resolve the spin components, we apply a Stern-Gerlach pulse that separates the spin components on the imaging axis orthogonal to the momentum direction. This method allows us to image all $|m_F, k\rangle$ states of the BEC.

In the first 2 ms of TOF we decrease Ω_R adiabatically to 0 while simultaneously ramping the detuning $\delta \gg E_L$ from resonance. This process maps the laser-dressed system into a single spin-momentum state BEC [83], and in addition imparts a position-

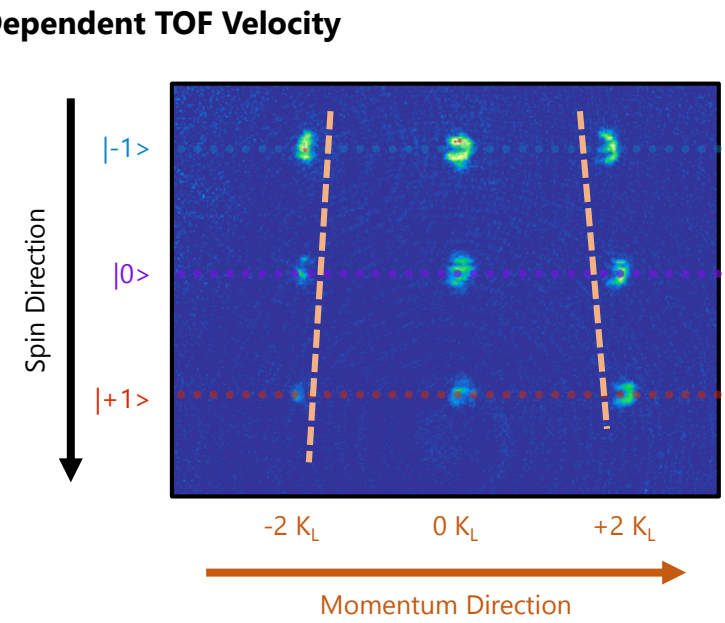

Figure 6.11: Projection of each $|m_F, k_\mathrm{L}\rangle$ state on the camera. The spins travel in different amounts along the Raman coupling momentum direction.

dependent artificial electric field as A becomes constant, inducing an overall shearing motion. This method works well for measuring the composition of the Raman eigenstates, or for observing structure such as vortices.

Calibrating the Raman Coupling Measurements

We found in our system that when performing snap-off style imaging, we saw that the $m_F = \pm 1$ states traveled asymmetrically during TOF. This effect, owing most likely to small background magnetic field gradients present during TOF, needs to be accounted for when doing experiments that measure the momentum state of the BEC as a function of position on the camera. To calibrate the spin and momentum states on the camera, we first prepared the system with an equal mixture of the m_F states using an RF pulse, then pulsed the Raman coupling briefly to populate momentum states at $-2, 0, +2\ k_\mathrm{L}$. This method produces a small population of atoms in all states, which can be measured simultaneously (Figure 6.11). By letting the apparatus run taking many shots like in Figure 6.11, we can gather a statistical measure of the location of each $|m_F, k_\mathrm{L}\rangle$ state on the camera along with uncertainties.

6.2 Raman Coupling in a Spin-1 System

In the limit of low biasing fields, such that $\epsilon_q < \Omega_{\mathrm{R}}$ (ϵ_q is the quadratic Zeeman shift, Section 3.1.1), the coupling scheme in Section 6.1.3 can address all of the m_F states equally, allowing full control of the $F = 1$ ground state. However, as biasing field strength increases, so as to have the energy gap between the states larger, ϵ_q will increase to where $\epsilon_q > \Omega_{\mathrm{R}}$ for all experimentally obtainable values of Ω_{R}. Previous experiments [84] with artificial gauge fields were performed in pseudo spin 1/2 systems where either the $m_F = -1$ or $m_F = +1$ state is detuned far away to where the Raman coupling only addresses a transition from one of the $m_F = \pm 1$ states to $m_F = 0$, using this single spin coupling as an advantage.

We developed a scheme that Raman couples all of the $F = 1$ states in ^{87}Rb together for an arbitrary strength biasing field, providing spin-1 spin-orbit coupling in all situations. To do this, we have two counter-propagating Raman beams with frequencies ω_1 and ω_2 intersecting the BEC as previously. However we now put a second frequency onto one of the beams such that there is a super position of ω_2 and ω_3 frequencies. In this scheme, the ω_2 frequency address the $m_F = -1$ to $m_F = 0$ transition and ω_3 frequency address the $m_F = +1$ to $m_F = 0$ transition (Figure 6.12).

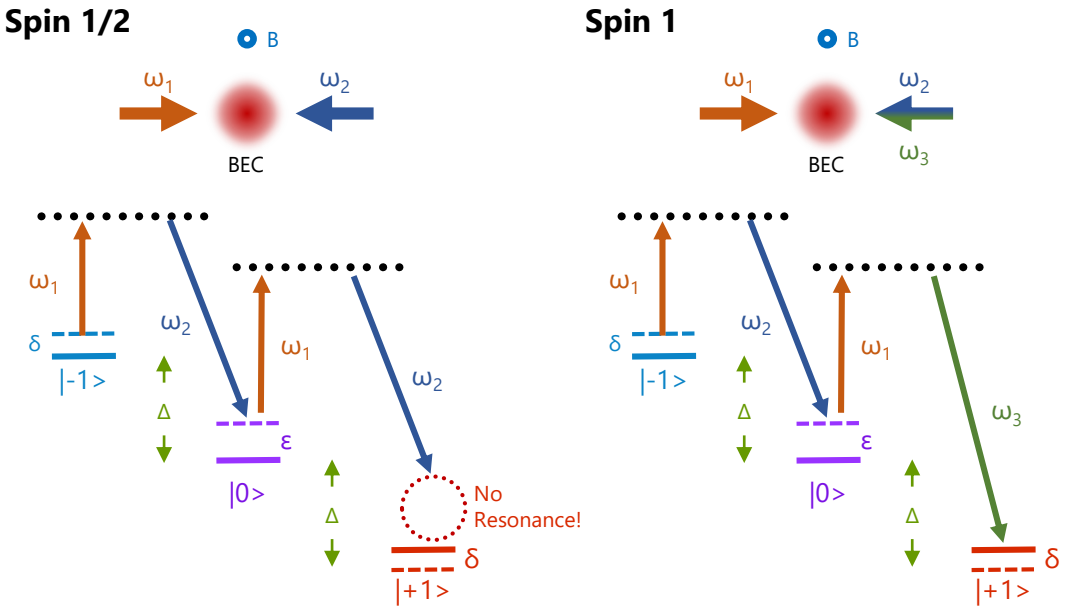

Figure 6.12: Energy level diagram for a spin-1/2 (left) and spin-1 (right) Raman coupling scheme. For large biasing magnetic fields, the quadratic Zeeman shift causes an asymmetry in coupling between the $m_F = \pm 1$ states, and only one transition can be on resonance with a two frequency Raman scheme, allowing for an effective spin-1/2 system. By adding a third frequency, all three states can be coupled, regardless of the quadratic shift.

6.2.1 An Optically Tunable Effective Quadratic Zeeman Shift

As before with the two beam case, we are interested in the interaction of the atoms and the effective magnetic field arising from the vector product of the electric field. If we write down the superposition of the field for a three frequency coupling scheme in a method similar to Section 6.1.2, we get:

$$\vec{\mathbf{E}} = E_1 \hat{\mathbf{e}}_\mathbf{i} e^{ikx - i\omega_1 t} + E_2 \hat{\mathbf{e}}_\mathbf{j} e^{-ikx - i\omega_2 t} + E_3 \hat{\mathbf{e}}_\mathbf{j} e^{-ikx - i\omega_3 t} \tag{6.12}$$

I will assume that E_2 and E_3 are the same (i.e. we put the same power into each frequency component of the beam, as done in experiments). Following the same steps as previously we can arrive at the interaction terms from these beams:

$$\hat{\mathbf{H}}_{\text{Raman}} = \frac{\hbar\Omega_{\text{R}}}{\sqrt{2}}\hat{\mathbf{F}}_x\left(\cos(2kx - (\omega_1 - \omega_2)t) + \cos(2kx - (\omega_1 - \omega_3)t)\right) \tag{6.13}$$

Here I define a relative frequency $\bar{\omega} = \omega_3 - \omega_2 = 2\epsilon_q + 2\epsilon_{\text{eff}}$ where ϵ_q is the quadratic Zeeman shift of the system, and ϵ_{eff} is a term we call the effective Zeeman shift which I will describe more momentarily. Using this definition and making a transformation into the frame rotating at $\omega_1 - \bar{\omega}/2$, we get a total Hamiltonian of the form:

$$\hat{\mathbf{H}}_{\text{Raman}} = \begin{pmatrix} \frac{\hbar^2}{2m}(p-2k)^2 - \delta & \Omega_R/\sqrt{2} & 0 \\ \Omega_R/\sqrt{2} & \frac{\hbar^2 p^2}{2m} + \epsilon_{\text{eff}} & \Omega_R/\sqrt{2} \\ 0 & \Omega_R/\sqrt{2} & \frac{\hbar^2}{2m}(p+2k)^2 + \delta \end{pmatrix} \tag{6.14}$$

Where

$$\epsilon_{\text{eff}} = \frac{\bar{\omega}}{2} - \epsilon_q = \frac{\omega_3 - \omega_2}{2} + \epsilon_q \tag{6.15}$$

By adjusting the relative frequencies of ω_2 and ω_3, we can alter the effective quadratic Zeeman shift that the $m_F = 0$ state experiences.

Floquet Theory in the Spin-1 Coupling Scheme

The spin-1 Raman coupling Hamiltonian has some subtlety hiding beneath the surface of Equation 6.14. The use of the rotating wave approximation in the transformation involving $\bar{\omega}$ is only that, an approximation. The introduction of a third frequency creates a plethora of issues arising from the different beat-tones present in the optical field. To be accurate and find the true energies of the system, we need to consider the system in a Floquet formalism [85]. Floquet theory is roughly a temporal version of Bloch's theorem for a spatially periodic Hamiltonian. For the time-dependent periodicity, we have a Hamiltonian of the form:

$$\hat{\mathbf{H}}(t) = \hat{\mathbf{H}}_0 + V(t) \tag{6.16}$$

With $V(t)$ being periodic with period T:

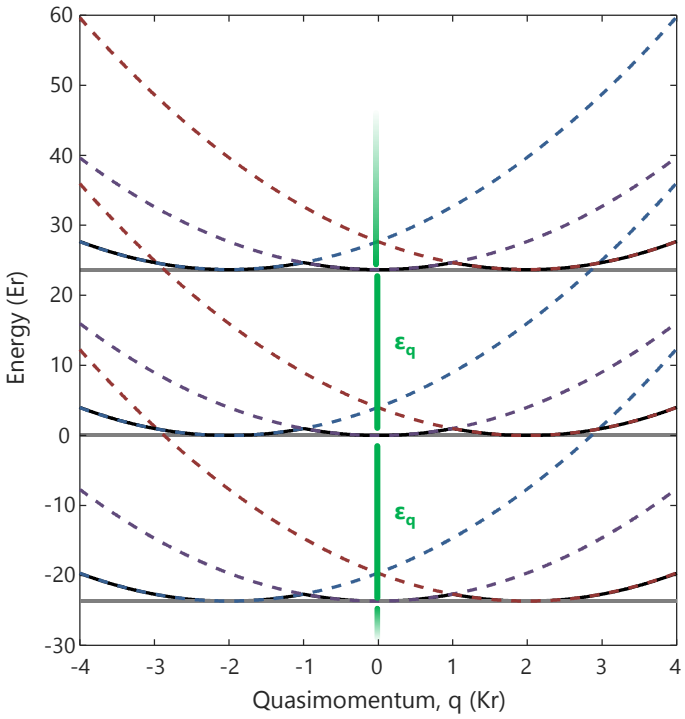

Figure 6.13: Three Floquet bands calculated for the spin-1 setup with $\epsilon_q \approx 90$ kHz, $\omega_R = 25$ MHz. Dashed lines represent the free-particle dispersions at zero coupling with $m_F = -1, 0, +1$ represented as blue, purple, red respectively.

$$V(t+T) = V(t) \tag{6.17}$$

Then the solutions take the form of:

$$\psi(t) = e^{-int}\phi(t) \tag{6.18}$$

$$\phi(t+T) = \phi(t) \tag{6.19}$$

Where n, as usual, is an integer. The idea of the Floquet solution then is to use these conditions to recast the periodic Hamiltonian into one in which we look for solutions in the frequency state basis. The solution gives a set of repeating energy-bands that are separated by the value of the real quadratic Zeeman shift ϵ_q. For this reason in the experiment in Chapter 7 we set the linear Zeeman shift (the difference in $\omega_1 - \omega_2$) to 25 MHz, yielding

$\epsilon_q \sim 90$ kHz, which helped to decouple interactions between the Floquet bands.

Although we work at high Zeeman splittings to reduce the coupling between the Floquet bands, there is still an effect present. For working at 25 MHz (such as in Chapter 7), the corrections to ϵ_{eff} due to the coupling Ω_{R} in the Floquet bands can be approximated by the polynomial:

$$\begin{aligned}\epsilon_q^*(\Omega_{\text{R}}) = \epsilon_q + \Omega_{\text{R}}^2 \{ &-4.9 \cdot 10^{-2} + 1.56 \cdot 10^{-2}\Omega_{\text{R}} - 4.41 \cdot 10^{-3}\Omega_{\text{R}}^2 \\ &- 5.8 \cdot 10^{-4}\Omega_{\text{R}}^3 - 2.76 \cdot 10^{-5}\Omega_{\text{R}}^4 \}\end{aligned} \tag{6.20}$$

Where all terms are in units of E_{L}.

6.2.2 Spin-1 Raman Coupling Parameter Space

From the spin-1 Hamiltonian in Equation 6.14, we can calculate the effect of tuning the effective Quadratic Zeeman shift in the system at a fixed value of Ω_{R}. For the rest of this discussion, I am assuming that the detuning $\delta = 0$, which keeps the symmetry between the $m_F = \pm 1$ states. In the regime of very little Raman coupling ($\Omega_{\text{R}} \sim 0$), we have that the bare quadratic Zeeman shift will shift the bare $m_F = 0$ dispersion state downward in energy compared to the $m_F = \pm 1$ states. However, as we increase the values of ϵ_{eff}, the $m_f = 0$ state will reach a critical value when all three states are degenerate in energy, and an increase further will put the $m_F = 0$ dispersion higher in energy than the other two states (Figure 6.14). A large enough value of ϵ_{eff} can even make the $m_F = 0$ state disappear into an unstable configuration.

If we hold the value of ϵ_{eff} constant and increase the value of Ω_{R}, a similar process occurs. As the coupling strength Ω_{R} increases, the bands between dispersion widen, and the $k = 0$ state can go from being stable to metastable to unstable (Figure 6.15).

From this description, we can see that between the values of ϵ_{eff} and Ω_{R}, there exist different regions where the Raman coupled dispersions will have three, two or one minima. Naturally, this leads to a parameter space with different phase transitions that can exist. Figure 6.16 shows a parameter space between ϵ_{eff} and Ω_{R} that shows the different regions

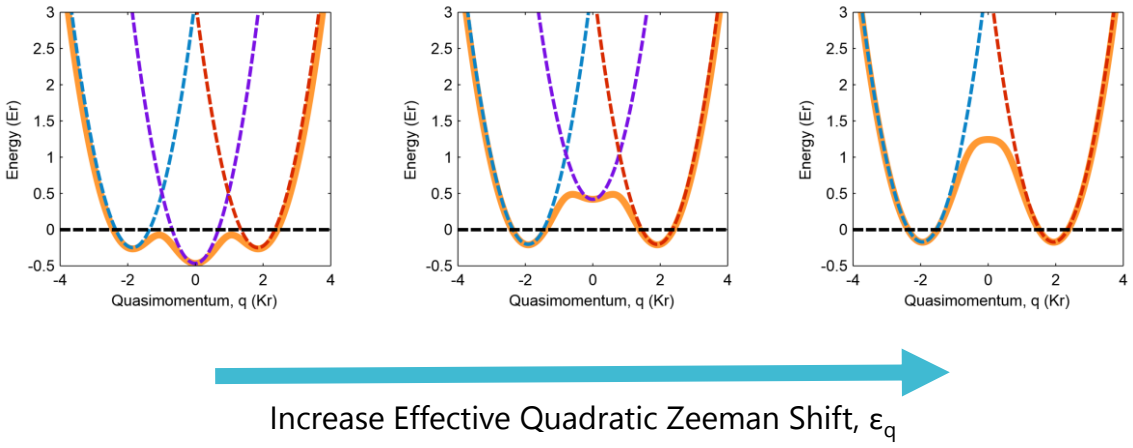

Figure 6.14: As the effective quadratic shift ϵ_q is increased (with $\Omega_{\mathrm{R}} = 2E_{\mathrm{L}}$ constant), the minima in the dispersion associated with the $m_F = 0$ bare state raises in energy with respect to the other minima. Increasing the value can take the system from 3 to 2 minima in the dispersion.

of dispersions that can exist within the system. Furthermore, there are regions in the parameter space that have metastable configurations, and sets of points where the energy of each dispersion minima is degenerate. The physics of this complex parameter space is explored in Chapter 7 in the context of a magnetic model with phase transitions. Here it is presented as a reference for the ideas presented later.

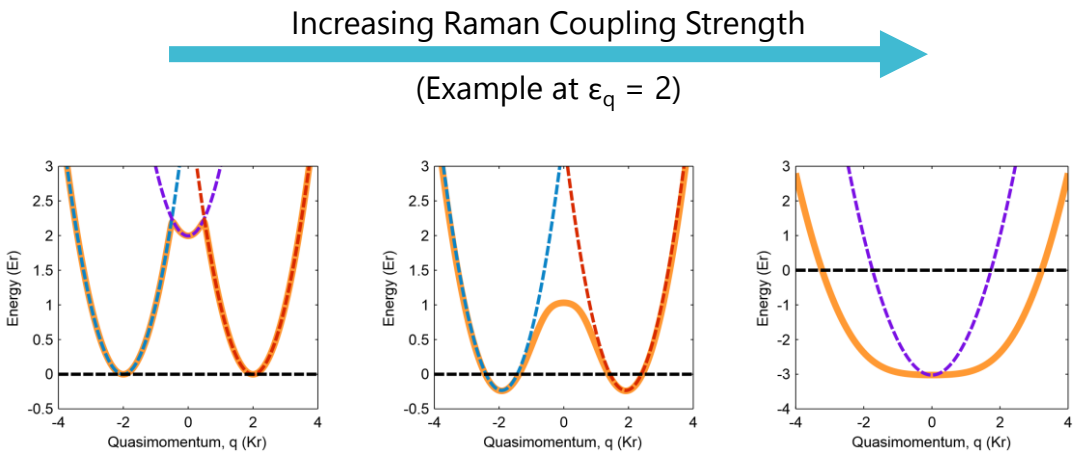

Figure 6.15: At particular fixed values of ϵ_q (here $= 2E_{\mathrm{L}}$), incrasing the Raman coupling strength Ω_{R} causes the system go from 3 to 2 to 1 minima as the increased coupling strength causes a flattening of the band.

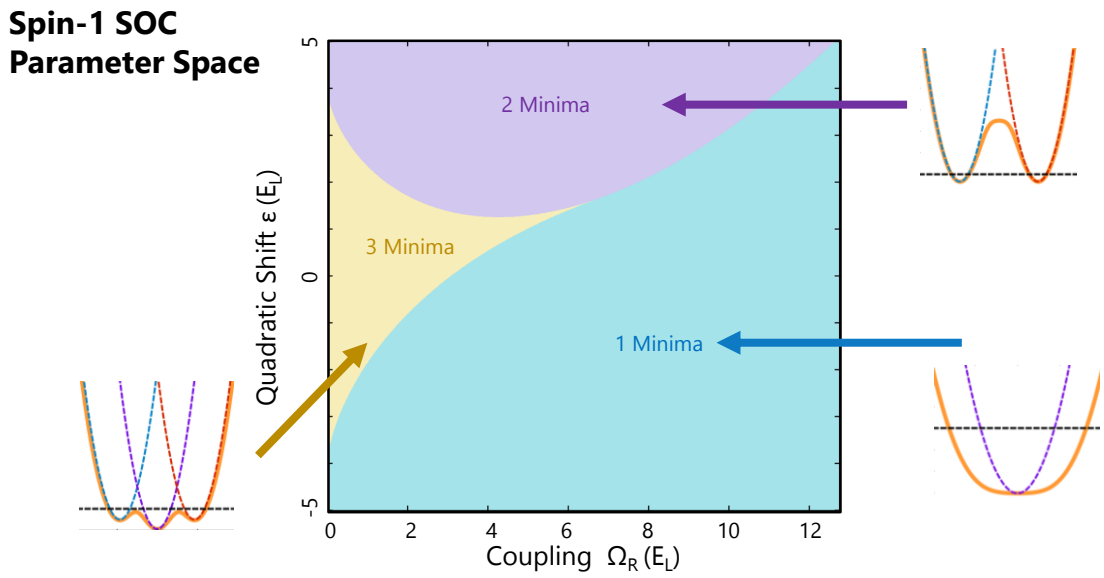

Figure 6.16: Tuning the parameters coupling (Ω_{R}) and relative frequencies (effective shift ϵ_q) of the Raman beams yields a parameter space with distinct classes of dispersion relations.

Critical Locations in Parameter Space

Starting from Equation 6.14 for the spin-1 Hamiltonian, it is possible to algebraically solve[6] for the locations where the system undergoes transitions between the number of minima and also solve for the line of points where all the energy minima in the system are degenerate.

The tricritical point of the system (where all of the regions touch) is located at[7]:

$$(\Omega_{\mathrm{C}}, \epsilon_{\mathrm{C}}) = (16\sqrt{5\sqrt{5}-11},\ 24\sqrt{5}-52) \tag{6.21}$$

$$\approx (6.795\, E_{\mathrm{R}}, 1.666\, E_{\mathrm{R}}) \tag{6.22}$$

The boundary between the 3 minima and 2 minima regions is given by (for Ω_{R} less than Ω_{C}):

$$\Omega = \sqrt{\frac{1}{8}\left[-16 + 72\epsilon_{\mathrm{eff}} - \epsilon_{\mathrm{eff}}^2 \pm (12+\epsilon_{\mathrm{eff}})\sqrt{-112 + \epsilon_{\mathrm{eff}}(88+\epsilon_{\mathrm{eff}})}\right]} \tag{6.23}$$

[6] Algebraically solve means use Mathematica

[7] All of these trends are true up to the annoying $\sqrt{2}$ factor that may or may not be in the definition of the coupling strength Ω_{R}

Where the boundary is given the term of $\pm$ that gives a real solution. Similarly, this equation gives the 2 to 1 transition boundary for the positive term, with $\Omega > \Omega_C$. The boundary for the 3 to 1 transition is given by (for (Ω_R, ϵ) less than (Ω_C, ϵ_C)):

$$\Omega = \sqrt{\frac{-8(4+\epsilon_{\text{eff}})^3}{27(\epsilon_{\text{eff}}-4)}} \tag{6.24}$$

The triple-degenerate line, where all three wells have the same energy minima is given by (for (Ω_R, ϵ) less than (Ω_C, ϵ_C)):

$$\Omega = \sqrt{-8\left(-72+\sqrt{-(-36+\epsilon_{\text{eff}})^2(-4+\epsilon_{\text{eff}})+10\epsilon_{\text{eff}}}\right)} \tag{6.25}$$

6.2.3 Experimental Implementation

Generating a Double Frequency Beam

We developed two methods to generate the double frequency beam for ω_2 and ω_3. When first testing the system and studying the physics, we originally sent the two frequencies to a single AOM via combing two RF signals prior to the AOM and amplifier. This method generated noticeable higher harmonics (measured as beat tones on a photodiode) that introduced noise and heating into our Raman experiments and measurements. After the experiment in Chapter 7, we had developed an RF filter circuit to mitigate this effect. However, for the experiment in (Chapter 7), we combined the light between two beam lines in free space via polarization optics, as described in Section 4.3.7. The optics used to focus the beam and set the polarization at the atoms is described in Section 4.1.5, and the Raman laser system in Section 4.3.7

BEC Lifetimes and Raman Coupling

The lifetime of the BEC when dressed with the Raman beams is much less than that of the bare condensate due to heating from spontaneous emission. This typically limits Raman experiments in our apparatus to around one second in length. However, in the original setup we found that the Raman coupling would cause the immediate destruction of the

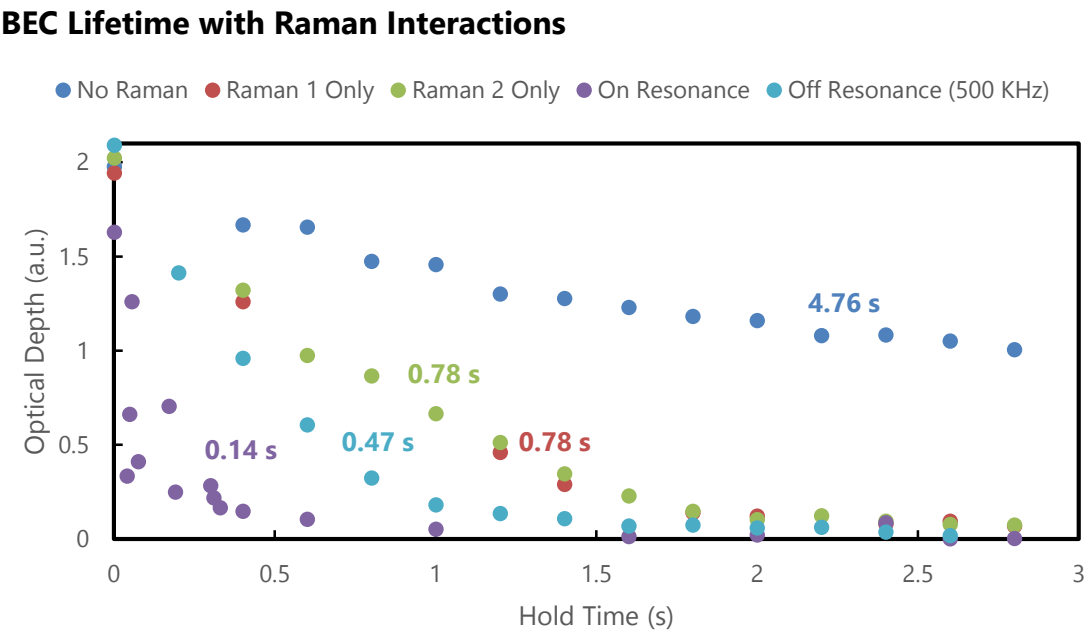

Figure 6.17: Measurements of the BEC lifetime prior to installing laser-line filters after the tapered amplifiers. The presence of the Raman beams quickly heated the condensate.

condensate. We traced this issue back to the amplified spontaneous emission (ASE) of the tapered amplifiers (TAs) (Section 4.3.7) we used to generate the Raman beams. To block the ASE, we placed a set of laser-line optical filters (Semrock 808 nm) after the TAs and adjusted the angle to maximize 790 nm transmission.

Chapter 7

Magnetic Phases of Spin-1 Spin-orbit Coupled Bose Gases

In Chapter 6, I laid the foundations for the spin-1 coupling scheme and described the parameter space of the dispersion energy as the function of the Raman coupling power Ω_{R} and an optically induced effective Zeeman shift ϵ_{eff}. For this spin-orbit coupling (SOC) system, Figure 6.16 described the various regions where the dispersion could have 1, 2 or 3 distinct energy minima corresponding to similarly distinct Raman states.

Here I describe our experiment investigating the connection of this system to a magnetic model involving quantum phase transitions of both first and second order. In the magnetic model, the system can transition between an unmagnetized state that is effectively a polar BEC state (all the atoms are in $|m_F = 0, k = 0\, k_{\mathrm{L}}\rangle$), to a 'ferromagnetic' state (all the atoms are in $|m_F = \pm 1, k_{\mathrm{L}} = \pm 2\, k_{\mathrm{L}}\rangle$). As the system undergoes transitions to have the global minima in the energy in different states, the system quickly condenses into this new ground state, as evidenced by our observations of a narrow first order transition.

7.1 Magnetic Ordering in the Spin-1 Spin-Orbit Coupled System

7.1.1 Definition of Magnetic Order in the Spin-1 SOC System

For spin-1/2 systems (i.e, total angular momentum, $f = 1/2$) like electrons, ferromagnetic order can be represented in terms of a magnetization vector $\mathbf{M} = \langle \hat{\mathbf{S}} \rangle / \hbar$. This is rooted in the fact that the three components of the spin operator $\hat{\mathbf{S}}$ transform vectorially under rotation. More specifically, any Hamiltonian describing a two level system may be expressed as $H = \hbar\Omega_0 + \mathbf{\Omega}_1 \cdot \hat{\mathbf{S}}$, the sum of a scalar (rank-0 tensor) and a vector (rank-1 tensor) contribution. The former, described by Ω_0, gives an overall energy shift, and the latter takes the form of the linear Zeeman effect from an effective magnetic field proportional to $\mathbf{\Omega}_1$. Going beyond this, fully representing a spin-1 (total angular momentum $f = 1$ with three m_F sublevels: $|-1\rangle$, $|0\rangle$, and $|+1\rangle$) Hamiltonian with angular momentum $\hat{\mathbf{F}}$ requires an additional five-component rank-2 tensor operator – the quadrupole tensor –

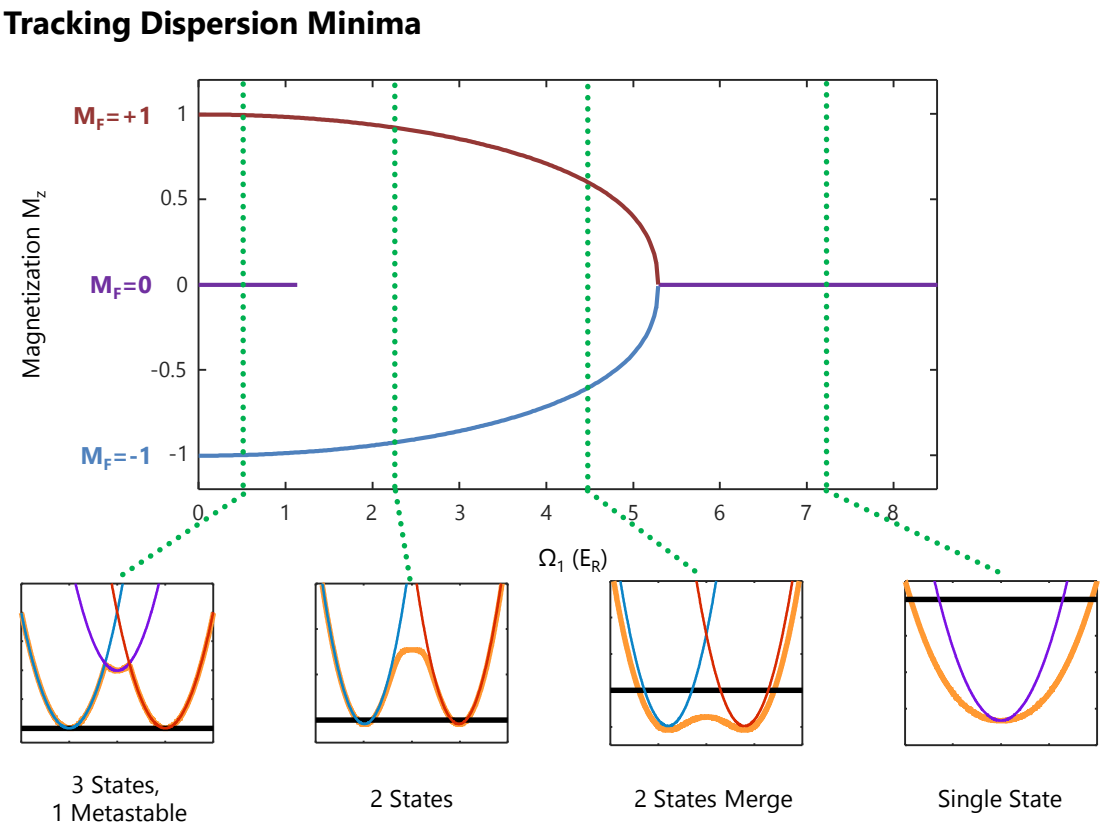

Figure 7.1: Calculation of the magnetization M_z in the magnetic system as function of Ω_1 at fixed $\Omega_2 = 2E_{\mathrm{L}}$. Insets: As Ω_1 is increased, the dispersion energy in the Raman coupling scheme (Section 6.2.2) will transition from having a different number of minima.

and therefore there exist "magnetization" order parameters that are not simply associated with any spatial direction [60, 62, 86].

Studies in GaAs quantum wells [87, 88] showed that material systems with equal contributions of Rashba and Dresselhaus SOC described by the term $\alpha k_x \hat{\mathbf{F}}_z$, subject to a transverse magnetic field with Zeeman term $\Omega_1 \hat{\mathbf{F}}_x$, can equivalently be described as a spatially periodic effective magnetic field. Our experiments with spin-1 atomic systems use Raman laser with wavelength λ to induce SOC of this form [89–95] with strength $\alpha = 2\hbar k_R/m$, where the single-photon recoil energy and momentum are $E_R = \hbar^2 {k_R}^2/2m$ and $\hbar k_R = 2\pi\hbar/\lambda$. This atomic system can therefore be described by the magnetic Hamiltonian:

$$\hat{\mathbf{H}} = \frac{\hbar^2 \mathbf{k}^2}{2m} + \mathbf{\Omega}_1(x)\cdot\hat{\mathbf{F}} + \Omega_2 \hat{\mathbf{F}}^{(2)}_{zz}, \tag{7.1}$$

describing atoms with mass m and momentum $\hbar\mathbf{k}$ interacting with an effective Zeeman magnetic field $\mathbf{\Omega}_1(x)/\Omega_1 = \cos(2k_R x)\mathbf{e}_x - \sin(2k_R x)\mathbf{e}_y$ helically precessing in the $\mathbf{e}_x$-$\mathbf{e}_y$; and an additional Zeeman-like tensor coupling with strength Ω_2. From Section 6.2.2, our value of Ω_{R} maps to the strength of the vector interaction with the spins, Ω_1. Here, $\hat{\mathbf{F}}^{(2)}_{zz}/\hbar = \hat{\mathbf{F}}_z^2/\hbar^2 - 2/3$ is an element of the quadrupole tensor operator, where the strength of the interaction Ω_2 is related to the effective Quadratic Zeeman shift in Section 6.2.1 by the relation $\Omega_2 = -\epsilon_q$.

For the magnetic model, we consider a magnetization term to track the relative population of the Raman states:

$$M_z = \frac{n_{\pm 1} - n_0}{n_{\pm 1} + n_0} \tag{7.2}$$

Where $n_{\pm 1}$ is the atom number in the sum of the $m_F = \pm 1$ states, and similarly n_0 is the population in the $m_F = 0$ state. Here M_z represents the order parameter of our model system. Because we are defining the magnetization based on the number of atoms in the absolute value of the spin component, the system is reminiscent of a spin-1/2 system with the spin states either pointing up or down.

However, in our system we can define a second order parameter M_{zz}:

$$M_{zz} = \frac{n_0}{n_{\pm 1} + n_0} \tag{7.3}$$

This order parameter, that we call the tensor magnetization, is related to the tensor operator Ω_2 in our model Hamiltonian.

7.1.2 Parameter Space in the Magnetic Model

As described in Section 6.2.2, this system contains a parameter space that, in the magnetic model, depends on the values of Ω_1, Ω_2. Figure 7.2 shows the parameter space within this new framework with the magnetization M_z shown.

From the discussion of critical lines and points in Section 6.2.2, we can calculate regions where first-order transitions and second-order transitions can occur. These two

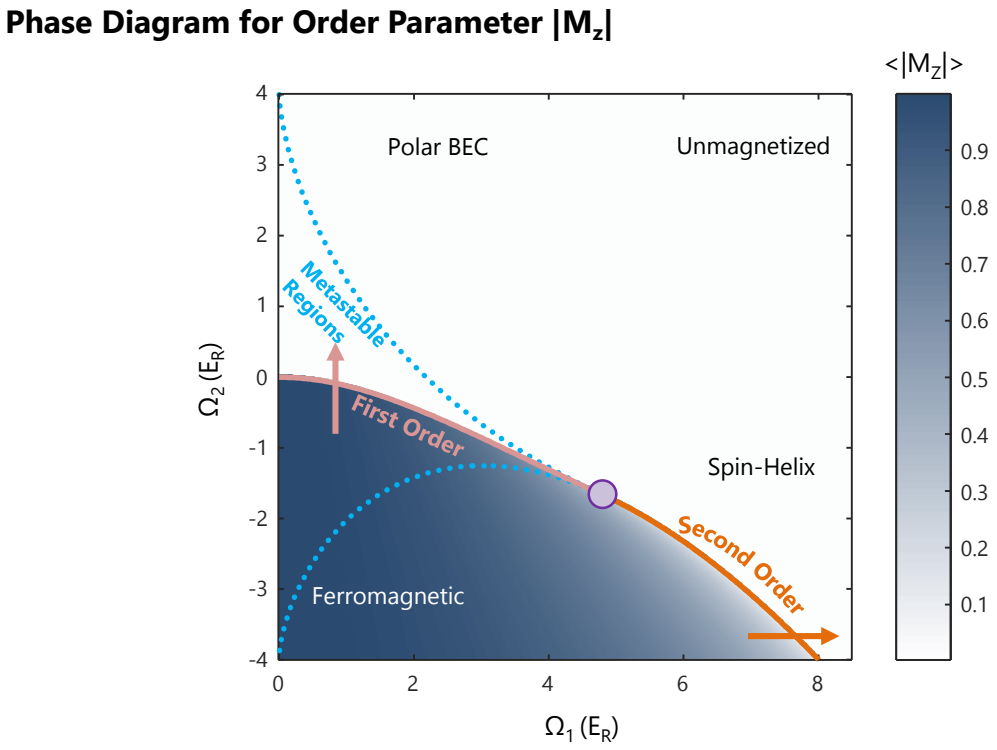

Figure 7.2: Phase Diagram for $|M_z|$ in the magnetic model with parameters Ω_1 and Ω_2. Dark blue shading represents the value of $|M_z|$, the first and second order transitions in the system are represented by pink and orange lines respectively. The region contained by the light blue dashed line represents where metastable magnetic states are present.

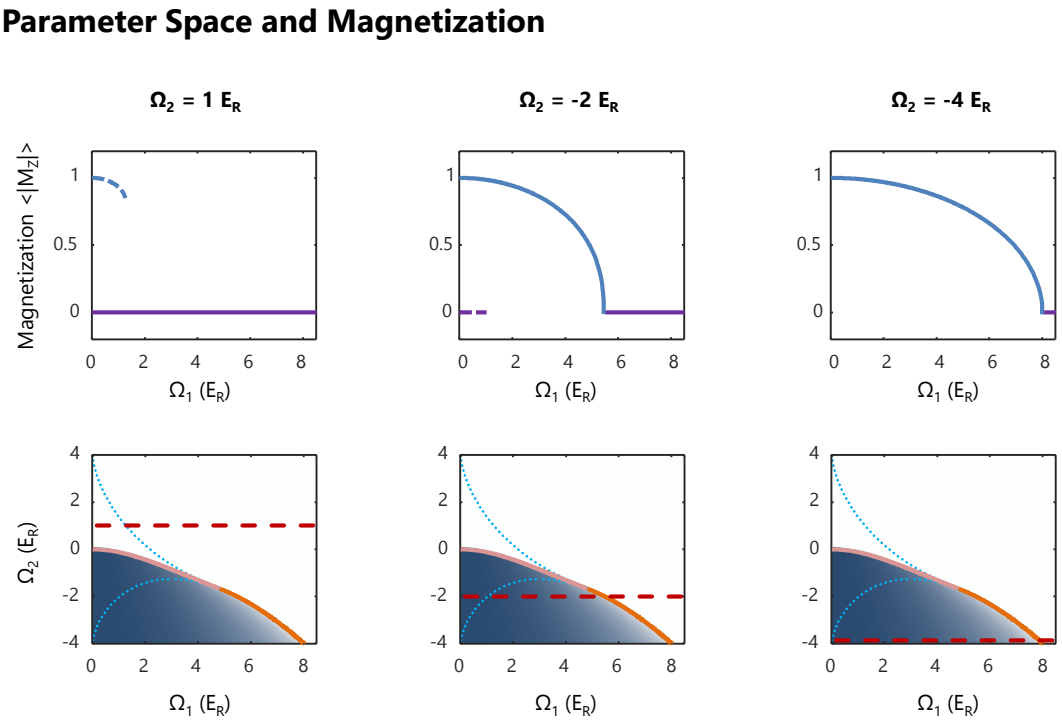

Figure 7.3: Magnetic states as a function of Ω_1 at select Ω_2. Left: At positive Ω_2, the system goes from having metastable magnetized ($M_z > 0$) states available (blue), to having a single unmagnetized state ($M_z = 0$, purple). Center: At lower Ω_2, the system can undergo a continuous transition from magnetized states to unmagnetized states in a second order transitions. At low Ω_1, the unmagnetized state can persist as a metastable state. Right: With Ω_2 decreased further, the magnetization profile no longer contains any metastable states.

phase-transitions continuously connect at the point (Ω_1^*, Ω_2^*) (as defined in Equation 6.22), the purple circle in Section 6.2.2, where the small-Ω_1 first-order phase transition gives way to the large-Ω_1 second-order transition, and together these regions constitute a curve of critical points $\{(\Omega_1^C, \Omega_2^C)\}$.

Second-Order Transitions

The second-order transition can be intuitively described starting in the large Ω_1 limit where the system forms a spin helix BEC. This order increases the system's kinetic energy, leading to the second-order phase transition into the ferromagnetic phase shown in Figure 7.4 as Ω_1 is varied. This second-order phase transition is analogous to other systems with effective spin-degrees of freedom such as double-leg ladders [96] or engineered optical lattices [97, 98].

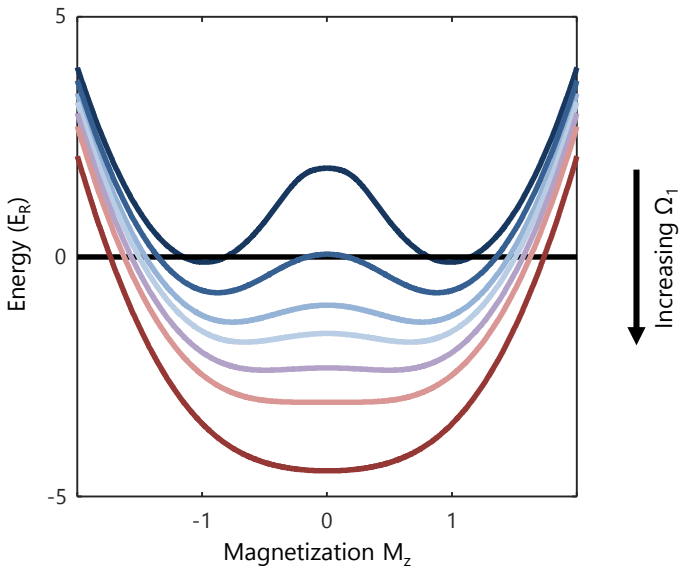

Figure 7.4: Second order phase transition. As Ω_1 is increased with $\Omega_2 \gtrsim 1.7\, E_R$, the ferromagnetic states begin to approach a value of $M_z = 0$. The two states merge continuously to a single unmagnetized state for large enough Ω_1. Solid black line represents the uncoupled minimum energy.

First-Order Transitions

In the limit of infinitesimal Ω_1, the tensor magnetization terms favors either a polar BEC for $\Omega_2 > 0$ ($m_F = 0$: unmagnetized, $M_z = 0$), or a ferromagnetic BEC for $\Omega_2 < 0$ ($m_F = +1$ or -1: magnetized, $|M_z| = 1$). As with spinor BECs [64], these phases are separated by a first-order phase transition at $\Omega_2 = 0$, where the $m_F = 0$ state is either lower or higher than the $m_F = \pm 1$ states due to the tensor energy shift (i.e. quadratic Zeeman shift of the $m_F = 0$ state). As bosons have a strong preference to condense into the lowest energy state of the system through Bose stimulation [99], immediately after the configuration has crossed the transition the state of the system will change.

Metastable States

From Figure 7.5, for values of Ω_2 not far from the first-order transition, all three magnetic states exist. Here a metastable state with $M_z = 0$ persists in the ferromagnetic phase,

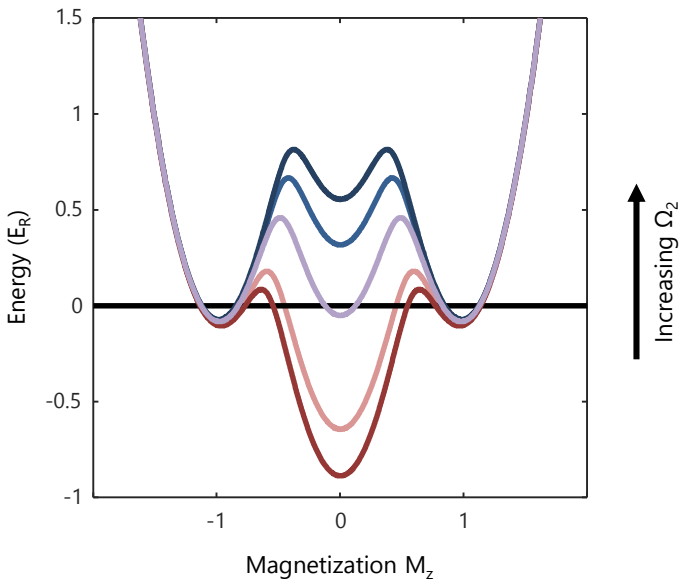

Figure 7.5: First order phase transition. As Ω_2 increases, the unmagnetized state (bare state $\approx |m_F = 0, k = 0\rangle$) raises in energy with respect to the symmetric ferromagnetic states. When at higher energy, the BEC will condense into the energetically favorable ferromagnetic states. For Ω_2 near the transition all three states exist, with either the unmagnetized state or magnetized states being metastable. Solid black line represents the uncoupled minimum energy.

and a pair of metastable states with $M_z \neq 0$ persists in the unmagnetized phase. As mentioned in the previous section, after crossing the first-order phase transition, the BEC will condense into the lowest energy state. However, this process takes dramatically longer for the first-order transition than the second-order transition (up to 1.5 s compared to 50 ms).

Another interesting configuration is one where the values of Ω_1 and Ω_2 place the system on a critical point of the first-order transition. In this situation, all three states are degenerate in energy[1] which can lead to interesting many-body phases where the miscibility of the different bare spin states is altered [100], including an tripartite mixture in-plane ferromagnetic phase with no analogue in spinor BECs or effective spin-1/2 SOC BECs [101].

[1] Our group lovingly refers to this condition as being on the 'triple degenerate line'

7.2 Experimental Setup and Measurements

As shown in Figure 7.6, we realized the magnetic system by illuminating ^{87}Rb BECs in the $F = 1$ ground state manifold with a pair of counter propagating and orthogonally polarized Raman lasers that coherently coupled the manifold's m_F states. Physically, the spatial interference of the orthogonally polarized laser beams give rise to the helical effective magnetic field with period $\lambda/2$. As first showed [90] using effective $F = 1/2$ systems, this introduces both a spin-orbit and a Zeeman term into the BEC's Hamiltonian, equivalent to Equation 7.1. Here the quadratic Zeeman shift from a large bias magnetic field $B_0\mathbf{e}_z$ split the low-field degeneracy of the $|-1\rangle \leftrightarrow |0\rangle$ and $|0\rangle \leftrightarrow |+1\rangle$ transitions, and we independently Raman coupled these state-pairs with equal strength Ω_1. We dynamically tuned the quadrupole tensor field strength Ω_2 by simultaneously adjusting the Raman frequency differences; as shown in Figure 7.6 we selected frequencies differences where the detuning from the $|+1\rangle$ to $|0\rangle$ and $|-1\rangle$ to $|0\rangle$ were both equal to Ω_2 (see Methods Summary). Without this technique, only the upper half-plane of the phase diagram (Figure

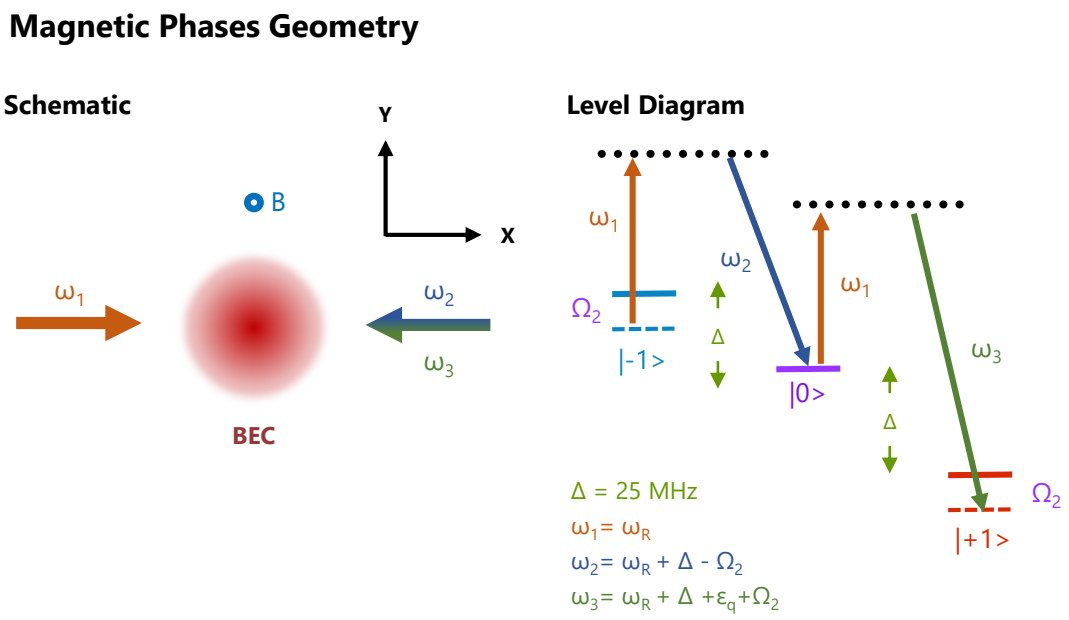

Figure 7.6: Schematic and level diagram. We used the spin-1 Raman coupling scheme described in Section 6.2 to probe the parameter space of the magnetic system. The $|-1\rangle \leftrightarrow |0\rangle$ and $|0\rangle \leftrightarrow |+1\rangle$ transitions of the $F = 1$ ground state manifold of ^{87}Rb were independently Raman coupled, giving experimental control of Ω_1 and Ω_2.

7.2) would be accessible, containing only an unmagnetized phase and lacking any phase transitions.

In each experiment, we first prepared BECs at a desired point in the phase diagram, possibly having crossed the phase transition during preparation. A combination of trap dynamics [102, 103], collisions, and evaporation [104] kept the system in or near (local) thermal equilibrium. We then made magnetization measurements directly from the Bose-condensed atoms measured in the spin resolved momentum distribution obtained using the time-of-flight (TOF) techniques described in Section 6.1.6.

7.2.1 Control of Magnetic Field Noise

In order to make precision measurements of the phase transitions, we needed to have absolute control of the magnetic fields within the experiment. Section 6.1.5 describes the effect of detuning the Raman coupling resonance, and the subsequent shifting of the minima of the energy dispersion. In our system, we attempt to combat this by using magnetic field stabilization techniques (Section 4.4.7), in particular using the flux gate field stabilization system (Appendix A) to remove long term drift.

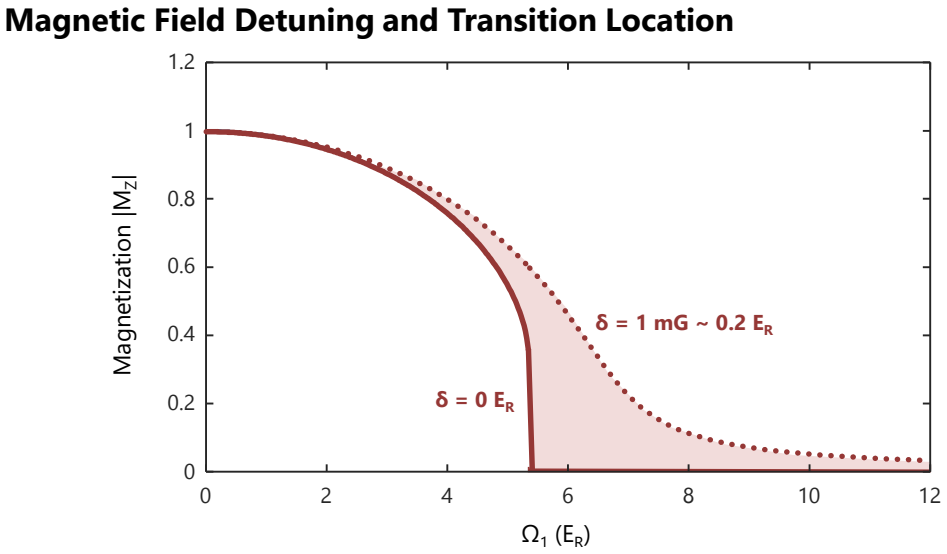

Figure 7.7: Magnetization $|M_z|$ as a function of Ω_1 at $\Omega_2 = 2.5E_R$. The solid curve represents zero detuning. The dotted curve represents the magnetization with a detuning of $\delta = 0.2E_R$. The shaded region between the two curves represents the region of uncertainty for such a detuning.

Through such efforts, we have an approximate 1 mG shot-to-shot variation in the magnetic field as measured by the atoms. However, this translates into an $\approx 0.2\, E_R$ detuning in the system. Figure 7.7 illustrates the woes of the magnetic field: a small detuning uncertainty can change the magnetization drastically near the transition lines described in Section 6.2.2. We can further try an post-select images that are obviously highly detuned (as measured by an imbalance in $m_F = \pm 1$ in the measurement process), however this ultimately limits the precision we can achieve.

7.3 Measurements

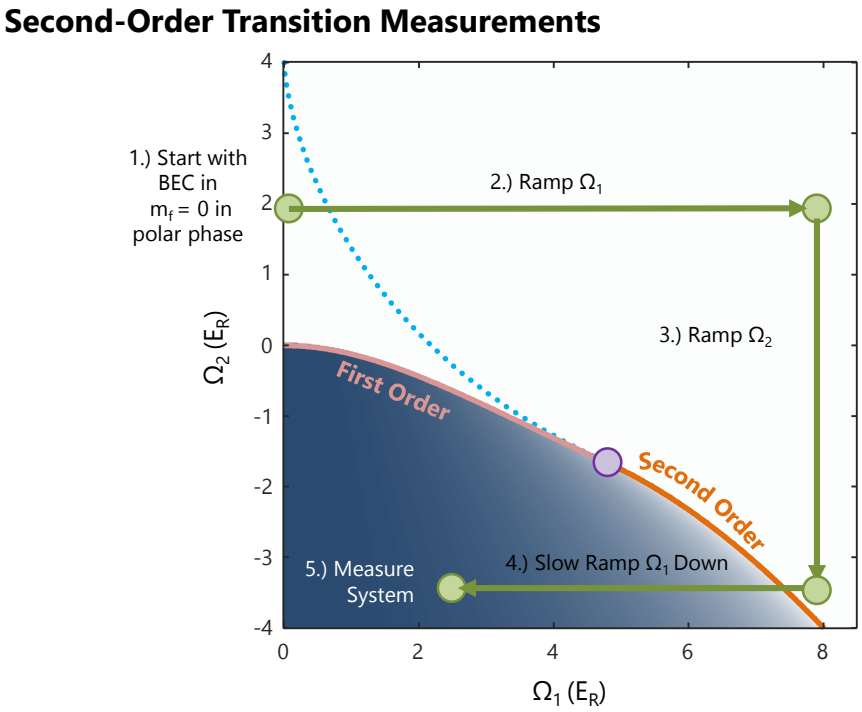

Figure 7.8: Ramping sequence used for the horizontal (primarily second-order transition) measurements. We adiabatically transfer the atoms to a highly coupled, but unmagnetized, state, and slowly lower Ω_1 to cross the second-order transition.

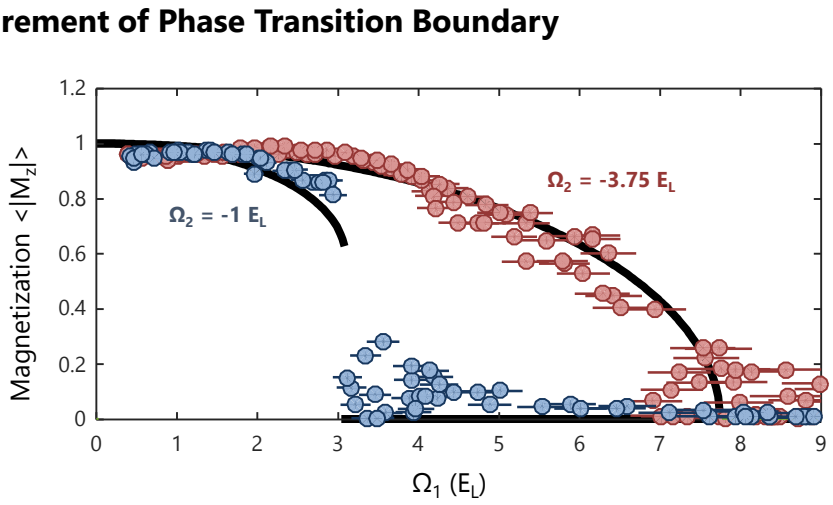

Figure 7.9: Magnetization M_z measured as a function of Ω_1, showing both second-order (red points) $[\Omega_2(\Omega_1 = 0) = -3.7500(3)E_R]$ and first-order(blue points) $[\Omega_2(\Omega_1 = 0) = -1.0E_R]$ phase transitions in comparison with theory (black solid lines).

7.3.1 Second-Order Scans

Our experiment first focused on second phase transitions. We performed the scans in the following sequence (see Figure 7.8). First, we prepared the condensate in the unmagnetized phase ($\Omega_2 > 0$) and ramped Ω_1 far into the spin-helix phase. We then reduced the value of $\Omega_2 > 0$ to the regime where second order transitions can occur. We then ramped Ω_1 toward zero, while trying to slowly cross the second order phase transition where the system goes from one to two minima (Figure 7.4). We ramped Ω_1 at a rate of $\approx -40E_R/\text{s}$, allowing the system to adiabatically track the ground state, and allowed 50 ms for equilibration before the measurement process described in Section 6.1.6.

By measuring at various end values of Ω_1 at a given Ω_2, we can map out the magnetization (Figure 7.9). In each case, data is plotted along with theory with no adjustable parameters. Repeating the horizontal scan processes for $\Omega_2^* < \Omega_2 < 0$, we found a sharp first-order transition within the magnetic system.

Using data of this type for a range of Ω_2 and fitting to numeric solutions of Equation 7.1, we obtained the critical points plotted in Figure 7.10, bottom. Because horizontal cuts through the phase diagram are nearly tangent to the transition curve for small Ω_2, this produced large uncertainties in Ω_1^C for the first-order phase transition.

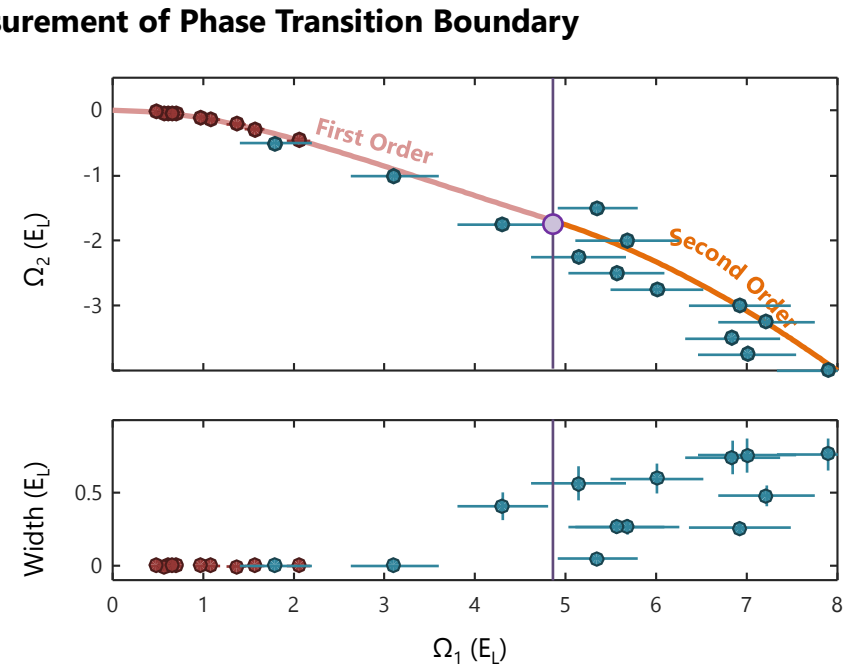

Figure 7.10: Top: Measurement of the phase transition locations for the magnetic system. Red circles represent vertical scans through parameters space, while teal circles represent horizontal scans. The theory lines for the first and second order transitions are highlighted by solid pink and orange lines, respectively. The critical location where the two transition orders meet (Ω_1^C,Ω_2^C) is represented by the purple circle with Ω_1^C mapped as a vertical purple line. Bottom: The width of the phase transitions (20% and 50% widths)

7.3.2 First-Order Scans

We studied the first-order phase transition with greater precision by ramping Ω_2 through the transition at fixed Ω_1 and found near perfect agreement with theory. To perform these scans, we start with the BEC in an unmagnetized state with $\Omega_2 > 0$, similar to the horizontal scans described previously. Here, we ramp $\Omega_1 < \Omega_1^C$ to stay primarily within the first-order transition regime. We then ramp Ω_2 across the first-order transition, and measure the tensor magnetization M_{zz} after a hold time between 0.2 ms and 2 s to allow for equilibration. The reason for this sequence is two fold. First, similar to the argument for horizontal scans for the second order transition, the curve for the first order transitions is perpendicular to a ramp in Ω_2. Secondly our control of Ω_2, set by the frequency difference in the Raman beams used in the experiment, can be controlled to incredibly high precision, allowing us to precisely measure the location and width of the first-order transitions.

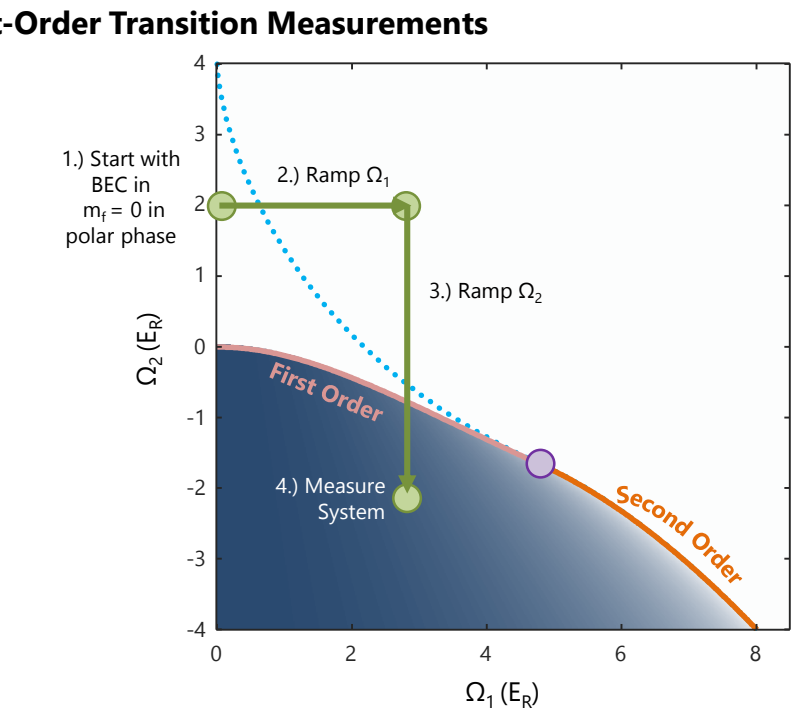

Figure 7.11: Ramping sequence used for the horizontal (primarily first-order transition) measurements. We first ramp to a constant Ω_1 in an unmagnetized state and then ramp Ω_2 across the transition to a target value.

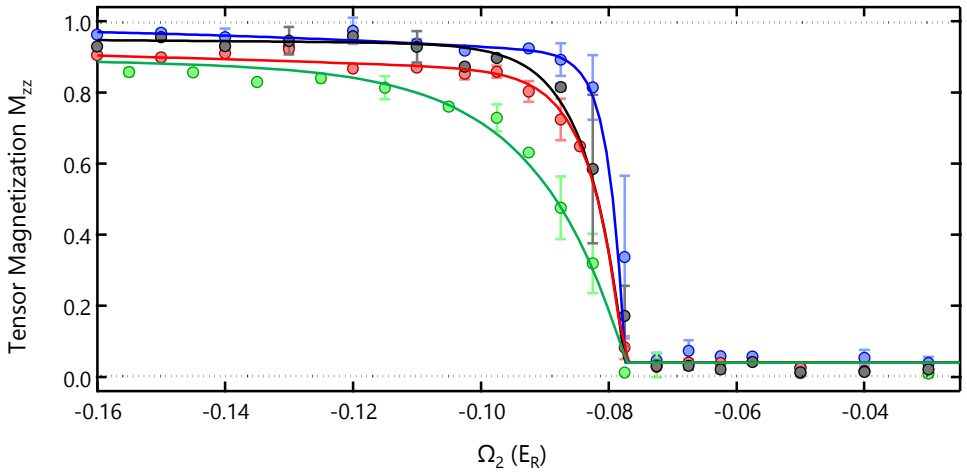

Figure 7.12: Quenching dynamics The system was prepared in the unmagnetized phase with $\Omega_1 = 0.74(8)E_R$ and Ω_2 was ramped through the phase transition at ramp-rates $d\Omega_2/dt = -0.2, -0.3, -0.4$, and $-0.5E_R$/s (blue, black, red, and green symbols, respectively). The curves are guides to the eye.

For all the experimentally measured critical points (Figure 7.10), separating the unmagnetized and ferromagnetic phase, we also measured the corresponding transition width defined as the required interval for the curve to fall from 50% to 20% of its full range. This width Δ decreases sharply at Ω_1^*, marking the crossover between second- and first-order phase transitions as shown in Figure 7.10, bottom. In these data, the width of the first-order transition becomes astonishingly narrow: as small as $0.0011(3)E_R = h \times 4(1)$Hz at $\Omega_1 = 0.41(1)$. This narrowness results from the energetic penalty associated with condensation into multiple modes for repulsively interacting bosons.

7.3.3 Metastable Scans

Systems taken through a first-order phase transition can remain in long-lived metastable states as described previously in Section 7.1.2. We began our study of this metastability by quenching through the first-order transition at $\Omega_1 = 0.74(8)E_R$ with differing rates from 0.5 to 0.2 E_R/s, as shown in Figure 7.12. We observed the transition width continuously decreases with decreasing ramp rate, consistent with slow relaxation from a metastable initial state.

We explored the full regime of metastability by initializing BECs in each of the m_F states, at fixed Ω_2, then rapidly ramping Ω_1 from zero to its final value fast enough that the system did not adiabatically follow into the true ground state, yet slow enough that the quasi-equilibrium metastable state was left near its local equilibrium. We found that the rate $\lesssim 200E_R/s$ was a good compromise between these two requirements. For points near the first-order phase transition three metastable states exist (Figure 7.14); near the second-order transition this count decreases, giving two local minima which merge to a single minimum beyond the second-order transition.

We experimentally identified the number of metastable states by using M_z and its higher moments, having started in each of the three m_F initial states. A small variance in M_z, less than 0.25, indicates the final states are clustered together (associated with a single global minimum) and it increases when metastable or degenerate ground states are present. We distinguished systems with two degenerate magnetization states ($M_z \approx \pm 1$) from those with three states by the same method, since when $M_z \approx \pm 1$, the variance of

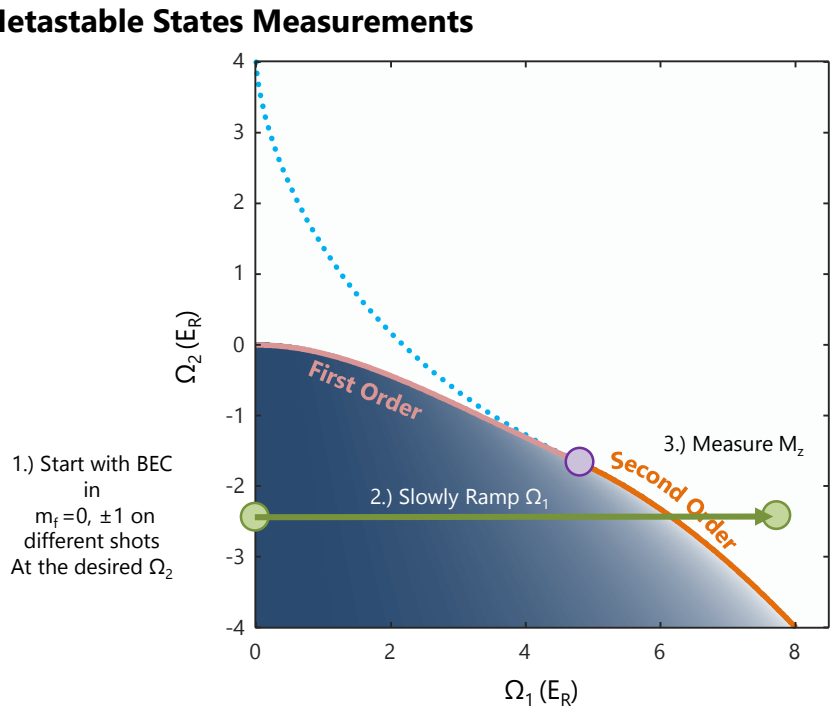

Figure 7.13: Experimental sequence for measuring the metastability in the magnetic system. For each value of (Ω_1,Ω_2) that we measured, we take three separate measurements. The three measurements are performed with the ramp shown, but initializing the BEC in either the $m_F = 1, 0, -1$ states.

$|M_z|$ is smaller than 0.25, and it distinguishably increases beyond 0.25 as a third metastable state appears with $M_z = 0$. In this way we fully mapped the system's metastable states in agreement with theory, as shown in Figure 7.14.

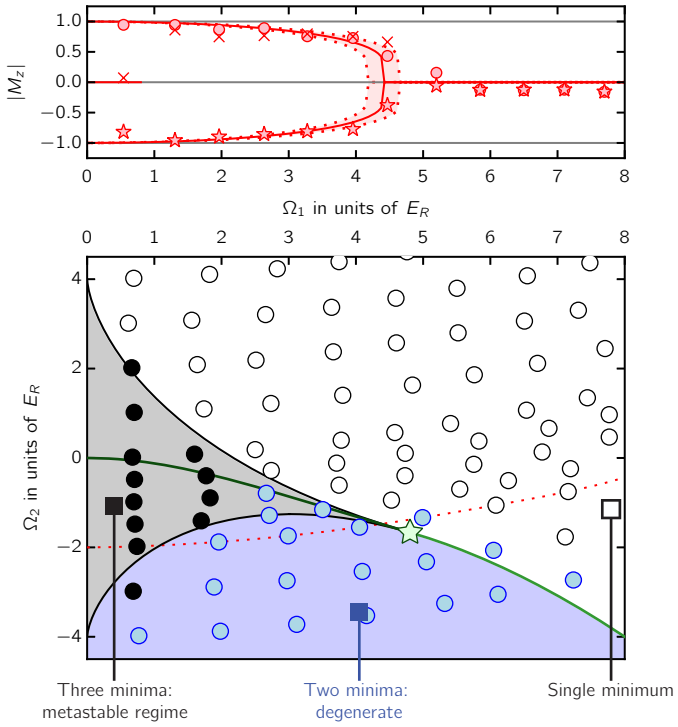

Figure 7.14: Top: Measured magnetization plotted along with theory. The system was prepared at the desired $\Omega_2 = -2E_R$; $\Omega_1(t)$ was then increased to its displayed final value; during this ramp Ω_2 also changed, and the system followed the curved trajectory in the bottom panel. Each displayed data point is an average of up to 10 measurements, and the colored region reflects the uncertainty in theory resulting from our $\approx 5\%$ systematic uncertainty in Ω_1. Circles/crosses/stars represent data starting in $m_F = +1$, 0, and -1 respectively. Bottom: Parameter space theory and experiment. Blue: two states; black: three states; white: one state. Colored areas denote calculated regions where the color-coded number of stable/metastable states are expected. Green star represents the critical point where the phase transitions (dark/light solid green) go from first to second order. Symbols are the outcome of experiment. Each displayed data point is an average of up to 20 measurements.

7.4 Conclusion

In conclusion, we accurately measured the two-parameter phase diagram of a spin-1 BEC, containing a ferromagnetic phase and an unmagnetized phase, continuously connecting a polar spinor BEC to a spin-helix BEC. The ferromagnetic phase in this itinerant system is stabilized by SOC, and vanishes as the SOC strength $\hbar k_R$ goes to zero. Our observation of controlled quench dynamics through a first-order phase transition opens the door for realizing Kibble-Zurek physics [50, 105] in this system, where the relevant pa-

rameters can be controlled at the individual Hz level. The quadrupole tensor field $\propto \hat{\mathbf{F}}^{(2)}_{zz}$ studied here is the $q = 0$ component of the rank-2 spherical tensor operator $\hat{\mathbf{F}}^{(2)}_{q}$, with $q \in \{\pm 2, \pm 1, 0\}$. The physics of this system would be further enriched by the addition of the remaining four tensor fields. The $q = 0$ term we included is the simplest of the tensor fields to deploy, as it required control over frequencies. The $q = \pm 1$ components are relatively simple to incorporate by RF-coupling the $|m_F = -1\rangle$ to $|m_F = 0\rangle$ and $|m_F = +1\rangle$ to $|m_F = 0\rangle$ transitions with different phases. The $q = \pm 2$ components require direct coupling between $|m_F = +1\rangle$ and $|m_F = -1\rangle$ which is straightforward using two-photon microwave transitions, but is challenging to include with significant strength.

Chapter 8

Vortices in Non-Uniform Magnetic Fields

8.1 Overview of Vortices in Quantum Fluids

Degenerate ultracold atomic gases are a kind of quantum fluid which can have behavior analogous to those present in other quantum systems ranging from exotic materials [106, 107], to neutron stars [108]. Quantized vortices are a common element present in superconductors [109], superfluids [110], and dilute atomic Bose-Einstein condensates (BECs) [74], or any system where the single valuedness of the wavefunction demands quantized circulation.

Here I discuss the physics of vortices in BECs, and the conditions in which they are energetically favorable to form within the condensate. In the following sections, I take a hydrodynamic approach that treats the condensate as a superfluid for all practical purposes.

8.1.1 Mass Flow and Conditions for Quantized Circulation

To consider the fluid flow of a condensate, we need to discuss the condensate in terms of a density and mass flow. We start we the time-dependent Gross Pitaevskii equation:

$$i\hbar\frac{\partial}{\partial t}\psi(\vec{\mathbf{r}},t)=\left(-\frac{\hbar^2}{2m}\nabla^2+V(\vec{\mathbf{r}})+g|\psi(\vec{\mathbf{r}},t)|^2\right)\psi(\vec{\mathbf{r}},t) \tag{8.1}$$

As mentioned we are interested in the density $n=|\psi|^2$. Using the hydrodynamic description of BECs [16], to find the velocity of the fluid we multiply Equation 8.1 by ψ^* and subtract by the complex conjugate to get:

$$0=\frac{\partial}{\partial t}|\psi|^2+\nabla\cdot\left(\frac{\hbar}{2mi}(\psi^*\nabla\psi-\psi\nabla\psi^*)\right) \tag{8.2}$$

We define the velocity of the condensate as:

$$\vec{\mathbf{v}}=\frac{\hbar}{2mi}\frac{(\psi^*\nabla\psi-\psi\nabla\psi^*)}{|\psi|^2} \tag{8.3}$$

Making the substitution that $n=|\psi|^2$ and the definition of v into Equation 8.2:

$$0=\partial_t n+\nabla\cdot(n\vec{\mathbf{v}}) \tag{8.4}$$

Which is the continuity equation for the dilute gas (directly analogous to the continuity for fluids [111] and for charge conservation in electromagnetism [112]).

If we consider a wavefunction of the form $\psi(\vec{\mathbf{r}})=f(\vec{\mathbf{r}})e^{il\phi(\vec{\mathbf{r}})}$, that has a real amplitude f and a imaginary phase factor term then by Equation 8.2 it follows that the velocity of the condensate is given as:

$$\vec{\mathbf{v}}=\frac{\hbar}{m}\nabla\phi(\vec{\mathbf{r}}) \tag{8.5}$$

The interesting result from this hydrodynamical model is that the velocity flow of the condensate is irrotational, i.e. $\nabla\times\vec{\mathbf{v}}=0$. The wavefunction of the condensate must also be single-valued and continuous, therefore along any closed loop in space, the phase of the condensate can only advance by $2\pi l$ where l is an integer value. This requirement, more

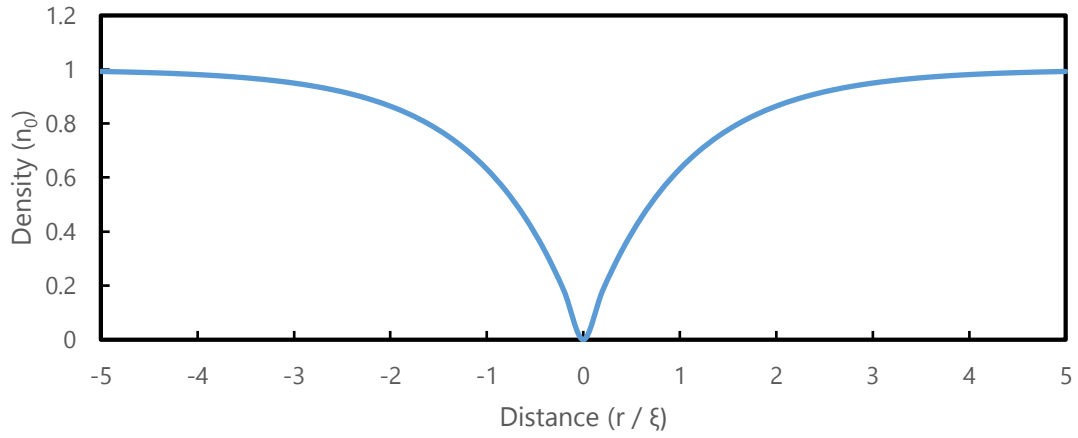

Figure 8.1: Radial cross-section of a uniform medium with a vortex at the center. Due to the conditions on the wavefunction, the density must go to zero at the vortex core and at far distance the density will approach a constant value.

mathematically stated is:

$$\Delta\phi = \oint \nabla\phi \cdot d\vec{\mathrm{l}} = 2\pi l \tag{8.6}$$

Using the identity in Equation 8.5, we get:

$$\phi = \oint \vec{\mathbf{v}} \cdot d\vec{\mathrm{l}} = \frac{2\pi\hbar l}{m} = \frac{h}{m} l \tag{8.7}$$

Therefore the circulation of the velocity around a closed curve is quantized in angular momentum, leading to singular defects in the density, i.e. vortices, at a central point. The winding phase of ϕ must become singular at a point in the advancement by 2π in a rotational geometry. Therefore to avoid a diverging wavefunction at the central point, the density f of the condensate goes to zero.

8.1.2 Vortices in BECs

A Single Vortex in a Uniform Fluid

Before going full into the physics of vortices in condensates, I start with an introductory case here for the vortex in a spatially uniform fluid (i.e. $V(x, y, z) = 0$). Here I focus on

the energy cost for a vortex to be placed into the system. We can calculate the energy cost of the vortex being present by looking at the Hamiltonian of the system:

$$\begin{aligned} E &= \langle\psi|\,\hat{\mathbf{H}}\,|\psi\rangle = \int \psi^*\hat{\mathbf{H}}\psi \ \mathrm{dr} \\ &= \int d\vec{\mathbf{r}}\left(\frac{\hbar^2}{2m}|\nabla\psi|^2 + V|\psi|^2 + \frac{g}{2}|\psi|^4\right) \end{aligned} \tag{8.8}$$

However, we can simplify for our case of a uniform gas with a trapping potential $V = 0$. From the discussion in the previous section, I start with a generic wavefunction with a real valued amplitude and imaginary phase term that can contain a phase winding:

$$\psi(r,z) = \rho(r,z)^{1/2}e^{il\phi} \tag{8.9}$$

Where ρ is the density of the BEC (a real-valued function), ϕ is the phase angle of the wavefunction, and l is an integer to account for multiples of 2π. If we cast the energy calculation in terms of cylindrical coordinates (i.e. no z dependence), and insert our generic wavefunction we get:

$$E = \int d\vec{\mathbf{r}}\left(\frac{\hbar^2}{2m}\left[(\partial_r\rho)^2 + \frac{\rho^2 l^2}{r^2}\right] + \frac{g}{2}\rho^4\right) \tag{8.10}$$

To perform this integral, we need to put bounds on the volume in which we are integrating over (as a uniform gas will have infinite energy in infinite space). Here I consider the volume of a cylinder of radius a, such that the integral becomes:

$$E = \int_0^a 2\pi r dr\left(\frac{\hbar^2}{2m}\left[(\partial_r\rho)^2 + \frac{\rho^2 l^2}{r^2}\right] + \frac{g}{2}\rho^4\right) \tag{8.11}$$

Note that this is the total energy of the system, including the vortex. To find the energy cost of the vortex, we need to subtract the energy of the system without the vortex. For the uniform system with no vortex, the density is a constant uniform value of $\rho = \rho_c$. If we take Equation 8.11 with $l = 0$ (no circulation) then we get the energy of the stationary state, E_0:

$$E_0 = \int_0^a 2\pi r dr \left(\frac{g}{2}\rho_c^4\right) \tag{8.12}$$

However, we also need to account for the difference in the density form the vortex and non-vortex configurations. Under the constraint of constant atom number in a given volume, when the vortex is present the density far from the core must be larger then in the uniform case as the mass near $r = 0$ has been displaced outward to larger r. This effect will change the interaction energy term in Equation 8.11 between the vortex and non-vortex scenarios. To account for this, we again consider our cylindrical volume of radius a. The atom number is constant, which means the integration over the number densities must be equal as well. The expression for the particles per unit length n_l for the no vortex case:

$$n_l = \pi a^2 \rho_c^2 - \int_0^a 2\pi dr \left(\rho_c^2 - \rho^2\right) \tag{8.13}$$

Note that in the limit of the vortex density profile ρ becoming constant, this expression simply evaluates to the average density in a uniform medium. Combining number density with the interaction energy definition, the energy density from interactions becomes:

$$E_{int} = \int_0^a 2\pi r dr \left(\frac{g}{2}\rho_c^4\right) - \rho_c^2 g \int_0^a dr\, 2\pi r(\rho_c^2 - \rho^2) \tag{8.14}$$

Using the correction from the density profile modifying interactions, we can subtract the energy of the system without a vortex, E_0, from the total energy of the system with the vortex, E_v:

$$E_v = \int_0^a 2\pi r dr \left(\frac{\hbar^2}{2m}\left[(\partial_r \rho)^2 + \frac{\rho^2}{r^2} l^2\right] + \frac{g}{2}(\rho_c^2 - \rho^2)^2\right) \tag{8.15}$$

Which vanishes if $l = 0$ (no vortex) and the density becomes constant. The amplitude of the condensate wavefunction can be determined directly (i.e. numerically) by solving the GPE for ρ:

$$\mu\rho = \frac{\hbar^2}{2m}\left[-\frac{1}{r}\partial_r\left(r\partial_r\rho\right) + \frac{l^2}{r^2}\rho\right] + g\rho^3 \tag{8.16}$$

In the case of a numerical solution, the energy of the vortex in the uniform fluid can be calculated using Equation 8.15 [16]:

$$E_v = \frac{\pi\hbar^2\rho_c}{m}\ln\left(1.464\frac{a}{\xi}\right) \tag{8.17}$$

Where $\xi = (8\pi a_{\text{scat}} n_0)^{1/2}$ (Section 2.2.3) is the healing length of the condensate.

Vortices in a Trapped Condensate

As an extension to the uniform condensate, we can advance the discussion to the energy associated with a vortex inside a confined condensate. For simplicity, I consider the case of the experimentally relevant geometry of a harmonic potential where there is a cylindrical symmetry $\omega_x = \omega_y \neq \omega_z$ with a vortex at $r = 0$. Because the radius of the condensate in plane, R_{TF}, is significantly larger than the size of the vortex, approximately the healing length ξ, the result in Equation 8.17 is valid for length scales intermediate to these two.

To account for the trapping potential in plane, we consider the kinetic energy of the rotating condensate for values of $R_{\text{TF}} > r > a$. Each particle at a distance r will have a kinetic energy of $E = 1/2mv(r)^2$. To find the total kinetic energy contribution, we integrate along the radial direction and multiply by the density of atoms as a function of the radius:

$$E_K = \frac{1}{2}m\int_a^{R_{\text{TF}}} dr\, 2\pi r n(r) v(r)^2 \tag{8.18}$$

Where $n(r)$ is the radial density of the condensate. The density profile of the condensate at a radius r away from the vortex core is simply given by the Thomas-Fermi profile (Section 2.2.4):

$$n(r) = n_0(1 - \frac{r^2}{R_{\text{TF}}^2}) \tag{8.19}$$

Where n_0 is the density at the center of the condensate if there were no vortex present. The velocity of the condensate can likewise be calculated from the expressions in Equation 8.5 and Equation 8.7:

$$v(r) = \frac{\hbar}{mr} \tag{8.20}$$

If we combine Equation 8.19 with Equation 8.20 in Equation 8.18, we get the kinetic energy contribution as:

$$E_K = \frac{\pi n_0 \hbar^2}{m} \int_a^{R_{\rm TF}} dr \, \frac{1}{r} \left[1 - \frac{r^2}{R_{\rm TF}^2} \right] \tag{8.21}$$

Evaluating Equation 8.21 gives the energy cost due to the trap as:

$$E_K = \frac{\pi n_0 \hbar^2}{m} \left[\ln(R_{\rm TF}) - \ln(a) + \frac{1}{2} \left(\frac{a^2}{R_{\rm TF}^2} - 1 \right) \right] \tag{8.22}$$

$$\tag{8.23}$$

Using the approximation that $a << R_{\rm TF}$ to neglect the quadratic term, we get a final approximate contribution of:

$$E_K = \frac{\pi n_0 \hbar^2}{m} \left[\ln \left(\frac{R_{\rm TF}}{a} \right) - \frac{1}{2} \right] \tag{8.24}$$

To find the total energy of the vortex in the trapped system, we add the kinetic energy in Equation 8.24 to the uniform case in Equation 8.17 to get the total energy of:

$$E_v = \frac{\pi n_0 \hbar^2}{m} \left[\ln \left(1.464 \frac{a}{\xi} \right) + \ln \left(\frac{R_{\rm TF}}{a} \right) - \frac{1}{2} \right] \tag{8.25}$$

$$= \frac{\pi n_0 \hbar^2}{m} \ln \left(0.888 \frac{R_{\rm TF}}{\xi} \right) \tag{8.26}$$

Thus the presence of the trap does not significantly change the functional form of E_v, but just the numerical constant within the logarithm.

To consider the energy cost for the full three dimensional system, under the condition that $R_z >> \xi$, we can approximate the energy of the vortex in the condensate as being composed of multiple two dimensional systems with a central vortex [113]. In

this description the density profile n_0, (and therefore the healing length ξ) and the radial extent of the condensate R_{TF} all become functions of z. For a radial slice, we get a small energy contribution described by Equation 8.26:

$$dE(z) = \frac{\pi n(z)\hbar^2}{m} \ln\left(0.888\frac{R_{\mathrm{TF}}(z)}{\xi(z)}\right) dz \tag{8.27}$$

Again, the Thomas-Fermi description of the condensate (Section 2.2.4) saves us from effort as we can quote the density and radius as:

$$\begin{aligned} n(z) &= n_0\left(1 - \frac{z^2}{R_z^2}\right) \\ R(z) &= R_{\mathrm{TF}}\left(1 - \frac{z^2}{R_z^2}\right)^{1/2} \end{aligned} \tag{8.28}$$

The healing length is slightly trickier, but likewise can be computed as:

$$\xi(z) = \xi_0 \left(n_0/n(z, r = 0)\right)^{1/2} \tag{8.29}$$

Where ξ_0 is the healing length at the center of the condensate, n_0 is the density at the center of the condensate and $n(z, r = 0)$ is the density along the z-axis of the condensate. Therefore we can express the vortex energy per slice of the condensate in Equation 8.27 as:

$$dE(z) = \frac{\pi n_0\hbar^2}{m}\left(1 - \frac{z^2}{R_z^2}\right) \ln\left(0.888\frac{R_{\mathrm{TF}}}{\xi_0}\left[1 - \frac{z^2}{R_z^2}\right]\right) dz \tag{8.30}$$

If we want the total energy of the vortex, we integrate across all values of z:

$$\begin{aligned} E_v &= \int_{-R_z}^{R_z} dE(z) \\ &= 2\int_0^{R_z} dz\, \frac{\pi n_0\hbar^2}{m}\left(1 - \frac{z^2}{R_z^2}\right) \ln\left(0.888\frac{R_{\mathrm{TF}}}{\xi_0}\left[1 - \frac{z^2}{R_z^2}\right]\right) \end{aligned} \tag{8.31}$$

Here I used the z axis symmetry of the condensate to alter the bounds of integration. Thanks to an old table of integrals hidden deep somewhere within the catacombs of math-

ematical knowledge, a similar integral can be evaluated as [113]:

$$\int_0^1 dx(1-x^2)\ln(1-x^2) = \frac{1}{9}(12\ln(2)-10) \tag{8.32}$$

Using the relationship in Equation 8.32 to evaluate Equation 8.31 for the vortex energy (using appropriate rescaling of the integration variable z), we get:

$$E_v = \frac{4\pi\hbar^2 n_0 R_z}{3m}\ln\left(0.671\frac{R_{\mathrm{TF}}}{\xi_0}\right) \tag{8.33}$$

Given the trap geometry the condensate is in, and the number of atoms within the condensate, the energy of a vortex forming can be calculated using Equation 8.33. The astute reader may wonder how a vortex can form, as Equation 8.33 suggests a vortex will always carry an energy penalty that the system will avoid. In the next section I will discuss the barrier of entry of vortices, and the associated rotational dynamics to create conditions favorable for vortices to nucleate within the BEC.

Rotating Condensates and the Barrier to Entry of Vortices

For a vortex to be energetically favorable, we must compare the energy of the stationary ground state compared to the energy of a condensate with a vortex in a frame rotating with an angular frequency Ω. The energy of the condensate rotating around the z-axis in the rotating frame is given as $E_R = E_S - \Omega L_z$, where E_R and E_S represent the rotating and non-rotating energies respectively [114]. Therefore we can define a critical value of the rotation frequency such that the rotating state will be energetically favorable as:

$$\Omega_c = \frac{E_R - E_S}{L_z} \tag{8.34}$$

We know the difference in the numerator as the vortex energy E_v from Equation 8.33. The angular momentum, on the other hand, is still to be calculated. The angular momentum L_z of the condensate is $\hbar$ multiplied by the number of particles in the condensate. Cast in terms of a density, we calculate:

$$L_z = \int_{-Z}^{Z} dz \int_0^{R_{\mathrm{TF}}} 2\pi dr \left(1 - \frac{r^2}{R_{\mathrm{TF}}^2} - \frac{z^2}{R_z^2}\right) \tag{8.35}$$

This is simply the result derived in Equation 2.42 for the atom number in the Thomas-Fermi approximation multiplied by $\hbar$:

$$L_z = \frac{8\pi}{15}\hbar n_0 R_z R_{\mathrm{TF}}^2 \tag{8.36}$$

We can combine Equation 8.34 with Equation 8.36 to get the critical angular frequency of rotation in which the vortex state becomes energetically favorable:

$$\Omega_c = \frac{E_v}{L_z} = \frac{5\hbar}{2mR_{\mathrm{TF}}} \ln\left(0.671\frac{R_{\mathrm{TF}}}{\xi_0}\right) \tag{8.37}$$

Connection Between Rotation and Magnetic Fields

In the context of Section 8.2, it is important to discuss the relationship between magnetic fields and rotation in terms of vortices. The equivalence of the Lorentz force for particles in uniform magnetic fields and the Coriolis force for a rotating system allows us to extend the discussion of vortices as introduced by magnetic fields, here specifically synthetic magnetic fields acting upon our charge neutral BECs. For a given synthetic field B, we can define a cyclotron frequency such that $\Omega = qB/m$. Here the cyclotron frequency has a direct correspondence to the rotation frequency in the previous section, allowing us to similarly define a critical synthetic magnetic field strength in which vortices appear:

$$\Omega_c = \frac{qB_c}{m} = \frac{5\hbar}{2mR_{\mathrm{TF}}} \ln\left(0.671\frac{R_{\mathrm{TF}}}{\xi_0}\right) \tag{8.38}$$

Or in terms of the magnetic field:

$$B_c = \frac{5\hbar}{2qR_{\mathrm{TF}}} \ln\left(0.671\frac{R_{\mathrm{TF}}}{\xi_0}\right) \tag{8.39}$$

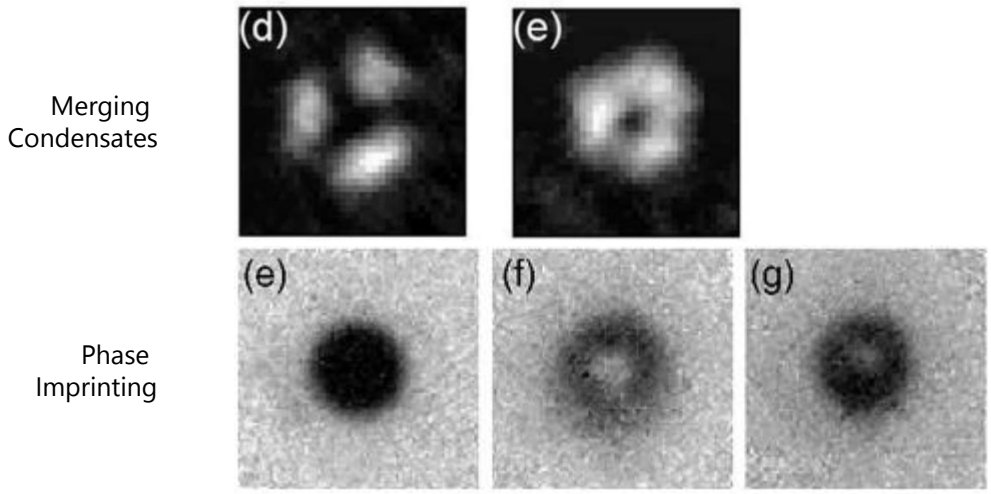

Figure 8.2: Top: Vortices generated by three separated BECs which are then merged together. The phase difference between the BECs can vary such that there is an azimuthal phase winding, thereby generating flow. Picture from experiment in [116]. Bottom: An inverting magnetic field is used to introduce a topological phase into the condensate. Picture from [117].

8.1.3 Experimentally Generating Vortices in Condensates

Since the first observation of vortices in BECs [115] there have been various mechanisms used to nucleate vortices into condensates. In this section I will provide an overview to the varying methods and their characteristics.

Engineering Phase Windings

In various experiments, vortices were created in BECs by generating a wavefunction that has a phase singularity imprinted into it, as described in Equation 8.5. From Equation 8.5, this will create an azimuthal mass flow, thereby generating a vortex. These methods typically generate a low number of vortices (order unity) as it becomes more experimentally difficult to generate the requisite number of phase windings required for more circulation. Examples are shown in Figure 8.2.

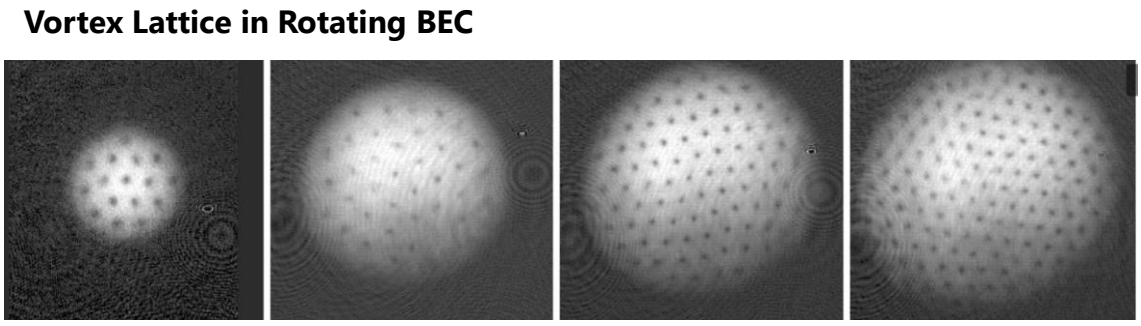

Figure 8.3: Vortices and vortex lattice generated from a stirring laser. Image from Reference [119]

Applied Rotation to Condensates

In comparison to imprinting the appropriate phase conditions, other experiments created vortices in a BEC via rotation of the cloud. This method includes those that use a blue detuned optical beam rotating in time (providing the time dependent force) and rotating traps. This method uses the rotation of the condensate to cause the vortex state to be energetically preferable as discussed in Section 8.1.2. In this method, a stationary BEC is subjected to a rotation, and the system is allowed to evolve into the rotating ground state configuration preferring vortex formation.

Rotating traps can produce large number of vortices (Figure 8.3) as the BEC relaxes into the rotating ground state. The number of vortices N_v the system can support at a given rotation Ω is given by:

$$N_v = \frac{2m\Omega}{h}A \tag{8.40}$$

Where A is the area of the condensate projected onto the rotation vector direction. From the density profiles of a confined condensate (Section 2.2.4), the area is related to the number of atoms in the condensate, hence a larger condensate with many atoms can support a larger number of vortices in rotational equilibrium. While the system can support many vortices in equilibrium, the time to equilibrate can be comparable to the lifetime of the condensates ($\sim$ 1 second). Over these long times, the vortices are predicted to form a triangular lattice (Figure 8.3) in an infinitively large medium [118].

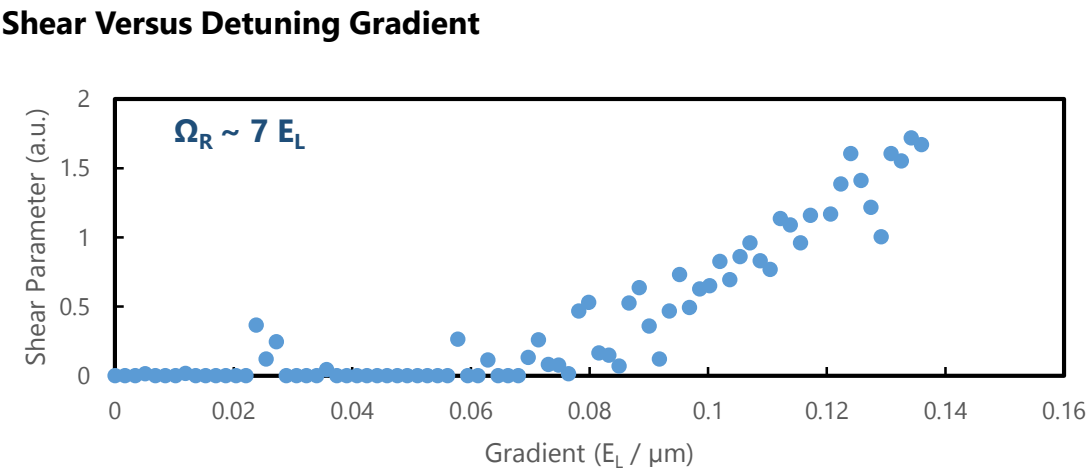

Figure 8.4: Onset of vortex nucleation via synthetic magnetic fields as measured by the shear in the BEC density after TOF [83]. The sudden increase in shear as the detuning gradient is increased (which determines the synthetic field strength, Section 6.1.5) coincides with the observation of vortices in the system.

Generating Vortices via a Synthetic Gauge Field

Owing to the analogy between the Lorentz force and the Coriolis force, a BEC of charged particles will experience the same vortex nucleation dynamics as a rotating charge neutral BEC. As described in Chapter 6, we can create a synthetic magnetic field that will drive vortex nucleation within the non-rotating condensate. This approach is unique in that there are no time-dependent potentials, i.e. the synthetic magnetic field is at rest in the lab frame.

This method can be extended into cases where the optical generation of the synthetic field is no longer uniform. In such cases, the non-uniform field can be high strength and tightly confined, creating regions where the effective rotational force overwhelms the other local energy scales, thereby rapidly nucleating vortices into the condensate. The experiment and observations of such effects is described in the latter half of the chapter in Section 8.2.

8.2 Rapid Entry of Vortices via Non-uniform Synthetic Gauge Fields

In this section I discuss the experiment exploring a new mechanism for vortex nucleation in BECs using non-uniform synthetic magnetic fields. In the uniform field experiments, the number of vortices and the rate in which vortices are created is dependent upon the rate of rotation and the density of atoms in the condensate [120–122]. It is energetically favorable for vortices to form at the systems edge, where the low atomic density facilitates vortex formation. These vortices then migrate toward the center of the condensate, where they can ultimately relax to form a vortex lattice.

Even in cases where the effective magnetic field is not uniform across the condensate, the same mechanisms of vortex nucleation, the coupling of perturbations to higher trap modes, applies [123]. Furthermore, the arrangement of the vortices across the condensate will be correlated with the geometry of the effective magnetic field, where vortices preferentially congregate in high field regions. We first prepared pairs of independent BECs in a double-well potential, with an engineered strong artificial magnetic field present in the barrier separating the BECs. We then merged the BECs by lowering the barrier and expanding the region of artificial field to nominally uniformly cover the resulting single BEC.

Here we created an inhomogeneous laser-induced artificial magnetic field ([124]) initially maximized in the space between a pair of separated BECs. Initially, the atomic density in the high field region was small but non-zero, allowing the ready formation of "hidden vortices" [125]. We then gradually expanded the region of high field while merging the BECs, eventually reaching a single BEC in the uniform field limit. In comparison to rotating trap experiments, this method rapidly nucleates vortices in the low atomic density regions between the condensates, which become located at the condensate center after the two BECs merge.

The strength and location of the artificial field, as well as the double-well potential is determined by two parameters, the strength of the Raman coupling interaction, and the spatial detuning used to generate the synthetic magnetic field.

8.2.1 Generating the Separated BECs and Synthetic Field

In Section 6.1.5, I outlined the methods to generate a synthetic magnetic field in BECs via optical interactions. However the original experiments did not fully explore the parameter space between the strength of the spatial detuning and the Raman coupling strength. Within experimentally accessible regimes, there can exist interesting linear vortex structures as predicted by GPE simulations. Here I want to develop the origin of the different parameter regimes in the system, and discuss the different behavior that is manifested.

First, as described in Section 6.1.3, I restrict the study of the system to the lowest dispersion band of the Raman Hamiltonian, under the assumption that the energy difference between the dispersion bands is larger than any other characteristic energy scale. Our system then can be described by an equivalent Hamiltonian for a spinless boson with an vector potential in the $\hat{\mathbf{x}}$ direction:

$$\hat{\mathbf{H}} = \frac{\hbar^2}{2m}(k_y^2 + k_z^2) + V(\mathbf{r}) + \frac{\hbar^2}{2m}(k_x - A_x(\Omega_R, \delta))^2 \tag{8.41}$$

Where A_x, the effective vector potential, depends on the Raman coupling strength Ω_R, and the detuning from the Raman resonance δ. Here I describe the energy and momentum, as per usual, by the characteristic units $E_L = \hbar^2 k_L^2/2m$ and $k_L = \sqrt{2}\pi/\lambda_R$, where λ_R is the wavelength of the Raman beams creating the interaction.

For small Ω_R and $\delta = 0$, the dispersion relationship in the $F = 1$ manifold of ^{87}Rb has three minima at $k \approx -2, 0, +2\, k_L$, with an energy degeneracy between the $k = \pm 2\, k_L$ states. As Ω_R is increased, the dispersion bands will transition from multiple minima to a single minima [84, 126]. As a detuning δ is added, the symmetry between the spin-momenta states is broken and as δ increases, the dispersion band will deform towards a single global minima as described back in Section 6.1.5.

For a pair of δ and Ω_R values, the dispersion relation for the lowest Raman band can be computed and its global minimum energy found. The value of the artificial vector potential A_x is defined at the momentum of the global dispersion minima, and the scalar value ϕ is defined as the downward shift in energy from the uncoupled state. For all

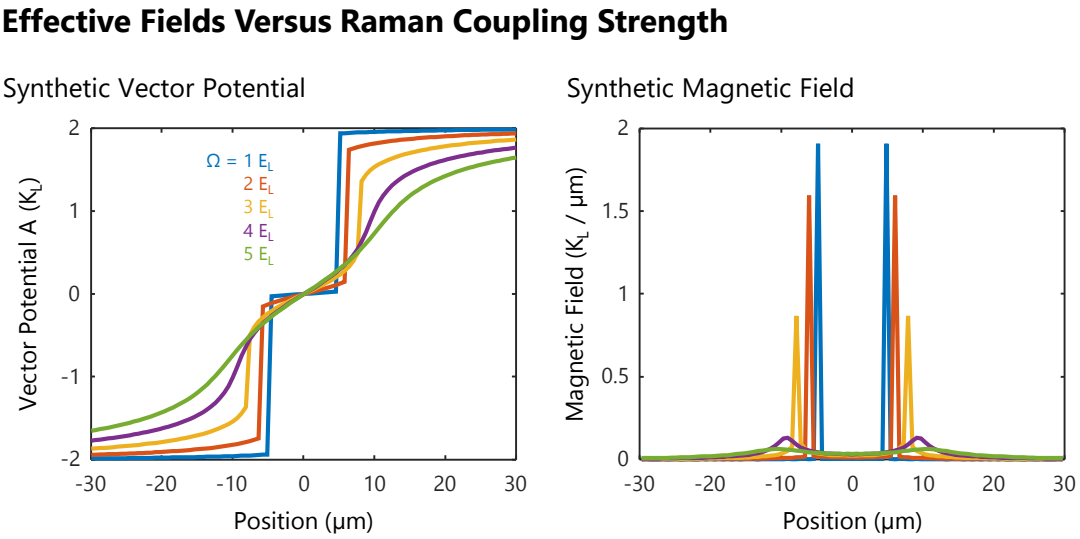

Figure 8.5: Left: Synthetic vector potential curves as a function of increasing Raman coupling strength Ω_{R}. At small values of Ω_{R}, the vector potential has large discontinuities, generating large magnetic fields. Left: Calculation of synthetic magnetic field at various values of Ω_{R}. Both plots are at $\delta' = 300$ Hz/ μm and colors correspond to same values of Ω_{R} on each plot.

$|\delta| > 0$, the presence of the Raman coupling will increase the magnitude of A and shift the minimum dispersion energy ϕ lower as $|\delta|$ becomes larger (see Figure 6.6).

When a linear spatially dependent detuning $\delta(y) = \delta' y + \delta_0$ is introduced, the vector potential becomes a function of y, $A_x(y)$. As a corollary, the spatially dependent vector potential causes the BEC to experience an effective magnetic field $\nabla \times A_x(y) = -B(y)\mathbf{e}_z$ as $\nabla \times A_x(y)$ becomes non-zero. Similarly, the energy shift ϕ becomes a spatially dependent scalar potential $\phi(y)$. Because $\phi(y)$ is negative semi-definite, it always acts as an effective 'anti-trapping' mechanism that competes with the trapping potential along the $\hat{\mathbf{y}}$ direction. It becomes immediately clear that depending on the parameters Ω_R, δ' generating $\phi(y)$ and the trapping potential geometry, there can be different regimes within the system.

In the limit of $\Omega_R \to 0$ and $\delta' > 0$, the system is described by a simple spin dependent potential $\phi(y)$ combined trapping potential. If the linear detuning is generated via magnetic field gradient in $\hat{\mathbf{y}}$, $\phi(y)$ simply becomes the linear Zeeman shift when $\Omega_R = 0$. Depending on the magnitude of δ', the spin components of the BEC will either phase separate in trap, or with large δ', spatially separate into multiple spin dependent trapping

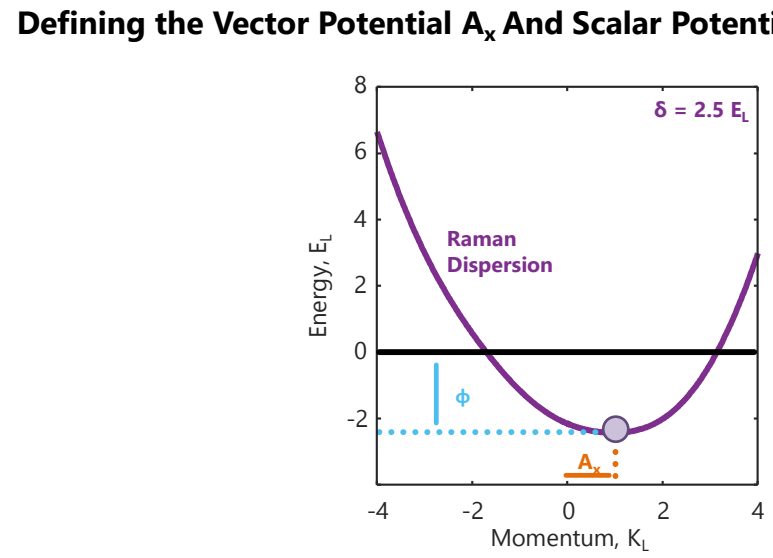

Figure 8.6: Pictoral definition of the scalar potential ϕ and the vector potential A_x. The value of A_x (orange) is the momentum value corresponding to the global minima in the Raman dispersion. The value of ϕ (light blue) is defined as the decrease in energy at the minima from the undressed state.

potentials. For the limit of large Ω_R, $\phi(y)$ becomes weak and the optical trap dominates. In this regime, both the effective trapping potential has a single minima and the vector potential smoothly varies over the BEC, producing a nearly constant effective magnetic field $\mathcal{B}$.

The regime of interest occurs with finite Ω_R and large δ'. Here the scalar potential $\phi(y)$ dominates at distance on the order of the BEC size and will create separated minima in position space with a potential barrier of height V_B. However with finite Raman coupling, the BECs in separate potential wells also experience a vector potential $A_x \approx \pm 2k_L$.

In this regime, Ω_R is small enough that at $\delta = 0$, the dispersion relation $\epsilon_x(k)$ has configurations that support three separate local minima. Small amounts of detuning will break the symmetry and favor a global minima at $\approx \pm 2\, k_L$. For a spatially dependent detuning, the value of $A_x(y)$ will undergo abrupt transitions located at $\pm y^*$ from $k = 0$ to $k = \pm 2$. These abrupt transitions in $A_x(y)$ correspondingly create large values of $B(y)\mathbf{e}_z$ around $\pm y^*$. Because of the design of the vector potential only being monotonically increasing along $\hat{\mathbf{y}}$ (owing to the linear detuning), all points in the BEC within the narrow one-dimensional band $\approx \pm y^*$ will experience the large effective field and areas outside the

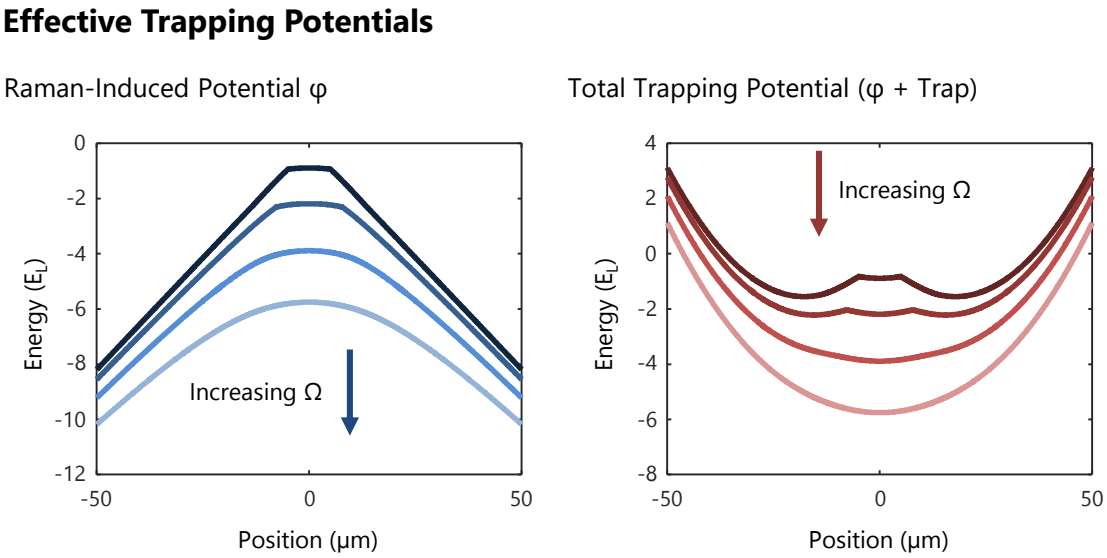

Figure 8.7: Left: Values of the scalar potential ϕ with increasing Raman coupling Ω_R as a function of position ($\delta' = 300$ Hz/ μm). As Ω_R increases from low values (darker blue) to larger values (light blues), the potential lowers and becomes more smooth. Right: The combination of the harmonic trapping potential and the scalar potential ϕ. For small Ω_R (dark reds), the combination of the trap and ϕ generates a double-well configuration. As Ω_R is increased (lighter reds), the potential becomes single-well as the harmonic trap becomes the primary contribution.

band will have $B \approx 0$.

If the scalar potential $\phi(y)$ creates a geometry with $V_B \approx \mu$, the chemical potential of the BEC, that supports a non-negligible atom density at $\pm y^*$, there will be a slice through the BEC with large effective magnetic field within a narrow band. The large field creates similarly large amounts of angular momentum over a narrow region, leading to phase singularities, i.e. vortices, that due to the 1D nature of the strong field, are restricted to a one dimensional strip at $\approx \pm y^*$ within the BEC, with a spacing equal to $2\pi/\Delta k$. Indeed, previous simulations have predicted that within these overlap regions linear vortex structures are formed and are in equilibrium [127].

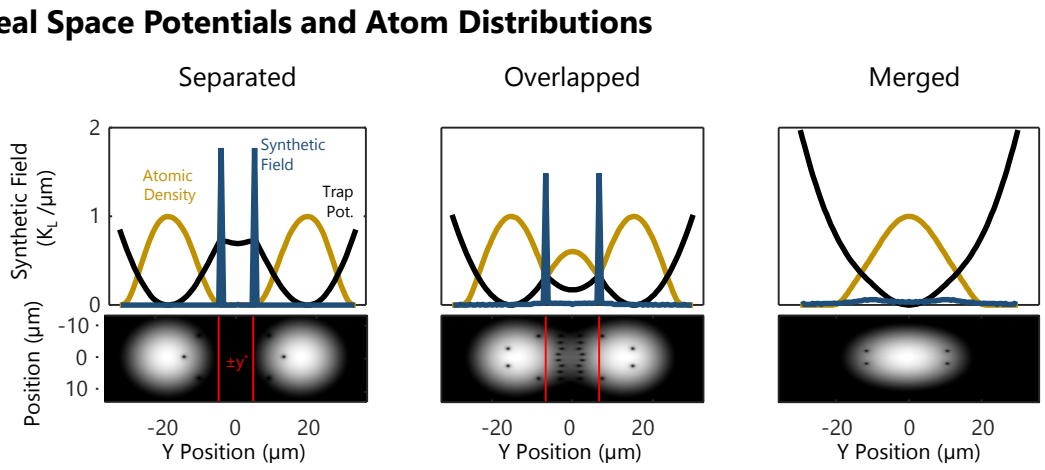

Figure 8.8: Top: The combined trapping potential (black), atomic density (yellow) and synthetic magnetic field (blue) plotted at $\Omega_R = 1, 3, 5$ from left to right respectively. The three values of Ω_R show three different regimes: One where the magnetic field and atoms do not intersect; one where the potential lowers to the point where the atoms can be located at the strong magnetic field; and one where the magnetic field is weak and uniform, and the condensate has merged into a single potential well. Bottom: GPE simulations of the spatial density of atoms at the corresponding values of Ω_R.

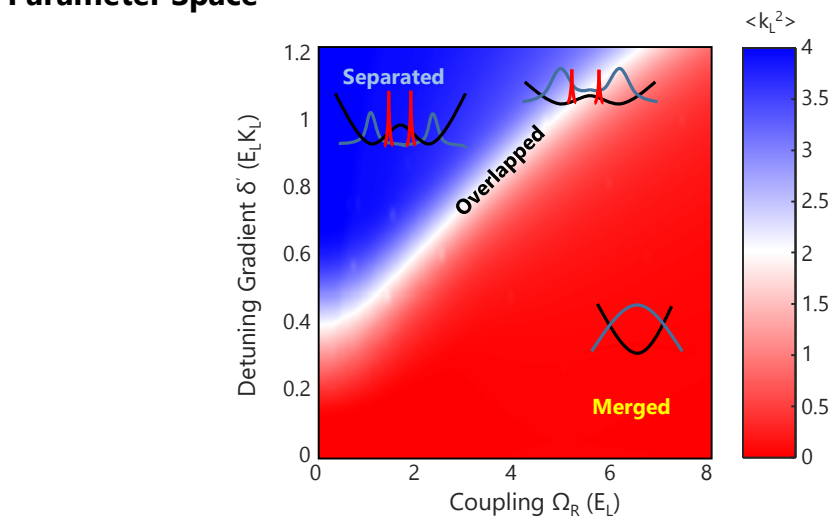

Figure 8.9: Second-moment of the momentum distribution as a function of the Raman coupling strength Ω_R and the detuning gradient δ' in our system. Regions with large moments yields large well separations that have a large synthetic magnetic field between the BECs.

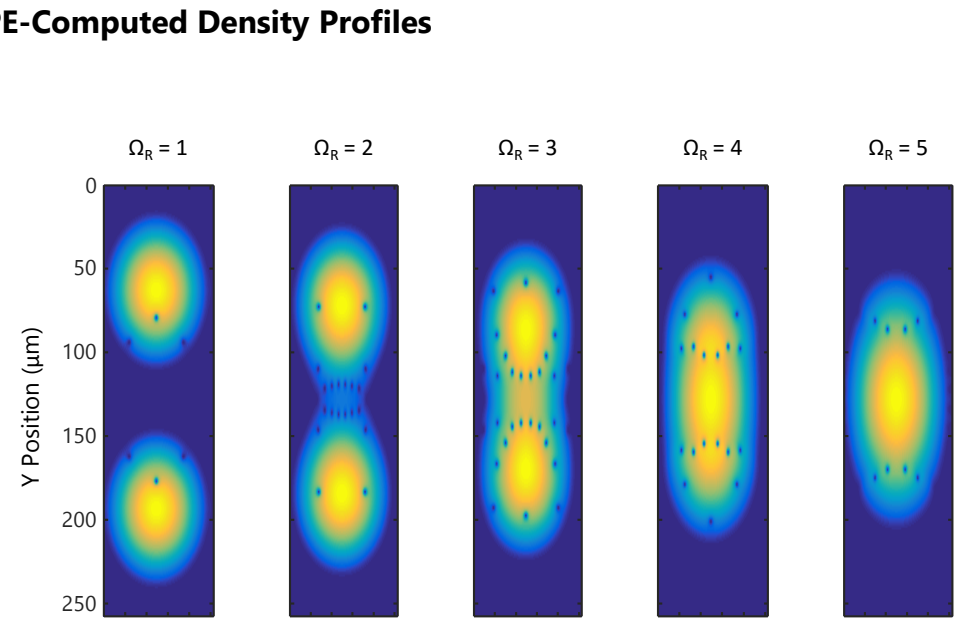

Figure 8.10: Progressions of GPE simulated ground state density profiles at increasing Ω_{R} from left to right at $\delta' = 300$ Hz/ μm. As Ω_{R} is increased, vortices are generated in the low density region between the condensates

8.2.2 Experimental Setup

To study the vortices in this system, we prepared our BEC with an equal fraction of atoms in the $m_F = \pm 1$ states and linearly ramped on the detuning gradient from zero to a desired final value δ' over half a second from 0 to the desired experimental value (up to $450\text{Hz}/\mu\text{m}$) over 0.5 seconds. When $\delta' \neq 0$, the magnetic gradient phase separated the two spin components, forming the precursors of the potential wells in Figure 8.7. We waited an additional 100 ms for the magnetic field environment to equilibrate before linearly ramping on the Raman lasers to a final coupling Ω_{R}. To measure the system at a given $(\Omega_{\text{R}}, \delta')$, we then linearly ramp up Ω_{R} to a measurement value.

Our gradient coils produced a small unwanted contribution to the bias field which we compensated for by adjusting the current in our bias coils, thereby keeping the bias at the system's center constant. The measurement of momentum distributions is highly sensitive to the trapping potential and any constant detuning will break the degeneracy between

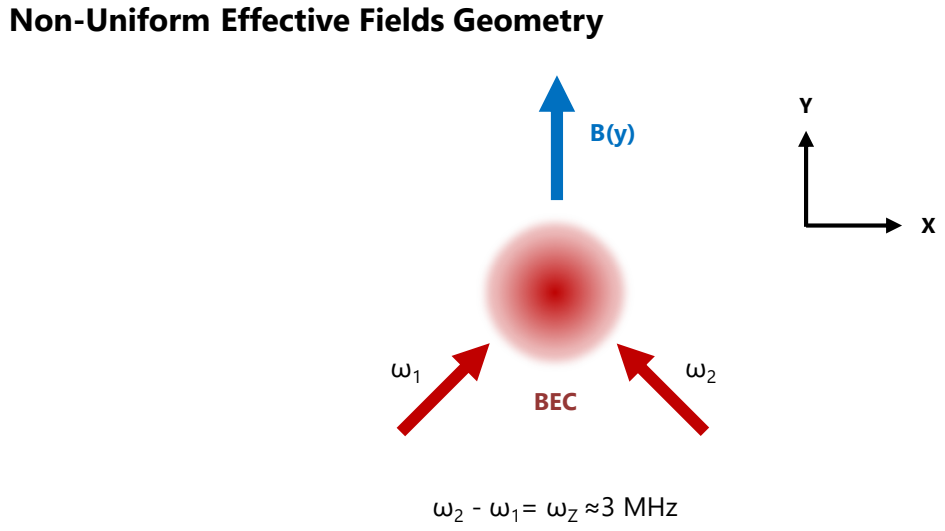

Figure 8.11: We subjected ^{87}Rb BECs to a linearly varying $\mathbf{B} = (B_0 + B'y)\mathbf{e}_y$ magnetic field which gave a position-dependent Zeeman splitting $\hbar\omega_{\text{Z}}(y) = g_F\mu_{\text{B}}|\mathbf{B}(y)|$ between the three m_F states of the $f = 1$ ground state manifold. We then illuminated our BECs with a pair of cross-polarized $\lambda = 790$ nm laser beams propagating along $\mathbf{e}_x \pm \mathbf{e}_y$. The frequency difference $\delta\omega$ between these lasers was detuned by a small $\delta = \hbar[\delta\omega - \omega_Z(y)]$ from the Zeeman-resolved transitions within $f = 1$ ground state manifold, allowing us to couple the Zeeman sub-levels with strength Ω_{R}.

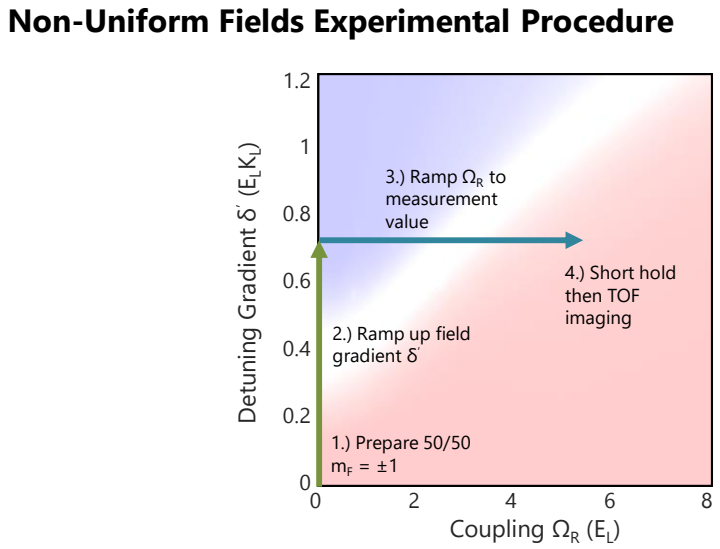

Figure 8.12: Experimental procedure used to measure the momentum distribution and vortex nucleation within the system.

states, and will skew the distribution accordingly. Even with the average detuning noise within our apparatus ($\approx 0.35\,E_L$), the location transition region can vary up to $2\,E_L$, and accordingly affects vortex nucleation properties. Similar to the discussions in Chapter 7, we used the magnetic field stabilization system as described in Section 4.4.7 and Appendix A to remove long term drift.

8.2.3 Measurement and Analysis

We measured our system using standard time-of-flight (TOF) techniques followed by absorption imaging. We initiated TOF by suddenly turning off the confining potentials and in the first 2 ms of TOF we ramped Ω_{R} to zero and simultaneously ramped the detuning $75\,E_L$ from resonance. This process mapped the laser-dressed system into a single spin state [83], and imparted a position-dependent artificial electric field as the vector potential becomes constant, inducing an overall shearing motion [83]. In the regime where one-dimensional vortex structures are predicted to form, it is exceedingly difficult to image the structures in-situ via absorption imaging because of the predicted minimum vortex spacing of $\lambda_R/2\sqrt{2} \approx 300$ nm.

Vortex Counting Algorithm

We developed a vortex counting algorithm in order to systematically measure the number of vortices observed with the BEC. The algorithm is as follows: First, a low-pass filter is applied to the image of the BEC density. This filter removes small scale noise and density modulations, leaving behind only the Thomas-Fermi profile. All regions within the image that are above a threshold value (typically set to be 20 percent of the max density) were considered to be within the BEC region.

The compared to only using a least-squares fitting algorithm to extract a Thomas-Fermi profile of the BEC is that in most images, the shearing and deformation of the gas from the vortex dynamics generates a profile that is no longer properly describe by a Thomas-Fermi shape. In the case of a BEC near the separated-chain region of parameter space, the cloud is thinly spread across momentum and position space. Next, using the low pass density profile, a high pass density profile is obtained by subtracting the unfiltered profile and the low pass profile. The result gives the density modulations that are convolved with the approximately Thomas-Fermi profile. This image also has the threshold applied, making all regions outside of the marked BEC region zero density, and leaving those within at their high-pass values.

Using the prepared density image as previously described, the core of the counting algorithm is to look for islands of negative values within the density modulations. The image is further prepared by setting all values greater than zero to zero, leaving only negative density modulations (the vortices).

Next, the minimum density value is found within the image. In small steps starting at this minimum value up to 0, the image has a threshold applied at min + Δ and all regions that are between the minimum density and the threshold are set to one, creating a binary (black and white) image showing regions that have a density within that region. To determine the location of each region, a boundary tracing algorithm is applied to generate a set of points that are on the perimeter of each region. To find the center of each region, a center of mass calculation is performed on the perimeter points, generating the approximate center of the bounded region. This process is repeated for each (x,y) region center found, and for each threshold value incremented.

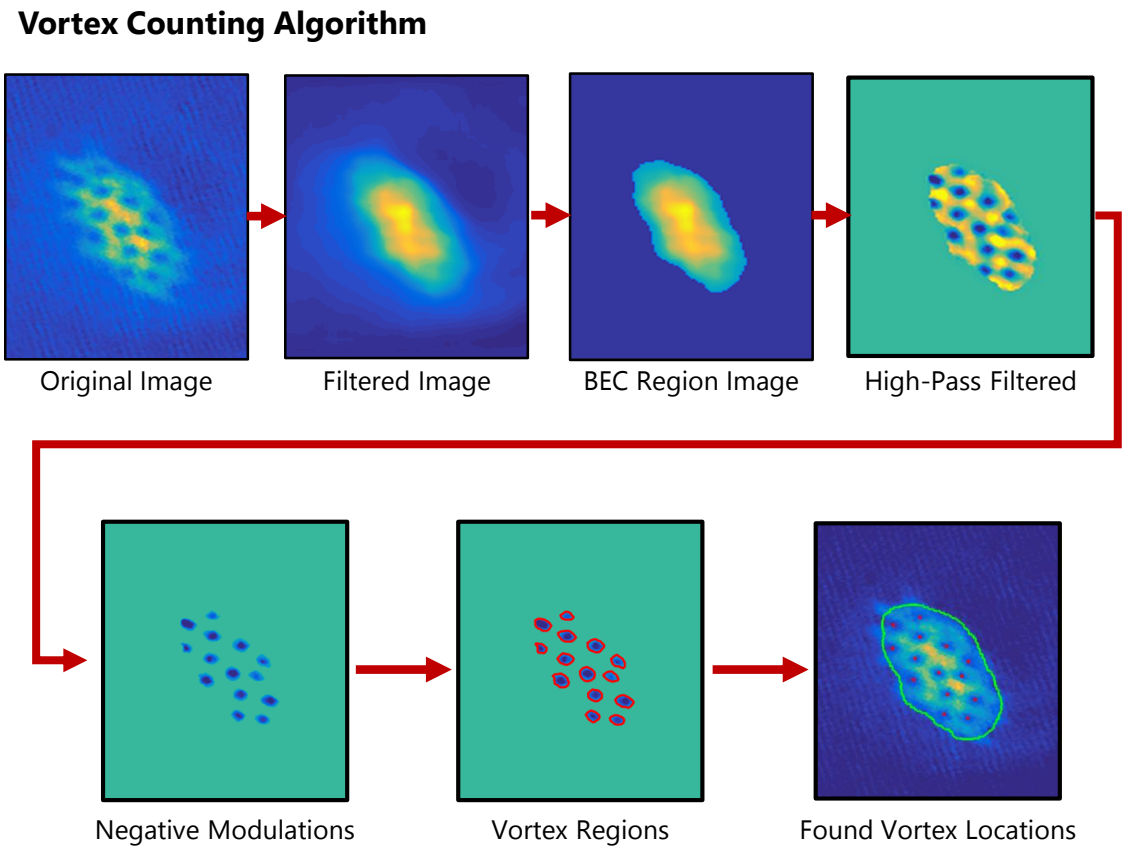

Figure 8.13: Algorithm to count vortices in images of the condensates. The procedure uses 2D filtering methods to extract the frequency modulations in the BEC density corresponding to vortices.

After iterating threshold values and determining regions, the set of center points is filtered to remove duplicate points. Next, a 2D minimization algorithm is applied iteratively using each center point as the starting value, generating a new set of vortex center points. This step weeds out any weak local minima within the density profile. Lastly the relative distances between each of the minima points is generated. Due to the discrete nature of the density profile data, the local minimization solver may find solutions that are separated by a grid point or two, marking them again as duplicate points. The points that remained are considered the vortices within the BEC.

Due to the chaotic nature of the vortex arrangement, only those vortices within the central region of the BEC were counted as they were clearly resolvable. This rejection criterion implies the counting algorithm conservatively reports the number of vortices within the BEC.

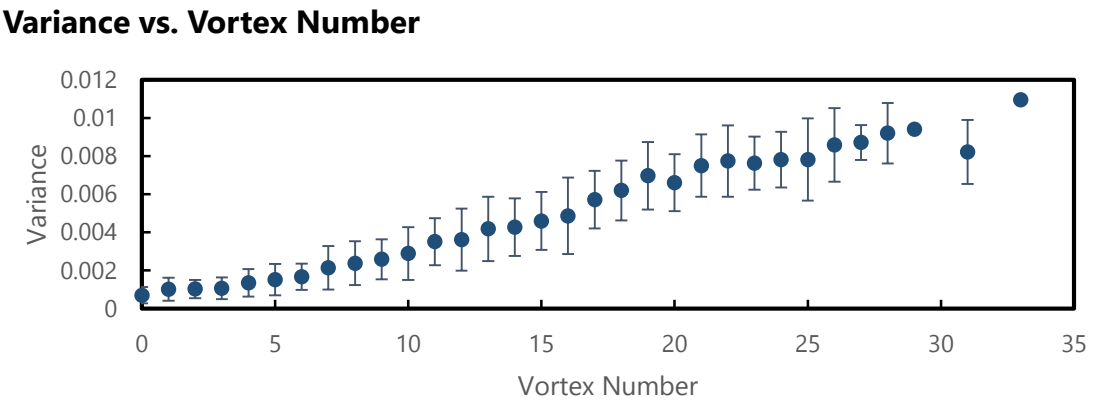

Figure 8.14: Plot of the variance measured in the condensate image after the high-pass filtering step versus the number of vortices reported by the vortex counting algorithm. The comparison was calculated on over $\sim$ 2500 independent realizations at various δ' and Ω_{R}.

Using Variance to Count Vortices

Our counting algorithm performs poorly for disordered vortices, and for those with poor contrast, especially in distributions when the two condensates are partially merged. We found that the variance of high-pass filtered images gave a signal proportional to the vortex-number in images where the counting algorithm succeeded. For BECs with few or no vortices, there should be relatively low variance as the Thomas-Fermi profile has been removed by the filter; only high spatial frequency imaging noise remains. For BECs with many vortices, the variance increases as the regions with and without vortices form a series of high and low peaks in the filtered image respectively. We compared the variance to the counter vortex number for $\sim$ 2500 independent realizations at various Ω_{R} and δ' values and confirmed that the variance is proportional to the vortex number. We therefore use these variances as a proxy signal for the vortex number. The variance measurement of the number of vortices shows a much more dramatic onset of vortices in the non-uniform field regime versus the uniform field regimes compared to the vortex counting algorithm (Figure 8.14). This method accounts for many more vortices that the counting algorithm could identify reliably.

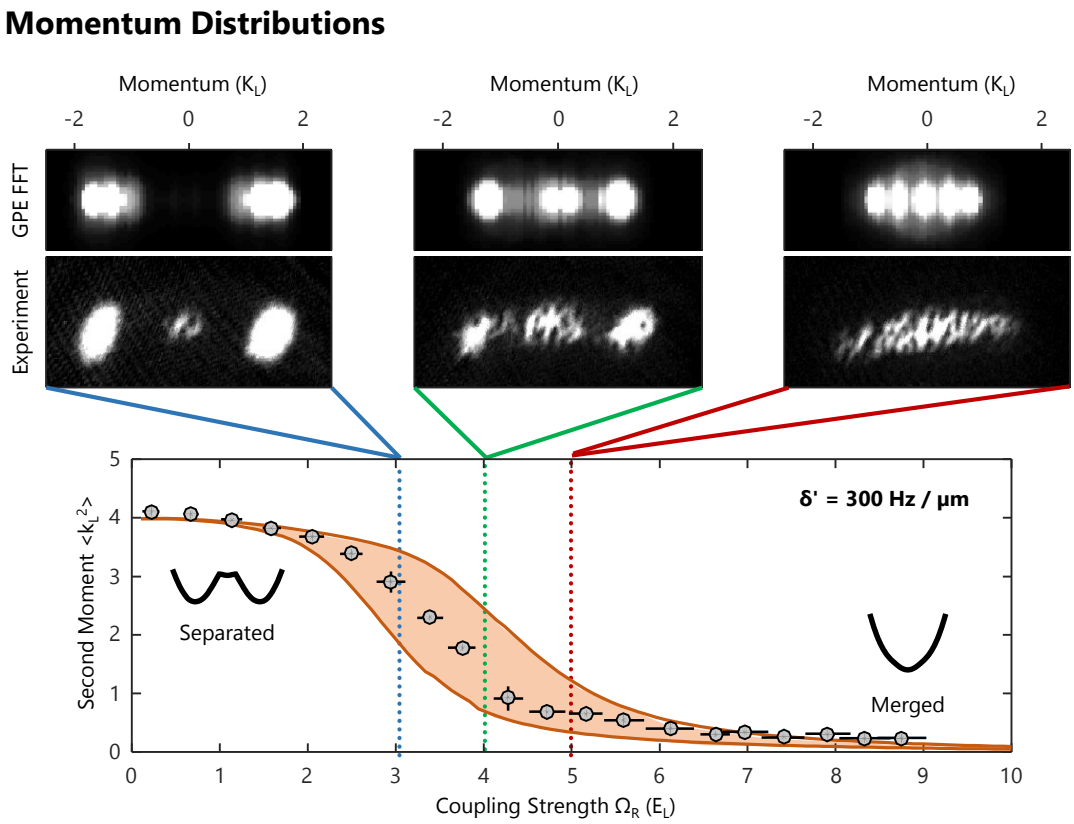

Figure 8.15: Second moment of the momentum distributions at $\delta' = 300$ Hz/μm as a function of Ω_{R}, with the left, center, and right columns being $\Omega_{\mathrm{R}} = 3, 4, 5\, E_L$ respectively. Top: GPE-computed 2D momentum distributions $k(x, y)$ using the same parameters. Middle: Experimentally measured momentum distributions after TOF Bottom: Experimentally measured second moment of the momentum distributions at $\delta' = 300$ Hz/μm as a function of Ω_{R}. Shared region represents theoretical prediction, accounting for uncertainties.

8.2.4 Results

Momentum Distributions

To examine where in the parameter space $(\Omega_{\mathrm{R}}, \delta')$ possessed regions of high magnetic field and rapid vortex nucleation within the BEC, we first examined the distribution of momentum in the BEC as a function of Ω_{R} and δ'. For the three different possible trap geometries, there can be equally three classes of momentum distributions that arise. First, when there are two separated BECs, there are two distinct peaks in the momentum distribution of the BECs at $\pm 2\, k_R$. In the regime where the two separated BECs are beginning to overlap (when $V_B \approx \mu$), the BEC will span a larger set of momenta. In the

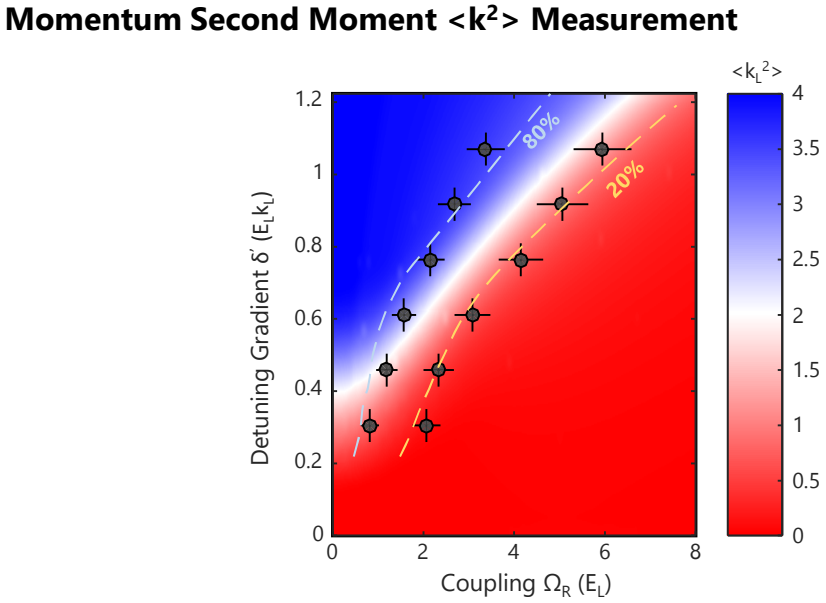

Figure 8.16: Magnitude of $\langle k^2 \rangle$ in the parameter space of Ω_R and δ'. The overlapped region between the dashed lines was calculated from theory to be at the 80% and 20% of the maximum moment at a given δ'.

high coupling limit when Ω_R creates a single well in both momentum space and position space, the momentum of the cloud is centered around $k = 0\, k_R$ (Figure 8.15, top)

The momentum distributions are drastically different in each of the three parameter regimes shown in Figure 8.15. Firstly, when there are two separated BECs (left column) the momentum distribution is sharply peaked at $\pm 2\, k_R$, maximizing $\langle k^2 \rangle \approx 4\, {k_R}^2$. As these BECs begin to overlap (center column) (when $V_B \approx \mu$), the momentum distribution spans the full regime from $-2\, k_R$ to $2\, k_R$, reducing $\langle k^2 \rangle$. Lastly, in the coupling limit when Ω_R when the BECs merge (right column), the momentum distribution is sharply peaked at $k = 0\, k_R$ and $\langle k^2 \rangle \to 0$. Thus $\langle k^2 \rangle$ parameterizes these different regimes.

To study $\langle k^2 \rangle$ for a range of Ω_R and δ', we prepared our system at the desired δ' with $\Omega_\mathrm{R} = 0$, with a BEC consisting of an equal mixture of $m_F = \pm 1$. When $\delta' \neq 0$, the magnetic gradient phase separated the two spin components, forming the precursors of the potential wells in Figure 8.8. We then ramped on Ω_R with a $\approx 10 E_R/\mathrm{s}$ rate chosen to be adiabatic with respect to the system's center of mass dynamics (but not the time scale for vortex formation), and then held Ω_R constant at the final value for 150 ms, allowing the system to equilibrate.

Figure 8.15, bottom depicts the evolution of $\langle k^2 \rangle$ at $\delta' = 300$ Hz/μm as a function

of Raman coupling strength Ω_{R}, and shows the three qualitative regimes outlined above. For $\Omega_{\mathrm{R}} \gtrsim 3$, $\langle k^2 \rangle$ decreases slowly, as expected for the separated well configuration, then as the wells merge ($3 \lesssim \Omega_{\mathrm{R}} \lesssim 5$) $\langle k^2 \rangle$ drops rapidly, before saturating to zero in the single well regime.

We observe that for the separated BEC regime, $\langle k^2 \rangle \approx 4{k_R}^2$. As the coupling is increased the two separated BECs begin to merge as the scalar potential $\phi(y)$ begins to weaken as Ω_{R} increases. This onset of the merging of the condensates is correlated to a rapid decline in $\langle k^2 \rangle$, indicating a measurement in the $V_B \approx \mu$ region of the parameter space. As Ω_{R} increases further, $\phi(y)$ becomes weak in comparison to the trapping potential, and the system forms a single well potential. In this region where the BEC has a single potential well, $\langle k^2 \rangle$ asymptotes towards zero (Figure **??**e).

Rapid Entry versus Standard Entry

Because the variance acts a proxy measurement of vortex number that is indifferent to the chaos of the vortex distribution, we took advantage of the metric and studied the variance in two different regions of the BEC: the inner and outer halves. Since in a conventional nucleation process the vortices come from the system's edge, we expect for this regime the outer signal to be larger as vortices nucleate and smaller in the inner region as vortices must migrate inwards. In contrast, for our merged BECs we expect vortices to be preformed in the system's center, quickly dispersing across the BEC once the merging process has occurred. We distinguished these two potential mechanisms for vortex formation by studying the variance in the inner and outer halves of the system.

For parameters where a high strength magnetic field does not intersect the BEC at all Ω_{R}, the variance in the outer region of the BEC begins to increase noticeably before the variance in the inner region (Figure 8.17). The interpretation here is that, similar to previous rotational experiments, the vortices are nucleated on the periphery of the BEC and evolve inward toward a lower energy state. For parameter trajectories that do have a high-strength magnetic field region, the variance in both the inner and outer regions simultaneously increase at the onset of vortices within the system at approximately where the theory predicts the two spatial wells to combine. The simultaneity of the increases

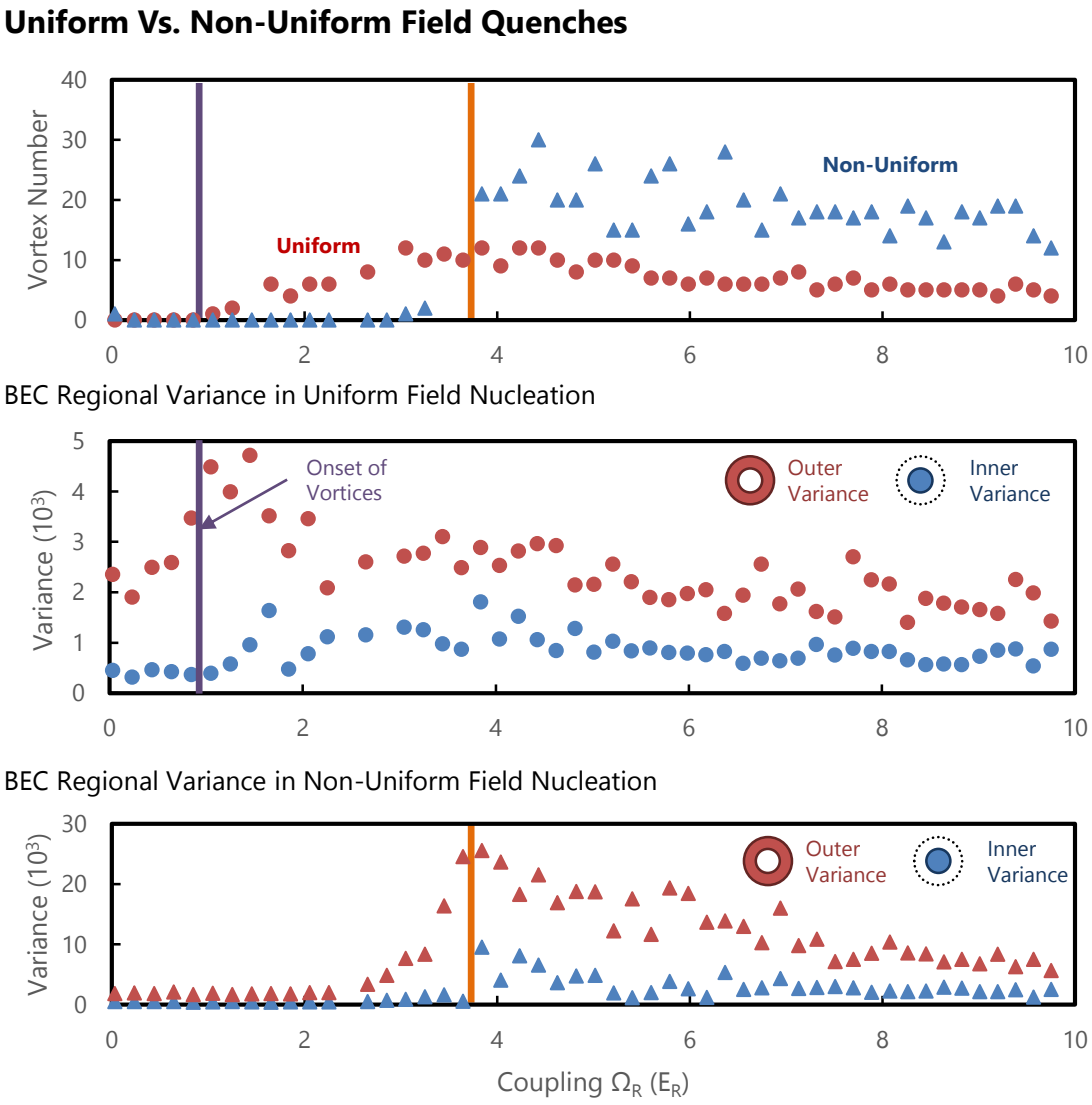

Figure 8.17: Top: Vortex number as a function of Ω_R in the non-uniform (blue triangle) and uniform (red circles) effective field regimes (at $\delta' = 300$ Hz/μm, 100 Hz/μm respectively). The vortices suddenly enter when the BECs merge. The vertical purple and orange lines represent the onset of vortices in the uniform and non-uniform cases respectively. Middle: Variance in the outer (dark red) and inner regions (light red) of the BEC for the uniform field method regime. Here the inner variance lags the outer variance, suggesting vortex formation at the condensate periphery. Bottom: Variance in the outer (dark blue) and inner regions (light blue) of the BEC for the non-uniform field method regime. For a non-uniform field, the condensate experiences a jump in inner and outer variance simultaneously.

implies that the vortices were nucleated from the inside of the BEC and quickly disperse across the cloud.

For parameter regimes where there was not a large effective magnetic field, we observed a slow increase of vortices as Ω_R was ramped up. At higher values, the number

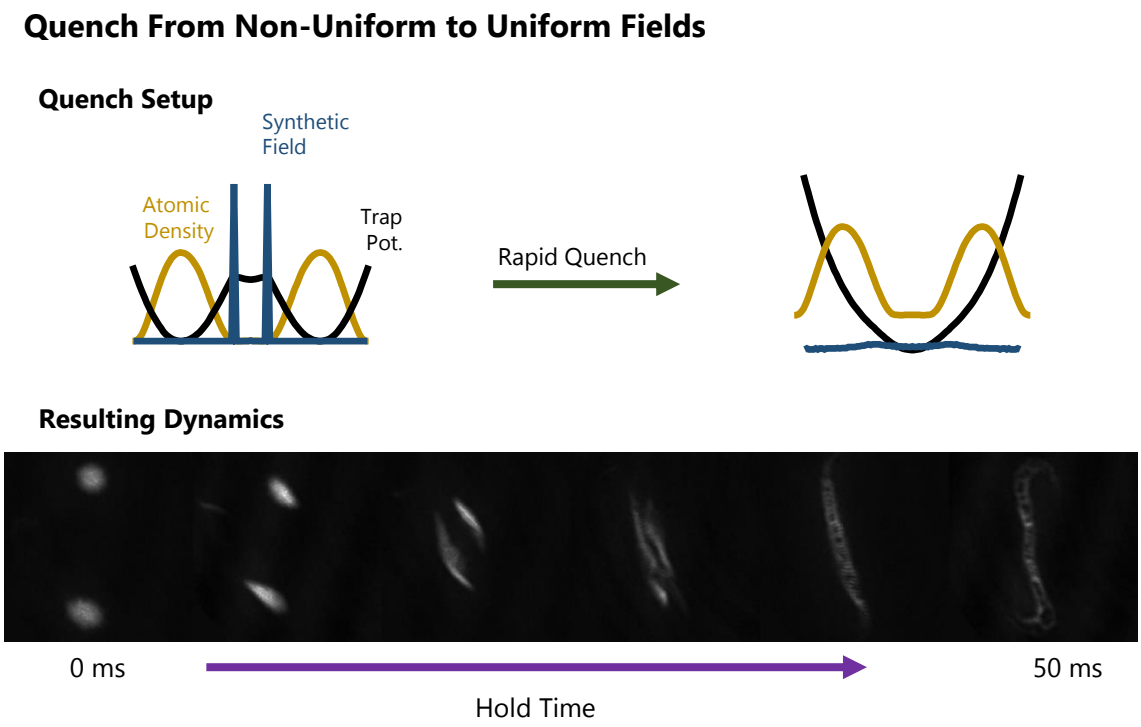

Figure 8.18: Dynamics after a quench through the separated to merged regions of the experimental parameter space. By varying the hold time, the two BECs can be seen to collide, producing many vortices.

of vortices began to drop as the density of the BEC lessened as well for the longer ramps (Figure 8.17). By comparison, for parameter regimes where a vortex chain was predicted, there was a sudden turn on of vortices as Ω_R was increased. The stark difference in rapid appearance of vortices, together with higher vortex number, suggests that the vortices are being nucleated into the system via a different mechanism.

Rapid Quenches To Uniform Field

In a separate study I examined the dynamics of the system after crossing between the non-uniform to uniform transition suddenly. To do this I first ramped up the detuning gradient as described in Section 8.2.2 to a specific value. Next I ramped Ω_R up to a value before the transition region. Next the value of Ω_R was increased instantly to a value beyond the transition. Lastly, the system was held for a variable hold time to observe the resulting dynamics.

When performing the quench across the transition, the two separated BECs in a

double well potential are suddenly placed into a single well potential and offset from the center. This causes the two BECs to gain momentum as they fall toward the trap center. The two clouds, both with different momentum characteristics due to the vector potential, begin to collide, producing a set of interference patterns and vortices (Figure 8.18). If held for much longer, the system will relax into a single BEC with many vortices present.

Appendix A

Flux Gate Magnetic Field Stabilization System

This chapter details the operation of the flux gate magnetic field stabilization system described in Section 4.4.7. This system uses an FPGA circuit board that I designed to read the background magnetic field in our experiment, and produce a correction signal that drives our biasing coils to cancel the noise at the atoms. The performance of this system is also described in Section 4.4.7

A.1 Theory of Operation

A.1.1 Flux Gates

To measure the magnetic field, we use a set of Stefan-Mayer model FL1-100 flux gates (Figure A.1). These units work well within our experiment, as they are compact and low power. The total measurement range of 1 Gauss over 10 Volts allows for a wide window of measurement with high resolution.

As helpful as the sensors are at measuring small magnetic field, there are many problems for us to use them in a direct feedback form of stabilization. The flux gates, due

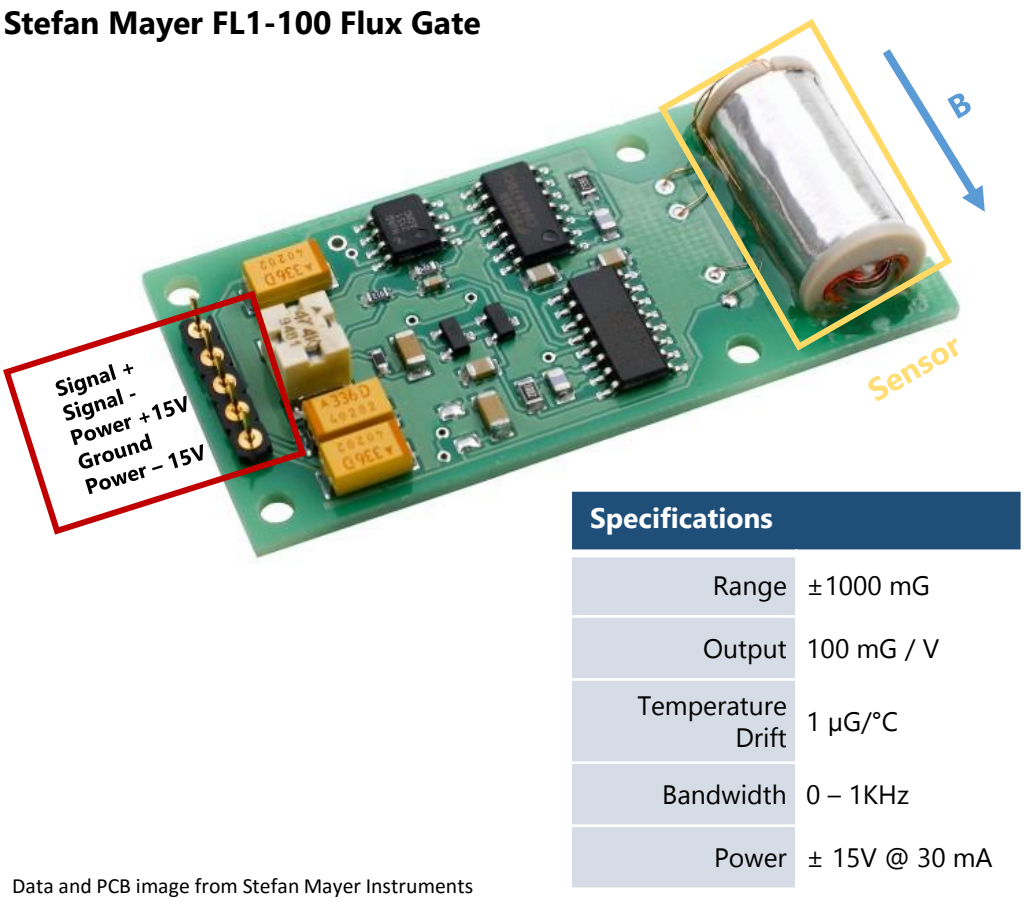

Figure A.1: Stefan-Mayer FL1-100 Flux Gate

to their method of measuring the field, generate a magnetic field in the 10 kHz − 30 kHz frequency range (see section iv of reference [128]). This field can cause a back action with the atoms, making direct feed forward or feed back schemes difficult. Even worse, the field generated from our bias coils are registered on the flux gates themselves, thus any feedback to correct a field will cause a feedback loop, making conventional locking impossible.

To combat these issues, we do a few things. First, to help reduce the radiated kilohertz noise from the flux gates, we enclosed them in aluminum shields. Secondly, I had developed a way to toggle the power of the flux gates on and off via a 5V TTL line, allowing us to turn off the flux gates at sensitive portions of the experiment. The last problem is the most difficult: every other coil in the experiment (quadrupole, Zeeman slower, bias coils, etc.) produces a signal at the flux gate that can quickly saturate the 1 Gauss full range. Therefore for most of the experimental cycle, the flux gates cannot be

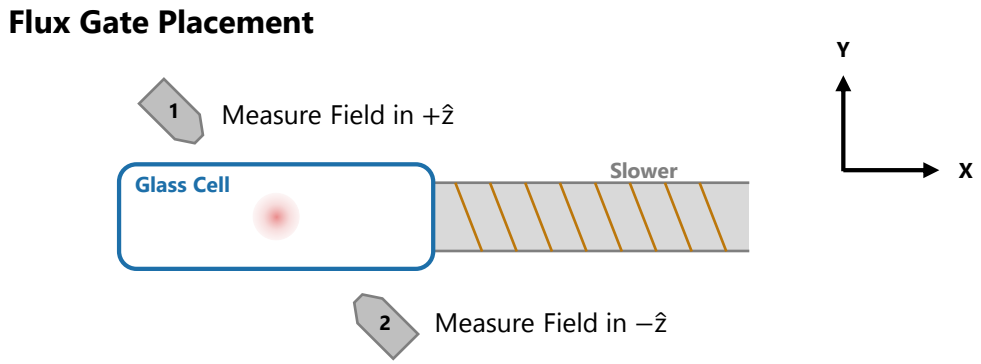

Figure A.2: Placement of fluxgates to measure the magnetic field in $\hat{\mathbf{z}}$

engaged as their output signal is railed and useless, another reason direct feedback will not work.

The solution was to make a track and hold measurement system, with a complexity that required the flexibility of the FPGA system. The idea is that at the end of the evaporation in the optical dipole trap, all of the electromagnetic coils in the experiment are off (or canceling true DC background fields), therefore a measurement at this time is a (or at least the best) measurement of the background field. For any other times outside of this window, the correction system can keep the flux gates powered down, and output a correction signal based on the last measurement. By measuring the drifting field during this window each cycle and then updating the correction signal to a cancellation coil, we can remove long term field drifts (see Section 4.4.7).

Due to the bulky size of the flux gates, we are not able to get the flux gate sensors any closer to the atoms than ≈ 10 cm. Since we cannot put a flux gate close, or on the atoms, we cannot directly measure the field at the atoms. To improve our measurement of spatially uniform background fields, we deployed a pair of flux gates symmetrically across the glass experimental cell. The two flux gate sensors are placed in opposite directions ($\pm\hat{\mathbf{z}}$). We then calculate the average background field signal from the two sensors as:

$$V_{\mathrm{FG-Total}} = \frac{1}{2}(V_{\mathrm{FG1}} - V_{\mathrm{FG2}}) \tag{A.1}$$

The assumption we are using is that the background field does not vary in a discontinuous

fashion over the 30 cm distance between the two sensors, hence to a linear order we are extrapolating the field at the glass cell. That said, we still do find the magnetic field sensed by the flux gates and atoms is different, and still needs to be calibrated.

A.1.2 Low Frequency Field Rejection

To remove the long term drifts in the experiment, there is a track-and-hold algorithm that uses non-continuous measurements to overcome the issues previously mentioned. To do this, first the flux gate signal is connected to the FPGA system at an analog input channel. The FPGA board is set to have the channel be read differentially so that both the flux gate positive and negative values can be read. The ADC subtracts these two values and reports them as a digital value within the FPGA. Next, the measured signal is subtracted by a reference value that we set. This gives us the field strength difference from now and where we *want* to be (the reference). Next, the difference in the field, ΔB, is fed into the track and hold system. To prevent feedback loops, this part of the algorithm must be enabled remotely. When the Measurement Active signal is enabled, ΔB is continuously averaged for the length of the enable signal, thereby extracting the low frequency components of the ΔB signal. This operation is naturally implemented with a low-pass filter algorithm in hardware. With the DC value of ΔB, the system multiplies by a scaling coefficient that is the combination of: the flux gate scaling, the calibration of flux gate field versus field at the atoms, the field generated in the correction coil per amp run through it, and the coil

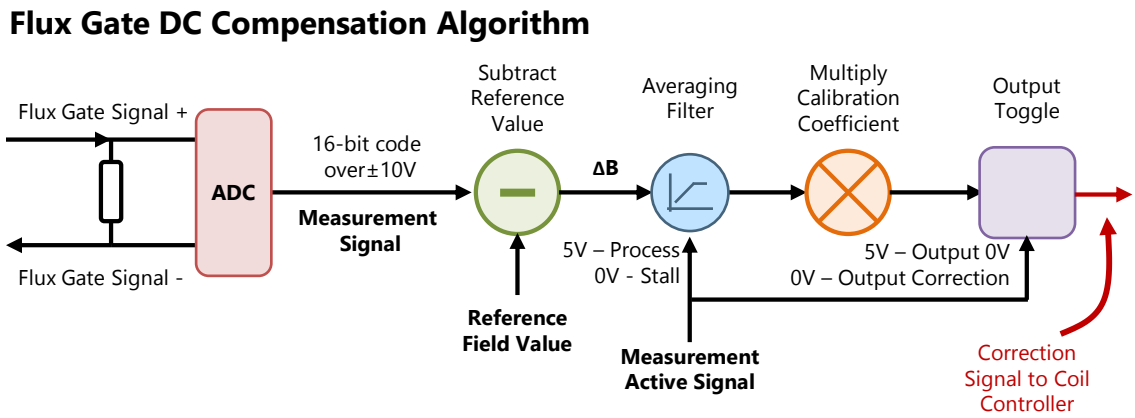

Figure A.3: Flux gate low frequency compensation algorithm

amps per command volt (see Section A.2.4). After ΔB is scaled appropriately to give a feedback signal, this signal is output from the FPGA device to the correction coil current command port. When the measurement active signal is enabled, the output of the device puts out 0 V so that the field from the correction coils is disabled, allowing measurement of the true field.

A.1.3 60 Hz Field Rejection

Line noise (aka 60 Hz noise) originates from currents flowing in the 120 V AC lines, powering most lab equipment. That said, it is hard to remove all the sources of 60 Hz magnetic field noise in the lab without having any electricity left[1]! To counteract the effects of 60 Hz magnetic field noise at the atoms, we can measure the spatially uniform

[1] All plans about interchanging lead-acid +12V battery banks aside

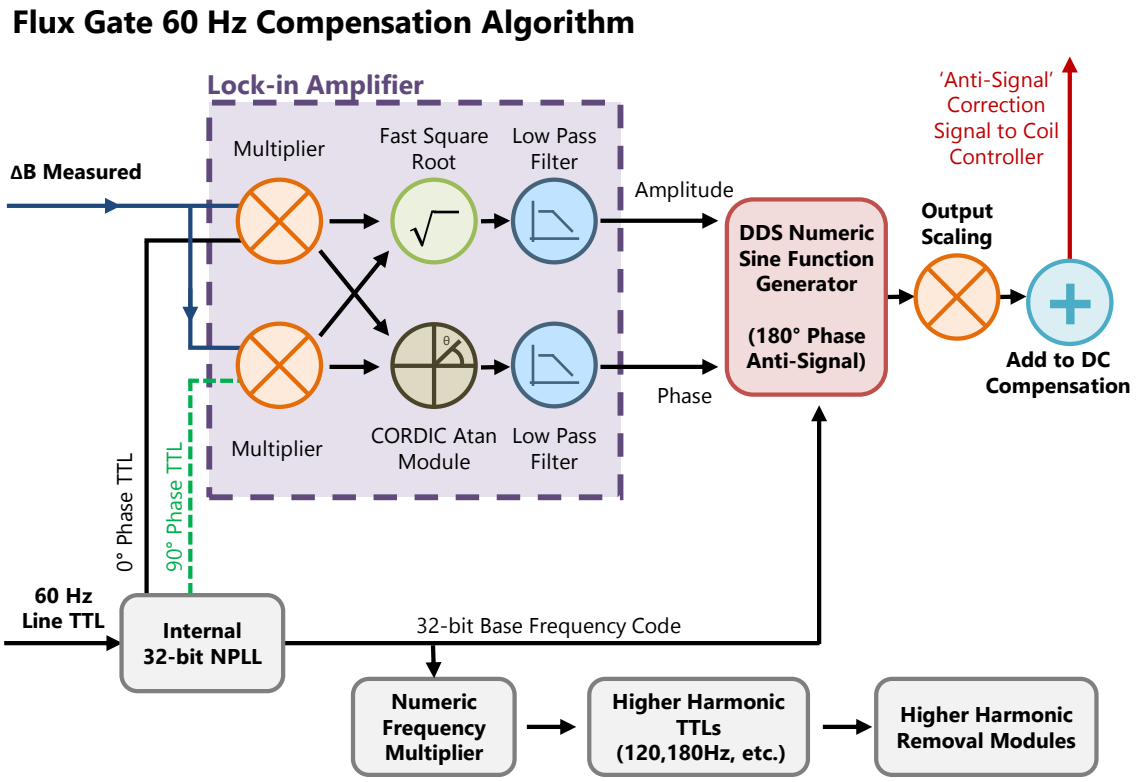

Figure A.4: Flux gate 60 Hz line noise compensation algorithm

60 Hz signal between the flux gate pair and send a signal back to the correction coils to counteract the effect.

However, this plan requires a few things. First, the correction coil and current source must be able to operate faster than 60 Hz, so that the phase lag between measurement and correction is negligible. Second, in order to send a 60 Hz anti-signal, we need to know the amplitude and phase of the measured background field. This is where the FPGA flexes its muscle.

To get the amplitude and phase out of the flux gate measured signal, I deployed a phase-sensitive detector: a lock-in amplifier. A 60 Hz 5V TTL is generated from a direct connection to the 120 V AC line, with appropriate electronics to downsize the voltage and filter out high frequency noise. This input oscillator tied to the line frequency acts as the reference signal for the lock-in amplifier. One could simply digitally synthesize a 60 Hz signal with great precision, however the line frequency varies in time to maintain synchronization with atomic clocks and across the power grid. Because we want a very narrow filter at exactly the power line frequency, it is simple enough to digitize the power line signal into a clock itself. All that said, herein I refer to this frequency varying signal still as the 60 Hz signal.

With the 60 Hz TTL in the FPGA, a digital-numerical PLL is used to determine the phase-increment value of a 32-bit DDS clock source. The digital PLL pulls back the 32-bit frequency code and phase that follows the 60 Hz signal, with a stable lock to within a microsecond. This code allows digital synthesis of TTL signals at higher harmonics, as well as arbitrarily phase shifted versions of the 60 Hz line signal. This arbitrary phase shift allows the creation of a 0 degree and 90 degree phase separated pair of TTL signals at 60 Hz. These TTL signals are individually multiplied against the calculated ΔB in Figure A.3, generating a pair of signals X and Y such that:

$$A = \sqrt{X^2 + Y^2} \tag{A.2}$$

$$\tan(\theta) = Y/X \tag{A.3}$$

Where A is the amplitude of the 60 Hz signal present on the ΔB signal and θ is the phase delay between it and the 0 degree phase TTL.

It is worth mentioning that the extraction of the amplitude and phase requires a square root function and arctangent computation in hardware. To avoid excessive resource usage, a hardware friendly square root approximation that only involves two additions and bit shifts is used, at the cost of $\approx 3\%$ accuracy. To compute the arctangent, I wrote a hardware CORDIC algorithm consisting of a few pre-stored values of arctangent that computes arbitrary angles via successive shift and add operations.

With the amplitude, frequency and phase of the 60 Hz signal known precisely, these parameters are fed into a DDS sine wave generation module that I wrote, creating an anti-signal that can be fed to the correction coils. Lastly this signal is added to the DC correction signal in Section A.1.2.

To further improve the reduction of line noise, the digital-numerical PLL gives the ability to easily multiply the base frequency of the 60 Hz input TTL, allowing us to create higher harmonic TTLs (i.e. 120 Hz and 180 Hz), and deploy the same lock-in amplifier algorithm to generate an anti-signal at those frequencies as well. Using this algorithm for the 60 Hz and the next 2 harmonics, most of the flux gate line noise components can be matched and eliminated (see Figure A.5).

It is important to note, because of the track-and-hold method of measuring the B field, the 60 Hz amplitude and phase are measured during the Measurement Active signal enabled; the frequency is measured continuously from the input clock line. Therefore the anti-signal fed to the correction will be locked at phase, amplitude and frequency until the next measurement is enabled. As mentioned previously, the 60 Hz waveform can drift over time, but the 1 minute timescale of a normal BEC experiment from start to finish is much shorter than this variance time. In fact, the SoftScope trace in Figure A.5 was taken a few minutes after the measurement trigger in order to see the feed forward stability.

Lastly, this 60 Hz removal method is independent of the flux gate measurement, that is it is general enough in design to remove 60 Hz signals from any digitized signal. It would be possible, considerable device resource constraints aside, to place such a filter on every analog in line on an FPGA system where the input analog signal is immediately

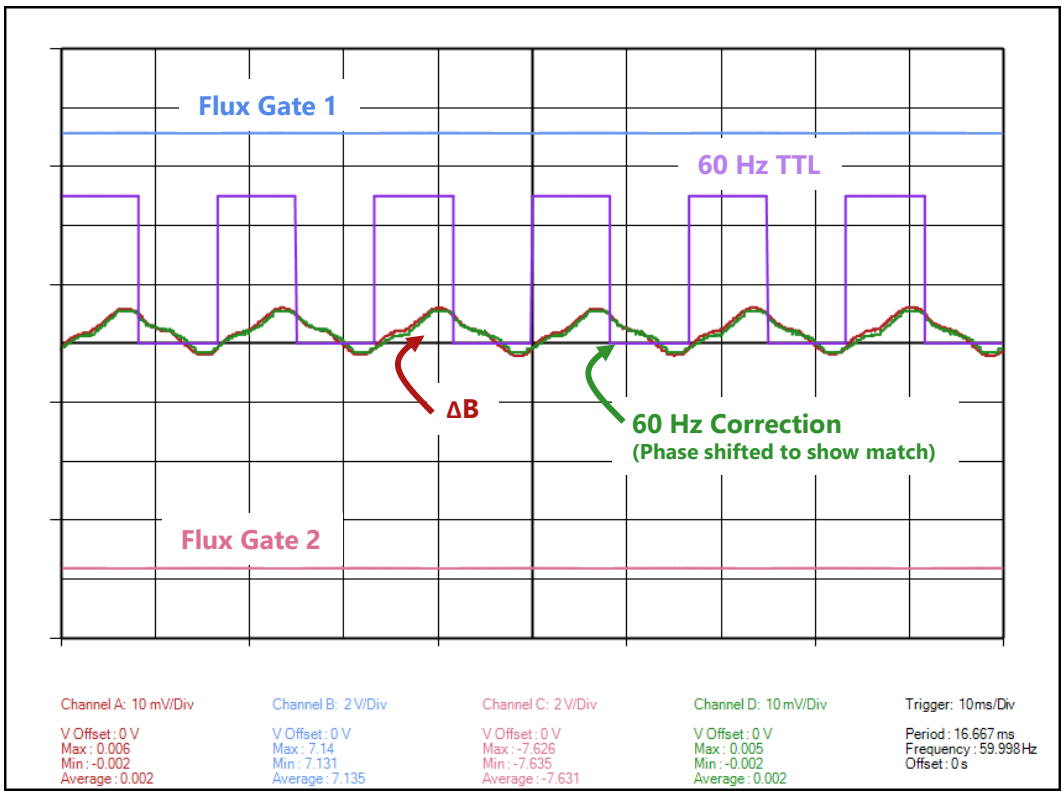

Figure A.5: SoftScope measurement from the FPGA device showing the 60 Hz matching waveform. Look closely, they lie right on top of each other.

subtracted by the anti-signal before being processed else where.

A.2 Usage and Calibration Protocols

A.2.1 Flux Gate Controller Box and Connections

The flux gate controller is based on the FPGA PCB (Appendix B) that I designed. There are a few simple modifications to the board. First, the ADC channels for the flux gates were set to read a differential signal; at no point are the inputs connected to ground. Given the 100 mG/V measurement of the flux gates, the FPGA system when reading over ±10 V has a maximum precision of 30 microgauss. To aid in the 60 Hz cancellation, a simple circuit connected to the AC power entering the box takes the 120 V line waveform

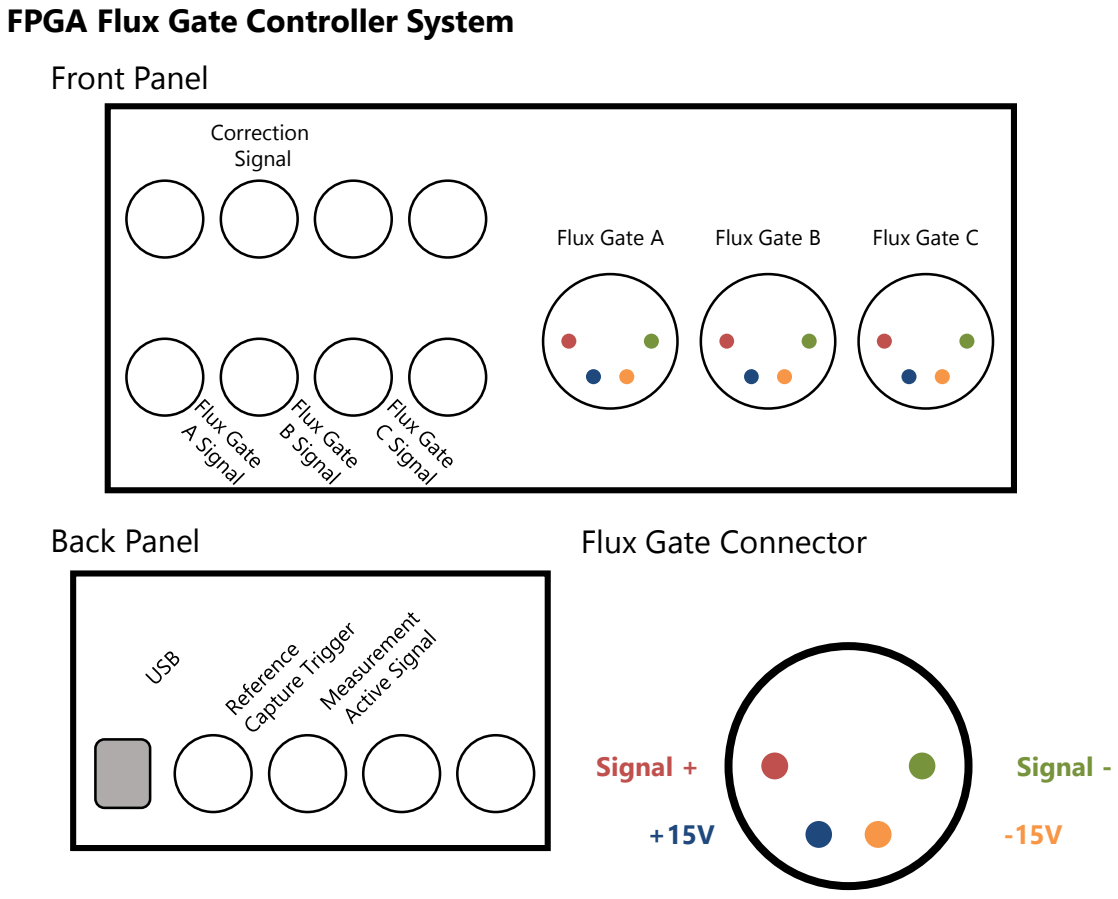

Figure A.6: Connections for the FPGA-based flux gate controller

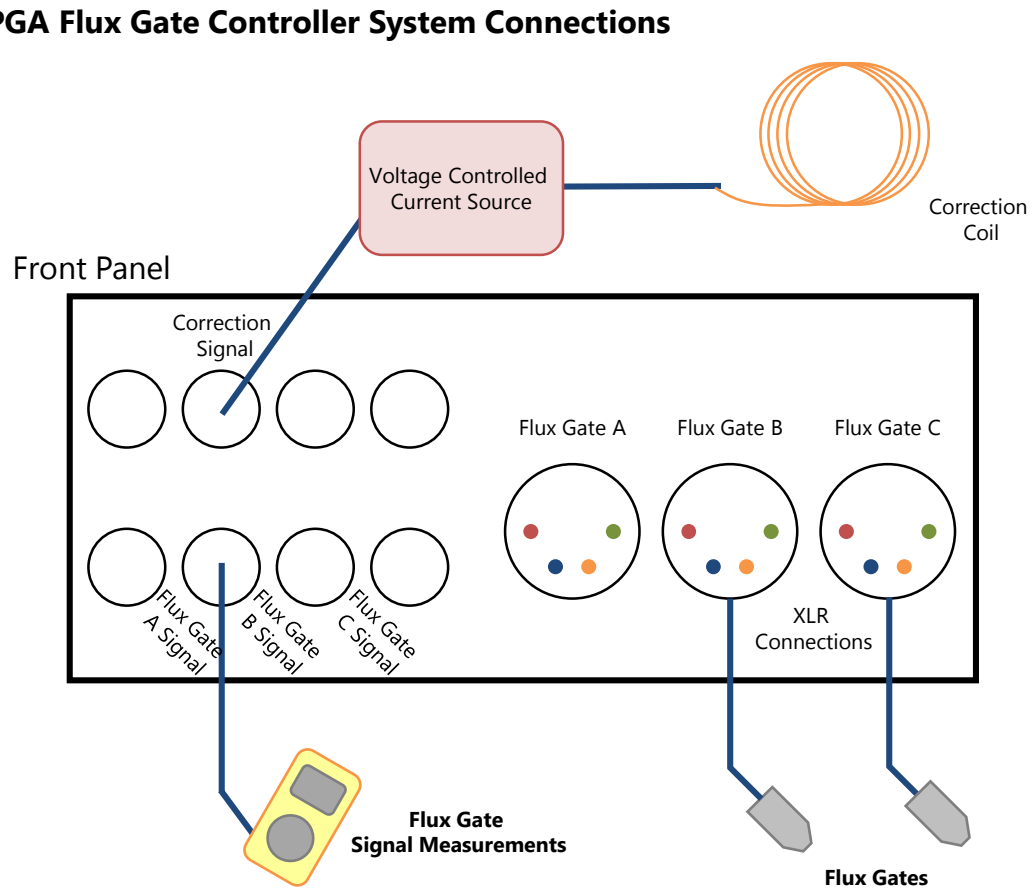

Figure A.7: Front panel connection guide

and turns it into a 60 Hz 5V TTL signal that the FPGA can process. This TTL provides the reference signal for the 60 Hz cancellation lock-in amplifier.

The front side of the box has connections for up to 3 flux gates. Flux gate port A is a simple monitor port. Flux gate ports B and C are used in the cancellation system, providing the signals in the averaging mechanism described in Equation A.1. Each of the three flux gate signals can be read out of three BNC ports on the box, removing the need for separate differential amplifiers if one wants to simply see the field measurements. Note that the flux gates need to be powered on to see a signal[2].

When constructing the current source and correction coil, it is useful to consider the voltage to current to field calibrations. It is a sad fact that there is a few mV of noise on the correction signal line. If through the calibrations the correction signal for a

[2]Because I've fooled myself enough times wondering where the signal went, only to find I did not toggle the power to the flux gates

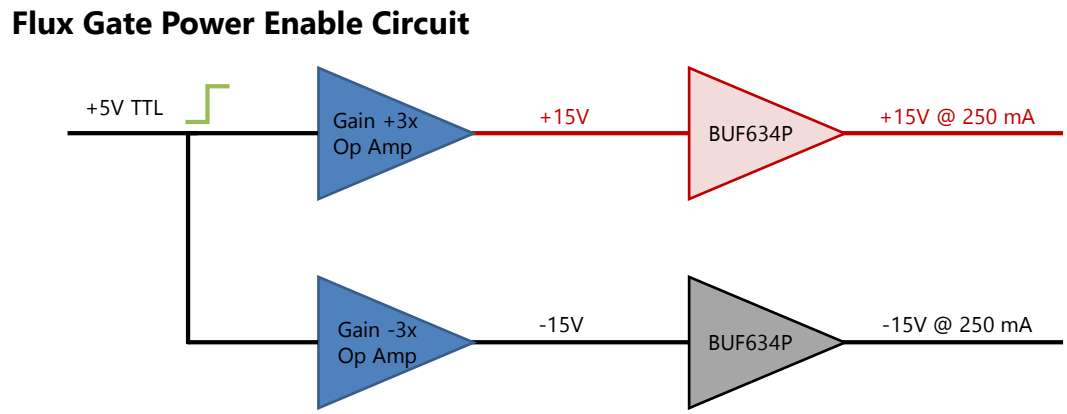

Figure A.8: Power on/off TTL toggle circuit schematic

milligauss field jump is the same size, then the correction signal noise will introduce more magnetic field noise than it corrects. For this reason, it is helpful to use the large 'table coils' (Section 4.4.6) to make feedback corrections. For example, the bottom table coil has a 64.3 mG/A magnetic field and 11.4 Ω resistance. Given a 1:3 voltage command:output (which is currently true), the coils generate 16.9 mG per volt from the correction signal. In this scheme, the millivolt noise on the line only translates into tens of microgauss magnetic field, far below our usual shot-to-shot stability.

Flux Gate Power Control

To disable the flux gate power when not making a measurement in order to avoid any magnetic noise at the atoms, I quickly constructed a TTL compatible power enable/disable circuit. The circuit consists of an input 5 V signal that is passed through two operational amplifier circuits: one that has gain +3 and the other gain -3. The op amps then output low current ±15 V voltages. To provide the ≈ 30mA currents to each flux gate, a set of BUF634p buffer chips are placed at the outputs of the operational amplifiers. These devices each can provide 250 mA at ±15 V (given the correct power supply), more than enough power sourcing for multiple flux gates. Although functional, this design could be better improved with a dedicated high current switching IC, such as ADG5434, and use of surface mount component PCB fabrication, versus the wire and vector board construction currently deployed.

A.2.2 Manual Readings From Flux Gates

To make a measurement of the field as given by the flux gates when not in an experimental cycle, one can use the signal output ports on the front of the device (Figure A.6). Given the default state of the system in manual control to make a MOT, remember to set the currents of the quadrupole, slower bias and slower taper coils to zero, or else the flux gates will saturate and the signal will be useless. Also, the flux gates need to be powered on using the DO4-13 digital line.

A.2.3 Experimental Cycle Setup

To get the feedback system to work, the timing of the measurement active signal must be set correctly, and the feed forward coefficient must be calibrated. First, the experimental cycle must have the FPGA device measuring at a time step when all of the other coils are off, or the bias coils are on at low field (the flux gates cannot be saturated). There also needs to be wait time before measuring if coils have been recently($\approx$ 200 ms) turned off, as coils such as the quadrupole have long eddy current and inductive timescales. Next the flux gates need to be powered on for $\approx$ 100 ms, then the measurement active signal enabled. The more time given on this step, the better the measurement for both DC and AC magnetic fields will be. When done, disable the measurement line and power to the

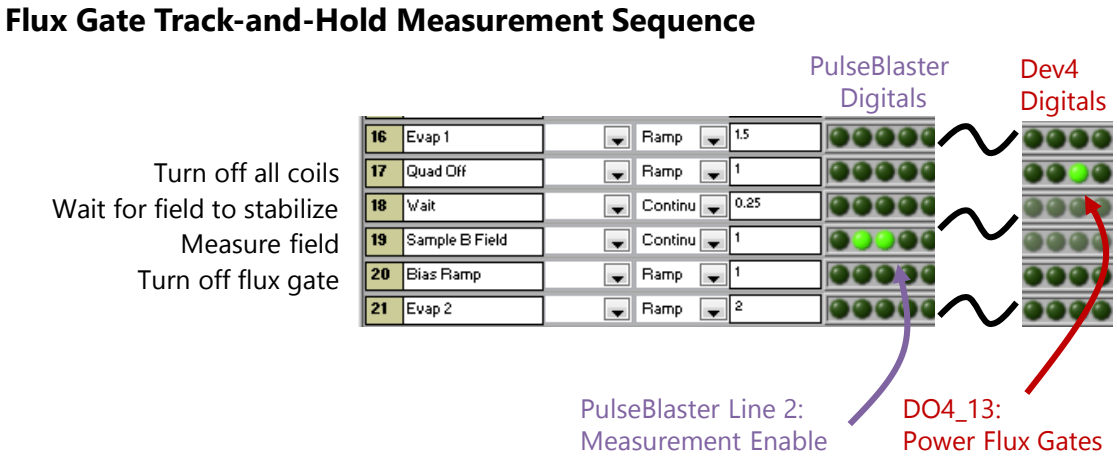

Figure A.9: Measurement steps for flux gates in CycleX experiment

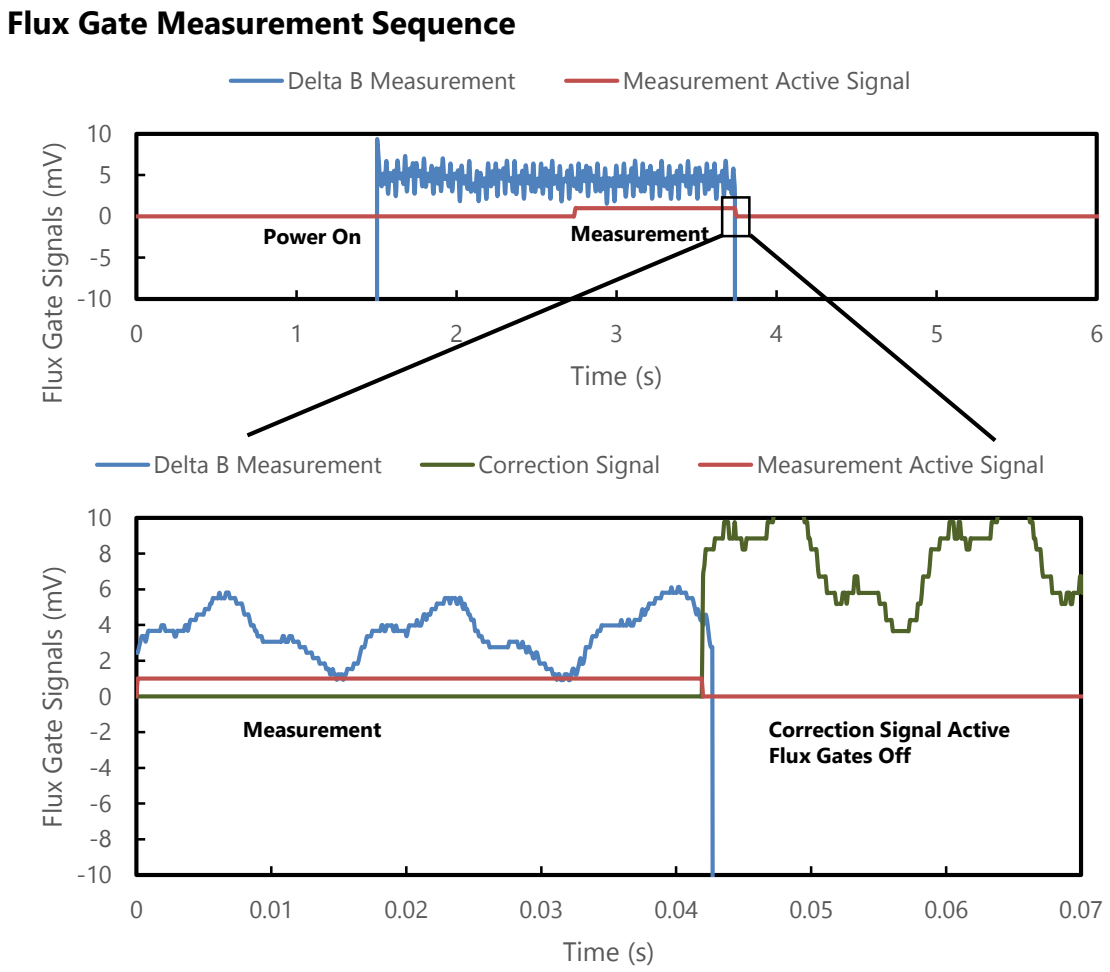

Figure A.10: Measurement and Correction signals during the track and hold process

flux gates, the new correction value will be updated at the output.

A.2.4 DC Correction Calibration Protocol

Before calibrating for the feed forward coefficient, the reference magnetic field value needs to be set. The reference magnetic field values act as the 'zero field value' in the sense that the flux gate system will always output the signal required to correct to get this field measurement back.

After setting the experimental cycle up as described above, one needs to use their favorite method (usually Adiabatic Rapid Passage, Section 3.1.2) to get the background magnetic field plus applied field at a known atomic resonance. Once on resonance, we set the reference value to the background field measured during the magnetically quiet stage

in the cycle. To do this in an easy way with the cycle running, take the measurement signal connected to the FPGA device and connect it to the Reference Capture Trigger (Figure A.6, back panel schematic) for a cycle or two. This will cause the FPGA device to set the internal reference value to what the field is when triggered at the magnetically quiet portion of the experiment. After the one or two cycles, connect the signal back into the Measurement Active TTL line.

To get the feed forward coefficient we require 4 values:

- The conversion of flux gate voltage to field measured at the flux gates. This is simply the 100 mG/V calibration in Figure A.1.
- The field at the atoms (measured through ARP, Section 4.4.7) as a function of field at the flux gates. This is the value of a in equation A.4.
- The field generated at the atoms as a function of current on the correction coil. This is the value of b in equation A.4.
- The current flow in the correction coils as a function of voltage command to the power supply or servo the coils are connected to. This is the value of c in equation A.4.

All of these allow one to calculate the feed forward coefficient as:

$$C_{\mathrm{FG}} = \frac{100\,\mathrm{mG_{FluxGate}}}{1\,\mathrm{V_{FluxGate}}} \times \frac{a\,\mathrm{mG_{Atoms}}}{1\,\mathrm{mG_{FluxGate}}} \times \frac{1\,\mathrm{A_{Coil}}}{b\,\mathrm{mG_{Atoms}}} \times \frac{1\,\mathrm{V_{CoilCMD}}}{c\,\mathrm{A_{Coil}}} \tag{A.4}$$

Knowing the coefficient C_{FG} gives the FPGA the knowledge to compute the command signal to the correction coil:

$$V_{\mathrm{Output}} = C_{\mathrm{FG}} \Delta B_{\mathrm{Measured}} \tag{A.5}$$

Now it is very simple[3], the experimentalist just needs to find the values of a, b, and c in equation A.4. If using the bias coils in the experiment to provide a correction signal, the value of c is a freebie, see Section 4.4.3. After getting all these values, hook up the

[3] I kid.

Coil Command Voltage (V)	Coil Current (A)	Coil Voltage (V)	Resonance (A)	Flux Gate Voltage (V)
0	0.001	0.002	3.62375	0
0.25	0.3046	0.457	3.6140	0.058
0.5	0.6814	1.105	3.6045	0.117
-0.25	-0.2845	-0.4023	3.6335	-0.057
-0.5	-0.6750	-1.105	3.643	-0.115

Figure A.11: Example raw data set required for calibrations of flux gate system

correction coil of your choice to power supply of your choice. Next, find resonance with no current in the coil. Then introduce current into the correction coil, enough to where you see the resonance change at the atoms, but not wildly far away. At this point, you need to record the voltage across the coil and the current on the coil, as well as the amount of current in the bias coil required to get the system back to resonance and the measurement of the voltages on the flux gates (via softscope or the analong output ports on the front of the box). Repeat this procedure for many different currents, both positive and negative. With enough points, the linear relationship between the flux gate field measurement and atomic field measurement should become clear. A bonus is that the correction coil is now calibrated, with the linear relationship between field shift measured by the atoms and current in the coil. Now crunch numbers[4], get value.

A.2.5 60 Hz Correction Calibration Protocol

Previously it was found that the scaling factor for the 60 Hz field noise correction system was approximately 2, owing to the fact that I had not included in hardware the 1/2 factor in amplitude measurement from the lock-in amplifier calculation. Thus a scale factor of 2 input into the software for the 60 Hz correction (see Section A.2.6) is required for normal operation. If there are fears that the calibration is somehow different, a calibration and measurement procedure can be performed.

To do this calibration, I measured the change in resonance (and hence field described

[4]Useful - ^{87}Rb $F = 1$ ground state: 0.7 MHz/G

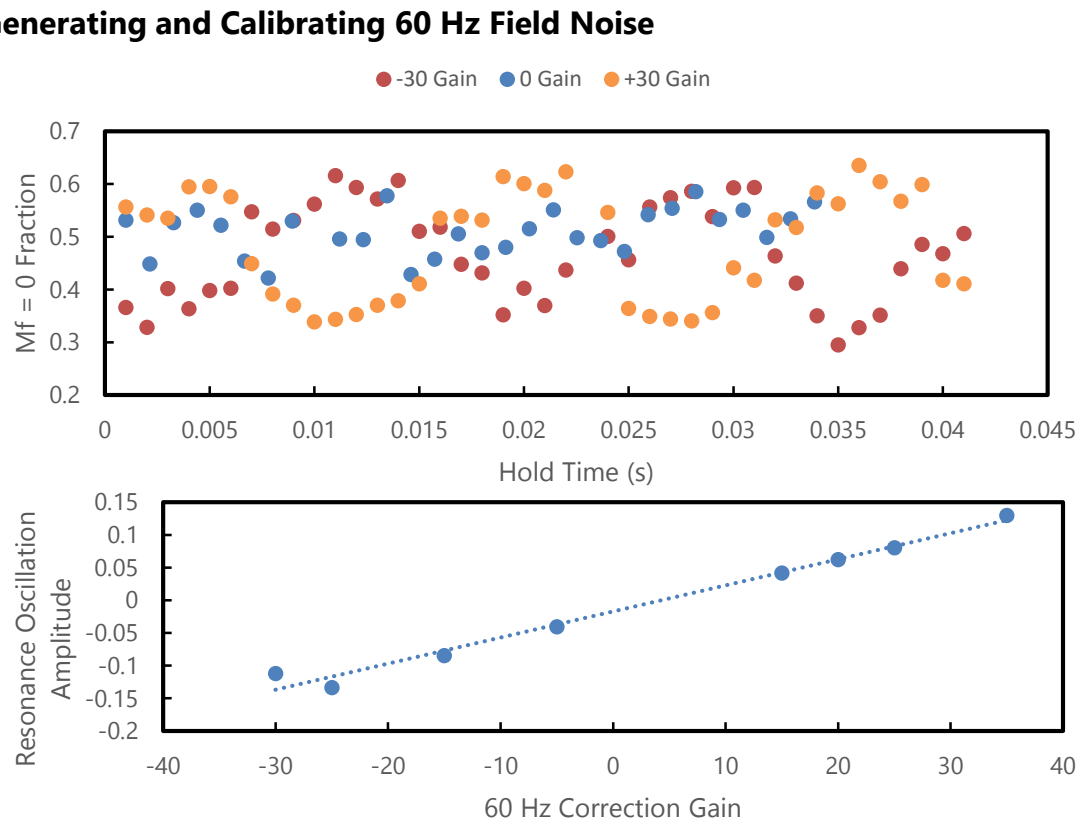

Figure A.12: Example raw data set required for calibrations of flux gate system

in Section 4.4.7) as a function of time, over ≈ 50 ms, a large enough time window to see 60 Hz oscillations. The idea is that by changing the gain of the 60 Hz correction signal, there should be coefficients that 'overdrive' the system and induce 60 Hz oscillations, or those the over correct the 60 Hz waveform and change the phase of the oscillation by 180 degrees. I repeated the resonance oscillation scan for many different 60 Hz correction signal gain coefficients to see how the oscillations changed Section A.12. By measuring the amplitude of the oscillation as a function of the gain, a linear trend appears where the x-axis intercept gives the gain that cancels out the 60 Hz noise at the atoms.

Two things to note about the amplitude to gain relationship in Section A.12. First, measuring the oscillation amplitude near the correct gain value is difficult, and the intrinsic noise in the system washes it out, requiring measurements at larger gain magnitudes. Second, if the gain is too high, the shift in the field can be larger than the resonance width, causing non-linear effects or signal clipping.

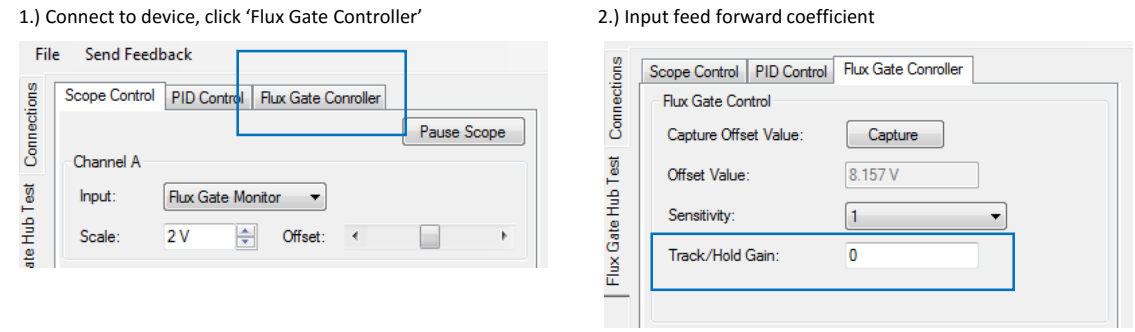

Figure A.13: Example raw data set required for calibrations of flux gate system

A.2.6 Programming the Coefficients

(This section may change in the future if the newer FPGA software is deployed for the Flux Gate controller box)

To program in the calibration coefficient for the control signal, connect to the flux gate box via the USB connection. Click the 'Flux Gate Controller' tab, and put the value into the 'Track/Hold Gain' box. Note this value can be positive or negative, make sure you are removing the signal, not doubling it! As of this moment, to insert the 60 Hz gain coefficient, similar to before, go to the PID control tab and type into the P gain setting. This is a band-aid method, co-opting an already established 32-bit register to act as the gain coefficient for the 60 Hz waveform.

A.2.7 Troubleshooting

Turn the box off, then back on. Repeat till working.

Sometimes this box and oscilloscopes do not behave together and a lot of noise appears on the line.

Appendix B

Modern FPGA Instrument System

This appendix chapter serves as documentation of work performed on the current FPGA based platform. This work encompasses extensive hardware and software development (being a large portion of my technical work within the RbLi experiment) and as such is a lengthy read. Enjoy!

B.1 Hardware

After the experience with the development of the first version of the FPGA board, there were many shortcomings that needed to be addressed. First, the FPGA board design borrowed from previous research groups did not have the analog-digital conversion focus that we require for our experiment. As a result, the older system had many electronic noise issues that caused signal degradation in our experiments. Furthermore the FPGA chip itself was an outdated part with relatively few resources to implement more complex calculations, effectively forcing corners to be cut in code so that it would reduce its firmware footprint and compile and execute in the chip.

The goal for the next version was to have a more robust analog front end that could adapt to arbitrary signal control within the experiment (for example the flux-gate based magnetic field stabilization scheme described in Section 4.4.7). Also, the holy grail of such a project was to have that such devices could integrate with the computer control sys-

tems within the experiment, bypassing the need for commercial analog-digital conversion instruments at all. In our current implementation, the computer control systems convert digital signals to analog waveforms, which then control various laboratory instruments via those analog signal levels. However, when the analog signal is sent to a remote device, it will inevitably acquire electronic noise, degrading the precision of the signal. Some of these analog control signals are sent to FPGA based devices to control a servo set point for instance. At the FPGA instrument, the signal has to be re-digitized with an ADC, which will not acquire all of the information originally sent *and* acquire noise. However, if the FPGA devices were sent data digitally, there would be ϵ amount of signal degradation, no 60 Hz line noise, or update timing issues. Thus, one objective for the next version was to be able to load a set of digital sequence values (i.e. the set point for a PID controller) for each step in an experimental sequence, effectively an arbitrary waveform generator embedded within each device.

To address these issues, a custom PCB for analog control was designed around the use a cheap, but powerful, off-the-shelf FPGA development unit.

B.1.1 DE0-NANO FPGA Board

For the second generation FPGA instruments, I used a Terasic DE0-NANO FPGA development boards as the starting point of the design. The boards come built with a modern (as of 2013) Altera Cyclone IV FPGA, built in USB-JTAG programming circuitry, and importantly 32 MB of RAM to which sequencing data can be stored. It is worth noting that while 32 MB is small for today's systems, there is enough space to store 4 million experimental steps for a four channel PID controller. Assuming that the data is triggered intelligently, this is more than adequate amount of space for the typical experimental cycle run within the lab.

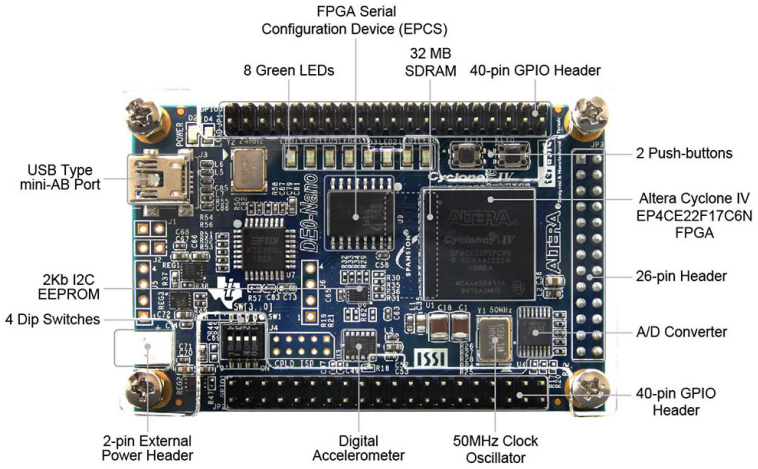

Figure B.1: DE0-Nano Development board. (Figure from Terasic website)

B.1.2 Custom Circuit Board for Digital Control of Analog Signals

The design of the PCB is divided into two separate regions - the analog and digital sections of the board. To help prevent high speed switching noise from the FPGA from contaminating the analog portion of the board, the analog and digital sections are electrically disconnected from each other, with digital isolators bridging the connection between the FPGA and analog-digital converter ICs.

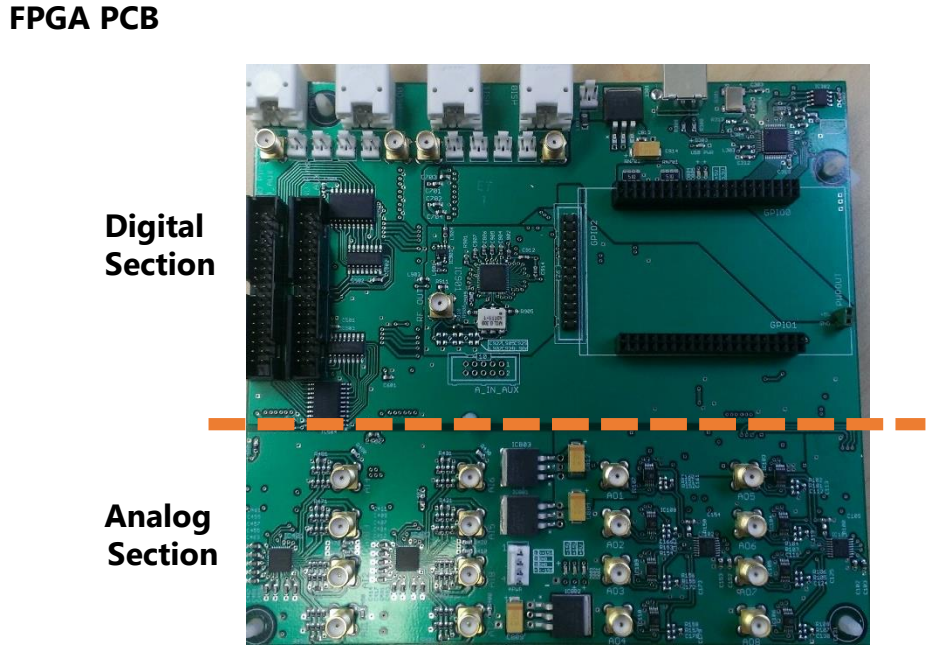

Figure B.2: The second version of the FPGA board

B.1.3 Digital Section

FPGA

One of the most prominent features on the digital side of the custom PCB is the socket for attaching the DE0-Nano development board to the FPGA board. To remove the need for ribbon cables (which can radiate digital noise), the boards 'socket' into one another. A helpful feature of the development board is the physical arrangement of the connector pins. All pins are neatly arranged into two separate banks, making it simple to directly connect the board into another appropriately designed PCB. Similarly the power pins on the development board can be attached in the same way, providing all requisite power and communication connections. Another advantage of having a socketed design allows 'hot swapping' of different development boards that are flashed with different code set.

Figure B.3

Direct-Digital-Synthesis IC for RF Waveforms

Another digital subsystem of the custom PCB is the inclusion of a Direct-Digital-Synthesis (DDS) IC. This IC, the AD9911, was chosen as it is able to drive frequencies up to 250 MHz with 10 bits of amplitude resolution. The large frequency range allows for the device, with an appropriate external amplifier, to act as a precise AOM driver that can be digitally controlled. The device also features digital triggering lines for near-instantly switching between pre-programmed frequency values, helpful for doing high-speed frequency ramps.

The DDS output contains, in series with the RF signal path, a mini-circuits AD1T1 transformer to AC couple the RF waveform. Also there are placements on the PCB for a

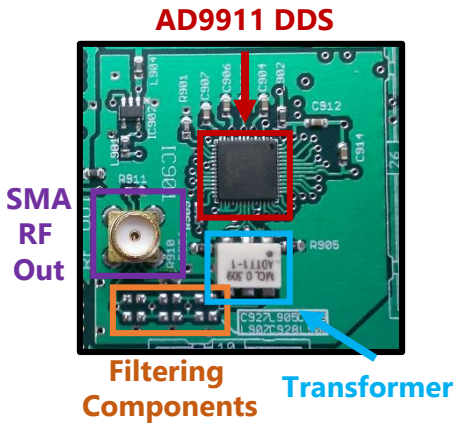

Figure B.4: DDS region of the FPGA PCB

frequency filter that attenuates frequencies above 250 MHz, helping to reject noise from the waveform.

USB Remote Communication

The second most important portion of the custom PCB (next to the FPGA itself) is the USB communication section of the board. The design is centered around an FTDI FT232H USB-to-Parallel interface chip. This chip was specifically chosen for its ability to communicate at full USB2.0 speeds (480 Mbps), especially helpful if loading experimental ramps into the FPGA memory. The design runs 8 bits in parallel from the FPGA to the FT232H chip, with all data transactions timed to a provided 60 MHz clock source (see FTDI 245 synchronous communication documentation on the FTDI website). There is also an attached EEPROM chip that stores the USB configuration information, such as vendor and part ID numbers, that is provided to the remote operating system upon USB connection.

Digital Inputs and Outputs

A set of pins on the custom PCB are digital lines that run directly to and from the FPGA, to be used for high speed digital signaling and timing. To adapt the design for laboratory electronics, a set of 8 lines each were dedicated to providing digital inputs and outputs respectively. The inputs are 50 Ω terminated lines, connected via BNC or SMA connectors. The outputs have a high current digital driver allowing interface to other 50 Ω

terminated instruments. The trace spacing and widths on the PCB were calculated to give approximately 50 Ω impedance as well, to further reduce ringing on the digital lines.

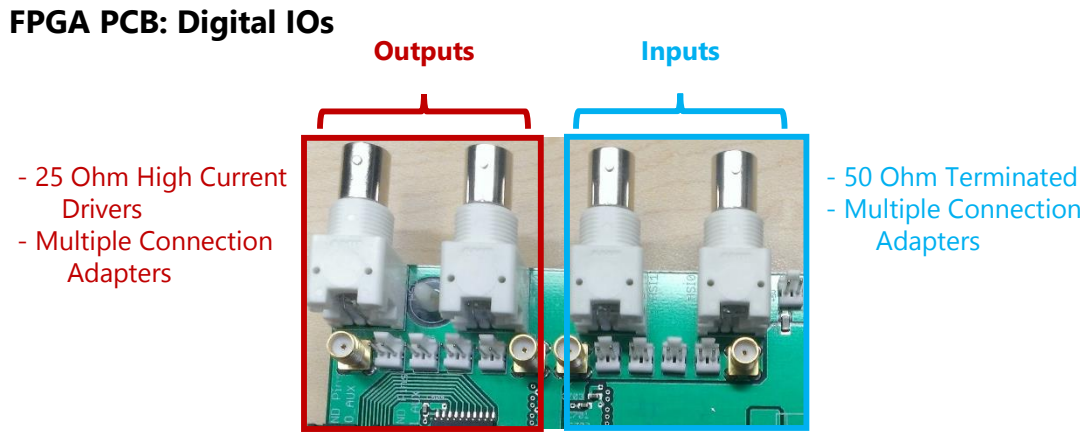

Figure B.5

Secondary Digital Inputs and Outputs

In addition to the high speed digital line, a bank of 16 digital inputs and 16 digital outputs were placed on the board using a set of shift register ICs, effectively multiplexing 3 FPGA digital lines into 16. These lines, because of the shift register design, are best served for digital timing the is not faster than $\approx$ 100 kHz. These uses include things such as LED indicators, front panel knobs and switches. The input lines have a 50 Ω terminated arrangement, along with a Schmitt trigger IC to help reduce any 'bounce' effects from switches and knobs. The outputs equivalently have 50 Ω digital drivers for interfacing with other laboratory instrumentation or providing moderate current to objects such as LEDs.

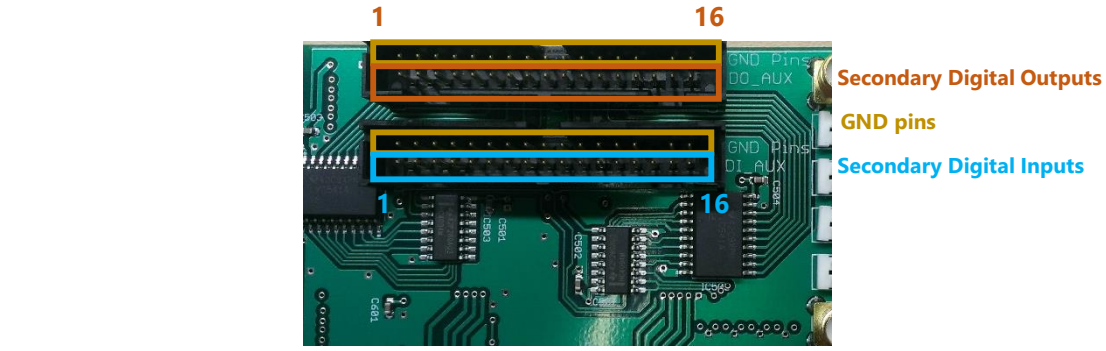

Figure B.6

B.1.4 Analog Section

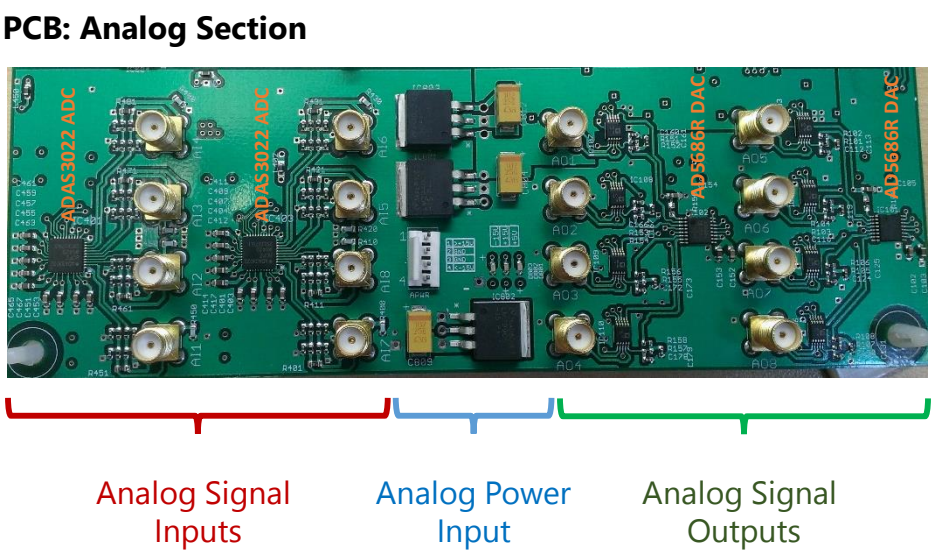

Figure B.7

The main usage of the FPGA system is to interface with experimental instruments and objects via analog signals, and as such there is a half of the PCB dedicated to the digitizing of analog signals.

Analog-to-Digital Converters (ADCs)

For analog signal acquisition, the PCB is loaded with Analog Devices ADAS3022 16-bit ADCs. The ADCs provide high resolution, high update frequency up to 1 MHz along with built in variable gain amplifiers for resolution of $\pm 300\,\mu$V to $10\,\mu$V per bit, with the maximum input voltage range being ± 20.48V

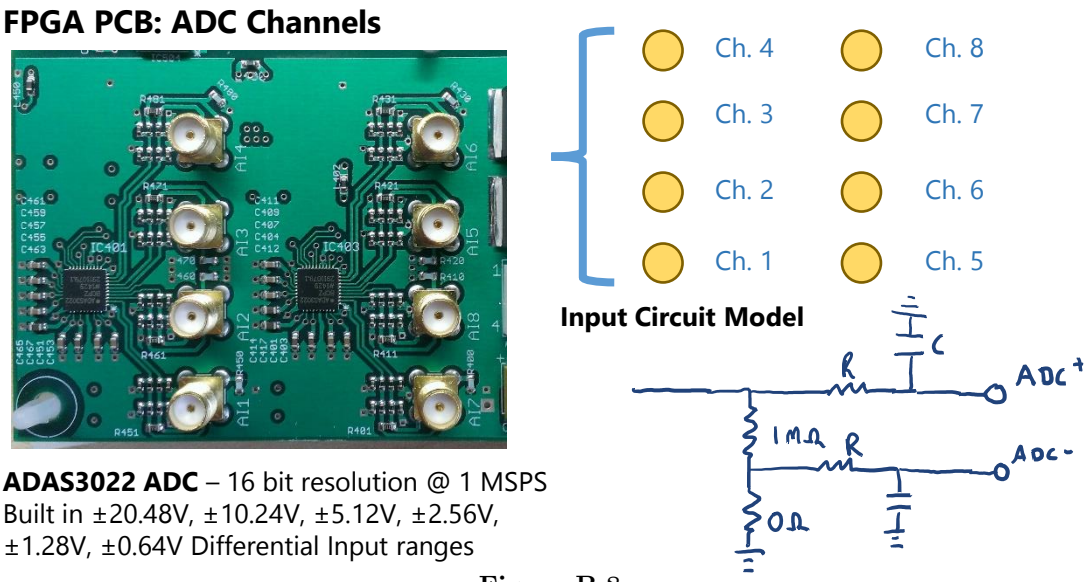

Figure B.8

The ADC is a compromise between high precision and high speed. It was chosen to be well-rounded in performance for all experimental control situations, from intensity stabilization to thermal regulation. Each of the four channels of the ADCs are differentially coupled, thereby rejecting any common mode (ground) noise in the signal. By default there is an in-line anti-aliasing filter at 1 MHz to help reject high frequency noise from being injected into the ADC. By default each input channel is terminated into 1 MΩ to ground, with the option of making the termination float to the outer connection of the SMA connector by removing a 0 Ω resistor. For measurements that require a current dropped across a resistor, for instance a hall probe for current, the 1 MΩ resistor can be replaced with a more suitable 50 Ω or 100 Ω resistor.

Digital-to-Analog Converters (DACs)

For generation of analog signals, the system uses a pair of Analog Devices AD5686R DACs, with four 16-bit channels, to provide 8 output channels. To provide a bipolar signal from the usually unipolar AD5686Rs, each channel has a AD8251 instrumentation amplifier before the output connector that subtracts the value of the voltage reference from the output signal, giving a bipolar output.

The reasons for using the AD8251 are that they provide differential outputs for the analog output channels, but more importantly have 2-bit digitally adjustable gain settings,

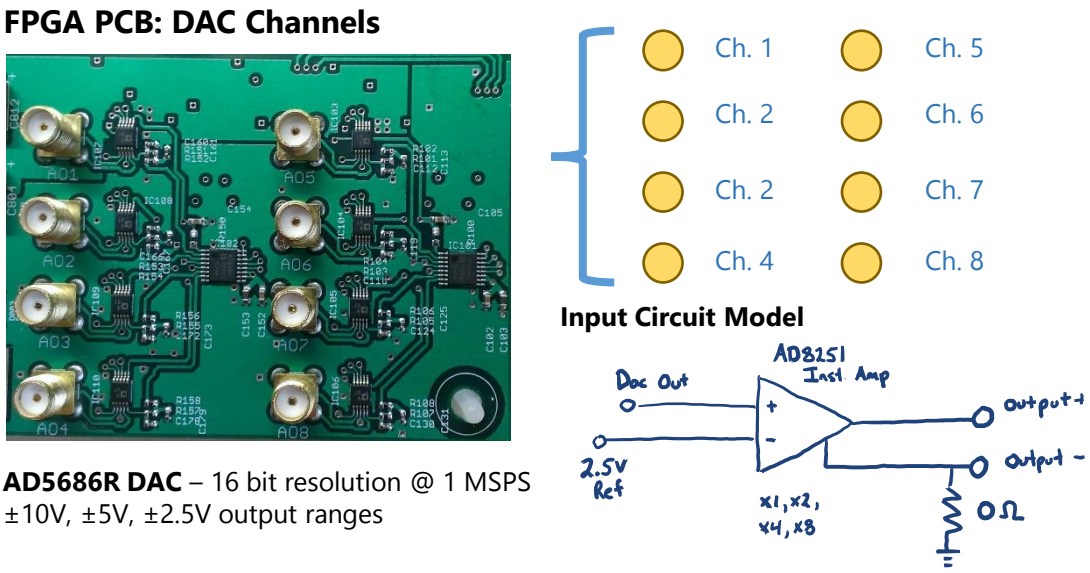

Figure B.9

giving options of gain $1, 2, 4, 8$, which leads to possible output ranges of $\pm 2.5, 5, 10, 20$ V. The additional output options are helpful for commanding systems that do not need large voltage range, keeping the 16-bit resolution over a small range of voltages. By reducing the output range, the resolution in voltage increases, thus providing more stabilization to the system or signal. The gains on the instrumentation amplifiers are set in code via the FPGA, and as such can be adjusted dynamically from a remote system, on the fly, no resistors or jumpers required. An improved version of the board would benefit from a multiplier based DAC system with adjustable offsets and limits for full resolution control.

Analog Power

The analog section uses a separate power supply from the digital section of the PCB to remove the switching noise from any analog signals. The analog portion of the board requires both ± 15 V power to provide the bipolar input and output ranges required. The board is equipped with a pair of 7815 / 7915 equivalent ± 15 V regulators so that the user can simply connect bipolar sources greater than 15V to it. A 5V regulator in series with the 15V regulator is also used to provide digital power to the ADCs and DACs. To help with diagnostics, there are 3 'power good' led indicators that verify the correct operation of the $\pm 15, +5$ V power sources. If the LEDs do not light up, there is an issue with the power supply as labels on the PCB. For reference, the board draws approximately 350 mA

of current on the positive and negative inputs during operation[1].

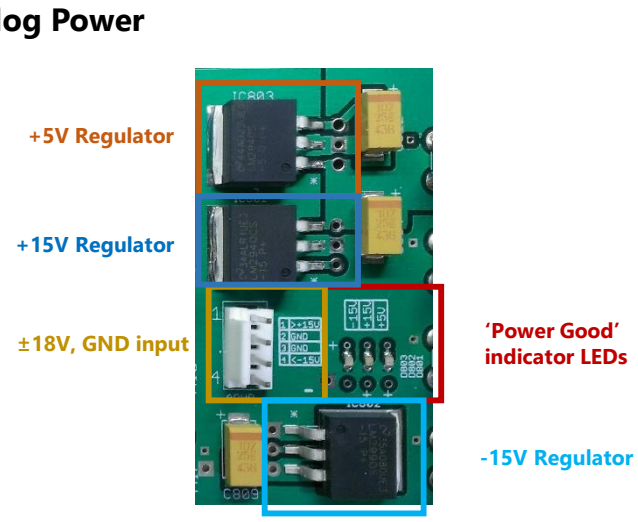

Figure B.10

To help reduce noise in the system, all ICs are connected in series to the power supplies with a ferrite bead, and to ground with a pair of 10 uf and 0.1 uf capacitors. The combination acts as an LC filter over a wide range of frequencies, and the ferrite bead ohmically dissipates the power at high frequencies.

B.2 FPGA Software Design

The firmware on the FPGAs consists of both Verilog code to generate hardware logic for digital signal processing, but also an Altera Nios 2 'soft' processor programmed into the FPGA hardware. By embedding a microprocessor into the FPGA, operations such as communication and low speed calculations can be easily facilitated into the system with no cost to hardware resources.

B.2.1 System-on-Chip (SOC) Design

To take advantage of the microprocessor in the system, the FPGA instrument system was build in a system-on-chip design style. All DSP hardware hardware blocks are embedded

[1]I did not test for the max current draw, i.e. all outputs are dumped into low resistance loads at high voltage, etc.

as different objects in the interconnected system, along with the processor, memory and other auxiliary functions such as timers. All of the devices are connected to one another through an interconnection bus that assigns memory address space to the various objects connected, allowing for arbitrary communication between objects.Each of these objects have different regions of memory that can be assigned. For a custom made PID controller object connected to the system, the registers within its address range correspond to different parameters, such as the proportional gain, or a maximum output value. Each of the hardware objects attached to the system can also communicate to remote ICs and external hardware logic as well using their own external connections.

B.3 USB Remote Communication

B.3.1 Packet Structure

To communicate with the FPGA devices over USB, a custom packet structure and protocol was developed. Because the actual USB communication protocols are transparent to the FPGA, the packet structure helps to define a protocol for flow control, data length and error checking. Without such structure, if multiple commands are queued up within the FPGA's read buffer, it would not be able to delineate where the commands begun or end thus causing possible data corruption that would go unaccounted for[2]. When dealing with large data transfers, like programming arbitrary waveform generation or retrieving data logging tables, having the communications buffer fill up is a fact of life.

The packet structure is designed to be similar to both of the common internet UDP and TCP protocols. There is a header that contains the size and relevant information as to the payload of the packet, a data section and all followed by a checksum value. In detail, the first two bytes of the packet contain the size of the packet, including header, data and checksum bytes. The next two bytes provide a command sequence. This tells the the FPGA device how to interpret the data in the address and data fields. For instance,

[2]Which did happen when first testing...

the command field can distinguish between reading data and writing data into memory locations. The packet number field is a 4 byte field that increments upon each packet transaction. This field is primarily used for flow control purposes, similar to the TCP sequence number field. The data field contains the data payload sent to the device. The interpretation of the bytes in this field depend on the command. The last two bytes of the packet are for an appended checksum value. The checksum is calculated using the CRC-16-CCITT convention with polynomial 0x1021. On these instruments, the hardware logic for USB data transfer automatically[3] handles the generation of the CRC as bytes are read in or out (see Section B.4.2).

All the fields in the packet are represented in a little endian format. Because the embedded processor uses a little endian format as well, this allows quick copying of data from the packet to a location in the instrument's memory space in a data content agnostic method. This ambivalence to the packet content also allows for the use of a direct-memory-access (DMA) controller to copy data from a packet to system memory-space at high speed, drastically increasing efficiency for large data set operations.

B.3.2 Commands

The following are a list of commands can be sent to a standard instrument.

Command Code	**Description**
0x3000	Returns list of all registered custom devices on the system. Reported in a single ASCII string, sub fields divided by commas, devices by semicolons in format: Type, Name, Memory Base Address, IRQ Number, IRQ Controller ID, Memory Span, Saveable Flag, Structure Pointer, Structure Size;
0x3001	Read the device's name
0x3002	Write the device name
0x3010	Read from memory at the value in the address field of the packet, for the length specified in the data field of the packet.
0x3011	Write to memory at the value in the address field of the packet, for the length of the data field of the packet
0x3020	Returns an identical packet to the one sent, a 'ping' for simple communication diagnostics

[3]The hardware calculates the checksum, but the code on the soft processor checks if the CRC is correct when it reads out each packet, therefore can be disabled in the code if checksum is unwanted.

B.3.3 Device Communication Model

Given the small subset of commands for communication with the device, it may seem confusing as how to go about setting parameters within the system. The SOC design methodology describes in Section B.2.1 the memory-mapped structure of all the subdevices within a system. To set a parameter on a function generator, such as the frequency, one requires the base address of the function generator and the knowledge of what the memory offset is to the frequency registers. By sending a command 0x3011 with the correct address (the device's base plus offset), the correct parameter will be updated. Command 0x3000 to the device is especially useful, as it enumerates the various subdevices in the system, and their memory-mapped locations in the instrument.

This model was deployed as it requires a minimal number of commands for an arbitrary amount of subdevices within the system. This means being able to have a single physical FPGA and PCB that can easily operate multiple distinct laboratory instrument functions, and having easy access to them.

To provide extra information about the different subdevices, the user can access the structure in the processor memory associated with specific subdevice. This structure in the CPU memory, located at the address given in by command 0x3000, can have unique identifier fields for each device. For instance for an oscilloscope subdevice, the names of the channels, and their scalings, can be saved into the CPU memory versus a resource intensive setup in the hardware itself.

B.4 System Sub-devices

The following is an enumeration of the different devices that can be found on one of the FPGA devices, and their memory-mapped structures.

B.4.1 System Info

Memory Offset	Access (Reading and Writing)	Register Description
0	**R**	Number of 1 second ticks since the device was powered
1	**R/W**	Firmware Version Code
2	**R/W**	QSYS Code Build Time
3	**R/W**	QSYS Code Build ID
4	**R**	Upper 64-Bit number of CPU ticks since start
5	**R**	Lower 64-Bit number of CPU ticks since start

Figure B.11: System Info Subdevice Memory-Mapping

B.4.2 USB

Memory Offset	Access (Reading and Writing)	Register Description
0	**--**	--
1	**--**	--
2	**R**	RXD Buffer Fill
3	**R**	TXD Buffer Fill
4	**R**	IRQ State
5	**R/W**	Number of bytes in the RXD buffer that triggers and IRQ to the CPU to indicate data received
6	**R**	RXD Buffer Size
7	**R**	TXD Buffer Size
8	**R**	Number of bytes sent from the device
9	**R/W**	Running CRC value on the RXD channel, writing anything causes the running CRC to reset (useful at end of packet)
10	**R/W**	Running CRC value on the TXD channel, writing anything causes the running CRC to reset (useful at end of packet)
11	**R**	Number of bytes in the current RXD CRC calculation
12	**R**	Number of bytes in the current TXD CRC calculation
15	**R**	Number of bytes read into the device

Figure B.12: System Info Subdevice Memory-Mapping

B.4.3 PID

Memory Offset	Access (Reading and Writing)	Register Description
0	**R**	Data size (in bits)
1	**R**	Coeffcient size (in bits)
2	**R**	Shift of the proportional gain for fixed-point arithmetic
3	**R**	General fixed point shift of coeffcients
4	**R**	Sampling rate, in Hz
5	**R/W**	Error Offset
6	**R/W**	Maximum Output
7	**R/W**	Minimum Output
8	**R/W**	Enable PID Controller
9	**R/W**	Enable Integrator
10	**R/W**	Enable Derivative
11	**--**	--
12	**R**	Read Input A
13	**R**	Read Input B
14	**R**	Read Input C
15	**R**	Read Input D
16	**R**	Read output signal
17	**R**	State of PID Controller (0 - Off, 1- Bad Lock, 2 – Locked, 3- Locked near minimum / maximum output)
20	**R/W**	Enable external lock signal port
21	**R**	State of external lock
32	**R/W**	P Coeffcient
40	**R/W**	I Coeffcient
48	**R/W**	D Coeffcient

Figure B.13: Function Generator Subdevice Memory-Mapping

B.4.4 Function Generator

Memory Offset	Access (Reading and Writing)	Register Description
0	**R/W**	Amplitude Value
1	**R/W**	Offset Value
2	**R/W**	Phase Value
3	**R/W**	Frequency Value
4	**R/W**	On/Off Toggle
5	**R/W**	Function Selector
6	**R**	Read default output
7	**R**	Read triangle output
8	**R**	Read sawtooth output
9	**R**	Read square output
10	**R**	Read sine output
11	**R**	Read cosine output
12	**R**	Read tangent output
13	**R**	Read TTL output

Figure B.14: Function Generator Subdevice Memory-Mapping

B.4.5 Analog IO Controller

Memory Offset	Access (Reading and Writing)	Register Description
0-7	**R**	Read Analog Out (AO) value, Channel 1-8
8-15	**R**	Read Analog In (AI) value, Channel 1-8
16-23	**R/W**	Static Analog Out value, Channel 1-8
24-31	**R/W**	Analog Out gain 0 - ±2.5V 1 - ±5V 2 - ±10V 3 - ±20V)
32-39	**R/W**	Analog In gain 0 - ±24.576 1 - ±10.24V 2 - ±5.12V 3 - ±2.56V 4 - ±1.28 5 - ±0.64V 7 - ±20.48
40	**R/W**	Enable Static analog out values

Figure B.15: Analog IO Controller Subdevice Memory-Mapping

Bibliography

[1] W. D. Phillips and H. Metcalf, "Laser deceleration of an atomic beam," *Physical Review Letters*, vol. 48, no. 9, p. 596, 1982.

[2] A. L. Migdall, J. V. Prodan, W. D. Phillips, T. H. Bergeman, and H. J. Metcalf, "First observation of magnetically trapped neutral atoms," *Physical Review Letters*, vol. 54, no. 24, p. 2596, 1985.

[3] E. Raab, M. Prentiss, A. Cable, S. Chu, and D. E. Pritchard, "Trapping of neutral sodium atoms with radiation pressure," *Physical Review Letters*, vol. 59, no. 23, p. 2631, 1987.

[4] M. A. Joffe, W. Ketterle, A. Martin, and D. E. Pritchard, "Transverse cooling and deflection of an atomic beam inside a zeeman slower," *JOSA B*, vol. 10, no. 12, pp. 2257–2262, 1993.

[5] M. H. Anderson, J. R. Ensher, M. R. Matthews, C. E. Wieman, and E. A. Cornell, "Observation of bose-einstein condensation in a dilute atomic vapor," *science*, vol. 269, no. 5221, pp. 198–201, 1995.

[6] K. B. Davis, M.-O. Mewes, M. R. Andrews, N. Van Druten, D. Durfee, D. Kurn, and W. Ketterle, "Bose-einstein condensation in a gas of sodium atoms," *Physical review letters*, vol. 75, no. 22, p. 3969, 1995.

[7] K. O'hara, S. Hemmer, M. Gehm, S. Granade, and J. Thomas, "Observation of a strongly interacting degenerate fermi gas of atoms," *Science*, vol. 298, no. 5601, pp. 2179–2182, 2002.

[8] R. Onofrio, C. Raman, J. Vogels, J. Abo-Shaeer, A. Chikkatur, and W. Ketterle, "Observation of superfluid flow in a bose-einstein condensed gas," *Physical Review Letters*, vol. 85, no. 11, p. 2228, 2000.

[9] M. Greiner, O. Mandel, T. Esslinger, T. W. Hänsch, and I. Bloch, "Quantum phase transition from a superfluid to a mott insulator in a gas of ultracold atoms," *nature*, vol. 415, no. 6867, pp. 39–44, 2002.

[10] N. Hinkley, J. Sherman, N. Phillips, M. Schioppo, N. Lemke, K. Beloy, M. Pizzocaro, C. Oates, and A. Ludlow, "An atomic clock with 10–18 instability," *Science*, vol. 341, no. 6151, pp. 1215–1218, 2013.

[11] J. Baron, W. C. Campbell, D. DeMille, J. M. Doyle, G. Gabrielse, Y. V. Gurevich, P. W. Hess, N. R. Hutzler, E. Kirilov, I. Kozyryev, *et al.*, "Order of magnitude smaller limit on the electric dipole moment of the electron," *Science*, vol. 343, no. 6168, pp. 269–272, 2014.

[12] A. Abramovici, W. E. Althouse, R. W. Drever, Y. Gürsel, S. Kawamura, F. J. Raab, D. Shoemaker, L. Sievers, R. E. Spero, K. S. Thorne, *et al.*, "Ligo: The laser interferometer gravitational-wave observatory," *Science*, vol. 256, no. 5055, pp. 325–333, 1992.

[13] H. Yao and S. A. Kivelson, "Exact chiral spin liquid with non-abelian anyons," *Physical review letters*, vol. 99, no. 24, p. 247203, 2007.

[14] D. Sherrington and S. Kirkpatrick, "Solvable model of a spin-glass," *Physical review letters*, vol. 35, no. 26, p. 1792, 1975.

[15] D. Hsieh, Y. Xia, D. Qian, L. Wray, J. Dil, F. Meier, J. Osterwalder, L. Patthey, J. Checkelsky, N. Ong, *et al.*, "A tunable topological insulator in the spin helical dirac transport regime," *Nature*, vol. 460, no. 7259, pp. 1101–1105, 2009.

[16] C. J. Pethick and H. Smith, *Bose-Einstein condensation in Dilute Gases*. Cambridge University Press, July 2002.

[17] S. S. L. Pitaevskii, *Bose-Einstein Condensation*.

[18] L. De Broglie, *Recherches sur la théorie des quanta*. PhD thesis, Migration-université en cours d'affectation, 1924.

[19] R. K. Pathria, *Statistical Mechanics*. Butterworth-Heinemann.

[20] D. J. Griffiths, *Introduction to Quantum Mechanics*. Prentice Hall.

[21] J. Sakurai, *Modern Quantum Mechanics*. Addison-Wesley.

[22] C. J. Foot, *Atomic Physics*.

[23] C. C. Bradley, C. Sackett, J. Tollett, and R. G. Hulet, "Evidence of bose-einstein condensation in an atomic gas with attractive interactions," *Physical Review Letters*, vol. 75, no. 9, p. 1687, 1995.

[24] J. M. Gerton, D. Strekalov, I. Prodan, and R. G. Hulet, "Direct observation of growth and collapse of a bose–einstein condensate with attractive interactions," *Nature*, vol. 408, no. 6813, pp. 692–695, 2000.

[25] F. Schreck, G. Ferrari, K. Corwin, J. Cubizolles, L. Khaykovich, M.-O. Mewes, and C. Salomon, "Sympathetic cooling of bosonic and fermionic lithium gases towards quantum degeneracy," *Physical Review A*, vol. 64, no. 1, p. 011402, 2001.

[26] G. Modugno, G. Ferrari, G. Roati, R. Brecha, A. Simoni, and M. Inguscio, "Bose-einstein condensation of potassium atoms by sympathetic cooling," *Science*, vol. 294, no. 5545, pp. 1320–1322, 2001.

[27] E. P. Gross, "Hydrodynamics of a superfluid condensate," *Journal of Mathematical Physics*, vol. 4, no. 2, pp. 195–207, 1963.

[28] L. Pitaevskii, "Vortex lines in an imperfect bose gas," *Sov. Phys. JETP*, vol. 13, no. 2, pp. 451–454, 1961.

[29] G. Baym and C. Pethick, "Ground-state properties of magnetically trapped bose-condensed rubidium gas," *Physical review letters*, vol. 76, no. 1, p. 6, 1996.

[30] K. E. Wilson, Z. L. Newman, J. D. Lowney, and B. P. Anderson, "In situ imaging of vortices in bose-einstein condensates," *Physical Review A*, vol. 91, no. 2, p. 023621, 2015.

[31] M.-S. Chang, "Coherent spin dynamics of a spin-1 bose-einstein condensate."

[32] Y. Castin and R. Dum, "Bose-einstein condensates in time dependent traps," *Phys. Rev. Lett.*, vol. 77, pp. 5315–5319, Dec 1996.

[33] H. J. Metcalf, *Laser Cooling and Trapping*.

[34] P. Zeeman, "On the influence of magnetism on the nature of the light emitted by a substance.," *The Astrophysical Journal*, vol. 5, p. 332, 1897.

[35] D. A. Steck, "Rubidium 87 d line data." 2003.

[36] P. D. Lett, R. N. Watts, C. I. Westbrook, W. D. Phillips, P. L. Gould, and H. J. Metcalf, "Observation of atoms laser cooled below the doppler limit," *Physical Review Letters*, vol. 61, no. 2, p. 169, 1988.

[37] J. Dalibard and C. Cohen-Tannoudji, "Laser cooling below the doppler limit by polarization gradients: simple theoretical models," *JOSA B*, vol. 6, no. 11, pp. 2023–2045, 1989.

[38] S. Chu, J. Bjorkholm, A. Ashkin, and A. Cable, "Experimental observation of optically trapped atoms," *Physical Review Letters*, vol. 57, no. 3, p. 314, 1986.

[39] D. Hall, M. Matthews, J. Ensher, C. Wieman, and E. Cornell, "Dynamics of component separation in a binary mixture of bose-einstein condensates," *Physical Review Letters*, vol. 81, no. 8, p. 1539, 1998.

[40] D. Hall, M. Matthews, C. Wieman, and E. Cornell, "Measurements of relative phase in two-component bose-einstein condensates," *Physical Review Letters*, vol. 81, no. 8, p. 1543, 1998.

[41] D. R. Scherer, C. N. Weiler, T. W. Neely, and B. P. Anderson, "Vortex formation by merging of multiple trapped bose-einstein condensates," *Physical review letters*, vol. 98, no. 11, p. 110402, 2007.

[42] M. Andrews, C. Townsend, H.-J. Miesner, D. Durfee, D. Kurn, and W. Ketterle, "Observation of interference between two bose condensates," *Science*, vol. 275, no. 5300, pp. 637–641, 1997.

[43] A. Beer, "Bestimmung der absorption des rothen lichts in farbigen flüssigkeiten," *Annalen der Physik*, vol. 162, no. 5, pp. 78–88, 1852.

[44] G. Reinaudi, T. Lahaye, Z. Wang, and D. Guéry-Odelin, "Strong saturation absorption imaging of dense clouds of ultracold atoms," *Optics letters*, vol. 32, no. 21, pp. 3143–3145, 2007.

[45] C. Stan, "Experiments with interacting bose and fermi gases."

[46] B. Anderson and M. Kasevich, "Loading a vapor-cell magneto-optic trap using light-induced atom desorption," *Physical Review A*, vol. 63, no. 2, p. 023404, 2001.

[47] A. Putra, D. L. Campbell, R. M. Price, S. De, and I. Spielman, "Optimally focused cold atom systems obtained using density-density correlations," *Review of Scientific Instruments*, vol. 85, no. 1, p. 013110, 2014.

[48] A. Putnis, *An Introduction to Mineral Sciences*. Cambridge University Press, Oct. 1992.

[49] A. Hubert and R. Schäfer, *Magnetic Domains*, vol. 21. Springer, 1998.

[50] T. W. B. Kibble, "Topology of cosmic domains and strings," *J. Phys. A: Math. Gen.*, vol. 9, p. 1387, Oct. 1976.

[51] C. N. Weiler, T. W. Neely, D. R. Scherer, A. S. Bradley, M. J. Davis, and B. P. Anderson, "Spontaneous vortices in the formation of Bose–Einstein condensates," *Nature*, vol. 455, pp. 948–951, Oct. 2008.

[52] T.-L. Ho, "Spinor bose condensates in optical traps," *Phys. Rev. Lett.*, vol. 81, pp. 742–745, Jul 1998.

[53] T. Ohmi and K. Machida, "Bose-Einstein condensation with internal degrees of freedom in alkali atom gases," *J. Phys. Soc. Jpn.*, vol. 67, no. 6, pp. 1822–1825, 1998.

[54] D. M. Weld, P. Medley, H. Miyake, D. Hucul, D. E. Pritchard, and W. Ketterle, "Spin gradient thermometry for ultracold atoms in optical lattices," *Phys. Rev. Lett.*, vol. 103, no. 24, p. 245301, 2009.

[55] M. Hoefer, J. Chang, C. Hamner, and P. Engels, "Dark-dark solitons and modulational instability in miscible two-component Bose-Einstein condensates," *Phys. Rev. A*, vol. 84, p. 041605, Oct. 2011.

[56] D. S. Hall, M. R. Matthews, J. R. Ensher, C. E. Wieman, and E. A. Cornell, "Dynamics of component separation in a binary mixture of Bose-Einstein condensates," *Phys. Rev. Lett.*, vol. 81, no. 8, pp. 1539–1542, 1998.

[57] K. M. Mertes, J. W. Merrill, R. Carretero-González, D. J. Frantzeskakis, P. G. Kevrekidis, and D. S. Hall, "Nonequilibrium Dynamics and Superfluid Ring Excitations in Binary Bose-Einstein Condensates," *Phys. Rev. Lett.*, vol. 99, p. 190402, Nov. 2007.

[58] E. Bookjans, A. Vinit, and C. Raman, "Quantum Phase Transition in an Antiferromagnetic Spinor Bose-Einstein Condensate," *Phys. Rev. Lett.*, vol. 107, p. 195306, Nov. 2011.

[59] Z. Dutton and C. Clark, "Effective one-component description of two-component Bose-Einstein condensate dynamics," *Phys. Rev. A*, vol. 71, no. 6, p. 063618, 2005.

[60] R. Barnett, A. Turner, and E. Demler, "Classifying Novel Phases of Spinor Atoms," *Phys. Rev. Lett.*, vol. 97, p. 180412, Nov. 2006.

[61] Y. Kawaguchi and M. Ueda, "Symmetry classification of spinor Bose-Einstein condensates," *Phys. Rev. A*, vol. 84, p. 053616, Nov. 2011.

[62] J. Stenger, S. Inouye, D. M. Stamper-Kurn, H. J. Miesner, A. P. Chikkatur, and W. Ketterle, "Spin domains in ground-state bose-einstein condensates," *Nature*, vol. 396, pp. 345–348, 11 1998.

[63] W. Zhang, D. L. Zhou, M.-S. Chang, M. S. Chapman, and L. You, "Dynamical instability and domain formation in a spin-1 bose-einstein condensate," *Phys. Rev. Lett.*, vol. 95, p. 180403, Oct 2005.

[64] L. E. Sadler, J. M. Higbie, S. R. Leslie, M. Vengalattore, and D. M. Stamper-Kurn, "Spontaneous symmetry breaking in a quenched ferromagnetic spinor Bose–Einstein condensate," *Nature*, vol. 443, pp. 312–315, Sept. 2006.

[65] M. Vengalattore, J. Guzman, S. R. Leslie, F. Serwane, and D. M. Stamper-Kurn, "Periodic spin textures in a degenerate $f = 1$ ^{87}rb spinor bose gas," *Phys. Rev. A*, vol. 81, p. 053612, May 2010.

[66] J. Guzman, G.-B. Jo, A. N. Wenz, K. W. Murch, C. K. Thomas, and D. M. Stamper-Kurn, "Long-time-scale dynamics of spin textures in a degenerate $f = 1$ ^{87}rb spinor bose gas," *Phys. Rev. A*, vol. 84, p. 063625, Dec 2011.

[67] D. M. Stamper-Kurn and M. Ueda, "Spinor Bose gases: Explorations of symmetries, magnetism and quantum dynamics." arXiv:1205.1888.

[68] K. E. Strecker, G. B. Partridge, A. G. Truscott, and R. G. Hulet, "Formation and propagation of matter-wave soliton trains," *Nature*, vol. 417, pp. 150–153, May 2002.

[69] S. E. Pollack, D. Dries, M. Junker, Y. P. Chen, T. A. Corcovilos, and R. G. Hulet, "Extreme Tunability of Interactions in a 7Li Bose-Einstein Condensate," *Phys. Rev. Lett.*, vol. 102, p. 090402, Mar. 2009.

[70] E. A. Donley, N. R. Claussen, S. L. Cornish, J. L. Roberts, E. A. Cornell, and C. E. Wieman, "Dynamics of collapsing and exploding Bose-Einstein condensates," *Nature*, vol. 412, pp. 295–299, July 2001.

[71] Y.-J. Lin, A. R. Perry, R. L. Compton, I. B. Spielman, and J. V. Porto, "Rapid production of ^{87}Rb Bose-Einstein condensates in a combined magnetic and optical potential," *Phys. Rev. A*, vol. 79, p. 063631, 2009.

[72] W. Gerlach and O. Stern, "Der experimentelle nachweis der richtungsquantelung im magnetfeld," *Zeitschrift für Physik A*, vol. 9, no. 1, pp. 349–532, 1922.

[73] P. B. Blakie, A. S. Bradley, M. J. Davis, R. J. Ballagh, and C. W. Gardiner, "Dynamics and statistical mechanics of ultra-cold bose gases using c-field techniques," *Advances in Physics*, vol. 57, no. 5, pp. 363 – 455, 2008.

[74] M. R. Matthews, B. P. Anderson, P. C. Haljan, D. S. Hall, C. E. Wieman, and E. A. Cornell, "Vortices in a bose-einstein condensate," *Phys. Rev. Lett.*, vol. 83, pp. 2498–2501, Sep 1999.

[75] P. Haljan, I. Coddington, P. Engels, and E. Cornell, "Driving bose-einstein-condensate vorticity with a rotating normal cloud," *Physical Review Letters*, vol. 87, no. 21, p. 210403, 2001.

[76] M. Tsubota, K. Kasamatsu, and M. Ueda, "Vortex lattice formation in a rotating bose-einstein condensate," *Physical Review A*, vol. 65, no. 2, p. 023603, 2002.

[77] M. V. Berry, "Quantal phase factors accompanying adiabatic changes," in *Proceedings of the Royal Society of London A: Mathematical, Physical and Engineering Sciences*, vol. 392, pp. 45–57, The Royal Society, 1984.

[78] Y.-J. Lin, R. L. Compton, K. Jiménez-García, W. D. Phillips, J. V. Porto, and I. B. Spielman, "A synthetic electric force acting on neutral atoms," *Nature Physics*, vol. 7, no. 7, pp. 531–534, 2011.

[79] Y.-J. Lin, R. L. Compton, K. Jimenez-Garcia, J. V. Porto, and I. B. Spielman, "Synthetic magnetic fields for ultracold neutral atoms," *Nature*, vol. 462, no. 7273, pp. 628–632, 2009.

[80] N. Goldman, G. Juzeliunas, P. Ohberg, and I. B. Spielman, "Light-induced gauge fields for ultracold atoms," *Rep. Prog. Phys. 77 126401*, 2014.

[81] N. Lundblad, M. Schlosser, and J. Porto, "Experimental observation of magic-wavelength behavior in optical lattice-trapped 87rb," *arXiv preprint arXiv:0912.1528*, 2009.

[82] A. Derevianko and H. Katori, "Colloquium: Physics of optical lattice clocks," *Reviews of Modern Physics*, vol. 83, no. 2, p. 331, 2011.

[83] L. LeBlanc, K. Jiménez-García, R. Williams, M. Beeler, W. Phillips, and I. Spielman, "Gauge matters: Observing the vortex-nucleation transition in a bose condensate," *arXiv preprint arXiv:1502.07443*, 2015.

[84] Y.-J. Lin, K. Jimenez-Garcia, and I. Spielman, "Spin-orbit-coupled bose-einstein condensates," *Nature*, vol. 471, no. 7336, pp. 83–86, 2011.

[85] P. A. Kuchment, *Floquet theory for partial differential equations*, vol. 60. Birkhäuser, 2012.

[86] D. M. Stamper-Kurn and M. Ueda, "Spinor Bose gases: Symmetries, magnetism, and quantum dynamics," *Rev. Mod. Phys.*, vol. 85, pp. 1191–1244, July 2013.

[87] T. D. Stanescu and V. Galitski, "Spin relaxation in a generic two-dimensional spin-orbit coupled system," *Phys. Rev. B*, vol. 75, p. 125307, Mar 2007.

[88] J. D. Koralek, C. P. Weber, J. Orenstein, B. A. Bernevig, S.-C. Zhang, S. Mack, and D. D. Awschalom, "Emergence of the persistent spin helix in semiconductor quantum wells," *Nature*, vol. 458, pp. 610–613, 2009.

[89] C. Wang, C. Gao, C.-M. Jian, and H. Zhai, "Spin-Orbit Coupled Spinor Bose-Einstein Condensates," *Phys. Rev. Lett.*, vol. 105, p. 160403, Oct. 2010.

[90] Y.-J. Lin, K. Jiménez-García, and I. B. Spielman, "Spin-orbit-coupled Bose-Einstein condensates," *Nature*, vol. 471, pp. 83–86, 2011.

[91] T.-L. Ho and S. Zhang, "Bose-Einstein Condensates with Spin-Orbit Interaction," *Phys. Rev. Lett.*, vol. 107, p. 150403, Oct. 2011.

[92] J.-Y. Zhang, S.-C. Ji, Z. Chen, L. Zhang, Z.-D. Du, B. Yan, G.-S. Pan, B. Zhao, Y.-J. Deng, H. Zhai, S. Chen, and J.-W. Pan, "Collective Dipole Oscillations of a Spin-Orbit Coupled Bose-Einstein Condensate," *Phys. Rev. Lett.*, vol. 109, p. 115301, Sept. 2012.

[93] P. Wang, Z.-Q. Yu, Z. Fu, J. Miao, L. Huang, S. Chai, H. Zhai, and J. Zhang, "Spin-Orbit Coupled Degenerate Fermi Gases," *Phys. Rev. Lett.*, vol. 109, p. 095301, Aug. 2012.

[94] L. W. Cheuk, A. T. Sommer, Z. Hadzibabic, T. Yefsah, W. S. Bakr, and M. W. Zwierlein, "Spin-injection spectroscopy of a spin-orbit coupled Fermi gas." arxiv:1205.3483, 2012.

[95] V. Galitski and I. B. Spielman, "Spin–orbit coupling in quantum gases," *Nature*, vol. 494, pp. 49–54, Feb. 2013.

[96] M. Atala, M. Aidelsburger, M. Lohse, J. T. Barreiro, B. Paredes, and I. Bloch, "Observation of chiral currents with ultracold atoms in bosonic ladders," *Nat. Phys.*, vol. 10, no. 8, pp. 588–593, 2014.

[97] J. Struck, C. Ölschläger, R. Le Targat, P. Soltan-Panahi, A. Eckardt, M. Lewenstein, P. Windpassinger, and K. Sengstock, "Quantum Simulation of Frustrated Classical Magnetism in Triangular Optical Lattices," *Science*, vol. 333, pp. 996–999, Aug. 2011.

[98] C. V. Parker, L.-C. Ha, and C. Chin, "Direct observation of effective ferromagnetic domains of cold atoms in a shaken optical lattice," *Nature Physics*, vol. 9, pp. 769–774, Dec. 2013.

[99] H.-J. Miesner, D. Stamper-Kurn, M. Andrews, D. Durfee, S. Inouye, and W. Ketterle, "Bosonic stimulation in the formation of a bose-einstein condensate," *Science*, vol. 279, no. 5353, pp. 1005–1007, 1998.

[100] D. Campbell, "Engineered potentials in ultracold bose-einstein condensates."

[101] S. S. Natu, X. Li, and W. S. Cole, "Striped ferronematic ground states in a spin-orbit-coupled s= 1 bose gas," *Physical Review A*, vol. 91, no. 2, p. 023608, 2015.

[102] Y.-J. Lin, R. L. Compton, A. R. Perry, W. D. Phillips, J. V. Porto, and I. B. Spielman, "Bose-Einstein condensate in a uniform light-induced vector potential," *Phys. Rev. Lett.*, vol. 102, p. 130401, 2009.

[103] Y.-J. Lin, R. L. Compton, K. Jimenez-Garcia, W. D. Phillips, J. V. Porto, and I. B. Spielman, "A synthetic electric force acting on neutral atoms," *Nature Physics*, vol. 7, pp. 531–534, 2011.

[104] S.-C. Ji, J.-Y. Zhang, L. Zhang, Z.-D. Du, W. Zheng, Y.-J. Deng, H. Zhai, S. Chen, and J.-W. Pan, "Experimental determination of the finite-temperature phase diagram of a spin–orbit coupled Bose gas," *Nature Physics*, vol. 10, pp. 314–320, Mar. 2014.

[105] W. H. Zurek, "Cosmological experiments in superfluid helium?," *Nature*, vol. 317, pp. 505–508, Oct. 1985.

[106] I. Bloch, J. Dalibard, and S. Nascimbène, "Quantum simulations with ultracold quantum gases," *Nature Physics*, vol. 8, no. 4, pp. 267–276, 2012.

[107] M. Greiner and S. Fölling, "Condensed-matter physics: Optical lattices," *Nature*, vol. 453, no. 7196, pp. 736–738, 2008.

[108] M. W. Zwierlein, J. R. Abo-Shaeer, A. Schirotzek, C. H. Schunck, and W. Ketterle, "Vortices and superfluidity in a strongly interacting fermi gas," *Nature*, vol. 435, no. 7045, pp. 1047–1051, 2005.

[109] H. Träuble and U. Essmann, "Flux-line arrangement in superconductors as revealed by direct observation," *Journal of Applied Physics*, vol. 39, no. 9, pp. 4052–4059, 1968.

[110] R. E. Packard and T. Sanders Jr, "Observations on single vortex lines in rotating superfluid helium," *Physical Review A*, vol. 6, no. 2, p. 799, 1972.

[111] E. L. L.D. Landau, *Fluid Mechanics*.

[112] J. Jackson, *Classical Electrodynamics, 3rd Edition*.

[113] E. Lundh, C. J. Pethick, and H. Smith, "Zero-temperature properties of a trapped bose-condensed gas: Beyond the thomas-fermi approximation," *Physical Review A*, vol. 55, no. 3, p. 2126, 1997.

[114] F. Dalfovo and S. Stringari, "Bosons in anisotropic traps: Ground state and vortices," *Physical Review A*, vol. 53, no. 4, p. 2477, 1996.

[115] M. Matthews, B. Anderson, P. Haljan, D. Hall, C. Wieman, and E. Cornell, "Vortices in a bose-einstein condensate," *Physical Review Letters*, vol. 83, no. 13, p. 2498, 1999.

[116] D. R. Scherer, C. N. Weiler, T. W. Neely, and B. P. Anderson, "Vortex formation by merging of multiple trapped bose-einstein condensates," *Phys. Rev. Lett.*, vol. 98, p. 110402, Mar 2007.

[117] A. E. Leanhardt, A. Görlitz, A. P. Chikkatur, D. Kielpinski, Y. Shin, D. E. Pritchard, and W. Ketterle, "Imprinting vortices in a bose-einstein condensate using topological phases," *Phys. Rev. Lett.*, vol. 89, p. 190403, Oct 2002.

[118] V. Tkachenko, "Stability of vortex lattices," *Sov. Phys. JETP*, vol. 23, no. 6, pp. 1049–1056, 1966.

[119] J. Abo-Shaeer, C. Raman, J. Vogels, and W. Ketterle, "Observation of vortex lattices in bose-einstein condensates," *Science*, vol. 292, no. 5516, pp. 476–479, 2001.

[120] F. Dalfovo, S. Giorgini, L. P. Pitaevskii, and S. Stringari, "Theory of bose-einstein condensation in trapped gases," *Rev. Mod. Phys.*, vol. 71, pp. 463–512, Apr 1999.

[121] F. Chevy, K. Madison, V. Bretin, and J. Dalibard, "Formation of quantized vortices in a gaseous bose-einstein condensate," in *Trapped Particles and Fundamental Physics*, pp. 109–124, Springer, 2002.

[122] S. Stock, B. Battelier, V. Bretin, Z. Hadzibabic, and J. Dalibard, "Bose-einstein condensates in fast rotation," *Laser Physics Letters*, vol. 2, no. 6, p. 275, 2005.

[123] D. R. Murray, P. Öhberg, D. Gomila, and S. M. Barnett, "Vortex nucleation in bose-einstein condensates due to effective magnetic fields," *Physical Review A*, vol. 79, no. 6, p. 063618, 2009.

[124] I. Spielman, "Raman processes and effective gauge potentials," *Physical Review A*, vol. 79, no. 6, p. 063613, 2009.

[125] L. Wen, H. Xiong, B. Wu, *et al.*, "Hidden vortices in a bose-einstein condensate in a rotating double-well potential," *Physical Review A*, vol. 82, no. 5, p. 053627, 2010.

[126] D. Campbell, R. Price, A. Putra, A. Valdés-Curiel, D. Trypogeorgos, and I. Spielman, "Itinerant magnetism in spin-orbit coupled bose gases," *arXiv preprint arXiv:1501.05984*, 2015.

[127] J. Radić, T. A. Sedrakyan, I. B. Spielman, and V. Galitski, "Vortices in spin-orbit-coupled bose-einstein condensates," *Phys. Rev. A*, vol. 84, p. 063604, Dec 2011.

[128] C. Dedman, R. Dall, L. Byron, and A. Truscott, "Active cancellation of stray magnetic fields in a bose-einstein condensation experiment," *Review of scientific instruments*, vol. 78, no. 2, p. 024703, 2007.